LOCKHEED MARTIN ENERGY RESEARCH LIBRARIES
3 4456 0515704 0

CENTRAL RESEARCH LIBRARY
DOCUMENT COLLECTION

cy 1

ORNL-4545
UC-20 – Controlled Thermonuclear Processes

# THERMONUCLEAR DIVISION
# ANNUAL PROGRESS REPORT
# FOR PERIOD ENDING DECEMBER 31, 1969

OAK RIDGE NATIONAL LABORATORY
CENTRAL RESEARCH LIBRARY
DOCUMENT COLLECTION
LIBRARY LOAN COPY
DO NOT TRANSFER TO ANOTHER PERSON
If you wish someone else to see this document, send in name with document and the library will arrange a loan.
UCN-7969
(3 3-67)

OAK RIDGE NATIONAL LABORATORY
operated by
UNION CARBIDE CORPORATION
for the
U.S. ATOMIC ENERGY COMMISSION

Printed in the United States of America. Available from Clearinghouse for Federal Scientific and Technical Information, National Bureau of Standards, U.S. Department of Commerce, Springfield, Virginia 22151
Price: Printed Copy $3.00; Microfiche $0.65

LEGAL NOTICE

This report was prepared as an account of Government sponsored work. Neither the United States, nor the Commission, nor any person acting on behalf of the Commission:

A. Makes any warranty or representation, expressed or implied, with respect to the accuracy, completeness, or usefulness of the information contained in this report, or that the use of any information, apparatus, method, or process disclosed in this report may not infringe privately owned rights; or

B. Assumes any liabilities with respect to the use of, or for damages resulting from the use of any information, apparatus, method, or process disclosed in this report.

As used in the above, "person acting on behalf of the Commission" includes any employee or contractor of the Commission, or employee of such contractor, to the extent that such employee or contractor of the Commission, or employee of such contractor prepares, disseminates, or provides access to, any information pursuant to his employment or contract with the Commission, or his employment with such contractor.

ORNL-4545
UC-20 – Controlled Thermonuclear Processes

Contract No. W-7405-eng-26

# THERMONUCLEAR DIVISION

# ANNUAL PROGRESS REPORT

## For Period Ending December 31, 1969

AUGUST 1970

OAK RIDGE NATIONAL LABORATORY
Oak Ridge, Tennessee
operated by
UNION CARBIDE CORPORATION
for the
U. S. ATOMIC ENERGY COMMISSION

LOCKHEED MARTIN ENERGY RESEARCH LIBRARIES

Reports previously issued in this series are as follows:

| | |
|---|---|
| ORNL-2693 | Period Ending January 30, 1959 |
| ORNL-2802 | Period Ending July 31, 1959 |
| ORNL-2926 | Period Ending January 31, 1960 |
| ORNL-3011 | Period Ending July 31, 1960 |
| ORNL-3104 | Period Ending January 31, 1961 |
| ORNL-3239 | Period Ending October 31, 1961 |
| ORNL-3315 | Period Ending April 30, 1962 |
| ORNL-3392 | Period Ending October 31, 1962 |
| ORNL-3472 | Period Ending April 30, 1963 |
| ORNL-3564 | Period Ending October 31, 1963 |
| ORNL-3652 | Period Ending April 30, 1964 |
| ORNL-3760 | Period Ending October 31, 1964 |
| ORNL-3836 | Period Ending April 30, 1965 |
| ORNL-3908 | Period Ending October 31, 1965 |
| ORNL-3989 | Period Ending April 30, 1966 |
| ORNL-4063 | Period Ending October 31, 1966 |
| ORNL-4150 | Period Ending April 30, 1967 |
| ORNL-4238 | Period Ending October 31, 1967 |
| ORNL-4401 | Period Ending December 31, 1968 |

# Contents


INTRODUCTION ..... 1

ABSTRACTS ..... 4

1. PLASMA THEORY AND COMPUTATION ..... 9

1.1 Synopsis ..... 9

1.2 Mirror Systems ..... 9

1.2.1 Microinstabilities in a Model Mirror Plasma ..... 9
1.2.2 Modification of the Electrostatic Dispersion Relation Due to Coupling to Electromagnetic Modes ..... 13
1.2.3 An Estimate of the Maximum Stable Pressure in the ELMO Device ..... 16
1.2.4 Simulation of the High-Beta Hot-Electron Plasma ELMO ..... 17
1.2.5 Electrostatic Instabilities in Multicomponent Hot-Electron Plasmas ..... 18
1.2.6 An Electromagnetic Loss-Cone Instability ..... 20

1.3 Toroidal Systems ..... 21

1.3.1 Introduction ..... 21
1.3.2 MHD Equilibria ..... 22
1.3.3 High-Beta Equilibria in TOKAMAK's with Large Toroidal Curvature ..... 25
1.3.4 Magnetic Field of a Current Loop in a Toroidal Conductor ..... 25

1.4 Turbulent Heating and Nonlinear Problems ..... 25

1.4.1 Turbulent Heating of Ions in Beam-Plasma Experiments ..... 25
1.4.2 Beam-Plasma Interaction with a Plasma Density Gradient ..... 28
1.4.3 Wave-Particle Energy Transfer and Wave Amplitude Limiting Effects ..... 31
1.4.4 Relativistic and Finite Cyclotron Radius Effects in Electron-Cyclotron Heating ..... 32
1.4.5 Numerical Solution of the Nonlinear Vlasov Equation ..... 34

1.5 Abstracts of Preprints ..... 36

1.5.1 Microinstabilities in Inhomogeneous Plasmas: Theory ..... 36
1.5.2 Explosive Plasma Instabilities ..... 36
1.5.3 Stability of TOKAMAK's ..... 36
1.5.4 Theory of High-Frequency Instabilities in Mirror-Confined Plasmas ..... 36
1.5.5 Classical Plasma Phenomena from a Quantum Mechanical Viewpoint ..... 36
1.5.6 Integral Solutions to the Generalized Helmholtz Equation ..... 37
1.5.7 Damping of Plasma Oscillations in Atoms ..... 37

2. TARGET PLASMAS ..... 38

2.1 Introduction ..... 38

2.2 INTEREM ..... 39
2.2.1 Introduction ..... 39
2.2.2 Target Plasma Studies in INTEREM ..... 39
2.2.3 Target Plasma Parameters ..... 40
2.2.4 Electron Energy Distributions ..... 41
2.2.5 Instability Studies ..... 41
2.2.6 Electron-Beam–Plasma Interaction ..... 44
2.3 IMP ..... 46
2.3.1 Introduction ..... 46
2.3.2 Descriptions of the Apparatus and Diagnostics ..... 46
2.3.3 Assembly and Checkout ..... 50
2.3.4 Mirror Plasma in IMP ..... 50
2.3.5 Trapping Calculations ..... 50
2.3.6 Acknowledgments ..... 56
2.4 Scatter Experiments ..... 56
3. TOROIDAL CONFINEMENT ..... 58
3.1 Introduction ..... 58
3.2 ORMAK ..... 58
3.3 Toroidal Multipole ..... 58
4. HIGH-BETA PLASMA ..... 59
4.1 Off-Resonant Heating ..... 59
4.1.1 Introduction ..... 59
4.2 Off-Resonant Heating with $\omega > \omega_{ce}$ ..... 59
4.3 Driven Losses with Low-Frequency Microwave Power ..... 61
4.3.1 Perpendicular Energy Measurements ..... 62
4.3.2 Wall X-Ray Energies ..... 63
4.3.3 Time Dependence of Wall X Rays ..... 64
4.3.4 Effect of Low-Frequency Microwave Power on the Electron Distribution in ELMO ..... 64
4.3.5 Spatial Diffusion ..... 65
4.3.6 Neutrons ..... 66
4.3.7 Calorimetric Measurements ..... 67
4.4 Instability Studies ..... 68
4.4.1 Near Gyrofrequency Instability ..... 68
4.4.2 Mirror Instability ..... 68
4.4.3 Flute Modes ..... 69
4.5 Ion Hybrid Heating ..... 69
4.6 Summary ..... 70
5. TURBULENT HEATING ..... 72
5.1 Theoretical Models ..... 72
5.1.1 Introduction ..... 72
5.1.2 Limitations on Beam-Plasma Heating of Electrons and Ions ..... 72

5.1.3 Turbulent Heating Mechanisms ..... 73
5.1.4 Electron and Ion Heating in Beam-Created Plasmas ..... 75
5.1.5 Limitations of the Beam-Plasma Facility Hot-Electron Plasma ..... 76
5.1.6 Stochastic Electric Pumping ..... 77
5.1.7 Possible Ion-Heating Mechanism ..... 77

5.2 Burnout V ..... 78

5.2.1 Introduction ..... 78
5.2.2 Four Ion-Heating Modes ..... 78
5.2.3 Ion Energy-Density Distribution from Neutral-Particle Flux ..... 79
5.2.4 Plasma Structure ..... 80
5.2.5 Use of Forbidden Spectra to Measure Large High-Frequency Fields ..... 82
5.2.6 Plasma Impurity Reduction ..... 86
5.2.7 Soft X-Ray Emission ..... 86
5.2.8 Plasma Lifetime ..... 87
5.2.9 Doppler Studies on Copper Impurity Spectral Lines ..... 88
5.2.10 Radio-Frequency Spectrum ..... 89

5.3 Basic Turbulence Experiments ..... 90

5.3.1 Introduction ..... 90
5.3.2 Anomalous Resistivity in a Steady-State Plasma ..... 91
5.3.3 Finite Plasma Effects in a Reflex Discharge ..... 93
5.3.4 Investigation of a Glass Liner in a Small Burnout Unit ..... 97
5.3.5 Computer Simulation of Transient Sheath Formation and Ion Bursts by Numerical Solution of the Vlasov Equation ..... 97

5.4 Diagnostics ..... 98

5.4.1 Introduction ..... 98
5.4.2 Correlators ..... 98
5.4.3 Far-Infrared Laser-Interferometer ..... 99

6. PLASMA PHYSICS ..... 104

6.1 Wave Studies in a Uniform Magnetic Field ..... 104

6.1.1 Introduction ..... 104
6.1.2 Electron Landau Damping of Ion Acoustic Waves in a Unform Magnetic Field ..... 104
6.1.3 Ion Acoustic Wave Excitation in a Weak Magnetic Field Via a Virtual Transmitter ..... 104
6.1.4 Dispersion Measurements of Externally Excited Drift Waves ..... 106
6.1.5 Observation of Slow Waves Propagating Across a Uniform Magnetic Field ..... 106

6.2 Computer Simulation Studies of Low-Frequency Nonlinear Plasma Behavior ..... 108

6.2.1 Introduction ..... 108
6.2.2 Ion Acoustic Wave Excitation and Ion Sheath Evolution ..... 108
6.2.3 Interaction Between Ion Acoustic Wave and Sheath ..... 109
6.2.4 Expanding Plasma Into a Vacuum ..... 109

6.3 Pseudowaves ..... 110

6.3.1 Introduction ..... 110
6.3.2 Reflection of Pseudowaves ..... 111
6.3.3 Multiple Pseudowaves ..... 111

6.4 Diagnostic Techniques ..... 114

6.4.1 Introduction ..... 114

6.4.2 A Pulsed Grid for Measuring Plasma Ion Density and Electron Temperature . . . . . 114
6.4.3 A Negatively Biased Grid for Exciting $\omega_{pi}$ in a Magnetic Field . . . . . 115

7. INJECTION AND ACCUMULATION . . . . . 116

7.1 Neutral Injection Experiments (DCX-1.5) . . . . . 116

7.1.1 Evolution and Stabilization of Flutes in a Magnetic Mirror . . . . . 116
7.1.2 Harris Instabilities in a Plasma of Finite Length . . . . . 116

7.2 Multiple-Pass Experiments (DCX-2) . . . . . 116

7.2.1 Introduction . . . . . 116
7.2.2 Gas Breakup Instability Behavior . . . . . 117
7.2.3 Energetic Proton Plasma Behavior . . . . . 119
7.2.4 Discussion . . . . . 123

8. ATOMIC AND MOLECULAR PHYSICS . . . . . 124

8.1 The Coulomb Logarithm for Energetic Test Ions . . . . . 124

8.2 Electron and Ion Spectrometry . . . . . 126

8.3 Multiple Excitation of Neon by Photon and Electron Impact . . . . . 132

8.4 Electron Energy Levels in Free Atoms from $Z = 1$ to $Z = 60$ . . . . . 132

8.5 Scattering from Inelastic Collisions . . . . . 132

8.6 Energy Loss in Foils . . . . . 136

8.7 Detector Development . . . . . 136

8.8 Atomic and Molecular Processes Information Center . . . . . 137

9. ENERGETIC-PARTICLE INJECTION . . . . . 138

9.1 Introduction . . . . . 138

9.2 Intense Low-Energy Hydrogen Ion Beams . . . . . 138

9.3 Hydrogen Cluster Ion Source . . . . . 141

10. MAGNETICS AND SUPERCONDUCTIVITY . . . . . 147

10.1 Review of Basic Work on Applied Superconductivity . . . . . 147

10.2 Thermal Equilibrium of Superconducting Wires in the Flux-Flow State . . . . . 148

10.3 Niobium-Titanium Compound Conductors with Twisted Filaments . . . . . 150

10.3.1 Short-Sample Tests . . . . . 150
10.3.2 Cusp-Coil Tests . . . . . 152
10.3.3 Magnets . . . . . 152
10.3.4 Conclusion . . . . . 154

10.4 A New Design Principle for Three-Dimensional Magnet Windings . . . . . 155

10.5 Temperature-Compensated Trimming Windings for Water-Cooled Magnet Coils . . . . . 155

10.6 Progress on Engineering of the IMP Facility (Phase II) . . . . . 161

10.6.1 Introduction . . . . . 161
10.6.2 $Nb_3Sn$ Conductors for the Quadrupoles . . . . . 161

10.6.3 Stress Analysis of the Coil Cans . . . . . 166
10.6.4 Status of Principal Mechanical Components . . . . . 167

11. FUSION FEASIBILITY . . . . . 168

11.1 Introduction . . . . . 168

11.2 Fusion Reactor Materials . . . . . 168

11.2.1 Sputtering . . . . . 168
11.2.2 Radiation Damage . . . . . 169

11.3 Neutronics . . . . . 170

11.4 Mirror Feasibility . . . . . 170

11.5 General Considerations . . . . . 170

11.6 Work in Progress . . . . . 170

PUBLICATIONS, ORNL REPORTS, AND PAPERS . . . . . 172

# Introduction

H. Postma

This annual report contains the results of a number of programmatic changes that took place during the past year. The DCX-2 experiment and the levitated multipole programs were terminated to free manpower, money, and talents for the new Oak Ridge TOKAMAK experiments (ORMAK). At the same time, the Plasma Physics Group joined the turbulent heating program to provide more capabilities for exploiting the plasmas created there. We see sprinkled throughout the report a shift in interests in order to implement these new programs, whether they be the theory of magnetohydrodynamic equilibria in tori, or the development of low-energy ion analyzers.

Thus this annual is one that reports transition. There are the old programs being given their final touches and also the new (IMP and ORMAK) being described. While seemingly disjointed by variety, the annual contains much that threads through several programs and has broad applicability. In this Introduction we point out many instances of these traits.

There are experimental-theoretical remainders of a program closed down for several years: the final elegant touches on flute stability and Harris instabilities are applied to the DCX-1.5 plasma (Sect. 7.1). As is indicated by experiments described there, the effects of finite length on the plasma characteristics can be well correlated with theory. Though these are the final parts of an experimental correlation, the theory it represents is applicable and important to quite different plasmas, even those that are reactor-like (Sect. 1).

During the first half of the year DCX-2 ran well, and the correspondence between theory and experiment grew closer; yet attempts to increase the density by turbulence or endplate-fed rf to force it to a more pertinent density regime failed, and the flexibility of the machine was insufficient to allow more significant changes. Thus, only somewhat prematurely, it was closed down in July 1969. In reviewing the DCX-2 experiments there can be much pride in the discovery of the mechanisms that were responsible for the plasma's central peak and heating mechanisms. These could be well defined and calculated through the theory of the modified-negative-mass instability developed by that group. This theory explained not only the DCX-2 but other important mirror experiments performed elsewhere: PR-6; DECA-II; experiments in magnetic wells, in simple mirrors; with moderate densities, or with low densities. The physics was clear – thus DCX-2 fulfilled its task to succeed or to explain why the approach should be abandoned. This annual gives in Sect. 7.2 a sample of the final experiments done on that facility.

The toroidal multipole also ceased operation in July so that its resources, along with those of DCX-2, might be devoted to the ORMAK. The work there, however, was not completed. The many experiments planned on effects of induced electric field effects and scaling at high magnetic fields were unfortunately not carried to the point of obtaining definitive results, even though the methods were clearly proven. So we have in the annual here only an interim report; fortunately this work is now being carried out at the University of Rochester by Moshe J. Lubin, and significant results on the plasma loss dependence on magnetic fields were reported by this group and by Lubin at the Dubna conference.

Another program changing direction this year was that of basic plasma physics. The past annuals have depicted an elegant array of experiments focusing on wave studies of plasmas both with and without magnetic fields. This has been a prolific group in the Division, and even though they devoted only the first half of this year to those studies, we find in the annual in Sect. 6 a variety of important work involving computer simulation, new diagnostic techniques, pseudowaves, and waves in magnetic fields. And further, though they were involved with turbulence studies only during the latter half of this year, we find significant

contributions in the mechanisms of turbulent heating (Sect. 5) as well as an elegant experiment on anomalous resistivity in a steady-state plasma (Sect. 5.3). These studies are probably related to the turbulent processes that heat particles in the TOKAMAK geometries, and thus our interest.

To change now to continuing programs, Sect. 4 on high-$\beta$ plasmas contains, with typical understatement, only a hint that there exists a steady-state $\beta \sim 1$ plasma created by electron-cyclotron heating in which two-frequency heating has quenched instabilities. This in itself is remarkable, but the inferences are even greater: the fact that the application of two frequencies adjusts electron distributions so as to quench instabilities portends well for the target plasma. This additional control provides much more leeway in developing proper targets. The application of this technique to a series of closed mirrors suggests an important way of examining high-$\beta$ effects in tori. In addition, the demonstration of high $\beta$ in mirror devices bodes well for mirror reactors. As you may recall, feasibility calculations almost demand that level of performance in order that the mirror approach remain viable. In addition to these messages, Sect. 4 depicts experiments on heating at "cheaper" wavelengths, on driven losses, and on two methods to heat ions through appropriate wave coupling. In the theory (in Sect. 1) we find explanations for some of these losses as well as proper recognition that high-$\beta$ plasmas can still be line-tied. Two holdovers remain mysteries – the larger-than-expected neutron flux and the annular shape of the high-$\beta$ portion of the plasma. Recent experimental cross-section measurements by a German group on the dissociation of deuterium by electrons have only intensified the mystery about the mechanism for the enhanced neutron flux. Theory comforts us only in saying that the annular shape is a possible equilibrium – we do not yet know why the plasma chooses this particular one.

The target plasma program (Sect. 2) remains a strong theme of the ORNL CTR program. While progress on the construction of the IMP facility has not met expectations, we can balance that disappointment with the excellent understanding from INTEREM. There, experiments have accurately defined the parameters of a target created by electron-cyclotron heating in a magnetic well. These target parameters (target quality of 30 and target density of $10^{12}$ cm$^{-3}$), though controlled by instabilities, seem to scale well for the IMP experiment at its higher microwave frequencies; but we are thankful for the ELMO experiment, where through two-frequency heating similar instabilities seem to be eliminated. The IMP experiment began in August 1969, though only in phase I (simple mirror configuration). The coils met design criteria and have operated trouble free since being commissioned; the diagnostics and coils performed as expected, and the target plasma itself was consistent with the previous experience in ELMO. The phase II operation, with quadrupole coils, is eagerly awaited since the IMP can prove the validity of target plasmas created by electron-cyclotron heating and since the INTEREM and ELMO experiences suggest the success of the target formation. The trapping calculations outlined here indicate a somewhat easier task of ion buildup than previously calculated. The account of the development of the quadrupole coils is given in Sect. 10.6.

The new closed confinement program, embodied in its experimental form as ORMAK, represents an exciting undertaking for the Division. The brief recounting given in Sect. 3 hardly does justice to the significance of the experiment. The success of the Russian TOKAMAK's is now well known. The description of ORMAK here is brief, since its details are in easily obtainable form as a technical memo. What is not told is the eagerness with which we are all looking forward to measuring the parameters, seeking scaling laws, and understanding the physics of what so far has been the most fusion-like plasma in the worldwide CTR effort.

We find emphasized in Sect. 5, on turbulent heating, a search for mechanisms that cause the ions to be heated in Burnout V. There are as well, in Sect. 1, tentative explanations of the heating mechanisms. It is too early to distinguish one or two instabilities or models as accounting for the extraordinarily efficient heating modes, but when we do have that knowledge we will extend this understanding to the ORMAK or use it to heat ions in electron-cyclotron plasmas, to create targets, or perhaps to heat ions in some other configuration. Among the best of the physics appearing this year was the use of forbidden spectral lines described in Sect. 5.2.5. We have already mentioned the contributions of the former Plasma Physics Group to the efforts of turbulent heating. These appear most obviously in Sects. 5.1 and 5.3.

We acknowledge here the very evident help of our guest graduate students who under NSF, NASA, and ORAU fellowships have aided greatly through their vigor, inquisitiveness, and skills to our programs; their contributions are to be noted particularly in Sects. 5.4 and 6.2.

Injection remains vital to all anticipated mirror confinement experiments. We note with particular pride the impressive results obtained in the low-energy injection systems that are described in Sect. 9. While

the bolder cluster source is presently encountering difficulties, the beams obtained already are a good beginning toward the objective.

We observe in Sect. 8 increasingly stronger coupling of the Atomic and Molecular Physics Group to a variety of questions ranging from the energies of Franck-Condon neutrals, vital in all target plasmas, to the development and calibration of very low-energy analyzers suitable for use in almost all experiments now under way at ORNL.

The involvement of magnetics and superconductivity goes much further than the winding of coils for IMP. The diversity necessary for the design and construction of conventional coils as well as for exploitation of the latest in superconducting techniques is evident. The work in superconductivity ranges from basic studies of flux flow states to complex coil test procedures. These are given in detail in Sect. 10.

With only modest beginnings toward an enormous task we recognize in Sect. 11 some of the salient undertakings in fusion feasibility. The problems are vast, ranging from how to start a fusion reactor to how long the vacuum wall is likely to last under the intense 14-MeV neutron flux. As is seen in Sect. 11 we can only take modest but hopefully the most critical parts to examine.

Finally, we have acknowledged throughout this Introduction, where it seemed appropriate, the guiding hand of theory. Yet those brief remarks have not done the proper justice to its influence. The inquiries have ranged from the study of electromagnetic modes, with their subsequent destabilizing effects for reactor-like plasmas, to the judgment of high-$\beta$ effects in ELMO. The investigations have ranged from understanding target plasma instability modes that are likely, whether they be cold-electron stabilizing nonresonant modes, to describing the limited range in which the double-hump distribution is not operative. We also see turbulent heating explanations as well as nonlinear effects being undertaken through computer simulation. Only through a thorough reading of Sect. 1 can one gain an appreciation of the contributions of theory throughout the programs.

The valuable work of our technicians, draftsmen, engineers, and administrative staff, though it does not appear separately, is implicit throughout the report in the competence with which these programs are being carried out.

# Abstracts

## 1. PLASMA THEORY AND COMPUTATION

We report work in several distinct areas: (1) stability of mirror-confined plasmas (Sect. 1.2), (2) toroidal equilibrium and stability (Sect. 1.3), and (3) turbulent heating and nonlinear effects (Sect. 1.4). In earlier analyses of velocity-space instabilities which threaten mirror confinement, we used an infinite homogeneous plasma model, simulating the loss-cone effect with simple distribution functions and restricting the dispersion relation to electrostatic waves and low $\beta$. We now enlarge upon these approximations by considering the effects of density variations along the magnetic field (Sect. 1.2.1); possible couplings between electrostatic and electromagnetic waves (Sect. 1.2.2); and the destabilizing effect of high plasma pressure (Sect. 1.2.3). For many problems of immediate interest, however, the earlier models are still expected to be applicable. In Sect. 1.2.5 we discuss such a problem: the electron gyroharmonic instabilities observed in INTEREM. These plasmas also seem likely to support purely electromagnetic modes such as whistlers; a new electromagnetic mode is reported in Sect. 1.2.6.

In Sect. 1.3 agenda are presented for considering important but insufficiently studied questions about TOKAMAK plasmas (equilibrium, stability, particle and energy confinement, field errors, etc.). The initial entry is MHD equilibrium, studies of which have been done for geometries where toroidal curvature is important, as in forthcoming experiments. Numerical techniques have been developed to treat general equilibria. Specific cases discussed are (1) plasma confined by image forces in the conducting walls and (2) plasma in the state free of particle loss. With the techniques now in hand, parametric variations will be made to seek equilibria with optimal stability, minimum plasma transport, and values of $\beta$ adequate for reactor use.

Stability of case 1, corresponding to the Bennett pinch in a linear system, is discussed in terms of microinstability and MHD criteria (Sect. 1.5.3).

Sections 1.4.1 and 1.4.2 discuss questions arising from the observations of efficient ion heating in Burnout V: (1) What mechanisms can convert the directed energy of the electron beam into ion thermal energy? (2) Why is the electron beam not subject to unstable interactions with the background electrons? Section 1.4.3 deals with the more general question of the behavior of single charged particles in specified fluctuating fields, with the objective of clarifying the transfer of energy between particles and waves. In Sect. 1.4.4 this energy transfer is studied for a relativistic electron gas in hopes of gaining insight into the processes by which relativistic electrons are heated in the ELMO experiments. Finally, Sect. 1.4.5 reports progress toward numerical solution of the complete nonlinear Vlasov-Poisson equation. Section 1.5 consists of very brief abstracts of work in general theoretical areas or of work available in published form.

## 2. TARGET PLASMAS

Progress toward the development of a high-density, scatter-loss-dominated plasma has continued. In INTEREM, an electron-cyclotron-heated plasma with a target "quality" (defined as the ratio of target to ambient neutral density $n_t/n_0$) in excess of 30 was generated at $n_0 \approx 3 \times 10^{10}$ cm$^{-3}$. One of the principal microinstabilities contributing to anomalous losses was identified as the double-distribution mode. It became more clear that a significant improvement in $n_t/n_0$ could result from the higher fields to be available in IMP, and experiments in mirror-quadrupole geometry are eagerly awaited. The development of the quadrupole coils for IMP is described in Sect. 10.6. Preliminary experiments using the superconducting mirror coils in IMP at 10 kG are discussed. Although the plasma density is limited in this configuration by the poor choice of heating zones available because of the cramped space ($n_e \sim 10^{11}$ cm$^{-3}$ at $n_0 \sim 10^{11}$ cm$^{-3}$), good use of the operating time for diagnostic development was made.

The IMP facility is now fully operational in mirror configuration. The facility uses superconducting coils and operates with $B_0$ to 20 kG. Diagnostic checkouts

are proceeding, with emphasis on the electron cyclotron plasma created by 35-GHz microwave power. The facility and diagnostics are described, and the nature of this plasma is reviewed. Other work which is summarized includes recent calculations of hot ion accumulation in an ideal spherical target plasma (large $n_t$ and $n_t/n_0$); this calculation treats the neutral density and its geometric distribution self-consistently.

## 3. TOROIDAL CONFINEMENT

The toroidal multipole experiment has been terminated here in favor of a new toroidal program, ORMAK (Oak Ridge TOKAMAK). The multipole experiment, however, is being continued by M. Lubin at the University of Rochester in collaboration with ORNL.

The ORMAK program exploits the features of a design in which a transformer-driven copper shell replaces the many coils ordinarily used to produce a toroidal magnetic field. This design provides a greater area for the magnetic induction needed to drive the plasma current, for a particular aspect ratio (major radius/minor radius). It thus permits experiments at smaller aspect ratios than possible otherwise at high magnetic fields. It also provides improved access and promises greater symmetry. Further improvements in symmetry result from other features of the design.

The immediate program proceeds in two phases. ORMAK I reproduces a TM-3-like plasma (plasma aspect ratio $A = 5$). It will be followed by ORMAK II with larger minor radius (17 cm) and $A = 2.3$. Experiments should begin in September 1970.

In addition to the experimental program, there is in progress a computer study of TOKAMAK plasma equilibria by R. A. Dory.

## 4. ELECTRON-CYCLOTRON HEATING

Heating studies have shown that large increases in stored plasma energy are produced by microwave power with frequencies higher than the cold electron resonance frequency. This increase, caused by off-resonance heating, is attributed to stochastic heating and to the control of instabilities through changes in the electron distribution function.

On the other hand, decreases in the stored plasma energy are produced by microwave power with frequencies lower than the cold electron resonance frequency. This effect is attributed in part to enhanced diffusion into the loss cone. However, since a small number of electrons gain energy, some of the effect may be due to a resonance between the microwave power and the relativistic electrons whose gyrofrequency has dropped to match the low-frequency radiation.

## 5. TURBULENT HEATING

In support of our turbulence studies, we are developing a program which includes heating experiments, diagnostics development, and theory. Our primary experiment is the Burnout V unit. There, for example, we use high-frequency auto- and cross-correlators to examine the frequencies and propagation directions of the waves responsible for the plasma heating; we employ soft x-ray counters that allow us to follow the energy degradation process of the incident electron beam; and we use spectroscopic studies of normally forbidden lines to measure both the magnitude and the frequency of the electric field present in the plasma core.

In our theoretical program, we concentrate on the mechanism responsible for the heating process. Computer studies (Sect. 1) examine nonlinear processes numerically. Analytic studies also allow us to investigate the nonlinear region. We have recently explored an instability that is driven by a radial electric field and may be responsible for the ion heating in Burnout V. This instability competes with the beam-plasma electron-heating instability, and this competition may explain the observed fact that ion and electron heating may be obtained separately, but not together.

In addition to the Burnout V experiment, we are studying current-driven instabilities in a linear glass discharge tube. The results show that a strong instability limits current flow, regardless of the applied voltage, when the drift velocity of the electrons rises approximately to the electron thermal velocity. We feel that studying current-driven instabilities will lead us into understanding the current-driven instabilities present inside TOKAMAK-type toroidal units.

Finally, the hot-electron experiments give us additional insight into the turbulent-heating processes. We find there that a strong longitudinal standing electron wave appears to extract energy from the beam and transfer it to the plasma.

## 6. PLASMA PHYSICS

The basic plasma studies can be divided into four main categories: wave studies in uniform magnetic fields (Sect. 6.1), computer simulation studies of low-frequency nonlinear plasma behavior (Sect. 6.2), pseudowaves (Sect. 6.3), and diagnostic techniques

(Sect. 6.4). The wave studies in magnetically supported plasmas include electron Landau damping of ion acoustic waves, ion acoustic wave excitation by a virtual transmitter, dispersion measurements of externally excited drift waves, and parameter studies of an unidentified slow wave which propagates perpendicularly to the magnetic field. The computer simulation studies include the evolution of an ion sheath about negatively biased nonlinear electrodes in a plasma and the relevance of the sheath evolution to the generation of ion acoustic waves, the interaction of an ion acoustic wave with a steady-state ion sheath, and the expansion of a plasma into a vacuum. The pseudowave studies include the reflection of "single" pseudowaves at a positively biased surface and the observation of "multiple" pseudowaves and their interpretation in terms of ions trapped and oscillating in an ion sheath. The diagnostic studies include the use of a pulsed grid to measure ion density and electron temperature in both discharge and magnetically supported plasmas and the use of a negatively biased grid for measuring ion density in a magnetically supported plasma.

During the last quarter of the year all basic plasma physics research done by the group was oriented toward plasma phenomena that appear to be more directly related to the achievement of the ultimate goal of the fusion effort, specifically, concerned with turbulent heating and residing in the new turbulence group (Sect. 5), which is a combination of the former plasma physics and turbulent heating groups.

## 7. INJECTION AND ACCUMULATION

Abstracts of two available reports are included that summarize instability studies performed on DCX-1.5. One involves flute instability, the other Harris modes of finite length.

The DCX-2 experiment ceased operation in June to provide funds and personnel for the new ORMAK experiment. Our basic understanding of the major features of the DCX-2 plasma behavior (instabilities, heating, and losses) remains unchanged. However, we doubt that an unstable coupling between a low-frequency stable drift wave and an ion cyclotron frequency microinstability has been positively identified in DCX-2. The same low-frequency amplitude modulation, previously seen in the instability rf activity at the proton cyclotron frequency and in the cold plasma current and identified as due to a drift wave in the side-lobe proton group, has now been observed in the charge-exchange current from both the central-peak and side-lobe proton groups. In addition, there is indirect evidence that a significant non-charge-exchange steady-state loss of central-peak protons is occurring.

## 8. ATOMIC AND MOLECULAR PHYSICS

A revised form of the Coulomb logarithm is presented in which

$$\ln \sqrt{\frac{m^3 v_+^4 v_-^2}{4\pi Z^2 n e^6}}$$

replaces

$$\ln \sqrt{\frac{9k^3 T_-^3}{4\pi Z^2 n e^6}}$$

for the case of heavy test ions slowing down in a sea of colder plasma electrons. At very high densities, such as those in the sun or supernovae, or for very sluggish ions, this revised form breaks down and the following expression is recommended:

$$\ln (1 + y^2)^{1/2} - \frac{0.5y^2}{1 + y^2} ,$$

where

$$y = \sqrt{\frac{m^3 v_+^4 v_-^2}{4\pi n Z^2 e^6}} \sim \frac{\lambda_D m v_+^2}{Ze^2} .$$

A newly constructed electrostatic energy analyzer is briefly described. The use and versatility of the instrument are illustrated by a number of examples, such as the Auger spectrum of neon, photoelectron spectrum of neon, and characteristic electron energy losses in $H_2$ and air. The energy distribution of protons from dissociative ionization of $H_2$ has been measured and found to be in good agreement with theory. Most of the protons come from the repulsive $2p\sigma_u$ state of $H_2^+$ following excitation by 300-eV to 2.3-keV electrons.

The relative differential scattering cross sections for the inelastic processes of stripping and electron capture have been determined for H and D. One- to ten-keV H and D beams were incident on target gases of $H_2$, He, $O_2$, $N_2$, $H_2O$, Ne, Ar, Kr, and $C_6H_6$. Typical results are presented for $N_2$ as target gas. In all cases the scattering from electron-capture collisions is less than that from stripping. Scattering arising from stripping of H and D was precisely the same at the same H and D acceleration energy.

Energy loss measurements of 2- to 10-keV hydrogen atoms in carbon foils have shown that the thickness of available foils is unknown to within a factor of 2, and energy losses for particles of energy less than 2 keV are inconsistent. The counting efficiency of a commercially available Johnston multiplier was increased to approximately 100% by biasing the entrance grid 30 V negative with respect to the first dynode.

The activities of the Atomic and Molecular Processes Information Center are reviewed.

## 9. ENERGETIC-PARTICLE INJECTION

Intense 1-keV $H^0$ and hydrogen cluster ion beams are being developed for injection into minimum $B$ magnetic mirror plasma physics experiments. These energetic particles can be ionized and trapped by charge-exchange collisions with cold ions in an electron-cyclotron-heated "target plasma." The resulting plasma can reach a collisional-dominated loss-cone distribution by Coulomb collisions in the target plasma. High-frequency electrostatic instabilities of the velocity-space type that might result from this distribution can be studied.

Using a gridded duoplasmatron ion source with accel-decel electrodes, a 100-mA $H^+$ ion beam can be extracted from a 2-cm-diam surface throughout an energy range of 200 to 1000 eV. The ion beam is space-charge neutralized by using electron-emitting thoriated tungsten grids for the decel electrode and also at the center of a magnetic lens. From this system one can obtain 30 to 50 mA of 1-keV $H^+$ ions with a divergence of $\approx 2°$. One present limitation is thermal dissipation of the plasma energy by the source electrodes.

The hydrogen cluster ion system uses warmed liquid-helium vapors to cool the hydrogen gas and expansion system. Particle currents of only a few milliampere equivalence have been obtained within a cluster mass range of 50 to 1000 atoms. The present limitation appears to be dispersion of the cluster ion from transverse electric fields within the ionizer.

## 10. MAGNETICS AND SUPERCONDUCTIVITY

During this report period our basic work on applied superconductivity was again jointly sponsored by the Controlled Thermonuclear Branch of the USAEC and by the George C. Marshall Space Flight Center, NASA, Huntsville. The new nonlinearized theory of the thermal equilibrium of bare and of stabilized superconducting wires which are in the flux-flow state has been extended to the most general case in which the heat flow inside "thick" superconducting filaments must be considered. In this connection, thermal conductivity measurements on superconductors have been made. Experimental studies on the peak effect of the critical current of superconductors gave results in favor of the rigidly pinned vortex model. In these experiments the observation of a positive differential quotient of the critical current density with respect to temperature indicated the existence of zones of intrinsic stability of the tested superconductors. Finally, additional experiments were made on flux-jump phenomena in superconductors; especially, cases of limited instabilities (which are pertinent to the stability criteria for superconducting magnet coils) have been studied in detail.

Our previous observations on parasitic currents in composite conductors with fine superconducting filaments demonstrated the occurrence of loops of currents which flow partly through superconducting filaments and partly through the low-resistance copper matrix. Since by means of twisted filaments the parasitic currents can be drastically reduced, we were immediately interested in performing experiments with conductors with twisted filaments as soon as such conductors became commercially available. We report here on short-sample and cusp-coil tests made with twisted superconducting niobium-titanium material. Furthermore, we present preliminary results obtained with three magnet coils that were made from such superconducting winding material. The largest coil, with an inside diameter of 4 in., reached the short-sample performance at a field of 77 kG. The stored magnetic energy is around 100 kJ.

For the production of $B_{min}$ fields, three-dimensional magnet windings are required. A new design principle for such magnet windings has been developed here and is demonstrated for the case of a pair of Yin Yang coils.

Since it is practically impossible to build magnet coils for the generation of high-homogeneity fields which match the calculated coil geometry exactly, field-trimming devices are necessary. For large water-cooled magnet coils, it is difficult to ensure that the temperature drifts of the main and of the trimming field are the same and thus that the achieved optimum trimming holds for all power levels and is not disturbed by changes in the temperature of the water or the surroundings. A new system was devised which employs trimming wires pulled through the hollow conductors of the main coil winding. Thus the trimming and the main winding are exposed to the same cooling water temperature. The application to the 6-MW high-homogeneity coil of our magnet laboratory is described.

A great number of tests have been performed with the $Nb_3Sn$ ribbons that were purchased for the quadrupole coils of IMP. Early pancake coil tests showed marginally acceptable critical currents of 600 to 800 A. For these tests no special insulation was provided between the stainless steel ribbon surfaces, and very appreciable helium vaporization indicated that additional insulation between the turns was necessary. Other tests showed that $Nb_3Sn$ windings exposed to simultaneously increasing currents and fields are very sensitive to the field component perpendicular to the ribbon face. These critical fields, observed for instance with cusp-coil windings, are much smaller than the corresponding critical fields for short samples. This undesirable performance of $Nb_3Sn$ windings is up to the present only partly understood, and it is imperative to find a practical remedy as fast as possible. One successfully tested solution is to provide copper shunts bridging 10 to 20 turns of conductor each. A more convenient alternative is to wind high-purity aluminum foil between turns. Preliminary tests with this second method yielded encouraging results, and if the final tests are satisfactory, the IMP coils will be wound in this way.

After completion of the very involved stress calculations, one pair of quadrupole coil cans with covers has been machined and is available. The other pair is expected to be on hand by the beginning of March 1970. A test tank with a 5-ft working diameter is near completion and will serve for testing the quadrupole coils without interrupting the phase I operation of IMP.

## 11. FUSION FEASIBILITY

Studies on the feasibility of engineering a fusion reactor have continued this year with emphasis on radiation damage, sputtering, neutronics, and environmental effects. These are reported in abstract form in Chap. 11, with referrals to the papers for details.

# 1. Plasma Theory and Computation

## 1.1 SYNOPSIS

This report reflects a notable transition in fusion research at ORNL; in place of the highly singular injection plasmas of the DCX experiments, we now confront non-Maxwellian but smooth hot-electron plasmas at relatively high $\beta$, with their attendant questions of MHD stability and electron-electron velocity-space instabilities now limiting the quality of target plasmas. Here we include some preliminary and rather crude material in both categories, obviously motivated by the ELMO and INTEREM experiments. If we are to design stable target plasmas rationally, then it is incumbent upon us to test the relevant stability criteria as carefully as possible by applying known principles to the existing experiments. In this report we are still feeling around the edges of the problem; in the coming year we anticipate considerable progress toward mode identification, tests of stability criteria, and extrapolation of these criteria into next-generation experiments.

Here we report, as a continuation of earlier work on stability of mirror-confined plasmas, progress in the study of microinstabilities in plasmas of finite length. We also seek to estimate the adequacy of the electrostatic model for such modes, and find it to be very limited for fusion purposes. These two problems – effects of finite length and finite $\beta$ on microinstabilities – are not likely to find easy resolution and are surely destined for continued study as new experimental results appear.

Our new involvement in axisymmetric toroidal traps is producing interesting fundamental results on plasma equilibria under conditions representative of the proposed ORMAK experiments. Here too, the important stability questions and their implications for scaling laws and maximum stable $\beta$ remain open and will be the focal points of the future efforts.

The material on beam-plasma and idealized wave-particle interactions represents a continuing effort to gain insight into the complex processes by which ions or electrons can be heated by electric fields introduced into the plasma via electron beams or microwave sources. The wave-particle problem is also instructive as regards the nonlinear evolution of microinstabilities. However, as suggested by the report on numerical solution of the Vlasov equation, we still hope for a more complete nonlinear analysis of at least those stability problems which seem inescapable in the target-plasma problem.

## 1.2 MIRROR SYSTEMS

### 1.2.1 Microinstabilities in a Model Mirror Plasma

C. O. Beasley W. M. Farr[1] H. Grawe[2]

In ORNL-TM-2852 we developed numerical methods for solving the linearized Vlasov-Poisson equations for an equilibrium in which the density varies along the magnetic field,

$$N(z) = N_0 \exp(-z^2/L^2) .$$

Since this model uses electrostatic containment in a uniform magnetic field, it is probably most useful for studying instabilities which are not highly resonant and hence not likely to be strongly affected by magnetic field variations. One such class of instabilities has been analyzed in an infinite plasma model by Dory, Guest, and Harris.[3] These modes propagate perpendicularly to the magnetic field with frequencies around the ion gyroharmonics $\omega \sim n\Omega$, $n = 0, 1, 2, \ldots$, and wavelengths such that $k_\perp a_i \gtrsim 2.4 + 1.4n$. Here $a_i$ is the average ion gyroradius. Because the fluctuating electrostatic potential must decrease in amplitude beyond the point at which $k_\perp^2 \lambda_{\mathrm{Debye}}^2 > 1$, a finite-length plasma

---

[1] Nuclear Engineering Department, University of Arizona.

[2] Scientific Controls Systems Ltd. and Co., GmbH, Hamburg, Germany.

[3] R. A. Dory, G. E. Guest, and E. G. Harris, *Phys. Rev. Letters* **14**, 131 (1965).

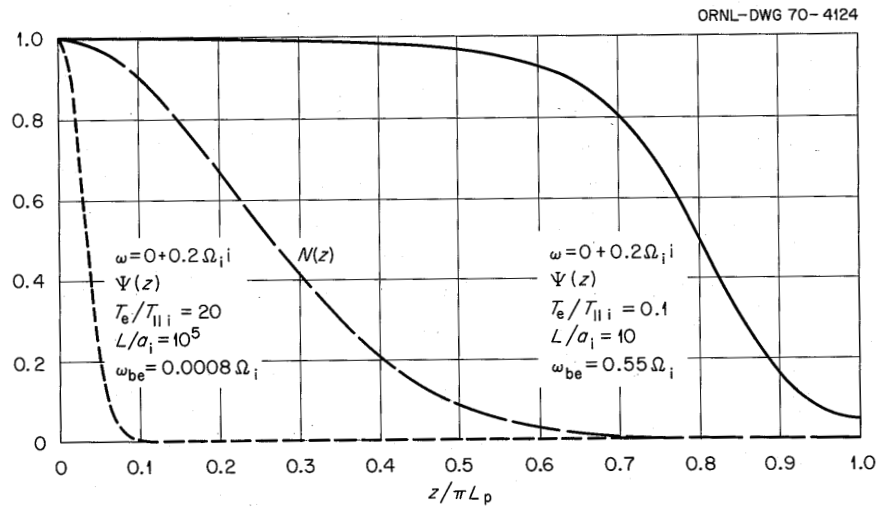


**Fig. 1.1. Perturbed Potentials and Density Distribution.**

must allow for axial electric fields which couple ions and electrons.

We distinguish two basic regimes for finite-length plasmas, depending on the magnitude of the electron bounce frequency, $\omega_{be}$, relative to other frequencies such as the wave frequency (if $\omega \neq 0$) or the growth rate $\gamma$:

1. If $\omega_{be} \ll \omega$, the eigenfunction (i.e., the fluctuating potential) can be localized in the region of maximum density, as illustrated by the dashed curve of Fig. 1.1. In the limit that $\omega_{be}$ is sufficiently small, a fluid model is adequate. One such model has been analyzed by Berk *et al.*[4] A comparison of their eigenfunctions and eigenvalues with those obtained using our numerical methods is shown in Fig. 1.2. The agreement is very good for longer plasmas ($L/a_i > 4 \times 10^3$), but for shorter plasmas, results disagree markedly. Note that for the case $\Theta = T_e/T_{\parallel i} = 0.1$, this is true even though $\omega_{be}/\Omega_i = 0.01 \ll \gamma$ at $L/a_i = 10^3$. One further observation is that in this limit, results are essentially independent of electron temperature, as shown in the $L/a_i = 10^5$ curves in Figs. 1.3 and 1.4.

2. If $\omega_{be} \gg \omega$ (or $\gamma$, for $\omega = 0$), the electrons provide good conduction along the magnetic field, and the eigenfunction remains nearly constant out to where $k_\perp \lambda_{\text{Debye}} \sim 1$, as shown by the solid curve in Fig. 1.1. In Figs. 1.2 and 1.3, the top curves show the dependence on electron temperature of the density required to support a given growth rate ($\gamma = 0.2\Omega_i$ in Fig. 1.4 for the zero-frequency mode, and $\gamma = 0.1\Omega_i$ in Fig. 1.4 for the $\omega \cong 1.2\Omega_i$ mode). The slow variation shown can be interpreted as a result of the good contact up to the point where $k_\perp \lambda_{\text{Debye}} \sim 1$ if one advances the hypothesis that the average density (over this interval) must remain constant. If

$$k_\perp^2 \lambda_{\text{Debye}}^2(z_f) = 1 = k_\perp^2 a_i^2 \frac{T_e}{T_{\perp i}} \left[ \frac{\omega_{pi}^2(0)}{\Omega_i^2} e^{-z_f^2/L^2} \right]^{-1} ,$$

then

$$\frac{z_f}{L} = \left\{ \ln \left[ \frac{\omega_{pi}^2(0)}{\Omega_i^2} \frac{1}{k_\perp^2 a_i^2} \frac{T_{\perp i}}{T_e} \right] \right\}^{1/2} .$$

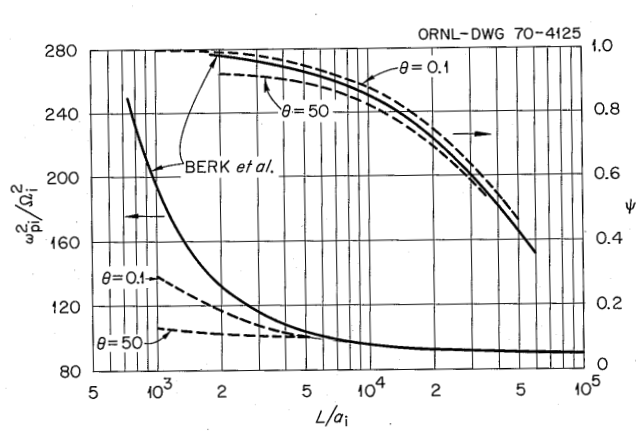


**Fig. 1.2. Density Required for $\lambda = 0.2\Omega_i$ for $\omega = 0$ ($\lambda = 0.9$, $j = 5$, $T = 3$), $\Psi$ ($z/L = \pi/20$).**

[4] H. L. Berk *et al.*, *Phys. Rev. Letters* **22**, 876 (1969).

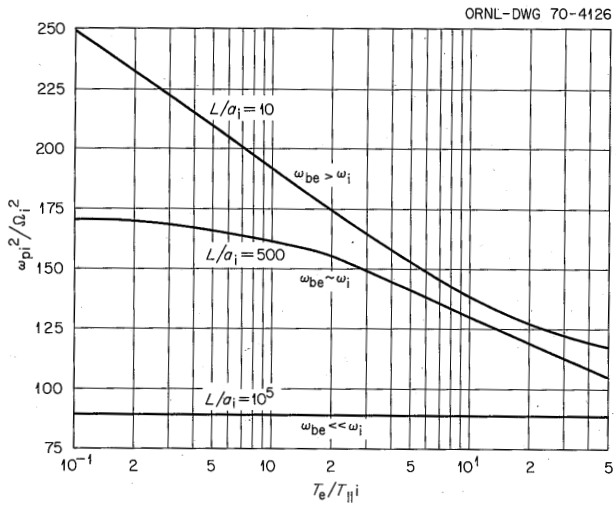


**Fig. 1.3. Density as a Function of Electron Temperature for Frequency = $(0 + 0.2i)\Omega_i$.**

The average density in this model is

$$\left(\overline{\frac{\omega_{pi}^2}{\Omega_i^2}}\right) = \frac{\omega_{pi}^2(0)}{\Omega_i^2}\,\frac{L}{z_f}\,\mathrm{erf}\,\frac{z_f}{L}$$

$$= \text{const}$$

if the growth rate is constant. Combining these gives

$$\frac{\omega_{pi}^2(0)}{\Omega_i^2} = \left(\overline{\frac{\omega_{pi}^2}{\Omega_i^2}}\right)\frac{1}{\mathrm{erf}\,z_f/L}\left\{\ln\left[\frac{\omega_{pi}^2(0)}{\Omega_i^2}\,\frac{1}{k_\perp^2 a_i^2}\,\frac{T_{\perp i}}{T_e}\right]\right\}^{1/2},$$

which describes the curve of Fig. 1.3 reasonably well, so long as $z_f/L \gtrsim 1$. The center curve in Fig. 1.3 shows a case where there is a transition between the two types of modes.

The discrete bounce frequencies characteristic of the parabolic potential used in the present model lead to difficulties of analysis and interpretation in regions of parameter space where the growth rate is less than but comparable with $\omega_b$, since the eigenvalues are affected by nearby bounce harmonics. This is illustrated in Fig. 1.5, which shows density vs growth rate for the mode with $\omega \approx 1.2\Omega$ for three plasma configurations: (1) infinite plasma (indistinguishable from $L/a_i = 10^5$), (2) $L/a_i = 10$ with $T_e/T_{\|i} = 100$, and (3) $L/a_i = 10$ with $T_e/T_{\|i} = 0.1$. The abrupt variation in curve 2 occurs when $\omega_{bi} = \gamma$. Similar curves showing the effect of the transition from $\gamma > \omega_{be}$ to $\gamma < \omega_{be}$ are shown in Figs. 1.6 and 1.7, which again display density vs growth rate but for the zero-frequency mode. In Fig. 1.6 we indicate the appearance of a new instability (at $\gamma \lesssim 0.08$) with $\omega \sim 0.1\Omega_i$ and density below the infinite-plasma value. This branching is shown for several plasma parameters in Fig. 1.7; the approximate locus of all the branch points is shown dashed. These results have been obtained only for high electron temperatures

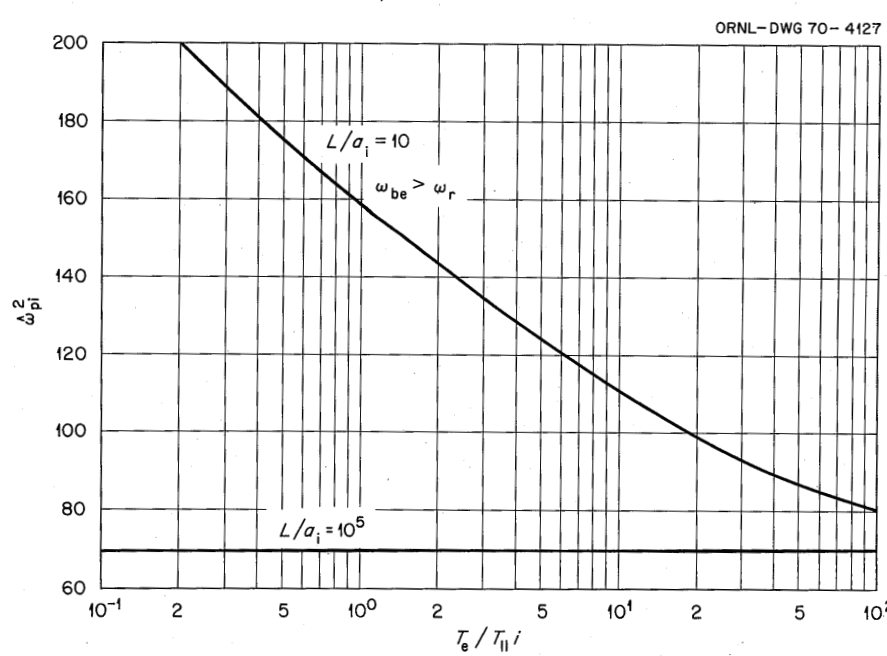


**Fig. 1.4. Density Variation with Electron Temperature for Frequency $\sim(1.2 + 0.1i)\Omega_i$.**

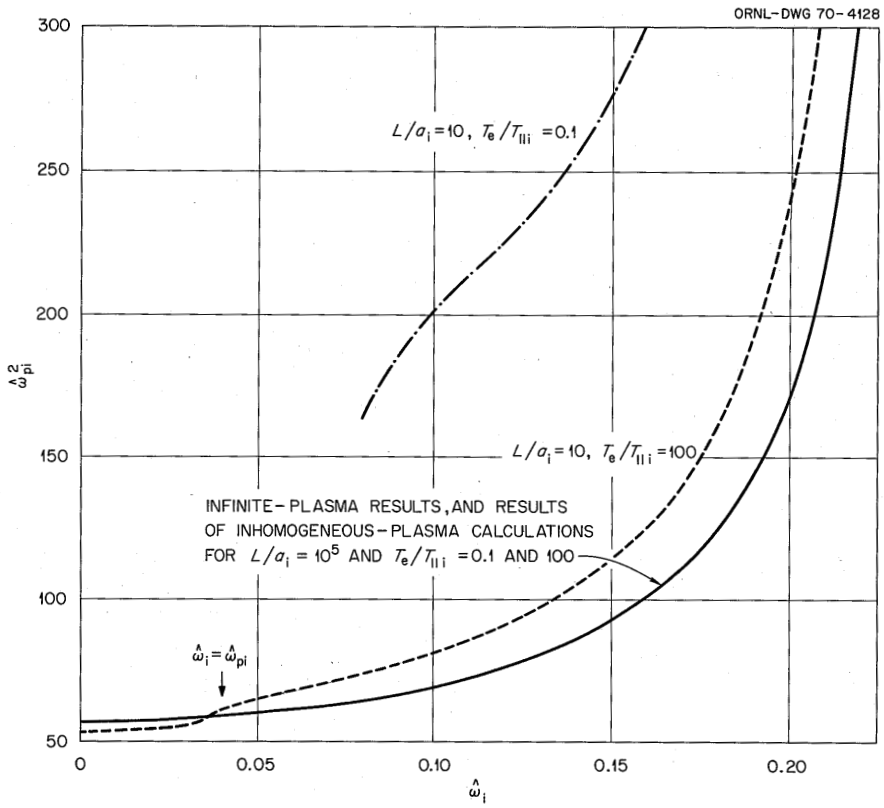


**Fig. 1.5. Density as a Function of Growth Rate.**

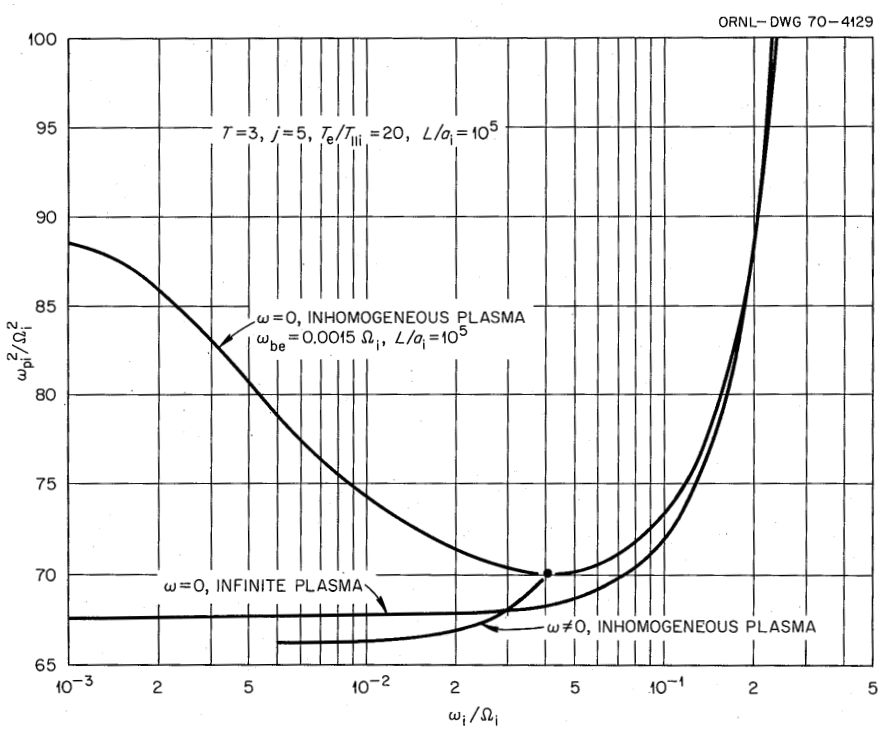


**Fig. 1.6. Density as a Function of Growth Rate for Infinite Plasma, Zero-Frequency Mode, and $\omega \neq 0$ Mode.**

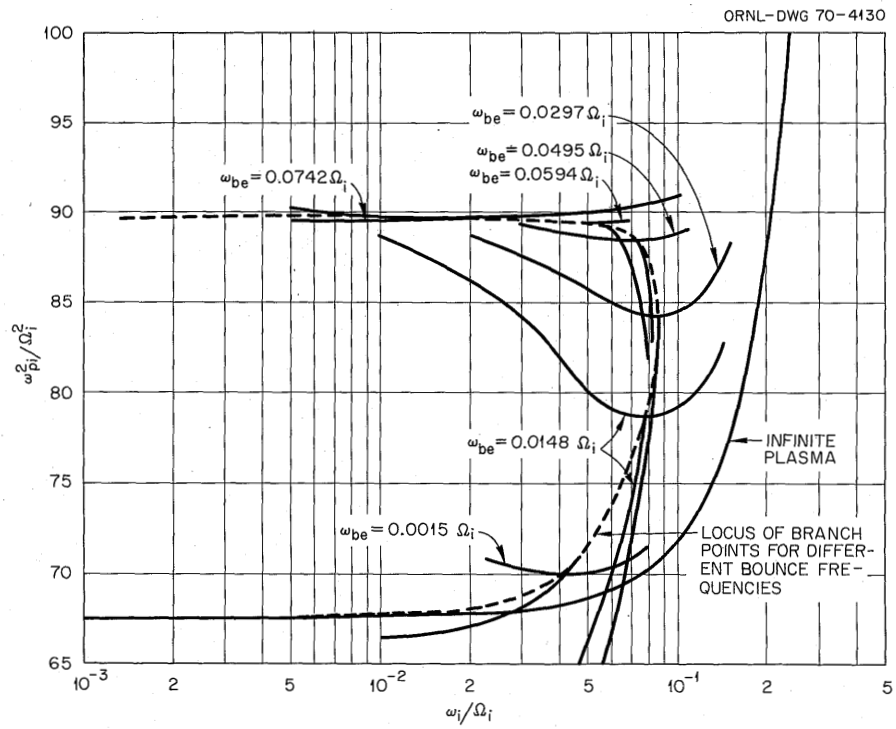


**Fig. 1.7. Density as a Function of Growth Rate for Infinite Plasma and for Inhomogeneous Plasma with $\omega \neq 0$.**

and correspondingly long plasmas. For lower $\Theta$, they would probably occur for much shorter plasmas, although these new modes cannot occur if $\omega_{be} \gtrsim 0.1\Omega_i$.

In conclusion, studies using the present idealized model of an inhomogeneous plasma have (1) permitted contact with the infinite-model predictions, (2) demonstrated the characteristics of localized modes when $\omega_{be} \ll \omega$ and more flutelike modes when $\omega_{be} \gg \omega$, and (3) shown the existence of modes with small but nonvanishing frequency and small growth rates which occur at relatively low densities when $\omega_{be} \lesssim 0.1\Omega_i$. Most of the cases examined here have been found to be relatively insensitive to variations in plasma length and electron temperature over the ranges of parameters examined: $0.1 \leqslant T_e/T_{\|i} \leqslant 100$ and $10 \leqslant L/a_i \leqslant 10^5$. Possible exceptions are the lower growth rate modes at $\omega \sim 0.1\Omega_i$. Also, the $\omega \sim 1.2\Omega_i$ modes have not been examined for $16 \leqslant L/a_i \leqslant 10^4$ with $T_e/T_{\|i} = 0.1$.

### 1.2.2 Modification of the Electrostatic Dispersion Relation Due to Coupling to Electromagnetic Modes

J. D. Callen[5] G. E. Guest

Beginning from the full 3 X 3 secular determinant dispersion relation,[6] we have computed (in an ordering scheme described below) the lowest-order electromagnetic corrections to the electrostatic dispersion relation[7] for waves propagating at an *arbitrary* angle to a homogeneous magnetic field $\mathbf{B}_0$ in a collisionless plasma. We restrict our attention to the ion-ion and ion-electron unstable (electrostatic) modes[3,8-12] with

[5]Consultant: Aeronautics and Astronautics Department, MIT.

[6]See, for example: E. G. Harris, *Proceedings of the Scottish University Summer School, Summer 1968* (to be published); G. Bekefi, *Radiation Processes in Plasmas,* p. 227, Wiley, New York, 1966.

[7]E. G. Harris, *Phys. Rev. Letters* **2**, 34 (1959); *J. Nucl. Energy: Pt. C* **2**, 138 (1961).

[8]Nonresonant loss-cone instability: M.N. Rosenbluth and R. F. Post, *Phys. Fluids* **8**, 547 (1965); M. N. Rosenbluth, p. 485 in *Plasma Physics,* IAEA, Vienna, 1965.

[9]Resonant loss-cone instability: G. E. Guest and R. A. Dory, *Phys. Fluids* **8**, 1853 (1965); *Phys. Fluids* **11**, 1775 (1968); J. D. Callen, Ph.D. thesis, MIT, April 1968.

[10]Temperature-anisotropy instabilities, $T_e \lesssim T_{\|i}$: C. O. Beasley and J. G. Cordey, *Plasma Phys.* **10**, 411 (1968) and references cited therein.

[11]Temperature-anisotropy instabilities, $T_e > T_{\|i}$: D. J. Sigmar, C. O. Beasley, and G. E. Guest, *Bull. Am. Phys. Soc.* **13**, 1493 (1968), to be published.

[12]L. D. Pearlstein, M. N. Rosenbluth, and D. B. Chang, *Phys. Fluids* **9**, 953 (1966).

frequencies $\omega \gtrsim \Omega_i$ (the ion gyrofrequency) and wave numbers $k_\perp$ such that $k_\perp a_i$ ($a_i$ is the ion gyroradius) is in the range of unity. In the derivation we do not make use of the fact that for most of the modes of interest[3,8-12] $k_\perp \gg k_\parallel$, but we do utilize this property in clarifying the physical phenomena involved. In order to avoid unstable electromagnetic modes and/or intrinsically strong coupling, we assume that $v_{i,e}/c$, $\omega/kc$, and $\beta$ are much less than 1, in which $v_{i,e}$ are the ion and electron thermal velocities, $c$ is the velocity of light, and $\beta$ is the ratio of plasma kinetic to magnetic field energy density.

If we orient the coordinate system so that the 3 component is in the wave-vector, $k$, direction and $B$ lies in the 1-3 plane, we obtain as the matrix equation for the longitudinal ("electrostatic," $E^L$) and the two transverse ($E_1^T$, $E_2^T$) components of the electric field:

$$\begin{pmatrix} 1-\frac{\omega^2}{c^2k^2}+\alpha_{11} & \alpha_{12} & \alpha_{13} \\ -\alpha_{12} & 1-\frac{\omega^2}{c^2k^2}+\alpha_{22} & \alpha_{23} \\ \alpha_{13} & -\alpha_{23} & -\frac{\omega^2}{c^2k^2}+\alpha_{33} \end{pmatrix} \begin{pmatrix} E_1^T \\ E_2^T \\ E^L \end{pmatrix} = \begin{pmatrix} 0 \\ 0 \\ 0 \end{pmatrix}$$

in which, as usual,[6] the initial conditions have been ignored. The exact dispersion relation is the condition that the determinant of the matrix multiplying **E** vanish. The $\alpha_{ij}$'s are due to the particle currents and are each proportional to $\omega_p^2$ ($\omega_p$ is the plasma frequency). Hence, for low enough plasma densities, the electrostatic and electromagnetic modes are decoupled and have the dispersion relations:

$$-\frac{\omega^2}{c^2k^2}+\alpha_{33}=0 \quad \text{(electrostatic)}$$

and

$$\begin{vmatrix} 1-\frac{\omega^2}{c^2k^2}+\alpha_{11} & \alpha_{12} \\ -\alpha_{12} & 1-\frac{\omega^2}{c^2k^2}+\alpha_{22} \end{vmatrix} = 0 \text{ (electromagnetic)}.$$

As the plasma density is increased, eventually the coupling of the electromagnetic modes to the electrostatic modes must become important. In order to determine the density at which significant coupling occurs, we adopt an ordering scheme which is appropriate to the physical parameters and unstable modes of interest: with $\epsilon$ a small expansion parameter of order $\sqrt{m_e/m_i}$ ($m_{e,i}$ are the electron and ion masses), we assume $v_e/c \sim \epsilon$, $v_i/c \sim \epsilon^2$, $\omega/kc \sim \epsilon^2$, $\omega/\Omega_e \sim \epsilon^2$, and $k_\perp a_e \sim \epsilon$. The scaling of the thermal velocities compared with the speed of light is generally true for thermonuclear conditions.[13] The remaining phase velocity, frequency, and wave-vector scalings follow from these velocity conditions and the fact that for the modes of interest $\omega \gtrsim \Omega_i$ and $k_\perp a_i \sim 1$. In addition, for $k_\parallel \neq 0$ we assume that $n\Omega_i\langle J_n^2\rangle k_\parallel v_i \lesssim 1$, in which $\langle J_n^2\rangle$ indicates any of the dimensionless averages of the familiar Bessel functions over the perpendicular velocity distribution or its $v_\perp$ derivative which arise. For modes having $k_\parallel = 0$, we order

$$n\Omega_i\langle J_n^2\rangle/(\omega - n\Omega_i) \sim \epsilon .$$

Finally, electron and ion temperatures parallel and perpendicular to **B** do not differ by more than a factor $\epsilon$.

Making use of these ordering schemes and expanding the exact dispersion relation about the electrostatic dispersion relation, we obtain (to lowest order)

$$0 = -\frac{\omega^2}{c^2k^2}+\alpha_{33}+\frac{\alpha_{13}^2}{1+\alpha_{11}}+\frac{\alpha_{23}^2}{1+\alpha_{22}} + \frac{2\alpha_{12}\alpha_{13}\alpha_{23}}{(1+\alpha_{11})(1+\alpha_{22})} . \quad (1)$$

Here the $-\omega^2/c^2k^2$ term represents $-\nabla^2\phi$ of Poisson's equation and $\alpha_{33}$ the perturbed charge density $\rho$. The remaining terms are electromagnetic coupling terms, which are easiest to interpret in the usual situation where $k_\perp \gg k_\parallel$. Then the $E_1^T$ wave propagates nearly perpendicular to $\mathbf{B}_0$ but has its electric field vector almost parallel to $\mathbf{B}_0$. The coupling of the $E_1^T$ mode to the electrostatic mode is due to the fact that a fluctuating perturbed potential along $\mathbf{B}_0$ (for $k_\parallel \neq 0$) creates a fluctuating current in the same direction. This fluctuating current produces a fluctuating azimuthal (about the magnetic field line) component of the magnetic field, which in turn, by Lenz's law, produces a back electromotive force that tends to cancel the electrostatic driving potential. The term in Eq. (1) which is proportional to $\alpha_{13}^2$ accounts for this effect. The $E_2^T$ mode has its **E** field nearly perpendicular to both **k** and $\mathbf{B}_0$. The coupling of this electromagnetic mode to the electrostatic mode proceeds in an analogous manner via the fluctuating current in the $\mathbf{k} \times \mathbf{B}_0$ direction arising from the fluctuating $\mathbf{E}^L \times \mathbf{B}_0/B_0^2$ drift

[13] D. J. Rose, *On the Feasibility of Power by Nuclear Fusion*, ORNL-TM-2204 (May 1968).

**Table 1.1. Order of the Various Terms in the Dispersion Relation [Eq. (1)]**

| | $\omega_{pe}^2/c^2k^2$ | $-\frac{\omega^2}{c^2k^2}$ | $\alpha_{33}$ | $\frac{\alpha_{13}^2}{1+\alpha_{11}}$ | $\frac{\alpha_{23}^2}{1+\alpha_{22}}$ | $\frac{2\alpha_{12}\alpha_{13}\alpha_{23}}{(1+\alpha_{11})(1+\alpha_{22})}$ |
|---|---|---|---|---|---|---|
| A) $k_{\|} \neq 0$ | $\epsilon^2$ | $\epsilon^4$ | $\epsilon^4$ | $\epsilon^6$ | $\epsilon^8$ | $\epsilon^9$ |
| | 1 | $\epsilon^4$ | $\epsilon^2$ | $\epsilon^2$ | $\epsilon^4$ | $\epsilon^3$ |
| | $1/\epsilon^2$ | $\epsilon^4$ | 1 | 1 | 1 | 1 |
| B) $k_{\|} = 0$ | $\epsilon$ | $\epsilon^4$ | $\epsilon^4$ | 0 | $\epsilon^6$ | 0 |
| | $1/\epsilon$ | $\epsilon^4$ | $\epsilon^2$ | 0 | $\epsilon^2$ | 0 |
| | $1/\epsilon^2$ | $\epsilon^4$ | $\epsilon$ | 0 | 1 | 0 |

velocity, except that now it is the electrostatically driven $\mathbf{E}_2^T \times \mathbf{B}_0/B_0^2$ drifts which lead to the modifications of the electrostatic dispersion relation as indicated by the terms proportional to $\alpha_{23}^2$ in Eq. (1). The last term in Eq. (1) indicates higher-order couplings of the various modes.

The only undefined parameter in the ordering schemes discussed above is the plasma density, which appears in Eq. (1) in the form $\omega_{pe}^2/c^2k^2$. In Table 1.1 we indicate the order of the various terms in Eq. (1) for some relevant orderings of the parameter $\omega_{pe}^2/c^2k^2$. Table 1.1 clearly shows that for $k_{\|} \neq 0$ and $\omega_{pe}^2/c^2k^2 \sim \epsilon^2$, the dispersion relation [Eq. (1)] is simply the electrostatic dispersion relation with relative corrections of $O(\epsilon^2)$. However, when $\omega_{pe}^2/c^2k^2 \sim 1$, we see that there is a significant correction due to the coupling of the electrostatic mode to the $E_1^T$ mode. Note also that when $\omega_{pe}^2/c^2k^2 \sim 1$ the $\nabla^2\phi$ term $(-\omega^2/c^2k^2)$ is negligible; however, we retain it in what follows to facilitate taking electrostatic limits. For densities such that $\omega_{pe}^2/c^2k^2 \sim 1/\epsilon^2 \gg 1$, Table 1.1A shows that the electrostatic and electromagnetic modes are so strongly coupled that it is not meaningful to speak of separate modes, and we should compute wave characteristics directly from the original $3 \times 3$ determinant. From Table 1.1B we see that basically the same pattern is followed for $k_{\|} = 0$, except that now the coupling is to the $E_2^T$ mode and the scale of $\omega_{pe}^2/c^2k^2$ where the coupling becomes important is increased by a factor of $1/\epsilon$.

For a Maxwellian electron velocity distribution the "electrostatic" dispersion relation including the lowest-order electromagnetic corrections as indicated in Table 1.1 can be written as[14]

$$1 + \frac{\omega_{pe}^2}{\Omega_e^2}\frac{k_\perp^2}{k^2}\left(1 + \frac{\omega_{pe}^2}{c^2k^2}\right) = \frac{(\omega_{pe}^2/k^2v_e^2)\, Z'(\omega/k_{\|}v_e)}{1 + (\omega_{pe}^2/c^2k^2)\,(\omega/k_{\|}v_e)^2\, Z'(\omega/k_{\|}v_e)\,(k_\perp^2/k^2)} + \frac{4\pi\rho_i}{k^2\phi} + \begin{cases} O\left[\frac{1}{\epsilon}\left(\frac{\omega_{pe}^2}{c^2k^2}\right)^2\right], & k_{\|} \neq 0 \\ O\left[\epsilon\left(\frac{\omega_{pe}^2}{c^2k^2}\right)^2\right], & k_{\|} = 0\,. \end{cases} \tag{2}$$

Here $Z'$ is the derivative of the plasma dispersion function[15] with respect to its argument, and $4\pi\rho_i/k^2\phi$ is simply the usual electrostatic ion contribution to the dispersion relation. In this form the modifications to the dispersion relation for $\omega_{pe}^2/c^2k^2 \gtrsim 1$ are explicitly demonstrated, and we readily see that the usual electrostatic result is recovered for $\omega_{pe}^2/c^2k^2 \ll 1$.[16]

As a first example of the use of our new dispersion relation, we consider the modifications to the Rosenbluth-Post "continuum limit" of the loss-cone instabilities[8] which ensue when the coupling to electromagnetic waves becomes important. Using the ion term derived by Rosenbluth and Post, we find that the

[14] The form of the electron term given on the right of Eq. (2) was first derived by L. D. Pearlstein [*Finite Beta Stabilization of Absolute Loss-Cone Instability,* UCRL-50397 (Mar. 12, 1968)] in a phenomenological manner.

[15] B. D. Fried and S. D. Conte, *The Plasma Dispersion Function,* Academic, New York, 1961.

[16] The condition $\omega_{pe}^2/c^2k^2 \ll 1$ for the validity of the electrostatic approximation has been obtained previously. Bernstein [*Phys. Rev.* **109**, 10 (1958)] pointed out its significance as the scale factor of off-diagonal matrix elements. It also follows from Eq. (101), p. 224, of T. H. Stix, *The Theory of Plasma Waves*, McGraw-Hill, New York, 1962, for the waves of interest since the largest dielectric constant here is $\omega_{pe}^2/\omega^2$. More recently it has been derived in a cold-plasma approximation by David Montgomery, "Validity of the Electrostatic Approximation" (to be published).

dispersion relation for these $k_{\|} \neq 0$ modes ($\omega/k_{\|}v_e \gg 1$) when $\omega_{pe}^2/c^2k^2 \lesssim 1$ is given by

$$1 + \frac{\omega_{pe}^2}{\Omega_e^2} = \frac{(\omega_{pe}^2/\omega^2)(k_{\|}^2/k^2)}{1 + (\omega_{pe}^2/c^2k^2)} + \frac{\omega_{pi}^2}{k^2 v_i^2} F\left(\frac{\omega}{k_{\perp}v_i}\right), \quad (3)$$

in which $F$ is a complex function of roughly unity magnitude which represents the continuum limit (Im $\omega > \Omega_i$) of the ion gyroharmonic resonance structure. In the limit $\omega_{pi}^2/k^2v_i^2 \gg 1$ the left side of Eq. (3) is negligible, and we find that the parallel component of the wave vector is given by

$$k_{\|}a_i \cong \frac{\omega}{\Omega_i}\sqrt{\frac{m_e}{m_i}\left(1 + \frac{\omega_{pe}^2}{c^2k^2}\right)F\left(\frac{\omega}{kv_i}\right)}.$$

This result differs from that of Rosenbluth and Post[8] only by the presence of the $\omega_{pe}^2/c^2k^2$ term. In the present analysis this new term is restricted to values smaller than or of order unity (as large as say $\sqrt[4]{m_i/m_e} \cong 6$). Hence we see that here the coupling to electromagnetic modes shortens the parallel (to $\mathbf{B}_0$) wavelength of the unstable modes and thus has a destabilizing effect.

As a second example we will consider the modifications to the Dory, Guest, and Harris[3] $k_{\|} = 0$ ion modes at high densities. Taking account of the lowest-order electromagnetic corrections, we find that the dispersion relation can be written as

$$\frac{\Omega_i^2}{\omega_{pi}^2}\left[1 + \frac{\omega_{pe}^2}{\Omega_e^2}\left(1 + \frac{\omega_{pe}^2}{c^2k^2}\right)\right] = \frac{1}{(ka_i)^2}\sum_n \frac{2n\Omega_i D_n}{\omega - n\Omega_i}. \quad (4)$$

Again, this dispersion relation differs from the usual electrostatic one[3] only by the presence of the term $\omega_{pe}^2/c^2k^2$. Instability occurs when the density is such that the left side of Eq. (4) is less than a positive minimum (with respect to $\omega$ for given $k$) of the right side. Stability occurs when the left side is greater than this positive minimum. In the usual electrostatic case, stability occurs only for $\omega_{pi}^2/\Omega_i^2 \lesssim 1$ or when the $v_{\perp}$ distribution is sufficiently thermalized.[3] Here the presence of the extra $\omega_{pe}^2/c^2k^2$ term causes the left side of Eq. (4) to have a minimum of $(m_e/m_i)(2ck/\Omega_e + 1)$ at $\omega_{pe}^2/\Omega_e^2 = ck/\Omega_e$. If this minimum is greater than all positive minima of the right side of Eq. (4), then stability is ensured. In practice, this effect of the electromagnetic correction occurs only at very high densities and even there leads to a relatively slight narrowing of the (already narrow) range of thermal spread in the $v_{\perp}$ distribution for which instability occurs.

Finally, let us consider the implications which this work has on theoretical calculations of plasma instabilities which might afflict a controlled thermonuclear fusion reactor. In particular, since we have found that significant modifications of the customarily employed electrostatic approximation occur when $\omega_{pe}^2/c^2k^2 \gtrsim 1$, we wish to evaluate this parameter for fusion conditions. In terms of the "dielectric constant" $\epsilon = \omega_{pi}^2/\Omega_i^2$, we can write the electromagnetic coupling parameter $(\omega_{pe}^2/c^2k^2)$ as

$$\frac{\omega_{pe}^2}{c^2k^2} = \left(\frac{\omega_{pi}^2}{\Omega_i^2}\right)\left(\frac{m_i v_i^2}{m_e c^2}\right)\frac{1}{(ka_i)^2}.$$

For thermonuclear fusion conditions we typically require[13] $m_i v_i^2/q_i > 10$ keV, $\omega_{pi}^2/\Omega_i^2 > 10^3$, and so we see that this parameter exceeds unity for all modes having $(ka_i)^2 \lesssim 20$, which encompasses the potentially most dangerous regime of $ka_i \sim 1$. Alternatively, in terms of $\beta$, we can write the electromagnetic coupling parameter as

$$\frac{\omega_{pe}^2}{c^2k^2} = \frac{m_i}{2m_e}\frac{\beta_i}{(ka_i)^2}.$$

Since we generally require[13] $\beta_i > 0.1$ for thermonuclear conditions, this representation indicates that all electrostatic modes having $(ka_i)^2 \lesssim 10^2$ will be significantly affected by coupling to electromagnetic modes. Note that since $\omega_{pe}^2/c^2k^2$ exceeds $\omega_{pe}^2/\Omega_e^2$ for many modes of interest, it is often inconsistent to retain only the latter term [e.g., in Eq. (3)] when studying the stability of high-density plasmas.

We thus conclude that in attempting to delineate the important unstable modes of a mirror-confined plasma of thermonuclear fusion interest, *the electrostatic approximation by itself is inadequate to describe the plasma dynamics.* At the very least, the fact that the electrostatic modes drive electromagnetic modes, giving rise to modifications of the electrostatic dispersion relation, must be taken into account. In the two simple examples discussed, we have found that these couplings can have either stabilizing or destabilizing effects.

### 1.2.3 An Estimate of the Maximum Stable Pressure in the ELMO Device

O. C. Eldridge[17] G. E. Guest

Experiments in ELMO (see Sect. 4 of this report) have demonstrated stable confinement of high-$\beta$

[17]Consultant: Physics Department, University of Tennessee.

plasmas provided (1) adequate line tying is maintained by cold-plasma throughput and (2) the pressure anisotropy is not too extreme. It has been pointed out that,[18] even with isotropic pressure and ideal line tying (i.e., all perturbations vanish on the end walls), there are reasons to expect a maximum stable pressure. The energy principles of Bernstein *et al.*[19] (for a scalar-pressure, ideal MHD fluid model) or Grad *et al.*[20] (for guiding center models with anisotropic pressures) provide the basis for estimates of this critical pressure. Here we describe one such estimate based on the scalar-pressure model of ref. 19. The more detailed guiding center theory is being analyzed at present.

The criterion for instability is that the variation in energy $\delta W(\psi)$ for a field line labeled by $\psi$ may be negative for a possible displacement $X$. From Eq. (6.24) of ref. 19,

$$\delta W(\psi) = \frac{\pi}{2}\int d\chi \left[\frac{1}{r^2B^2J}\left(\frac{\partial X}{\partial \chi}\right)^2 + p'JDX^2\right] + \frac{f^2}{4}\left(L' + \frac{V'}{\gamma p}\right).$$

Here the coordinates are $\psi, \theta, \chi$ [where distance along a magnetic field line is $ds_{\|} = JB\, d\chi$ and, perpendicular to $\hat{\chi}$ and $\hat{\theta}$, $ds_{\perp} = d\psi/(rB)$; $J$ is the Jacobian relative to $r$, $\theta$, $z$], and

$$D = -\frac{2}{rB^3}\,\hat{\psi}\cdot(\mathbf{B}\cdot\nabla)\,\mathbf{B} = \frac{2}{rB}\frac{1}{R_c}.$$

We obtain a necessary criterion for *instability* by neglecting the last (manifestly positive) term:

$$\delta W(\psi) \geqslant \frac{\pi}{2}\int \frac{ds_{\|}}{r^2B}\left[\left(\frac{\partial X}{\partial s_{\|}}\right)^2 + \frac{2}{B^2}\frac{\partial p}{\partial s_{\perp}}\frac{X^2}{R_c}\right],$$

with $\delta W(\psi) < 0$ for instability.

On the assumption of perfect line tying, we write

$$X = X_0 \sin\frac{\pi s_{\|}}{L}$$

and estimate $\partial p/\partial s_{\perp} = -p/\delta$, where the scale length $\delta$ will be taken from measurements made on the midplane of the experimental device.

Crudely, then, instability requires

$$\frac{2p}{B^2}\frac{1}{\delta R_c} > \frac{\pi^2}{L^2}$$

or

$$\left(\frac{\beta}{1-\beta}\right)_{\text{crit}} \sim \pi^2\frac{\delta R_c}{L^2},$$

where

$$\beta \equiv \frac{B_0^2 - B^2}{B_0^2} \cong \frac{2p}{B_0^2}.$$

Under typical conditions in ELMO, $\pi^2\delta R_c/L^2 \sim 1$, suggesting $\beta_c \sim \frac{1}{2}$. This is not inconsistent with observations of stable confinement with adequate line tying.

It is interesting to note the similarity of the present result to a primitive estimate based on the assumption that the plasma can be unstable only if $\gamma\tau > 1$, where $\gamma$ is the growth rate and $\tau$ is a wave transmit time to the walls. On this basis,

$$\left(\frac{\beta}{1-\beta}\right)_{\text{crit}} \approx \frac{R_pR_c}{lL^2},$$

where $R_p$ is the plasma radius and $k = l/R_p$ is the wave vector. For the hollow annular plasma in ELMO, $\pi^2\delta \sim R_p$.

### 1.2.4 Simulation of the High-Beta Hot-Electron Plasma ELMO[21]

R. A. Dory

A few tens of electron gyroperiods were simulated[22] using a $2\frac{1}{2}$-dimensional particle-following plasma simulation code. The orbits of $10^4$ particles were calculated for an axisymmetric system in which $P_\theta = \frac{1}{2}mR^2\dot{\theta} +$

[18] We are indebted to M. N. Rosenbluth for raising this question and to A. A. Ware and J. L. Johnson for helpful discussions.

[19] I. B. Bernstein *et al.*, *Proc. Roy. Soc. (London)* **A244**, 17 (1958).

[20] H. Grad, *Phys. Fluids* 9, 225, 498 (1966).

[21] This study was done at Los Alamos Scientific Laboratory using existing LASL codes. The efforts and hospitality of R. L. Morse, C. W. Nielson, and D. O. Dickman are gratefully acknowledged.

[22] See discussion: *Thermonuclear Div. Ann. Progr. Rept. Dec. 31, 1968*, ORNL-4401, pp. 18 ff.

$(e/c)A_\theta$ is preserved. The self-consistent inductive electric field $E_\theta$ was applied implicitly using the vector potential $A_\theta$ calculated taking into account the applied mirror field and the field generated by the large azimuthal electron currents.

By choosing parameters to fit the known properties of the ELMO plasma[23] (see Sect. 4), an equilibrium approximately like those calculated earlier[23] was set up. The conclusions to be drawn were that no cataclysmic instabilities occur despite high values for $\beta = 8\pi nkT/B^2 \cong 30\%$. Some axial particle loss occurred, but in the limited studies it was not possible to determine if this was caused by inaccuracies in setting up the initial conditions or by scattering (of particles by field perturbations) in the loss cone.

### 1.2.5 Electrostatic Instabilities in Multicomponent Hot-Electron Plasmas

D. J. Sigmar G. E. Guest

Experiments in the production of highly ionized target plasmas using electron-cyclotron heating (Sect. 2.2.5) have shown that at low ambient gas pressures, $p_0 \lesssim 10^{-6}$ torr, average electron lifetimes are limited by microinstabilities around the electron gyrofrequency. The dependence of the frequency on the plasma parameters has led to a tentative identification of this mode with an electrostatic instability first discussed by Hall, Heckrotte, and Kammash[24] – in their nomenclature, the "type-A double distribution" instability. As implied by this name, the instability can arise in mixtures of cold and hot electrons under a wide variety of conditions; it has been identified in several previous experiments.[25,26]

In search of ways of stabilizing this mode, we have extended the work of Hall *et al.*[24] to include more general classes of mirror-confined hot-electron distributions and an examination of convective-absolute growth characteristics. In ref. 24 the hot particles were assumed to have a sharply peaked distribution in perpendicular velocities $[\delta(v_\perp - \alpha_\perp)]$, whereas typical electron-cyclotron-heated plasmas exhibit a broad spread of energies. We adopt the model

$$f_0(\text{cold}) = \frac{N_C}{\pi^{3/2}\alpha_c^3}\exp\left(-\frac{v^2}{\alpha_c^2}\right),$$

$$f_0(\text{hot}) = \frac{N_H}{\pi^{3/2}\alpha_\perp^2\alpha_\parallel}\frac{v_\perp^2}{\alpha_\perp^2}\exp\left(-\frac{v_\perp^2}{\alpha_\perp^2}-\frac{v_\parallel^2}{\alpha_\parallel^2}\right),$$

with $\alpha_\parallel^2 \approx \alpha_\perp^2$.

As demonstrated earlier,[27] a rough (sufficient) criterion for stability against modes with $k_\parallel \neq 0$ is

$$\left.\frac{\partial f_0}{\partial v_\perp}\right]_{v_\parallel \approx \alpha_\parallel} \leqslant 0 .$$

At ambient gas pressures greater than $10^{-5}$ torr, this condition is probably satisfied in typical microwave heating experiments. But as the pressure is lowered, especially if the microwave power levels are high, the density and average energy of the cold electrons (relative to the more energetic electrons) may decrease enough to give a nonmonotonic and thus possibly unstable distribution.

If $k_\parallel \neq 0$, electrostatic waves in the cold-electron group can gain energy from the fast electrons via cyclotron damping. Near marginal stability we have for $\omega \gtrsim \Omega$,

$$\omega - \Omega \approx k_\parallel v_c \left\{ \ln\left[\frac{N_C}{N_H}\left(\frac{T_{\parallel,H}}{T_C}\right)^{3/2}\frac{C_1(C)}{-D_1(H)}\right]\right\}^{1/2},$$

where the parameters $C_n$ and $D_n$ are the usual moments of the distribution function:[28]

$$C_n = 2\pi\int v_\perp\, dv_\perp\, J_n^2(k_\perp v_\perp/\Omega)\, g_0(v_\perp),$$

$$-D_n = \frac{\alpha_\perp^2}{2}2\pi\int v_\perp\, dv_\perp\, J_n^2(k_\perp v_\perp/\Omega)\frac{1}{v_\perp}\frac{d}{dv_\perp}g_0(v_\perp),$$

and

$$f_0(v_\parallel, v_\perp) = \frac{g_0(v_\perp)}{\sqrt{\pi}\alpha_\parallel}e^{-v_\parallel^2/\alpha_\parallel^2}.$$

[23] *Ibid.*, pp. 22 ff.

[24] L. S. Hall, W. Heckrotte, and T. Kammash, *Phys. Rev.* **139**, A1117 (1965).

[25] W. A. Perkins and W. L. Barr, *Phys. Fluids* **11**, 388 (1968).

[26] R. A. Blanken and A. F. Kuckes, *Plasma Phys.* **11**, 321 (1968).

[27] R. A. Dory *et al.*, *Phys. Fluids* **12**, 2117 (1969).

[28] G. E. Guest and R. A. Dory, *Phys. Fluids* **8**, 1835 (1965); *Phys. Fluids* **11**, 1775 (1968).

Since the propagation is determined mainly by the cold electrons,

$$1 - \frac{\omega_{pe}^2(\mathrm{C})}{\omega^2}\frac{k_\parallel^2}{k^2} - \frac{\omega_{pe}^2(\mathrm{C})}{\omega^2 - \Omega^2}\frac{k_\perp^2}{k^2} \cong 0 .$$

Then for $k_\parallel^2/k^2 \ll 1$ and $\omega \sim \Omega \sim \omega_{pe}(\mathrm{C})$ the cold-electron density is given by

$$\frac{\omega_{pe}^2(\mathrm{C})}{\Omega_e^2} \approx \frac{2(\omega - \Omega)}{\Omega}$$

$$\approx \frac{2k_\parallel v_c}{\Omega}\left\{\ln\left[\frac{N_\mathrm{C}}{N_\mathrm{H}}\left(\frac{T_{\parallel,\mathrm{H}}}{T_\mathrm{C}}\right)^{3/2}\frac{C_1(\mathrm{C})}{-D_1(\mathrm{H})}\right]\right\}^{1/2} .$$

And for appreciable growth rates, $(\omega - n\Omega)/k_\parallel\alpha_\parallel \sim 1$. Threshold densities are therefore low and are proportional to the frequency shift. Clearly

$$\frac{N_\mathrm{C}}{N_\mathrm{H}} > \frac{-D_1(\mathrm{H})}{C_1(\mathrm{C})}\left(\frac{T_\mathrm{C}}{T_{\parallel,\mathrm{H}}}\right)^{3/2}$$

must hold for instability, giving a *minimum* unstable cold-electron density. The approximate sufficient condition for stability, $\partial f_0/\partial v_\perp \leqslant 0$ for $v_\parallel \approx \alpha_\parallel$, determines a *maximum* unstable cold-electron density. Since both of these rough boundaries are strongly temperature dependent, it is useful to construct numerically a marginal stability boundary in the $N_\mathrm{C}/N_\mathrm{H}$-$T_\mathrm{C}/T_{\parallel,\mathrm{H}}$ plane.

The marginal stability criterion ($\omega_i = 0$) is probably too pessimistic for $N_\mathrm{C}/N_\mathrm{H} > 1$, since growth rates go to zero very slowly along the upper part of the stability boundary. More realistic stability criteria can be obtained by evaluating the analogous curve for fixed nonzero growth rate or by determining the conditions for transition from convective to absolute growth (C-A boundary). An example is shown in Fig. 1.8, in which the hot-electron density is fixed at a high value, $\omega_{pe}^2(\mathrm{H})/\Omega_e^2 = 10$, and the growth rate is taken as $\omega_i/\Omega_e = 0.001$. Also a few points on the C-A boundary are shown.

In Fig. 1.9 we plot some transition data in a slightly different form, showing density vs $N_\mathrm{C}/N_\mathrm{H}$ for two particular temperature ratios; the solid lines show $\omega_p^2(\mathrm{H})/\Omega^2$, while the dashed lines show $\omega_{pe}^2(\mathrm{C})/\Omega^2$. It is encouraging, from the point of view of the target plasma experiments, to note that within the anticipated range of experimental parameters ($N_\mathrm{C}/N_\mathrm{H} \sim 1$, $T_\mathrm{C}/T_\mathrm{H} \sim 0.01$) the transition from convective to absolute

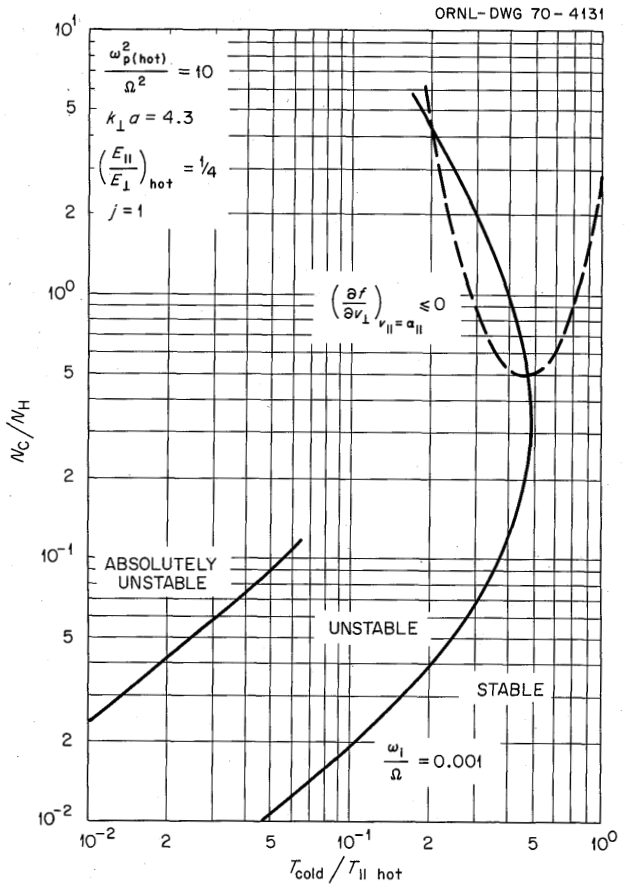


**Fig. 1.8. Near Marginal ($\omega_i/\Omega$ = 0.001) and Absolute Stability Boundaries of Double-Hump Mode in a Space Spanned by the Cold-to-Hot Temperature and Density Ratio.** Along the dashed curve the total particle distribution function satisfies $(\partial f/\partial v_\perp)_{v_\parallel=\alpha_\parallel} = 0$ (vanishing double hump).

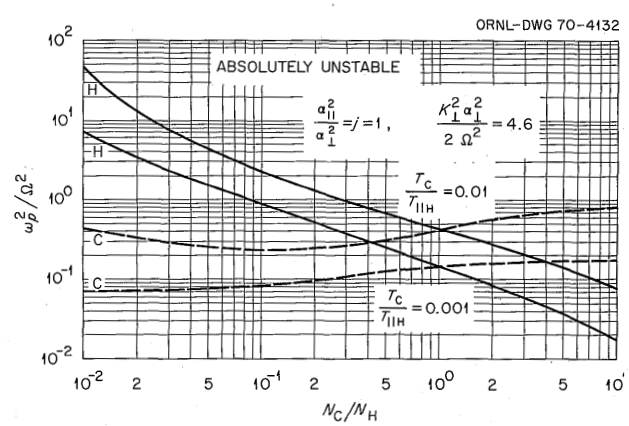


**Fig. 1.9. Convective-Absolute Transition Densities of Double-Hump Mode vs Cold-to-Hot Density Ratio for Two Values of the Cold-to-Hot Temperature Ratio.** The upper pair of curves shows the hot threshold density for the onset of absolute instability; the lower pair shows the concomitant cold threshold density.

growth for well-spread distribution functions occurs for $\omega_p^2(\text{total})/\Omega^2 \sim 1$, a frequently quoted design expectation.

Some consideration has also been given to possible nonresonant modes in target plasmas. If the electron temperature exceeds the hot-ion temperature, anisotropy-driven absolute modes at frequencies $\omega \cong (n + \frac{1}{2})\omega_{ci}$ at low threshold densities are possible.[24,29] However, the presence of cold electrons reintroduces Landau damping and Debye shielding, suppressing these modes, as indicated in Fig. 1.10. The parallel phase velocity of the nonresonant modes exceeds the parallel hot-ion thermal velocity slightly:

$$\frac{\omega}{k_{\|}\alpha_{\|i}} \gtrsim 1 .$$

Landau damping will therefore set in for $\alpha_e(\mathrm{C}) \gtrsim \alpha_{\|i}$, which explains the left branch of the curve in Fig. 1.10.

[29] A. V. Timofeev, *Soviet Phys. JETP* **12**, 281 (1961).

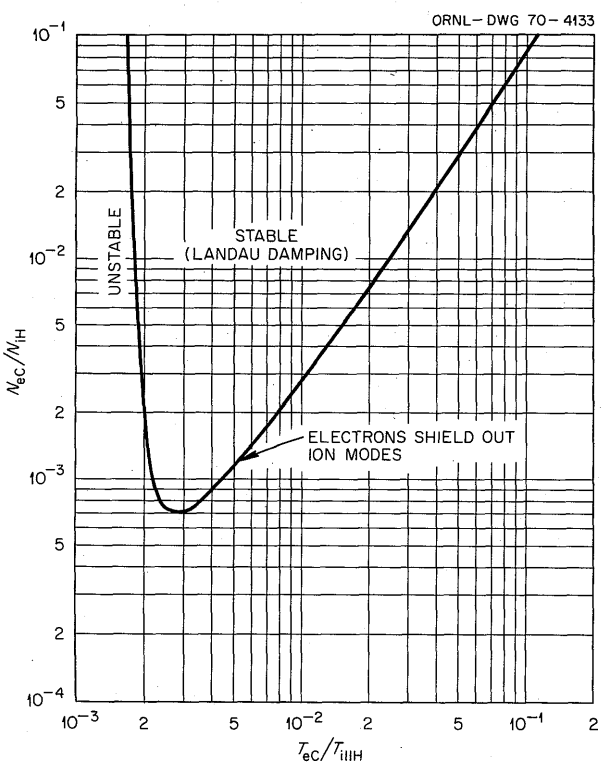


**Fig. 1.10. Marginal Stability Boundary for Nonresonant Ion Modes in the Presence of Cold Electrons in a Space Spanned by the Ratio of Cold-Electron to Hot-Ion Temperature and Cold-Electron to Hot-Ion Density.**

If the cold-electron temperature is increased, Landau damping decreases and the electron Debye length exceeds the wavelength of the unstable cold-ion oscillation so that Debye shielding breaks down also. This will occur when

$$\frac{\omega_{pi}^2(\mathrm{C})}{\omega^2} k_{\|}^2 = k_{D,e}^2(\mathrm{C}) ,$$

or

$$\frac{N_{e\mathrm{C}}}{N_{i\mathrm{C}}} = \frac{1}{2}\frac{T_{e\mathrm{C}}}{T_{\|i}} ,$$

where $k_{D,e}$ is the electron Debye length. This explains the right branch in Fig. 1.10. These conditions for stability should be met easily in experiments so that one may not observe nonresonant ion modes.

### 1.2.6 An Electromagnetic Loss-Cone Instability

S. Krishan[30] E. G. Harris[31]

We consider the instability of a transverse wave propagating through a plasma with a loss-cone distribution. The direction of propagation is perpendicular to the magnetic field. The electric field vector is polarized parallel to the magnetic field. The dispersion relation is

$$k^2 - \frac{\omega^2}{c^2}\epsilon_{33}(\mathbf{k}, \omega) = 0 ,$$

where $\mathbf{k}$ is the wave vector, $\omega$ is the frequency, and $\epsilon_{33}$ is a component of the well-known dielectric tensor of the plasma in a reference frame such that $\hat{z} = \mathbf{B}/B$ and $\mathbf{k}$ lies in the $\hat{x}$-$\hat{z}$ plane. This may be put into the form

$$-\frac{1}{2}D_0 - \sum_{n=1}^{\infty} D_n \frac{\Omega^2}{\Omega^2 - n^2} = \frac{1}{2\Omega_p^2}\left[\Omega^2 - (\Omega_p^2 + \Omega_k^2)\right] ,$$

where $\Omega = \omega/\omega_c$, $\Omega_p = \omega_p/\omega_c$, $\Omega_k = kc/\omega_c$, and

$$D_n = \int d^3\mathrm{v}\, \frac{\mathrm{v}_{\|}^2}{\mathrm{v}_{\perp}^2}\frac{\partial f_0}{\partial \mathrm{v}_{\perp}} J_n^2\left(\frac{k\mathrm{v}_{\perp}}{\omega_c}\right).$$

Also, $\omega_c$ is the cyclotron frequency, $\omega_p$ is the plasma frequency, $J_n$ is a Bessel function, $\mathrm{v}_{\|}$ and $\mathrm{v}_{\perp}$ are velocity components, and $f(\mathrm{v}_{\perp}, \mathrm{v}_{\|})$ is the velocity distribution of electrons. We have assumed that $f(\mathrm{v}_{\perp} = 0, \mathrm{v}_{\|}) = 0$.

[30] Physics Department, University of Tennessee.

[31] Consultant: Physics Department, University of Tennessee.

If $f_0$ is a monotonically decreasing function of $v_\perp$, then all of the $D_n$'s are negative, and there is no instability. If $f_0$ is a loss-cone distribution, then a simple graphical construction shows the possibility of an instability.

For

$$f_0 = \frac{f_{\|}(v_{\|})\,\delta(v_\perp - V)}{2\pi V},$$

a sufficient criterion for instability is

$$2M\frac{\langle v_{\|}^2\rangle}{V^2} - 1 > \frac{\Omega_k^2}{\Omega_p^2},$$

where $M$ is a number of order of unity whose exact value must be determined by detailed calculation. For $kV/\omega_c = 2.6$ we find $M = 1.521$.

These instabilities only occur at high densities. We have estimated the density threshold for instability to be

$$\frac{\omega_p^2}{\omega_c^2} > \lambda^2 \frac{c^2}{V^2},$$

where $\lambda$ is a number in the range $1.8 < \lambda < 3.8$.

## 1.3 TOROIDAL SYSTEMS

R. A. Dory

### 1.3.1 Introduction

The beginning of the ORMAK experiments (see Sect. 3) at Oak Ridge calls for related theoretical studies to help provide a framework with which to interpret the forthcoming experimental data and to aid in planning future directions for the experimental program.

A review of the wealth of existing theoretical work indicates that, unfortunately, a large proportion of the important questions have been answered sketchily or not at all. These gaps suggest the agenda given in Table 1.2 as a provisional outline of what needs to be done for the TOKAMAK experiments. For other areas of toroidal research, the 1967 report by the ad hoc panel[32] will be informative even though the emphasis and recommendations seem rather quaint in the light of current emphasis in the fusion community.

**Table 1.2. TOKAMAK Research – Agenda for Theoretical Studies**

I. Magnetohydrodynamic Equilibria
- A. Magnetic Surfaces
- B. Drift Surfaces
- C. Diffusion, Efflux, Heat Flow
- D. Stability (Interchange, Kink)

II. Nonideal MHD
- A. Resistivity
- B. Viscosity
- C. Sources and Sinks
- D. Tensor Pressure
- E. Ion Inertia
- F. Stability

III. Velocity Space Effects
- A. Particle Trapping
- B. Loss Cones
- C Stability

IV. Other
- A. Heating Processes
- B. Anomalous Resistivity
- C. Turbulence
- D. Field Perturbation Effects

Table 1.2 is incomplete, and the problems do not really separate as cleanly as shown. As agenda for a program of studies, the table is oversimplified, because each step must be done with a view toward preparing for the succeeding ones and each step is sufficiently important to merit study before the results of prior ones are in hand.

We are beginning at the beginning–MHD equilibria. The Russian work is extensive, but it is based normally on the simplification (valid for present TOKAMAK's) of expansion in the toroidal curvature $\kappa$, often on the assumption of low $\beta = 8\pi nkT/B^2$ and sometimes on the assumption that the plasma currents are known in advance. The expansions used in those studies can (in principle) be improved to include effects of higher-order corrections, but in the devices now thought to be most interesting $\kappa$ is of order $\frac{1}{2}$, so that expansion is a suspect technique and the number of terms needed becomes frightening.[33]

It is reasonable therefore to use numerical techniques for an initial study of the equilibrium question. Using a computer permits us to study cases with nonsmall $\kappa$ and $\beta$ and also yields another major benefit in that the techniques are broadly applicable and are not restricted

[32] M. N. Rosenbluth *et al.*, *Report of Ad Hoc Panel on Low Beta Toroidal Plasma Research*, TID-24228 (1967).

[33] See, for example, the fourth-order calculations of F. A. Haas and A. A. Ware, *Phys. Fluids* 9, 956 (1966).

in effectiveness by detailed assumptions needed to permit solution. The piper must be paid, however, and the usual drawback of numerics appears – we obtain answers instead of physical intuition. However, having the answers in hand we can proceed to augment them with analytical calculations to provide scaling laws and insight, and we give an example of this symbiosis between numerical and analytical techniques.

### 1.3.2 MHD Equilibria

The static MHD equations we will need are

$$\text{div}\,\mathbf{B} = 0\,, \tag{1}$$

$$\text{curl}\,\mathbf{B} = 4\pi\mathbf{J}\,, \tag{2}$$

$$\text{grad}\,P = \mathbf{J}\times\mathbf{B}\,, \tag{3}$$

$$\eta\mathbf{J} = \mathbf{E} + \mathbf{V}\times\mathbf{B}\,, \tag{4}$$

where the symbols have their usual meanings.[34]

The assumption of perfect azimuthal symmetry in a TOKAMAK permits the first three equations to be simplified considerably when written in terms of the flux function $\psi(R, Z)$ in the cylindrical coordinate system $(R, Z, \phi)$. Thus, if $\partial/\partial\phi \equiv 0$, then $\mathbf{B} = \hat{\phi}\, f(\psi)/R - R^{-1}\hat{\phi}\times\nabla\psi$. Both $P$ and $f = RB\phi$ are constant on surfaces where $\psi = R\,A_\phi(R, Z)$ is constant ($A_\phi$ = vector potential, so $P(R, Z)$ has the form $P[\psi(R, Z)]$ and $\nabla P = P'\nabla\psi$, $P' = P'(\psi) = dP/d\psi$, $f' = df/d\psi$, etc. To complete the solution[35] of Eqs. (1) to (3) one must solve

$$\Delta^*\psi = -4\pi R^2 P' - ff' \tag{5}$$

(where $\Delta^* \equiv \partial^2/\partial R^2 - R^{-1}\,\partial/\partial R + \partial^2/\partial Z^2$) subject to boundary conditions, such as $\psi$ = constant at boundaries that can be regarded as perfectly conducting for time scales of interest ($10^{-3}$–$10^{-1}$ sec).

**1.3.2.1 Ad Hoc Equilibrium.** – Within the approximations of MHD and axisymmetry, Eq. (5) is the general distillation of (1), (2), and (3). Using ad hoc functions $P(\psi)$ and $f(\psi)$ chosen to model the plasmas thought to occur in TOKAMAK's we can solve the second-order nonlinear partial differential equation (PDE) with its elliptic operator $\Delta^*$. Numerical solution is straightforward, using standard iterative procedures (with convergence enhancement), and examples have been given.[36]

To aid in discussion of the results, we show the geometry in Fig. 1.11*a*. The $Z$ axis is the axis of azimuthal symmetry. The curvature parameter $\kappa = a/R_0$ is the inverse of the (large) aspect ratio $A$. Figure 1.11*b* shows the sinusoidal pressure profile used. The function taken for $f(\psi)$ is the constant function, which implies that the plasma pressure is balanced by the poloidal field only, and $B_\phi$ falls out of the equilibrium calculation. This is analogous to the situation for the Bennett pinch in linear geometry (Sect. 1.5.3).

Figure 1.12 gives the calculated magnetic surfaces [level curves of function $\psi(R, Z)$], with the outer circle as the conducting wall. The curves are independent of distance scales, but to be specific we choose $a = 12$ cm and $R_0 = 40$ cm as in ORMAK-I; the border of the

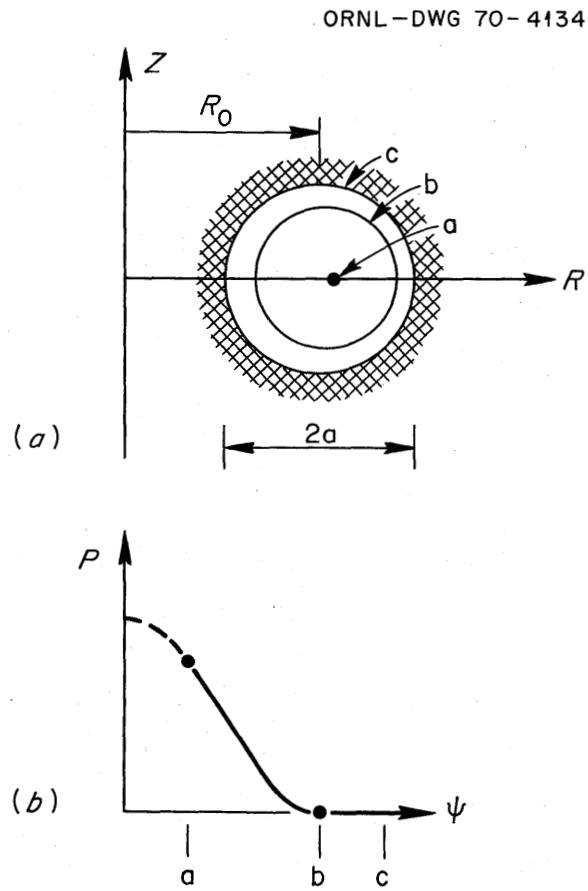


**Fig. 1.11. TOKAMAK Equilibria.** (*a*) Coordinate system and geometry; (*b*) pressure profile for the ad hoc equilibrium. The labels *a, b, c* refer to the magnetic axis, the plasma edge, and the conducting wall.

[34] L. Spitzer, *Physics of Ionized Gases*, p. 30, Interscience, New York, 1962.

[35] See, for example, V. D. Shafranov, p. 115 in *Review of Plasma Physics*, vol. 2, ed. by M. A. Leontovich, Consultants Bur., New York, 1966.

[36] R. A. Dory, *Bull. Am. Phys. Soc.* **14**, 1016 (1969).

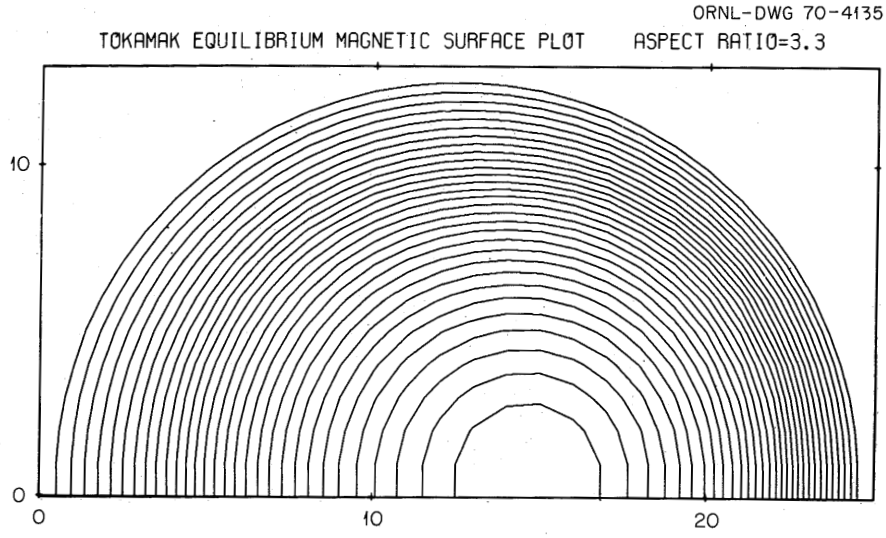


**Fig. 1.12. Magnetic Surfaces for the ad hoc Equilibrium.**

graph is $-0.5$ cm $\leqslant Z \leqslant 12.5$ cm and 27.5 cm $\leqslant R \leqslant$ 52.5 cm. The separation $\delta r$ between two lines can be used to find the local value of $B_{\text{poloidal}} = (\delta\psi/\delta r)/R$, where $\delta\psi$ is the poloidal flux between the lines.

Figure 1.13 gives, as functions of $\psi$, several quantities derived from the equilibrium solution. Curves *a* and *b* show the safety factor $q$ and the rotation transform $\iota$ in degrees. The two curves in *c* are concerned with interchange mode stability. The curve $V'(\psi)$ would determine stability *if the shear stabilization were ineffective*: at the larger values $\psi$ the slope $V''(\psi)$ is positive, implying instability.[37] Johnson and Greene[37] have given a stability criterion with better account taken of the shear. This criterion is that if $V^{**} \equiv dV^*/d\psi$ is everywhere negative, as it is here, then the equilibrium is relatively stable toward the "resistive" interchange mode, and the growth rate $\gamma$ is proportional to $\eta^\nu$ with $\nu < 1/3$. *Complete* stability does not appear in this model, because dissipation is included while source terms are not.

Curves *d* and *e* of Fig. 1.13 give the radii of the magnetic surfaces as functions of $\psi$. These may be used for detailed comparison with the analytic expansion approach,[38] in which the magnetic surfaces are

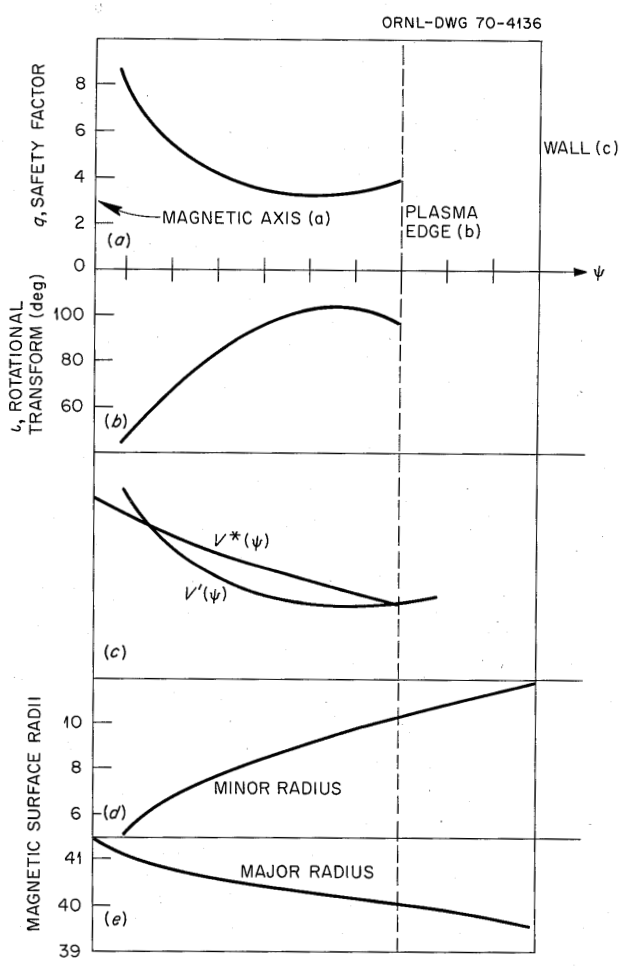


**Fig. 1.13. Parameters of the ad hoc Equilibrium as a Function of $\psi$.** Zeros are suppressed; units of $V'$, $V^*$, and $\psi$ are arbitrary.

[37] J. L. Johnson and J. M. Greene, *Plasma Phys.* 9, 611 (1967).

[38] L. S. Solovev and V. D. Shafranov, Kurchatov Institute Report IAE 1224 (Moscow, 1966); Culham Translation CLM-Trans 12 (Culham, 1967), and *Reviews of Plasma Physics*, vol. 5, ed. by M.A. Leontovich, Consultants Bur., New York, p. 1.

assumed to have circular cross section but the centers of the circles are assumed to vary.

The "poloidal beta," $\beta_{pol}$, which we define here as $8\pi$ max $(P)$/max $(B^2_{pol})$, is determined ex post facto but is controllable by the ratio of the $ff'$ and $4\pi R^2 P'$ terms in the PDE. In the present example the value is 1.4.

The "toroidal beta," $\beta = 8\pi \max(P)/B^2_\phi$, is arbitrary for the example since $B_\phi$ falls out of the equilibrium calculation when $f' = 0$. The stability curves, however, depend on $B_\phi$, and those shown correspond to $\beta \cong 1\%$. For this case $B_\phi$ could be lowered enough to raise $\beta$ to 10% before the minimum safety factor fell below unity. TOKAMAK's so far have been operated only in the $q \gtrsim 3$ regime, as here.

**1.3.2.2 Special Equilibrium.** – The $P$ and $f$ functions of the example just given were chosen to model the gross features (i.e., all that is known) of existing experiments. Besides this ad hoc choice, there is the "special equilibrium" model,[39] in which the $P(\psi)$ and $f(\psi)$ are given (implicitly) in terms of the applied Ohmic heating electric field $E_{OH}$ and the net plasma flux through each magnetic surface. This model is of interest for TOKAMAK plasmas that live as long as $\tau = r_p B/E_{OH}$, so that they have time to approach the special equilibrium. For the proposed ORMAK experiments, this state could be approached in the very late stages (10–50 msec), especially if enhanced plasma resistivity occurs as in the Russian experiments.

It was relatively simple to incorporate this model into our calculations and find solutions. The implicit nature of the prescriptions for $P$ and $f$ was evaded by using an iteration scheme with a convergence-improving parameter and a reasonable starting guess for the solution. It may be of interest that the calculation then is solved iteratively on three different levels: (1) application of the boundary conditions, (2) solution of the PDE, and (3) determination of the source functions $P$ and $f$.

In the theory of the special equilibrium, the only parameter which is not determined by self-consistency or by rescaling the problem is the toroidal curvature. Solving the equations using the value $A = 3.3$ as in ORMAK-I gives the results shown in Fig. 1.14. Notice that the radial displacement here is considerably less than in the previous example, reflecting the facts that the $ff'$ term in Eq. (5) is comparable with the $4\pi R^2 P'$ term, and that $B_{toroidal}$ is taking on much of the job of balancing $\nabla P$.

The resulting functions $P$ and $f$ are remarkably linear in $\psi$. This suggests reexamination of Eq. (5) for possible analytic solutions. Equation (5) is separable,[40] and solutions are of the form

$$\psi \propto \cos k_Z Z \, [C_1 \, F_0(k_R^2 R^2) + C_2 \, G_0(k_R^2 R^2)] \, ,$$

where $F_0$ and $G_0$ are the ($s$-wave) Coulomb wave functions.[41] From the graphs given in ref. 41, we see why the numerical solutions are characterized by

[39] H. Grad, *Phys. Rev. Letters* **24**, 1337(1970). Also see ref. 35, p. 145.

[40] E. W. Laing, S. J. Roberts, and R. T. P. Whipple, *J. Nucl. Energy: Pt. C* 1, 49 (1959).

[41] M. Abramowitz and I. Stegun, *Handbook of Mathematical Functions*, AMS-55, p. 537, U.S. National Bureau of Standards, Washington, D.C., 1964.

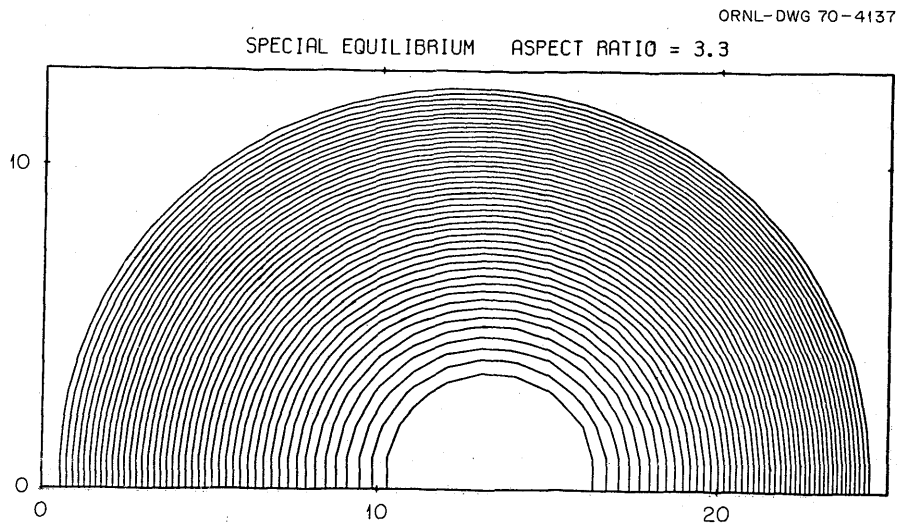


**Fig. 1.14. Magnetic Surfaces for Grad's "Special Equilibrium."**

smooth variations with quite circular magnetic surface cross sections: If the region of interest excludes $R = 0$, as in any experiment, the $F_0$ and $G_0$ functions are smooth and behave essentially like sin $k_R^2 R^2$ and cos $k_R^2 R^2$.

**1.3.2.3 Other Cases.** – By tailoring the $f$ and $P$ functions, we can easily find equilibria with other values of $\beta_{\text{poloidal}}$ and $\beta$ or other values and variations of $q$, $V^*$, etc. We can also study the effect of letting the plasma pressure be balanced by the toroidal field or by externally applied "vertical" $B_Z^{(\text{ext})}$, either of which would be desirable from the point of view of projected reactor designs because the nearby conducting wall might then be unnecessary.

**1.3.2.4 Conjectures.** – To the extent that experiments in the past and near future and hypothetical reactors with classical resistivity are not sufficiently longlived to assure evolution to the special equilibrium, we must expect that $P$ and $f$ are determined by the initial conditions and the subsequent history (quiesence, turbulence, instability, etc.) of the plasma. The study of this needs some input information from experiment or from dynamical studies of the system evolution. It is probably feasible to do these studies using computers to follow the time-dependent MHD equations, as has been done for stellarator systems.[42]

### 1.3.3 High-Beta Equilibria in TOKAMAK's with Large Toroidal Curvature[36]

R. A. Dory

The equilibrium condition $\mathbf{J} \times \mathbf{B} = \text{grad}\, P$ for scalar pressure is solved with Ampere's law, curl $\mathbf{B} = 4\pi\mathbf{J}$. Assumption of axisymmetry and perfectly conducting toroidal walls gives unique solutions when arbitrary "shape functions" $P(\psi)$ and $f(\psi)$ are chosen.[43] In cylindrical coordinates $(R, Z, \phi)$, the poloidal flux function is $\psi(R, Z) \equiv R A_\phi(R, Z)$, and $f(R, Z) \equiv R B_\phi(R, Z)$. A successive overrelaxation scheme has been used to solve the implicit equation for $\psi$:

$$\frac{\partial^2 \psi}{\partial Z^2} - R^{-1} \frac{\partial \psi}{\partial R} + \frac{\partial^2 \psi}{\partial R^2} = -f(\psi) f'(\psi) - 4\pi R^2 P'(\psi) ,$$

for sample $P(\psi)$ and $f(\psi)$. Convergence fails for sufficiently large $\beta = 8\pi P/B^2$, suggesting nonexistence of equilibrium or possible instability. This study should yield estimates of critical upper limits on $\beta$ and dependence on the shape functions. Profiles are found for $P$, $B$, $J$ as functions of $R$ and $Z$ for comparison with projected experiments.

### 1.3.4 Magnetic Field of a Current Loop in a Toroidal Conductor[44]

P. B. Burt[45]

In the limit of indefinitely large conductivity the magnetic field of a current loop enclosed by a conductor is itself completely enclosed by the conductor. The total field consists of the vacuum field in the absence of walls and the field due to the image currents in the walls. The current loop must be in equilibrium with these fields. As the first step in the study of toroidal equilibria, the magnetic field due to an axially symmetric current loop in the interior of a toroidal conductor of arbitrary aspect ratio, circular cross section, and indefinitely large conductivity is calculated.

## 1.4 TURBULENT HEATING AND NONLINEAR PROBLEMS

### 1.4.1 Turbulent Heating of Ions in Beam-Plasma Experiments

M. Widner G. E. Guest R. A. Dory

In the present investigations we seek to understand the mechansims by which the energy of a direct-current electron beam is transformed into thermal energy of a dense ion plasma in the Burnout V device.[46] Auto- and cross-correlation measurements reveal large-amplitude electric fields at frequencies $\omega \sim \omega_{pi}$, the ion plasma frequency, uniform along a magnetic field line but poorly correlated in azimuth, suggesting that the (ion) hybrid resonance, $\omega_H \approx \sqrt{\omega_{pi}^2 + \Omega_i^2}$, is being excited by the radial electric field of the electron beam. In order to understand the basic processes through which this resonant excitation can take place, we have studied the response of an inhomogeneous plasma column whose density varies only in the radial direction to the fields of an unneutralized (finite) electron beam,

[42] N. K. Winsor, J. L. Johnson, and J. M. Dawson, *A Fluid Model for Toroidal Low-Beta Confinement,* Plasma Physics Laboratory Report MATT-651, Princeton, N.J. (1968).

[43] V. D. Shafranov, p. 113 in *Review of Plasma Physics,* vol. 2.

[44] This paper is currently available as ORNL-TM-2895.

[45] Consultant: Physics Department, Clemson University.

[46] *Thermonuclear Div. Ann. Progr. Rept. Dec. 31, 1968,* ORNL-4401, p. 98.

switched on at $t = 0$. Under some simplifying assumptions, the response can be determined analytically and compared with the results of a plasma simulation scheme.

The model studied here assumes an infinitely long cold-plasma column with density $N = N(r)$ aligned along a uniform magnetic field, $\mathbf{B} = B_0\hat{\mathbf{z}}$. Only motions in the plane perpendicular to $\mathbf{B}$ are considered. The plasma is initially charged neutral; but at $t = 0$ an electron beam, uniform throughout its finite radial extent ($r \leqslant r_b$), is superimposed along the axis of the column. The response of the plasma to the resulting electric field is then computed.

To obtain analytical estimates, we use the cold-fluid equations and Poisson's equation:

$$\frac{d\mathbf{v}}{dt} = \frac{q}{m}(\mathbf{E} + \mathbf{v} \times \mathbf{B}) ,$$

$$\frac{\partial N}{\partial t} + \nabla\cdot(N\mathbf{v}) = 0 ,$$

$$\nabla\cdot\epsilon_0\mathbf{E} = q(N_i - N_e) - qN_b .$$

The equations are linearized about the static charge-neutral equilibrium, Fourier analyzed in $\theta$, the azimuthal angle, and Laplace transformed in time. In general, this analysis is complicated by the singular nature of the resulting differential equation for the electrostatic potential $\phi$.[47] However, for azimuthally symmetric fluctuations [i.e., $\phi \sim \phi(r)\exp(im\theta$ with $m = 0$], the basic features of the problem are displayed clearly. From $\nabla\cdot\tilde{\mathbf{D}} = \tilde{\rho}_b$, where $\tilde{\rho}_b$ is the charge density of the beam (Laplace transformed in time),

$$\frac{1}{r}\frac{\partial}{\partial r} r\,\kappa(r)\,\epsilon_0\tilde{E}_r = \tilde{\rho}_b(r) ,$$

whence

$$\kappa(r)\,\tilde{E}_r = \frac{1}{r\epsilon_0}\int_0^r dr'\,r'\,\tilde{\rho}_b(r') ,$$

where

$$\kappa(r) = 1 - \frac{\omega_{pi}^2(r)}{\omega^2 - \Omega^2} .$$

[47] A more general treatment of this problem may be found in J. A. Bernstein, *Phys. Rev.* **109**, 10 (1958); T. H. Stix, *Theory of Plasma Waves*, chap. 5, McGraw-Hill, 1962; S. J. Buchsbaum and A. Hasegawa, *Phys. Rev. Letters* **12**, 685 (1964); S. J. Buchsbaum and A. Hasegawa, *Phys. Rev.* **143**, 303 (1966); and D. E. Baldwin, *J. Plasma Phys.* **1**, 289 (1967).

If we describe the beam density as

$$\tilde{\rho}_b = -e\tilde{N}_b\,[U(r) - U(r - r_b)]$$

using the unit step functions $U(s)$, then

$$\kappa(r,\omega)\,\mathbf{E}_r(r,\omega) = -\frac{e\tilde{N}_b}{2\epsilon_0}\begin{pmatrix} r \\ r_b^2/r \end{pmatrix} \quad \begin{matrix} r \leqslant r_b \\ r \geqslant r_b \end{matrix} .$$

In the simulation we study the temporal response to beams for which

$$N_b(t) = N_b\,U(t) ,$$

or

$$\tilde{N}_b = iN_b/\omega .$$

A convenient parameter for comparison with results of the simulation is the relative electric field energy:

$$W\,E(t) \equiv \frac{\int r\,dr\,E^2(r,t)}{\int r\,dr\,E^2(r,0)} .$$

Here

$$E_r(r,t) = -\frac{e}{\epsilon_0}\frac{N_b}{2}\left[\frac{\omega_p^2(r)}{\omega_H^2(r)}\cos\omega_H(r)\,t + \frac{\Omega^2}{\omega_H^2(r)}\right] \times \begin{pmatrix} r \\ r_b^2/r \end{pmatrix} \quad \begin{matrix} r \leqslant r_b \\ r \geqslant r_b \end{matrix} .$$

In Fig. 1.15 we show $W\,E(t)$ for a model in which $N(r) = \exp(-r^2/r_b^2)$ and $\omega_p^2(0)/\Omega^2 = 1$. Note that although a spectrum of frequencies $\Omega \leqslant \omega \leqslant \omega_H(0)$ is excited, the dominant frequency is given by the local hybrid frequency near $r = r_b$, where the electric field and the

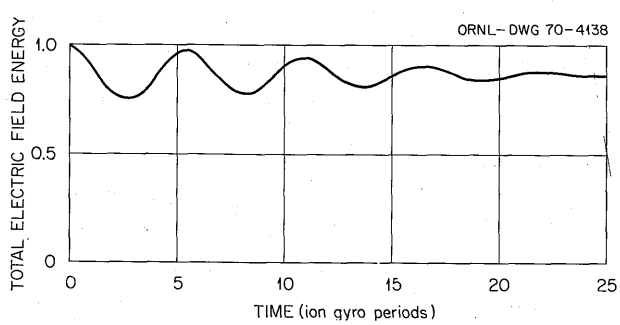


**Fig. 1.15. Total Electric Field Energy vs Time.**

density of particles are maximum. We attribute the apparent damping of the oscillations to phase mixing, which should occur with a rate $|\Delta\omega| = \omega_H(0) - \Omega$ and which results in a net transfer of kinetic energy to the ions.

The well-known cloud-in-cell (CIC) particle-following scheme[48,49] is used for the numerical simulation. The scheme represents the plasma as a collection of finite-size particle (clouds) which individually obey Newton's force law. The particles move through a fixed mesh at whose nodes the charge density and electric field are defined. At each time step the charge density is computed from the particle positions in an area weighting fashion. Poisson's equation is then solved for the self-consistent electric field, which in turn acts upon the particles the next time. The CIC technique has the property of smoothing the electric fields over a cell size. As there are fewer particles ($\sim 10^4$) for the simulation than for a real plasma ($\sim 10^{16}$), this smoothing tends to reduce the noise produced by statistical fluctuations of the number of particles within a given cell. The smoothing also has the undesirable effect of filtering short-wavelength disturbances.

As is apparent, practical limitations to the number of particles and cells demand careful attention to the artificially imposed constraints of the simulation. For example, to reduce the statistical fluctuations (which tend to heat the particles stochastically), it is necessary to increase the number of particles or to increase sharing (overlapping of particles). Increasing the number of particles is costly; however, sharing can be improved with a careful initial loading of the particles (quiet start).[50] Other practical considerations demand an accurate, efficient particle-following scheme and efficient programming.

The simulation solution should have the following properties to provide meaningful results (as ours does): (1) The total energy must remain virtually constant, or, more precisely, fluctuations in the total energy should be much smaller than electric field energy fluctuations. (2) The numerical solution must be insensitive to the artificially imposed constraints of the simulation. (3) Some comparison with analytic theory should be made.

The numerical simulation described here is based upon the plasma model previously mentioned. The electrons are treated as a background [$\mathbf{v}_e = (\mathbf{E} \times \mathbf{B}_0)/B_0^2$], permitting particle following on an ion time scale. The exact motion of the ions is computed. A rectangular mesh is used, at the center of which is the axis of symmetry for the plasma and the imposed beam. The boundary of the mesh is far from the plasma. Poisson's equation is solved on the mesh using cyclicreduction with $\phi = 0$ on the mesh boundary. The problem is scaled in terms of ion gyrofrequency, ion gyroradius, etc. Since the particles are started cold, the $\langle v_\perp \rangle$ for scaling purposes is chosen so that the physical size of the plasma and electron beam is the same as that of Burnout V.[46] The mesh used is typically 32 × 32 cells, with the beam radius corresponding to about five cell sides. At $t = 0$, particles are carefully loaded to minimize grid noise, with the electrons on top of the ions as shown in Fig. 1.16. The particle size is the same as a cell size, and there are ten or more particles per cell in the interior plasma. The plasma density has a Gaussian radial density profile [$n(r) = e^{-r^2/r_b^2}$, where $r_b$ = beam radius].

The various energy vs time curves are shown in Fig. 1.17. The similarity with the analytic result is quite apparent, with the same frequency excited, the same damping time, and the same amount of energy transferred to the ions.

These calculations reinforce our earlier conjectures that the ion heating mechanism involves coupling of the

ORNL-DWG 70-4139

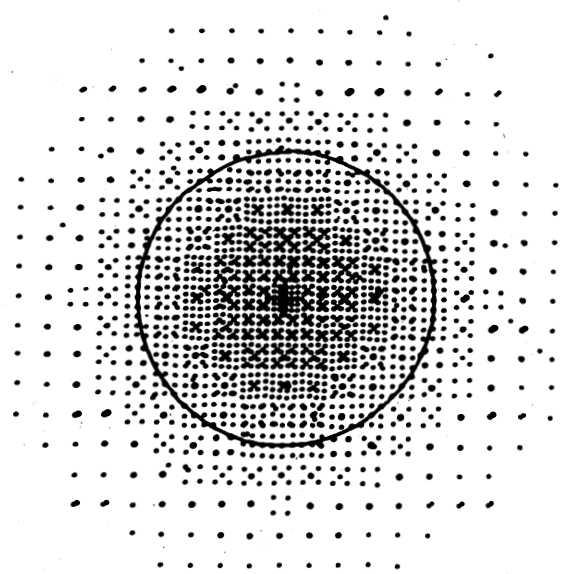

**Fig. 1.16. Particle Positions at Time = 0.0.**

[48] ORNL-4401, *op. cit.*, p. 18.

[49] C. K. Birdsall and D. Fuss, *Clouds-in-Clouds Physics for Many-Body Plasma Simulation,* UCRL-71068 (Aug. 9, 1968).

[50] J. A. Byers and M. Grewal, *Perpendicularly Propagating Plasma Cyclotron Instabilities with a One-Dimensional Computer Model,* UCRL-71870 (July 28, 1969).

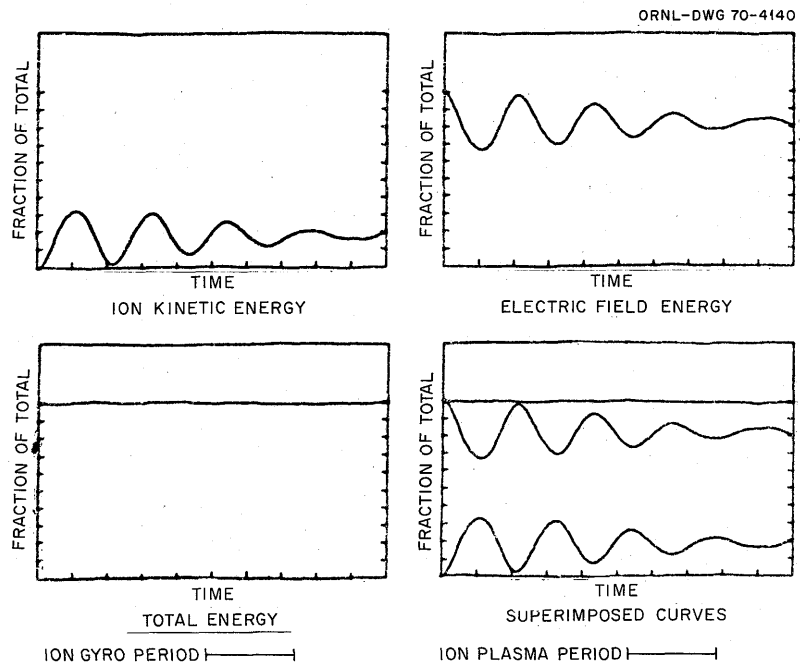


**Fig. 1.17. Energy vs Time Plots.**

electron beam to the broad ion hybrid resonance, with energy transfer by phase mixing.

**1.4.1.1 Acknowledgments.** – Discussions with I. Alexeff and R. V. Neidigh provided an experimental basis for formulating the problem. Suggestions of J. A. Byers and C. K. Birdsall of Lawrence Radiation Laboratory were very helpful for the numerical simulation.

### 1.4.2 Beam-Plasma Interaction with a Plasma Density Gradient

G. E. Guest L. S. Hall[51]

The one-dimensional beam-plasma interaction has been analyzed frequently in the past using various simplified models. The most ubiquitous ones have been infinite homogeneous models in which collisions or weak thermal connections were incorporated to yield finite growth rates for the electrostatic instability. Table 1.3 summarizes the results of these analyses.

Some recent computer experiments[52] have suggested that density gradients along the beam are more important in limiting growth than collisions, thermal effects, or even plasma or beam nonlinearities. Such observations raise the question of the importance of control of density gradients in experiments such as Burnout V.

We have applied a theory by Hall[53] to a one-dimensional system with plasma density gradients along the beam direction and find that growth is bounded even in the absence of collisions or thermal effects. The theory is a generalization of an earlier treatment of the long-time behavior of unstable systems in which one imagines a saddle-point analysis of the dispersion relation in a set of moving reference frames. The two relations, as applied to the present model, are

$$D(\omega, k) = 1 - \frac{\omega_p^2}{\omega^2} - \frac{\omega_b^2}{(\omega - ku_0)^2} = 0$$

and

$$Q(\omega, k, V) = \frac{\partial D}{\partial k} + V\frac{\partial D}{\partial \omega} = 0 .$$

These determine $\omega(V)$ and $k(V)$ at the saddle points in the reference frame having velocity $V$. The temporal

[51] Lawrence Radiation Laboratory, Livermore, Calif.

[52] J. A. Davis and A. Bers, Proceedings Polytechnic Institute of Brooklyn Symposium on Turbulence, April 1968.

[53] L. S. Hall, *Theory of Propagation of Non-Stable Waves*, UCRL-71648 (Apr. 18, 1969).

**Table 1.3. Linearized One-Dimensional Beam-Plasma Models**

Cold, Collisionless, Uniform

$$1 - \frac{\omega_p^2}{\omega^2} - \frac{\omega_b^2}{(\omega - ku_0)^2} = 0 \longrightarrow \text{Im}\, k \to \infty \text{ as } \omega \to \omega_p{}^*$$

Cold, Collisional, Uniform

$$1 - \frac{\omega_p^2}{(\omega + i\nu)^2} - \frac{\omega_b^2}{(\omega - ku_0)^2} = 0 \longrightarrow \text{Max Im}\, k \sim \frac{\omega_b}{u_0}\sqrt{\frac{\omega_p}{4\nu}}$$

Temperate, Collisionless, Uniform

$$1 - \frac{\omega_p^2}{\omega^2}\left(1 + \frac{3k^2 v_{\text{th}}^2}{\omega^2}\right) - \frac{\omega_b^2}{(\omega - ku_0)^2} = 0 \longrightarrow \text{Max Im}\, k \sim \frac{\omega_b}{u_0}\sqrt{\frac{u_0^2}{3v_{\text{th}}^2}}$$

*For large times, $\ln E(z, t) \sim z^{2/3}\, t^{1/3}$.

growth rate in such a frame is then $\gamma = \text{Im}\,(\omega - kV)$. Since $\ln E \sim \gamma t$ and the position of a pulse element is $z = Vt$, a plot of $\gamma$ vs $V$ gives the pulse shape of a growing disturbance. For the present example such a pulse shape is shown in Fig. 1.18, which illustrates the important point that $\gamma \to 0$ as $V \to 0$ and 1.

This description identifies each element of the pulse with a velocity which, for a slowly varying plasma, must change. If we take for our model

$$\frac{\omega_p^2(x)}{\omega_b^2} \equiv a(x) = a_0(1 - x^2/L^2)\,,$$

then Hall's theory predicts

$$\frac{dV}{da} = \text{Re}\left(-\frac{1}{k}\frac{\partial D/\partial a}{\partial D/\partial \omega}\right)$$

$$= \frac{1 - V}{4a}\,\frac{s(1 + 2s)}{1 + s + s^2}\,,$$

where

$$s \equiv \left(\frac{aV}{1 - V}\right)^{1/3}.$$

To obtain the asymptotic growth we integrate $dV/da$ from some initial value $V = V_0$ at $a = a_0$ until $V$ goes to zero. Then the total growth is obtained by computing

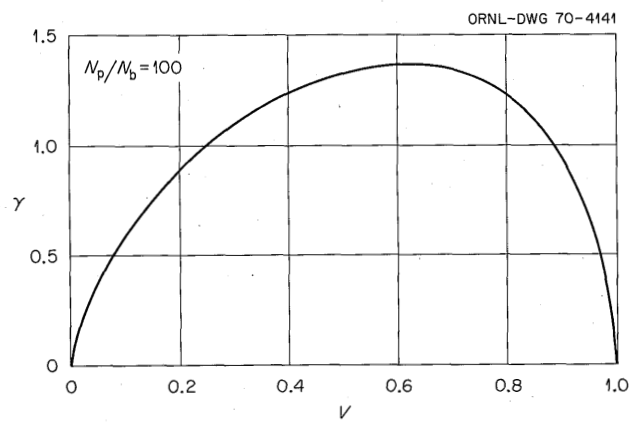


**Fig. 1.18. Temporal Growth Rate $\gamma$ (Normalized to $\omega_b$) as a Function of Observer's Speed $V$ (Relative to $u_0$).** The ratio of plasma to beam density, $a_0$, is 100 for the case shown here.

$$\ln\left(\frac{E(z)}{E_0}\right) = \int_0^\infty dt\, \gamma[a(t), V(t)]\,,$$

where the integration is along that trajectory (specified by $V_0$) whose limit point, $V = 0$, is $z$. The time dependence of the response at some point $z$ can be obtained by recording the instantaneous growth and arrival times of pulse elements whose limit points exceed $z$.

As noted in Table 1.3, the spatial growth rate has the general form

$$\operatorname{Im} k \sim \frac{\omega_b}{u_0} \times G(\omega_p, \gamma, v_{th}, \text{etc.}) \ ,$$

so that we expect asymptotic growth in a column of length $L$ to have the form

$$\ln \frac{E_\infty}{E_0} \sim \frac{\omega_b L}{u_0} \times G[\omega_p(z)] \ .$$

In Fig. 1.19 we display the form factors $G$ for three values of plasma-to-beam density ratio: $a_0 = \omega_{p0}^2/\omega_b^2$. The time dependence of the plasma response at three fixed positions, $z = x/L = 0.1, 0.3, 0.9$, is shown in Fig. 1.20, in which the solid lines are for a homogeneous plasma and the dashed lines for the present inhomogeneous case.

The point of this calculation is that density gradients can lead to a limitation on the asymptotic growth of the beam-plasma interaction which can be at least as important as collisions or thermal effects. Still, the anticipated growth is large, and beam behavior in Burnout V remains an open question.

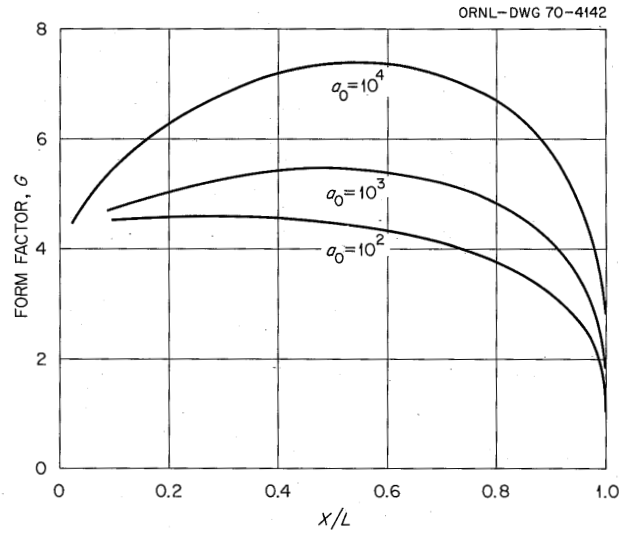


**Fig. 1.19. Growth Factor $G$ for Various Positions in the Plasma and for Three Different Density Ratios.** Here $E \sim \exp(G\omega_b L/u_0)$.

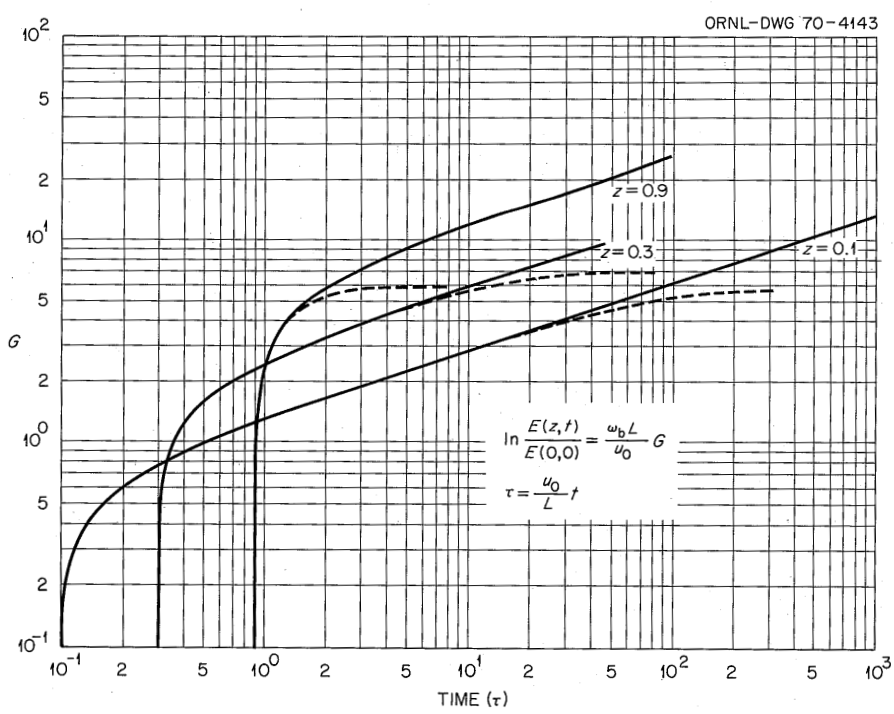


**Fig. 1.20. Time Dependence of the Growth Factor $G$ at Three Different Positions in the Plasma.** The solid lines are for a uniform plasma model; the dashed lines are for the present model.

### 1.4.3 Wave-Particle Energy Transfer and Wave Amplitude Limiting Effects

J. D. Callen[54] C. E. Parker D. J. Sigmar

We have studied the nonlinear problem of charged-particle motion in the presence of a wave

$$\delta \mathbf{E}_0 = \delta \mathbf{E}_0 \cos(kx - \omega t + \phi_0)$$

with frequencies $\omega$ near odd multiples of $\Omega/2$, where $\Omega$ is the particle gyrofrequency in a uniform magnetic field. For waves near gyroresonance, $\omega \sim n\Omega$, the energy transfer between wave and particle has been calculated in an adiabatic approximation.[55] But near half-harmonic frequencies, $\omega = (n + \frac{1}{2})\Omega$, the adiabatic approximation gives results in contradiction to known modes of instability.[56] The present work resolves this discrepancy and demonstrates, for both cases, that the nonlinearity in the particle orbits can detune resonant modes for electric field strengths such that

$$e\,\delta V_0/kT_\perp \gtrsim 2(k_\perp a)^{-1/2}\,(\omega - n\Omega)/n\Omega\,,$$

where $\delta V_0 = \delta E_0/k_\perp$ is the fluctuating potential, $a$ is the gyroradius, and $kT_\perp$ is the perpendicular energy. Substantial change in gyroradius will occur for times

$$\Omega t \sim \frac{n\Omega}{\omega - n\Omega} \sim 2(k_\perp a)^{-1/2}\,(e\,\delta V_0/kT_\perp)^{-1}\,.$$

Aamodt and Bodner[57] and Bodner and Byers[58] have recently arrived at similar scalings from much more exhaustive nonlinear studies in the short-wavelength limit.

We define the wave-to-particle energy transfer

$$\langle \Delta E(t) \rangle = \left\langle \frac{v^2(t)}{v^2(0)} - 1 \right\rangle ,$$

where angle brackets denote an average over the initial wave-particle phases. The time dependence shows fast gyration and a slower variation which we extract by averaging over a full gyroperiod for harmonic modes and half a gyroperiod for half-harmonic modes at each instant of time. The resulting coarse-grained $\Delta E$ is denoted $\langle \overline{\Delta E(t)} \rangle$. Examples for harmonic and half-harmonic waves are shown in Fig. 1.21, the harmonic case showing secular energy gain while the half-harmonic case shows the fast recurrence after two gyrations, that is, $\tau = 2\pi/|\omega - \Omega|$. Here we have chosen $k_\perp a = \pi$; the effect of variation of wavelength is illustrated in Fig. 1.22, where $\langle \Delta E(t = 2\pi/\Omega) \rangle$ (after one gyration) is plotted against $k_\perp a$ for $\omega/\Omega = \frac{1}{2}$ and 1.

If the electric field is that of an incipient instability, the bands of $k_\perp a$ giving $\langle \Delta E \rangle < 0$ permit the particles to transfer energy to the wave to reinforce its growth (in agreement with the instability results of ref. 56). If the electric field is provided by microwaves, our results can serve to illuminate the effects of finite Larmor radius on high-frequency heating of plasma.

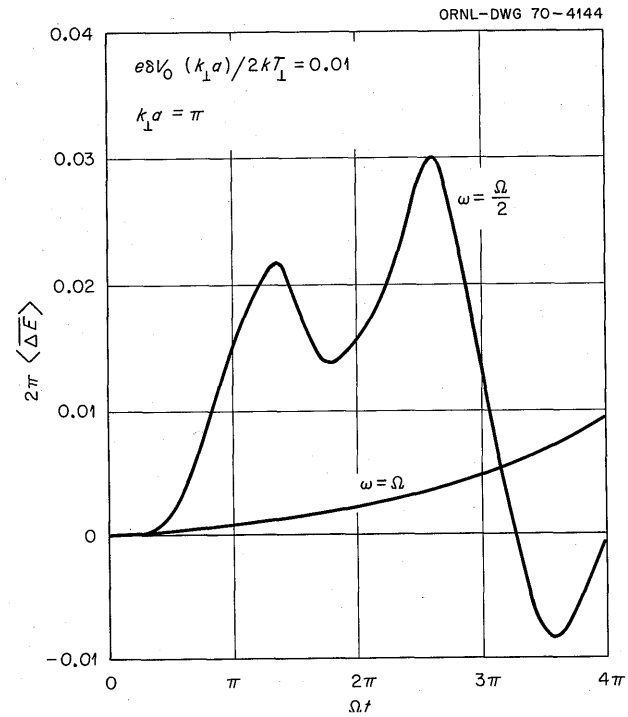


**Fig. 1.21. Coarse-Grained Particle Energy Gain vs Time for Harmonic and Half-Harmonic Modes.** For $\omega = \Omega$, the energy rises quadratically; for $\omega = \Omega/2$ there is near recurrence to energy-gain zero after two gyrations.

---

[54] Consultant: Aeronautics and Astronautics Department, MIT.

[55] L. S. Hall, W. Heckrotte, and T. Kammash, *Phys. Rev.* **139**, A1117 (1965).

[56] A. V. Timofeev, *Soviet Phys. JETP* **12**, 281 (1961).

[57] R. Aamodt and S. Bodner, *Phys. Fluids* **12**, 1471 (1969).

[58] S. Bodner and J. Byers, *Phys. Rev. Letters* **23**, 967 (Oct. 27, 1969).

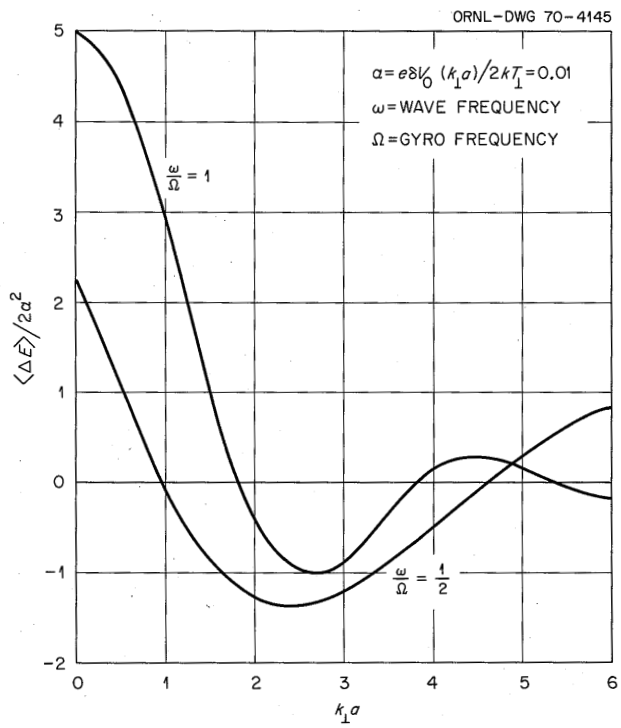


**Fig. 1.22. Particle Energy Gain After One Gyration vs $k_\perp a$ for Harmonic and Half-Harmonic Modes.** Notice the wide band of unstable wavelengths for $\omega = \Omega/2$.

### 1.4.4 Relativistic and Finite Cyclotron Radius Effects in Electron-Cyclotron Heating

Owen Eldridge[59]

**1.4.4.1 Introduction.** – Electrons in magnetic mirrors have been heated to relativistic energies by cyclotron heating (see Sect. 4). Several relativistic effects must be considered in order to understand the heating process.

*1. Finite Cyclotron Radius.* – The cyclotron radius $a = mc\gamma v_\perp/eB$ approaches the microwave wavelength when $v_\perp\gamma$ approaches $c$, with $\gamma = (1 - v^2/c^2)^{-1/2}$. The heating rate of an electron is decreased since the velocity cannot be in phase with the microwave field for an entire cycle.

*2. Resonance Condition.* – When $v/c \ll 1$, the resonance condition is $\omega = \Omega = eB/mc$. For relativistic velocities the frequency is Doppler shifted by electron motion along field lines and the cyclotron frequency is shifted by a factor $\gamma$. The resonance condition is $\omega = \Omega/\gamma + k_z v_z$. Defining a relativistic velocity $u_z, = \gamma v_z$, with a fourth component $u_0 = \gamma c$, the condition becomes

$$\frac{u_0\omega}{c} - \Omega - \frac{\omega\cos\beta}{c}u_z = 0\,, \tag{1}$$

where $k_z = (\omega/c)\cos\beta$ covers the range $\omega/c \geqslant k_z \geqslant -\omega/c$. The result is a resonant zone in velocity space, which is plotted in Fig. 1.23. Resonance may occur in the area bounded by the resonance curve, by the line $u_\perp = u_z$ that represents the loss cone for a mirror ratio of 2, and by the circle $u_\perp^2 + u_z^2 = \text{const}$, drawn for a 1-MeV electron.

*3. Cyclotron Harmonics.* – The microwave field can also resonate with harmonics of the cyclotron motion. The resonance condition is

$$\frac{u_0\omega}{c} - m\Omega - \frac{\omega\cos\beta}{c}u_z\,. \tag{2}$$

The resonant zones for $m = 2$ and $m = 3$ are shown in Figs. 1.24 and 1.25.

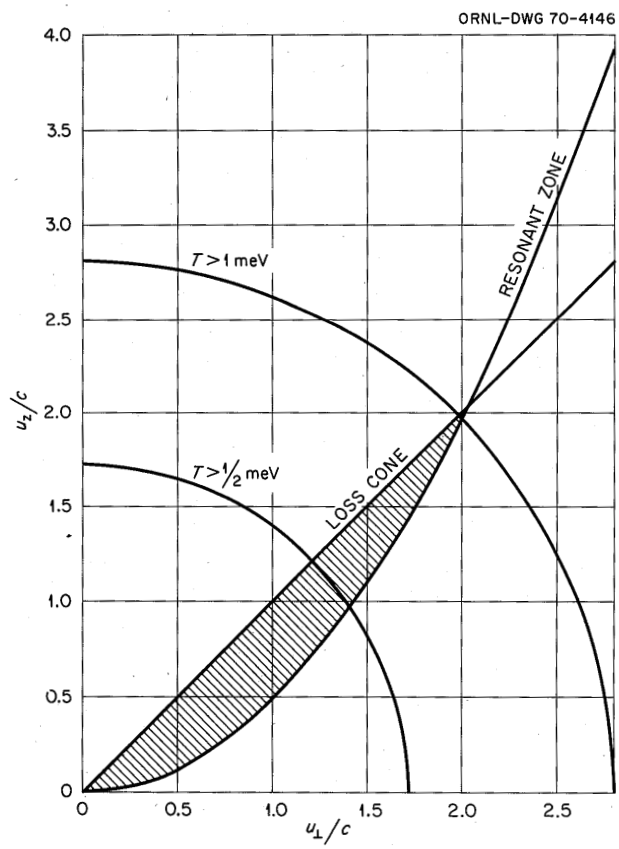


**Fig. 1.23. Resonant Zone for $m = 1$, Mirror Ratio = 2, $\omega = \Omega$.**

[59] Consultant: Physics Department, University of Tennessee.

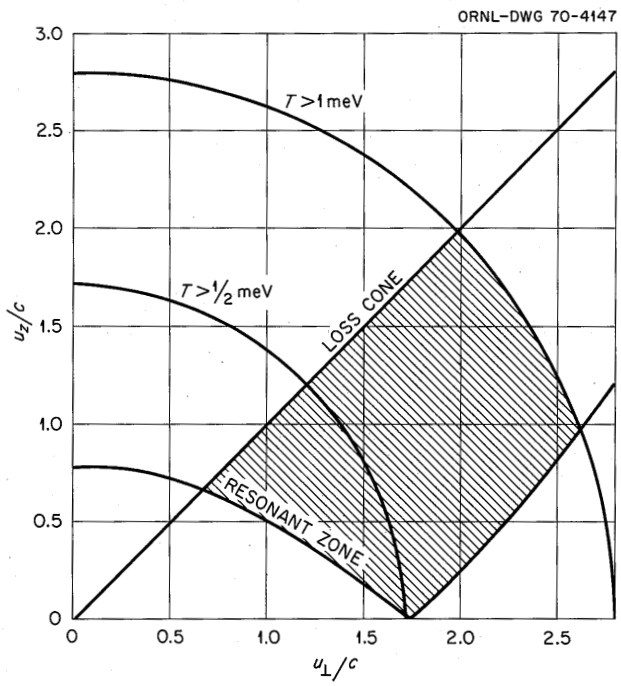


Fig. 1.24. Resonant Zone for $m$ = 2, Mirror Ratio = 2, $\omega = \Omega$.

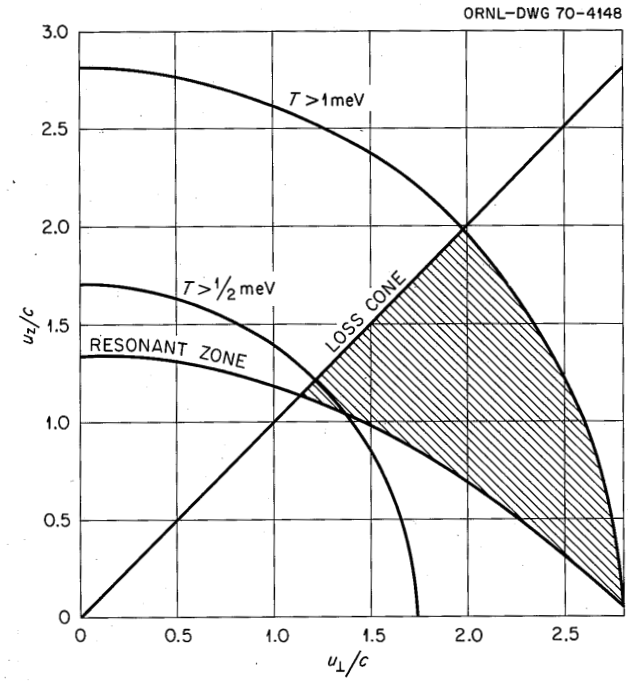


Fig. 1.25. Resonant Zone for $m$ = 3, Mirror Ratio = 2, $\omega = \Omega$.

*4. Spatial Diffusion.* – Since the Doppler shift can cause the microwave field to appear to have a low frequency for a fast electron, spatial diffusion is not negligible.

**1.4.4.2 Perturbation Calculation.** – A perturbation calculation of the orbits of single electrons leads naturally to a description of cyclotron heating as a diffusion in velocity space. The essential assumption is that the energy in the microwave field is small compared with the electron kinetic energy. This is always true in practice. No specific assumptions about the stochastic nature of the external microwave field are necessary, but if random shifts in the field do occur, the coherence time must be long compared with a cyclotron period.

We also assume that the static magnetic field is uniform or that it changes insignificantly within a cyclotron radius. Near the turning points of orbits in a mirror field this is probably not adequate, since the character of the orbits is changed drastically.

*1. Equations of Motion.* – An electron with relativistic velocity $\mathbf{u} = \gamma\mathbf{v}$, $u_0 = \gamma c$, orbiting in a static field $B_z = mc\Omega/e$, obeys the equation

$$\frac{d\mathbf{u}}{d\tau} = \mathbf{u} \times \Omega + \frac{e}{mc}(u_0\mathbf{E} + \mathbf{u} \times \mathbf{B}) \tag{3}$$

in the oscillating fields **E** and **B**. The proper time is $\tau = t/\gamma$. The equation for the motion of the electron guiding center,

$$\boldsymbol{\xi} = \mathbf{x} + \frac{\mathbf{u} \times \Omega}{\Omega^2}, \tag{4}$$

is

$$\frac{d\boldsymbol{\xi}}{d\tau} = \frac{e}{mc\Omega^2}(u_0\mathbf{E} + \mathbf{u} \times \mathbf{B}) \times \Omega \ .$$

The unperturbed orbits are

$$\begin{aligned} \boldsymbol{\xi} &= \text{const}, \\ u_z &= \text{const}, \\ u_x + iu_y &= u_\perp \exp[i\phi - i\Omega\tau] \ . \end{aligned} \tag{5}$$

*2. First Order.* – The microwave field is written as a sum over a finite number of plane waves,

$$\mathbf{E} = \sum_{\text{modes}} \mathbf{E}_k \exp(i\mathbf{k}\cdot\mathbf{x} - i\omega t) \ , \tag{6}$$

and zero-order orbits are used to specify the phase. The result of perturbation theory is to first order in $\mathbf{E}_k$:

$$u_x + iu_y|_1 = \frac{ie}{mc} \sum_{\text{modes}} \exp(i\mathbf{k}\cdot\boldsymbol{\xi} + i\phi - i\Omega t)$$

$$\times \sum_{m=-\infty}^{\infty} e^{im(\alpha-\phi)} \frac{e^{-i\Lambda\tau} - 1}{\Lambda}$$

$$\times [J_{m-1} e^{-i\alpha}(u_0 E^+ + iu_z B^+) - iJ_m u_\perp B_z] \ . \quad (7)$$

The effect of a finite cyclotron radius is expressed by the Bessel functions $J_m$ with argument $k_\perp u_\perp/\Omega$, and $k_x = k_\perp \cos\alpha$, $k_y = k_\perp \sin\alpha$. The velocities oscillate in time with frequency $\Lambda$, where

$$\Lambda\tau = \left(\frac{u_0\omega}{c} - m\Omega - k_z u_z\right)\tau \ .$$

For fixed $\Lambda$ they oscillate in time, but after a long time only the $\Lambda = 0$ terms contribute:

$$\lim_{\tau\to\infty} \frac{1}{\Lambda^2} \sin^2 \frac{\Lambda\tau}{2} = \frac{\pi\tau}{2}\delta(\Lambda) \ . \quad (9)$$

In the long time limit a resonant diffusion appears automatically.

*4. Diffusion and Heating.* – The results of first-order perturbation theory may be represented as diffusion coefficients:

$$u_{\perp_1}^2 = 4B_\perp t \ ,$$

$$u_{z_1}^2 = 2B_\parallel t \ , \quad (10)$$

$$\xi_{\perp_1}^2 = 4D_\perp t \ ,$$

with

$$B_\perp = \frac{\pi}{4}\left(\frac{e}{m}\right)^2 \int_{-1}^{1} \frac{d(\cos\beta)}{2} |E|^2 \sum_m \delta(ku_0 - m\Omega - ku_z\cos\beta) \frac{1}{u_0 c} [J_{m-1}^2(u_0^2 + u_z^2)(1 + \cos^2\beta) + J_m^2 u_\perp^2 \sin^2\beta] \ ,$$

$$B_\parallel = \pi\left(\frac{e}{m}\right)^2 \int_{-1}^{1} \frac{d(\cos\beta)}{2} |E|^2 \sum_m \delta(ku_0 - m\Omega - ku_z\cos\beta) \frac{1}{u_0 c} \left[J_m^2 u_0^2 \sin^2\beta + \frac{J_{m+1}^2 + J_{m-1}^2}{4} u_\perp^2 (1 + \cos^2\beta)\right] \ , \quad (11)$$

and

$$D_\perp = \frac{\pi}{4}\left(\frac{e}{m\Omega}\right)^2 \int_{-1}^{1} \frac{d(\cos\beta)}{2} |E|^2 \sum_m \delta(ku_0 - m\Omega - ku_z\cos\beta) \frac{1}{u_0 c} [J_m^2(u_0^2 + u_z^2)(1 + \cos^2\beta) + J_{m+1}^2 u_\perp^2 \sin^2\beta] \ .$$

Similar results are found for $\boldsymbol{\xi}$ and $u_z$.

*3. Averaging.* – To find how the velocities and guiding center change with time, we form $u_\perp^2$, $u_z^2$, and $\xi_\perp^2$ and (1) integrate over a volume large compared with a wavelength, (2) integrate over the phase $\phi$ of the velocity, and (3) specify the microwave field. We say that the field is external and transverse with

$$\mathbf{E}\cdot\mathbf{B} = \mathbf{k}\cdot\mathbf{B} = \mathbf{k}\cdot\mathbf{E} = 0 \ ,$$

$$|E^2| = |B^2| \ , \quad (8)$$

$$\omega = \pm kc \ .$$

We average over the angles that specify the direction of the wave vector.

As a result we find that $u_\perp^2$, $u_z^2$, and $\xi_\perp^2$ are proportional to

$$\frac{1}{\Lambda^2} \sin^2 \frac{\Lambda\tau}{2} .$$

All the relativistic effects are included in these coefficients. To calculate heating rates in a particular device, the coefficients should be averaged over the velocity and spatial distribution of electrons. This is rather difficult to do analytically and probably requires a computer integration.

From the diffusion coefficients it is possible to calculate the scattering of electrons into the loss cone and to compare this loss with radial diffusion. It is also possible to include the effects of a combination of wavelengths in the external field.

### 1.4.5 Numerical Solution of the Nonlinear Vlasov Equation

H. K. Meier

Numerical instabilities are one of the main difficulties in obtaining computer solutions of the nonlinear Vlasov equation. Because of the potential usefulness of such solutions, work has been done on understanding the source of these instabilities. They are now understood,

and a stable code has been developed for one-dimensional problems with distribution functions which are periodic in their $x$ dependence.

An example is the representation of the distribution function by a Fourier Hermite series,

$$f(x, \mathrm{v}, t) = \sum_{n=-N}^{N} \sum_{m=0}^{M} \left(\frac{-i}{\sqrt{2}}\right)^m f_{n,m}(t) \times \mathrm{H}_m\left(\frac{\mathrm{v}}{\sqrt{2}}\right) e^{-N^2/2}\, e^{iknt} . \quad (1)$$

The Vlasov equation,

$$\partial_t f = -\mathrm{v}\, \partial_x f + E\, \partial_\mathrm{v} f , \quad (2)$$

becomes

$$\partial_t f_{n,m} = kn[f_{n,m-1} - (m+1) f_{n,m+1}] + \sum_{n'=-N}^{N} E_{n-n'} f_{n',m-1} . \quad (3)$$

For a self-consistent electric field, $E$ is obtained from

$$\partial_x E = -\int_{-\infty}^{\infty} d\mathrm{v}\, f(x, \mathrm{v}) + 1 \quad (4)$$

$$= -\sqrt{2\pi} \sum_{\substack{n=-N \\ n\neq 0}}^{N} f_{n,0}(t)\, e^{iknt} , \quad (5)$$

and

$$E = \frac{i\sqrt{2\pi}}{k} \sum_{\substack{n=-N \\ n\neq 0}}^{N} \frac{f_{n,0}(t)}{n} e^{ikn} . \quad (6)$$

The $E_n$'s in Eq. (3) are

$$E_n = \frac{\sqrt{2\pi}\, f_{n,0}(t)}{k\, n} . \quad (7)$$

The initial conditions at time zero are to take a few $f_{n,m}$ nonzero and the remainder zero. In the past the problem was solved by taking all the $f_{n,m}$ equal to zero for $m$ greater than $M$ and $n$ outside the range of $-N$ to $N$. The spatial dimension posed little problem, but the velocity dimension soon became unmanageable. It was found that as time passed, $f_{n,m}$ would become nonzero, and from then on large mathematical errors would appear in the solution. This could be postponed by making $M$ large, but it could not be avoided. Montgomery and Armstrong,[60] at Iowa, for example, made $M$ as large as 1500 in their work.

It can be shown that the difficulty arises in the drift term

$$(\partial_t f_{n,m})_{\mathrm{drift}} = k_n [f_{n,m-1} - (m+1) f_{n,m+1}] . \quad (8)$$

If the $f_{n,m}$ are held at zero for all $m$ greater than $M$, the eigenvalues of the equation are purely imaginary; and since there are only a finite number of them, they tend, after a period of time, to come back into phase again instead of damping away indefinitely by phase mixing. By setting

$$f_{n,M+1} = \sum_{j=0}^{M} \frac{(-1)^j \lambda^{j+1}}{(j+1)!} f_{n,M-j} \quad (9)$$

and

$$f_{n,m} = 0$$

for

$$M + 1 < m ,$$

a negative real part equal to $\lambda$ is added to each of the imaginary eigenvalues. The mathematical instability can be eliminated by making $\lambda$ large enough to damp out the eigenfunctions before they can come back into phase.

It is found that the work of Montgomery and Armstrong can be reproduced with an $M$ of 25 to 50, depending on the desired accuracy. It is also found that the solutions are insensitive, over a wide range of $\lambda$, to the exact value taken for $\lambda$.

Work is continuing on extending the method to finite spatial systems and to more dimensions.

---

[60] T. P. Armstrong and D. Montgomery, *J. Plasma Phys.* **1**, 425 (1967).

## 1.5 ABSTRACTS OF PREPRINTS

### 1.5.1 Microinstabilities in Inhomogeneous Plasmas: Theory[61]

C. O. Beasley W. M. Farr[62] H. Grawe[63]

A formalism is presented for the determination of unstable electrostatic oscillations in a model mirror-confined plasma with a Gaussian density variation of arbitrary scale length along the magnetic field. A formal solution to the collisionless Boltzmann equation is obtained for a plasma confined in a parabolic well. Using this solution, one may numerically solve Poisson's equation to obtain the eigenfunctions (perturbed potentials) and eigenvalues (densities) of the system for a given frequency and growth rate. As no mathematical limits on plasma length exist for obtaining these solutions, one may recover the infinite-plasma results in the limit of very long plasmas.

### 1.5.2 Explosive Plasma Instabilities[64]

J. Fukai[65] E. G. Harris[66] S. Krishan[67]

We discuss the explosive instability caused by the nonlinear interaction of two positive energy waves and one negative energy wave and its stabilization by higher-order nonlinear effects.

### 1.5.3 Stability of TOKAMAK's[68]

E. G. Harris[66]

Following a conjecture by Morse and Freidberg we have investigated the stability of the Bennett pinch with a magnetic field parallel to the axis. We have found reason to believe that under centain conditions all instabilities may be eliminated except for localized MHD instabilities near the axis. According to a modified form of the Suydam criterion which we derive, these MHD instabilities are eliminated when the cylindrical Bennett pinch is bent into a torus if $\beta_z$, the toroidal $\beta$, is less than $(5/4)(r_0/R)^2$, where $r_0$ is the mean radius of the pinch and $R$ is the major radius of the torus. We suggest that TOKAMAK's may operate in this stable regime.

### 1.5.4 Theory of High-Frequency Instabilities in Mirror-Confined Plasmas[69]

Gareth Guest

The velocity-space instabilities of importance to mirror-confined fusion plasmas are reviewed briefly with an emphasis on the fundamental processes by which non-Maxwellian plasma constituents can transfer excess energy to plasma waves. The general dispersion relation and its electrostatic limit are discussed, together with various aspects of wave-particle energy transfer. The basic notions are illustrated by application to flutelike modes,[70,71] resonant[72] and non-resonant[73] loss-cone modes, drift-cone modes,[73] negative-mass instabilities,[74] and instabilities arising in finite-length plasma models.[75]

### 1.5.5 Classical Plasma Phenomena from a Quantum Mechanical Viewpoint[76]

E. G. Harris[66]

Nonlinear phenomena in a classical plasma are treated in this paper. The plasma is regarded as a collection of particles (electrons and ions) and quasi-particles (plasmons, phonons, photons, etc.). The interaction between particles and quasi-particles is described by an interaction Hamiltonian which is written in terms of creation and annihilation operators. The transition

---

[61] This paper is being submitted for publication in *Physics of Fluids.* It is currently available as ORNL-TM-2852.

[62] Nuclear Engineering Department, University of Arizona.

[63] Scientific Controls Systems Ltd. and Co., GmbH, Hamburg, Germany.

[64] Published in *Phys. Rev. Letters* **23**, 910 (1969). Also published as ORNL-TM-2652.

[65] Physics Department, University of Tennessee.

[66] Consultant: Physics Department, University of Tennessee.

[67] Physics Department, University of Tennessee.

[68] This paper is being submitted for publication in *Physics of Fluids.* It is currently available as ORNL-TM-2766.

[69] This paper is currently available as ORNL-TM-2864.

[70] R. A. Dory, G. E. Guest, and E. G. Harris, *Phys. Rev. Letters* **14**, 131 (1965).

[71] L. D. Pearlstein, M. N. Rosenbluth, and D. B. Chang, *Phys. Fluids* **9**, 953 (1966).

[72] Resonant loss-cone instability: G. E. Guest and R. A. Dory, *Phys. Fluids* **8**, 1853 (1965); *Phys. Fluids* **11**, 1775 (1968); J. D. Callen, Ph.D. thesis, MIT, April 1968.

[73] R. F. Post and M. N. Rosenbluth, *Phys. Fluids* **9**, 730 (1966).

[74] J. F. Clarke and G. G. Kelley, *Phys. Rev. Letters* **21**, 1041 (1968).

[75] H. L. Berk *et al.*, *Phys. Rev. Letters* **22**, 876 (1969).

[76] Published as ORNL-TM-2519 and subsequently in *Advances in Plasma Physics*, vol. 3, ed. by A. Simon and W. B. Thompson, Wiley, New York, 1969.

probability for any process may be calculated from the usual formulas of quantum mechanical perturbation theory. These quantum mechanical methods provide a straightforward method for deriving quasi-linear equations and the corrections to them due to wave-wave interactions and wave-particle scattering. The derivation of conservation laws and $H$ theorems is particularly simple.

Kinetic equations for a plasma are derived which in various limits reduce to the Wyld-Pines, Balescu-Lenard, Boltzmann, and quasi-linear equations.

A variety of nonlinear interactions of plasma waves is discussed.

### 1.5.6 Integral Solutions to the Generalized Helmholtz Equation[77]

P. B. Burt[78]

A method of solution of the differential equation $[Q + K^2(x)]\psi = 0$, where $Q$ is a linear second-order differential operator, is discussed. The method is based upon approximating $K^2(x)$ by a series of step functions whose strength is the value of $K^2$ in the specific interval. The relation of this method of solution to the Bremmer series, the W.K.B. approximation, and the Born approximation is exhibited.

### 1.5.7 Damping of Plasma Oscillations in Atoms

E. G. Harris[66] A. Sen[79]

The idea that electrons in heavy atoms may oscillate collectively is an old one.[80] However, the critical question of the damping of such oscillations has never been satisfactorily answered. If a plasma oscillation is damped out in a time which is short in comparison with its period, then the concept of a collective oscillation is meaningless. The mechanism of damping is the excitation of an atomic bound electron to an unbound state by absorption of energy from the collective oscillation. This process is analogous to Landau damping in gaseous plasmas. Using the Thomas-Fermi model of the atom we are calculating the damping of atomic plasma oscillations. Preliminary results indicate that the damping is small enough that collective oscillations can be said to exist.

---

[77]This paper is being submitted for publication in the *Journal of Mathematical Physics.* It is currently available as ORNL-TM-2658.

[78]Consultant: Physics Department, Clemson University.

[79]Summer visitor from the University of Tennessee.

[80]F. Bloch, *Z. Physik* **81**, 363 (1933).

# 2. Target Plasmas

## 2.1 INTRODUCTION

N. H. Lazar

During the past year, the roles to be played by the various experimental facilities in the mirror program at ORNL (IMP, INTEREM, and ELMO) have been more clearly defined. The general approach toward the production of dense mirror-confined reactor-like plasmas by injection and trapping of energetic atoms in a target plasma retains its initial appeal. However, before we can specify the design of a facility in which questions relating to reactor efficiencies can be answered (ion scattering loss rates, ion-electron energy exchange rates, ion stability at high $\beta$, influence of plasma length on ion stability, etc.), several fundamental questions relative to the target plasma approach remain. It is useful to divide the problems into three classifications although they are, in fact, only partially separable:

1. The demonstration of a target plasma with $n_t/n_0 \sim 10^3$.
2. The study of the stability of the energetic ion component in the presence of the (denser) target plasma distribution.
3. The choice of a suitable magnetic field configuration.

1. The observations on electron-cyclotron-heated plasmas in INTEREM have demonstrated that ionization of in situ gas can result in target "qualities" (defined as the ratio $n_t/n_0$) of >30 in the absolute magnetic well generated by a combination of mirror and quadrupole fields. However, the studies indicate that the equilibrium is controlled by microinstability-generated losses with instability thresholds at densities $(\omega_{pe}/\omega_{ce})^2 \sim 0.1$ ($n_t \sim 10^{11}$ cm$^{-3}$ at $B_0$ = 3000 G). By raising the heating power in INTEREM, the average density can be raised in the face of these losses to $(\omega_{pe}/\omega_{ce})^2 \sim 1$. However, the average electron confinement time resulting from these losses is approximately an order of magnitude lower than will be required to reach $n_t/n_0 \sim 10^3$ and cannot be tolerated. Since the instability threshold densities scale, theoretically, as $B^2$, the experiments in IMP at the higher magnetic field available should permit a significantly improved target quality before instabilities set in. Whether the resultant changes in electron distribution will raise instability thresholds high enough to permit the required target quality or whether the distribution can be influenced by nonresonant heating (see Sect. 4) are fundamental questions which can only be answered by the IMP experiments.

2. Electron-cyclotron-heated plasmas with sufficient target quality to provide meaningful answers to questions of ion stability are only just now available. Low-energy injection into INTEREM will permit us to initiate experiments immediately with dense components of both energetic and cold ions. Further, at these low energies ($E_i \sim 1$ keV) the influence of scattering of the energetic ions by the cold, dense background can be evaluated. These studies will, of course, be extended in IMP as target plasmas of higher quality are produced.

3. The choice of a suitable magnetic field configuration is intrinsically related to problems 1 and 2. However, since the magnetohydrodynamic stability of a plasma in a given configuration may be separated from $n_t/n_0$ or energetic ion density, the experimental attack on a given field choice can proceed using alternative plasma sources. An example is the possible use of "surface"-stabilizing fields in ELMO. The stability of the hot-electron, high-$\beta$ plasma in ELMO is dependent, at present, on "line tying" through cold plasma (Sect. 4). The effect of a positive radial magnetic gradient at the plasma radius, while the gradient might be negative on axis, would be highly informative. One can consider extrapolating such a configuration to a nearly cylindrical one (e.g., as in Scylla), should stability be established. Experiments of this nature are anticipated in ELMO, and the results will be applicable in the design of a next-generation facility.

In the more detailed discussions below, we document the observations of high target quality in INTEREM. It is of interest, as well, that $\beta \sim 0.25$ at the peak stored energy (averaged over a volume of ~1 liter). The study of microinstabilities which has led to the identification of the double-distribution mode is also discussed. Finally, we present the result of survey experiments in which an electron beam was injected through these highly ionized plasmas in an attempt to turbulently heat ions.

The IMP facility has been completed to the extent that the superconducting mirror coils have been installed and used up to their rated fields. The cavity shape prevents the use of heating surfaces as in ELMO, so only low ECH plasma densities are observed. Beam-injection experiments have been carried out so that the diagnostics which will be used in the quadrupole configuration can be tested. The superconducting quadrupole coil developments are discussed in Sect. 10.6.

## 2.2 INTEREM

M. C. Becker[1] W. J. Herrmann[3]
R. A. Blanken[2] N. H. Lazar
C. W. Blue J. F. Lyon
G. R. Haste O. D. Matlock
W. J. Schill

### 2.2.1 Introduction

In our earlier reports,[4] detailed outlines of the procedures used to determine the properties of the electron-cyclotron-heated plasmas produced in the absolute magnetic well in INTEREM were presented. In those earlier experiments, a high base pressure limited the operating regimes to molecular neutral densities $n_0 > 10^{11}$ cm$^{-3}$. The plasmas produced in this regime were described, and it was pointed out that the limitation on the density was set by the equilibrium which was controlled by losses resulting from microinstabilities in the plasma.

Since that report, improvements in the pumping speed have permitted the study of ECH plasmas down to $n_0 \sim 1.5 \times 10^{10}$ cm$^{-3}$. With optimum conditions $n_e/n_0 > 30$ is observed. The plasma losses continue to be dominated by microinstabilities, but their nature, as judged by the frequency spectrum of emitted radiation, is changed. One of the instability modes has been identified as arising from the mixture of hot and cold electrons, the so-called double-distribution instability.

An electron beam has been injected into the ECH plasmas at these low pressures in an attempt to turbulently heat the cold ions. The emitted radiation attests to a strong beam-plasma interaction when the magnetic field shape is optimized. However, no evidence of energetic ions could be detected.

### 2.2.2 Target Plasma Studies in INTEREM

The requirements of a target plasma are set by the particle equilibrium conditions when fast atoms are injected and trapped (predominantly by charge exchange with cold target ions), and lost either by charge exchange or scattering into the loss cone. This equilibrium results in the equation (assuming that charge-exchange loss dominates)

$$\frac{\omega_{pi}^2}{\omega_{ci}^2} = 0.1 I_0 \frac{n_t}{n_0'} \frac{\sigma_{01}}{\sigma_{10}} \frac{1}{E^{3/2}} \frac{1}{(r/\rho)(l/\rho)},$$

where $I_0$ is the injected neutral beam current in milliamperes, $E$ is the energy in kilo-electron volts, $n_t$ is the target density, $n_0'$ is the neutral density at the energetic ion plasma, and the plasma volume (taken as cylindrical) is expressed in units of ion Larmor radius. The target properties enter only in terms of the ratio $n_t/n_0'$ ($n_0$ is the ambient neutral molecular density). From the point of view of generating the target plasma by ionization of in situ atoms, the equilibrium is established when the flux of ions produced by ionization equals the loss of target ions. We find

$$\frac{n_t}{\tau_+} V = n_0 \frac{v_0}{4} A\eta ,$$

where $\eta$ is the ionization efficiency for the incident molecular flux on the plasma surface and $\tau_+$ is the effective confinement time of all ions produced. Thus

$$\frac{n_t}{n_0} = \tau_+ \eta \frac{v_0}{4} \frac{A}{V} .$$

Since $\eta \sim 1$ the target quality depends directly on the average ion confinement time, and since $\tau_+ = \tau_-$, it depends on the average confinement time of the electrons. For $n_t/n_0 \sim 10^3$ and $r \sim 10$ cm we require $\tau_+ \approx 0.1$ sec. In the experiments described below, $n_t/n_0 > 30$ with $r \approx 5$ cm, and thus $\tau_+ \gtrsim 1.5$ msec. The flight time of ions with energy ~5 eV to the walls would be

[1] Instrumentation and Controls Division.

[2] Consultant, MIT.

[3] Institut für Plasmaphysik, 8046 Garching bei München, Germany.

[4] *Thermonuclear Div. Ann. Progr. Rept. Dec. 31, 1968*, ORNL-4401, p. 26.

$\sim l/v = 25$ μsec. The ions are apparently confined for the inferred time by space potentials which are set up by the plasma to maintain neutrality.

### 2.2.3 Target Plasma Parameters

The base pressure in the cavity was improved to $5 \times 10^{-8}$ torr by placing several large surfaces cooled with liquid nitrogen at the ends and top of the machine. In addition, two new diagnostic tools were utilized: (1) The current to the multiple-aperture detector on a flux tube at one end of the cavity was fed to a gated integrator. The gate was opened after a variable delay (usually 5 msec) after the microwave power was shut off. The detector is biased so that only electrons with parallel energy greater than 500 eV are detected. Therefore the charge collected during the gate interval (usually 20 sec) is determined by the total number of energetic particles on the flux tube at the instant of turnoff. (2) A collimated lithium-drifted silicon surface-barrier detector was used in addition to the NaI(Tl) detector to permit energy measurements of x rays down to 3 keV. The energy resolution of this new detector was measured as ~500 eV. The program for unfolding the measured spectrum to determine the electron energy distribution on the LINC-8 on-line computer was modified so that the electron distribution function could be determined, on line, down to the minimum energy.

The plasma characteristics in various magnetic field configurations were determined as the neutral density and pressure were varied. In Figs. 2.1 and 2.2 are shown the density on axis and stored energy as a function of power and pressure for $B_0$ = 3000 and $B_0$ = 3600 G (nominal and 120% of nominal fields). For reference, Fig. 2.3 shows the flux line and $|B|$ contours in INTEREM relative to $B_0$ = 3000 G. The characteristic maximum in the density and stored energy is apparently related to a reduced lifetime at high powers due to microinstability-induced losses. When the power is raised appreciably past the peak, the plasma is extinguished; that is, an equilibrium cannot be maintained. The failure of equilibrium occurs at lower power as the pressure is reduced, and at a neutral density below $n_0 \sim 3 \times 10^{10}$ cm$^{-3}$ it limits the target density to a value below $10^{12}$ cm$^{-3}$. An examination of the rf spectrum at the higher powers gave no indication of new instability behavior, and we interpret the failure of equilibrium to an inadequate supply of electrons to replace those being lost following instabilities. That is, the average confinement time of electrons, as a result of the microinstabilities, was less than the required ~5 msec.

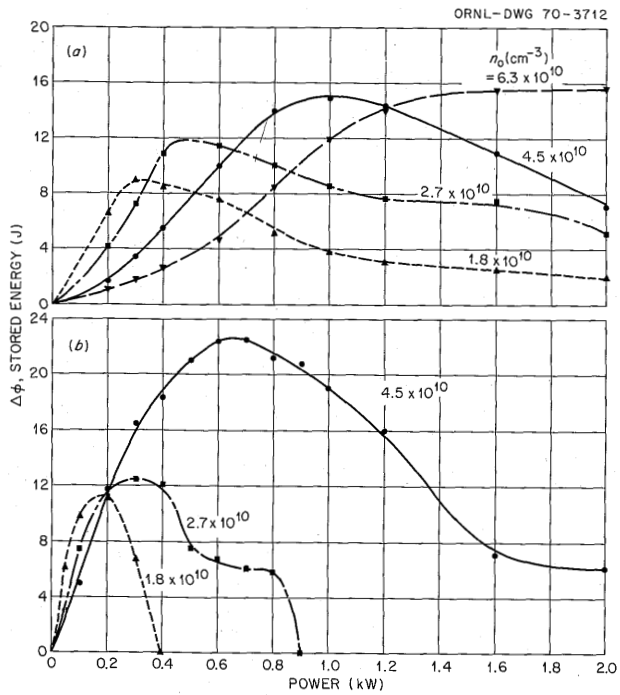


**Fig. 2.1. Stored Energy as a Function of Power.** Mirror field producing (*a*) $B_0$ = 3000 G (nominal field) and (*b*) $B_0$ = 3600 G (120% field) on axis in the midplane at various neutral densities.

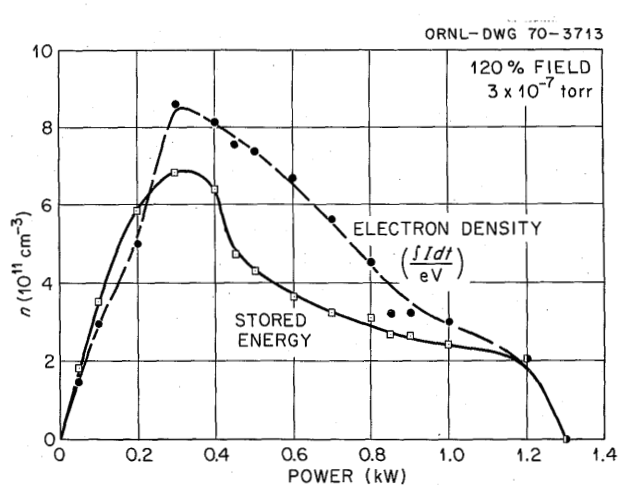


**Fig. 2.2. Variation of Stored Energy and Density on Axis as a Function of Applied Power.** $B_0$ = 3600 G, $n_0 = 3 \times 10^{10}$ cm$^{-3}$.

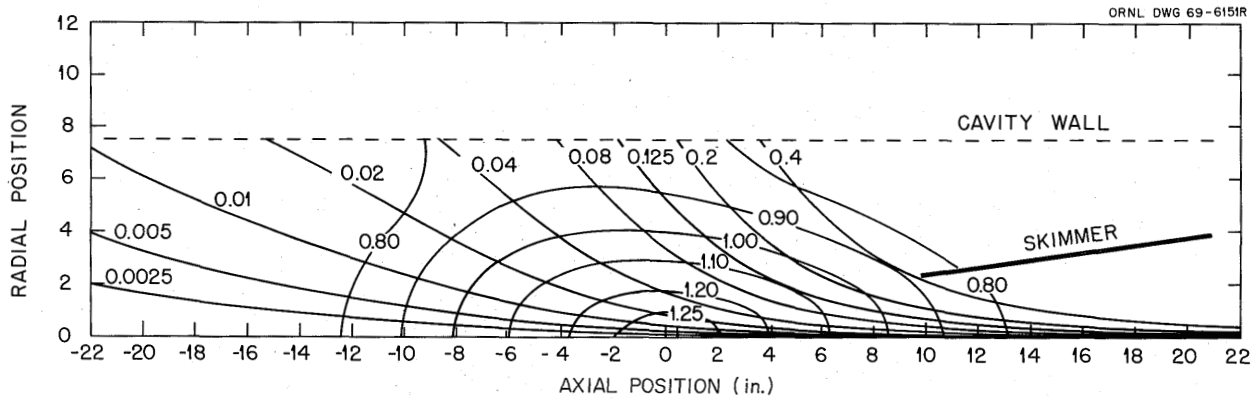


**Fig. 2.3. Flux Lines and Surfaces of Constant $|B|$ in the Vertical Plane of INTEREM.** Only the upper half plane is shown. The numbers on the $|B|$ surfaces are $B/B_{res.}$ for nominal field ($B_0$ = 3000 G). The numbers on the flux lines represent the position of the lines above the horizontal plane (in inches) when they intersect the cavity at the west end (end where skimmer is inserted).

### 2.2.4 Electron Energy Distributions

X-ray spectra taken with an NaI(Tl) scintillation spectrometer and with the lithium-drifted silicon barrier detector were analyzed to determine the average electron distribution in the plasma. Typical results are shown at $n_0 = 5 \times 10^{10}$ cm$^{-3}$ for various magnetic field strengths (Fig. 2.4). We note a characteristic decrease in the mean electron energy as the resonant zone is enlarged until $B_0 = B_0$ (nominal). Also, as the volume is increased, the presence of a higher-energy group is indicated. The relative increase in intensity of this high-energy group results in the higher average energy obtained in the cases with 80 and 90% of nominal field. A reasonable interpretation of these results is that with high magnetic fields (small volume) the heating is predominantly resonant, and electron temperatures are limited by the onset of instabilities, resulting in $T_e \approx 80$ keV. When the resonant surface is expanded, nonresonant heating of energetic electrons can take place, and higher-energy electrons are preferentially heated.

The spectra at low energies (below 50 keV) are determined from the data taken with the silicon detector. These spectra indicate a rather large component of low-energy particles with no peak in the distribution such as would be expected from enhanced scattering losses at these lower energies. This observation, illustrated in Fig. 2.5, leads to the conclusion that low-energy electrons are effectively confined by the rf heating field in the resonant region. The observations of Becker *et al.*[5] and Galaktionov *et al.*[6] that plasmas heated by resonant ECH are confined within the resonant $|B|$ surfaces suggest that the model of simple mirror confinement is insufficient to describe these plasmas. The absence of a "loss-cone" energy distribution in our measurements tends to confirm the implications in the earlier work.

### 2.2.5 Instability Studies

The simple superheterodyne receiver with a sweeping local oscillator, described in our previous report, was used to determine the radiation from the plasma in X band. The signals are attenuated >40 dB in order to protect the mixer crystal from radiation at the heating frequency. At high pressure ($n_0 > 10^{11}$ cm$^{-3}$) several characteristic radiations can be identified near instability thresholds. (A report on the observed instability radiation at high pressure was presented at the European Fusion Research Conference in Utrecht, Netherlands, June 23–27, 1969.) Figure 2.6 shows the spectrum seen with several hundred watts heating power at $n_0 \cong 1 \times 10^{11}$ cm$^{-3}$. Three characteristic bands of radiation, in addition to the heating frequency, can be identified. The bands lying just above and below the heating frequency can be suppressed by lowering the pressure. From correlations with electron current bursts on flux lines off axis and the absence of correlation with current near the axis, this radiation was found to originate near the surface of the plasma. In addition, when the skimmer shown in Fig. 2.3 is

[5] M. C. Becker *et al.*, *Thermonuclear Div. Ann. Progr. Rept. Dec. 31, 1968*, ORNL-4401, p. 88.

[6] B. V. Galaktionov *et al.*, *Soviet Phys. – Tech. Phys.* (English Transl.) 13, 838 (1968).

ORNL-DWG 69-5551A

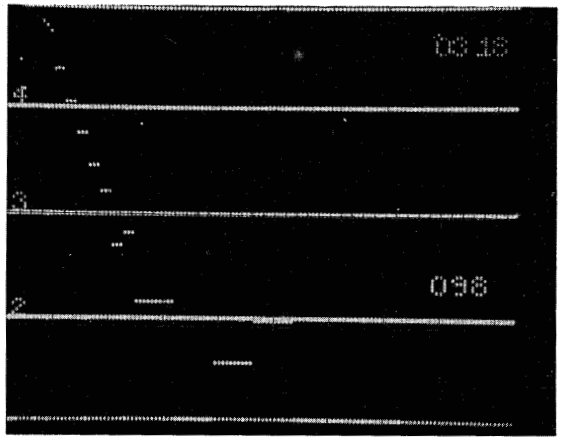


$B_0$ = 1.20 $B_0$ (NOM)
$P$ = 5 watts

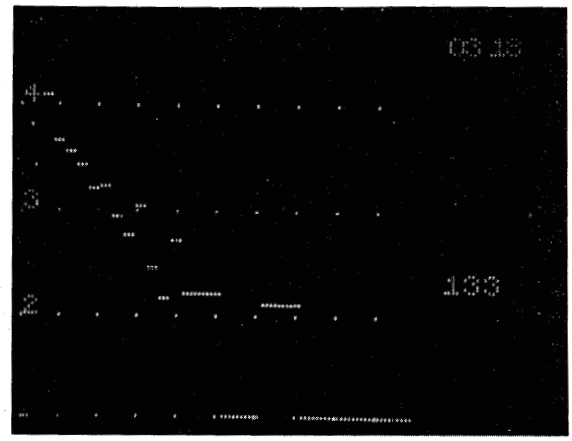


$B_0$ = 0.90 $B_0$ (NOM)
$P$ = 100 watts

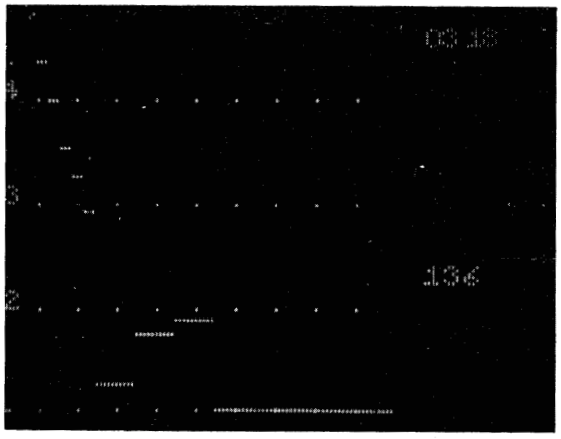


$B_0$ = 1.10 $B_0$ (NOM)
$P$ = 20 watts

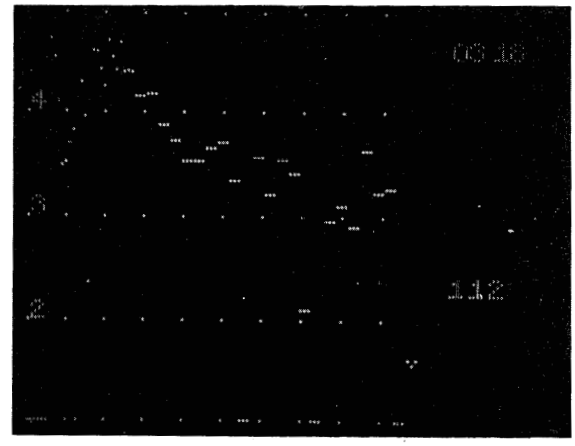


$B_0$ = 0.80 $B_0$ (NOM)
$P$ = 300 watts

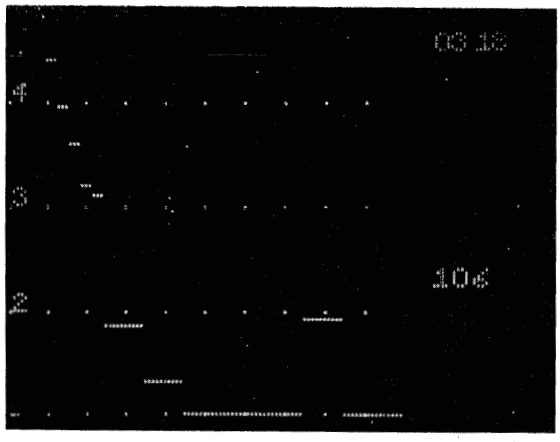


$B_0$ (NOM)
$P$ = 30 watts

**Fig. 2.4. Electron Distribution Function [$f(E)$] Determined from Bremsstrahlung Spectra.** The horizontal scale is 8 keV per point (800 keV full scale). Averages are taken over three or ten channels (indicated by the horizontal line length) when the statistics require it.

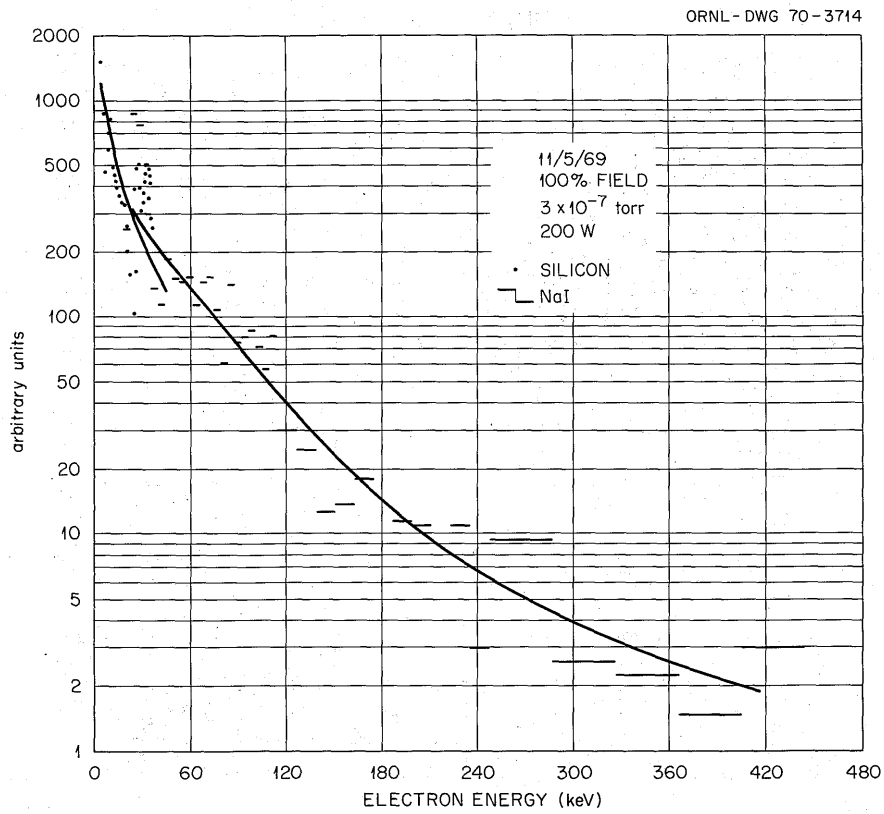


**Fig. 2.5. Electron Distribution Function $f(E)$.** At low energies the data are determined from Bremsstrahlung spectra taken with a lithium-drifted silicon barrier detector. The overlap of the data with those of the NaI(Tl) detector is shown.

inserted so as to just graze the plasma surface, the radiation also disappears. The frequency observed can be understood since the magnetic field in the plasma on the flux lines near the resonant surface is close to the resonant field; thus cyclotron radiation emitted will be close to the heating frequency. In fact, the radiation just above the heating frequency is attributed to hybrid radiation ($\omega^2 = \omega_{pe}^2 + \omega_{ce}^2$) from this region. The source of radiation just below the heating frequency has not yet been studied in sufficient detail to describe the instability mode. Several theoretical possibilities exist which can account for the observed frequency, including an unstable whistler mode[7] and a negative mass instability in the slightly relativistic electrons.[8]

The radiation at lower frequencies in Fig. 2.6 remains at lower pressure. It, too, is correlated with axial loss of electrons; however, in this case, along flux lines close to the axis. The frequency has been measured as a function of field at the lower pressures, and the results are shown in Fig. 2.7. The deviation of the data points above $f_{c0}$ is real and reproducible. This deviation has also been determined as a function of power and pressure for the case of nominal field ($B_0$ = 3000 G), and the results are indicated in Fig. 2.8. The cold plasma density is shown in Fig. 2.8*b*, and the relationship to the frequency is clearly established. The behavior is in good agreement with the theoretical model, proposed originally by Hall, Heckrotte, and Kammash,[9] in which one expects instability generated from the presence of a distribution of cold electrons as well as the anisotropic energetic electrons. The instability boundaries are described in greater detail in Sect. 1.2.5. The unstable frequency is predicted to be given by $\omega^2 = \omega_{pe}^2 + \omega_{ce}^2$

[7] R. N. Sudan, *Phys. Fluids* 8, 153 (1965).

[8] See, for example, J. D. Callen and W. Horton (to be published in *Physics of Fluids*).

[9] L. S. Hall, W. Heckrotte, and T. Kammash, *Phys. Rev.* **139**, A1117 (1965).

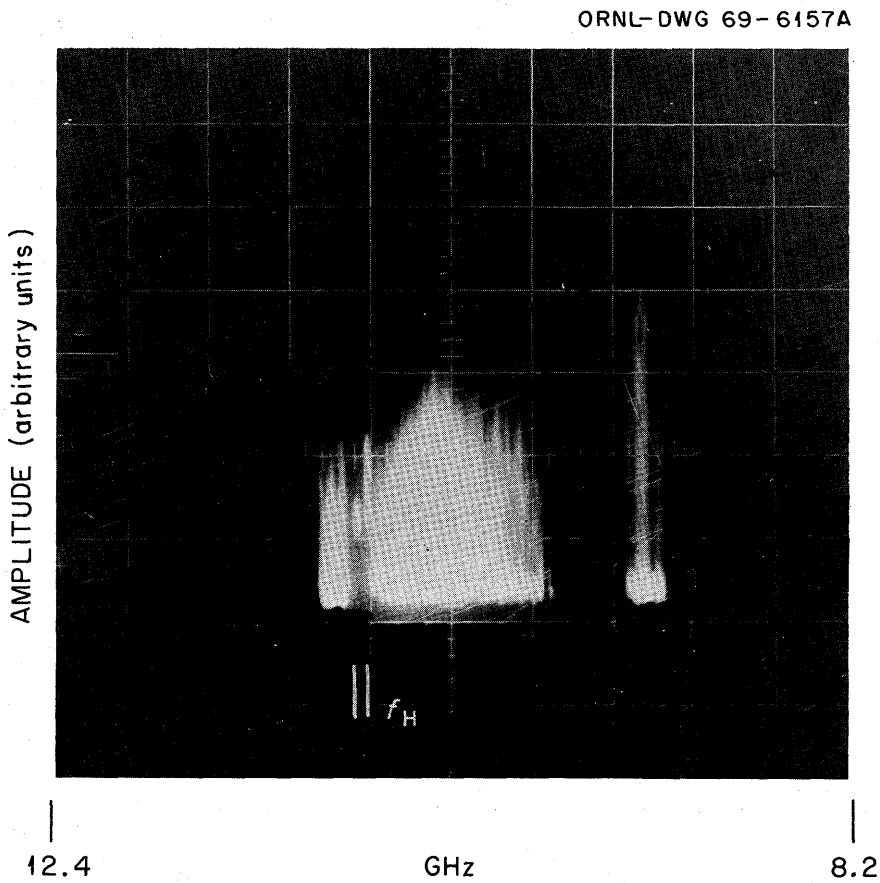


**Fig. 2.6. Radiation in the Band 8.2 to 12.4 GHz from INTEREM at $n_0 = 2 \times 10^{11}$ cm$^{-3}$.** $f_H$ indicates the response from the heating power.

since the model describes a wave carried by the cold electrons in the plasma driven unstably by the anisotropic energetic electron distribution.

The observed low-density thresholds ($\omega_{pe}^2/\omega_{ce}^2 < 0.1$) would also be predicted by the extended negative mass mode.[8] However, the growth time, as determined from the observed rise time of the radiation, is comparable with, or slightly shorter than, the electron bounce time. In calculations of the extended negative mass instability, one requires the opposite approximation.

### 2.2.6 Electron-Beam–Plasma Interaction

In the light of the success obtained in producing a highly ionized, high-density energetic electron plasma, an effort was made to exploit the possibility of turbulent heating to raise the ion energy. In most beam-plasma experiments in the past, the background plasma is produced by the beam itself, and, as a result, a dense cold electron component is usually present. Further, in order to maintain this high density of cold plasma, the neutral density is generally high as well. The details of the heating mechanism remain obscure in the experiments reported heretofore, although microinstabilities attributed to unstable ion sound waves are considered, at least in some experiments, to play a significant role. An experiment in which the parameters reported are not too different from those obtained in INTEREM has been reported by Akshanov *et al.*[10] In his case the hot electron plasma is also generated by a beam-plasma interaction. A second injected beam, either ion or electron, is then found to result in ion heating.

[10] B. S. Akshanov, Yu. Ya. Volkolupov, and K. D. Sinel'nikov, *Soviet Phys. – Tech. Phys.* (English Transl.) **11**, 446, 456 (1966).

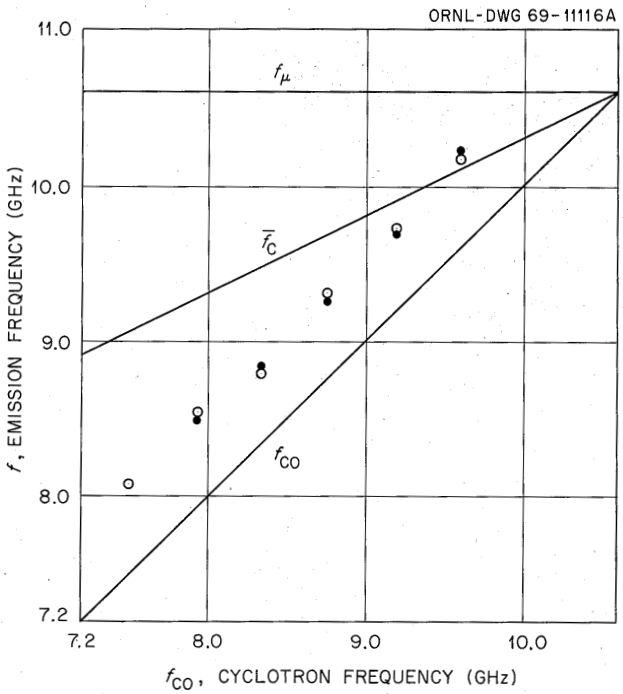


**Fig. 2.7. Frequency of Observed Radiation as a Function of Electron Cyclotron Frequency at the Minimum Magnetic Field.** $f_{co} = eB_0/2\pi m_e c$. $\bar{f}_c$ is the average cyclotron frequency for electrons oscillating between their mirror points.

The geometry in INTEREM led us to the use of a filamentary electron source, 10 cm long, extended along the fan of flux lines in the vertical plane leaving one end of the cavity. The width of the slit through which the electrons are accelerated was 1 mm, and it was found that when the quadrupole current is chosen so that the convergence of the flux lines in the vertical plane and the divergence of the lines intersecting the slit in the horizontal plane resulted in a nearly circular beam cross section in the midplane the maximum interaction was detected. Beam currents up to 1.5 A at voltages ranging up to 4 kV have so far been injected. Although a range of parameters has been investigated, the optimum choice has not yet led to a simple model of the interaction.

Two principal diagnostics have been utilized – a wide-band electrostatic probe has been used in conjunction with a frequency spectrum analyzer[11] to determine the plasma fluctuation spectrum, and the electron and ion current to the multiple-aperture probe at the cavity end opposite the electron source has been monitored. When the maximum interaction occurs, two effects can be noted. The frequency spectrum shows a

[11] Hewlett-Packard model 8551B.

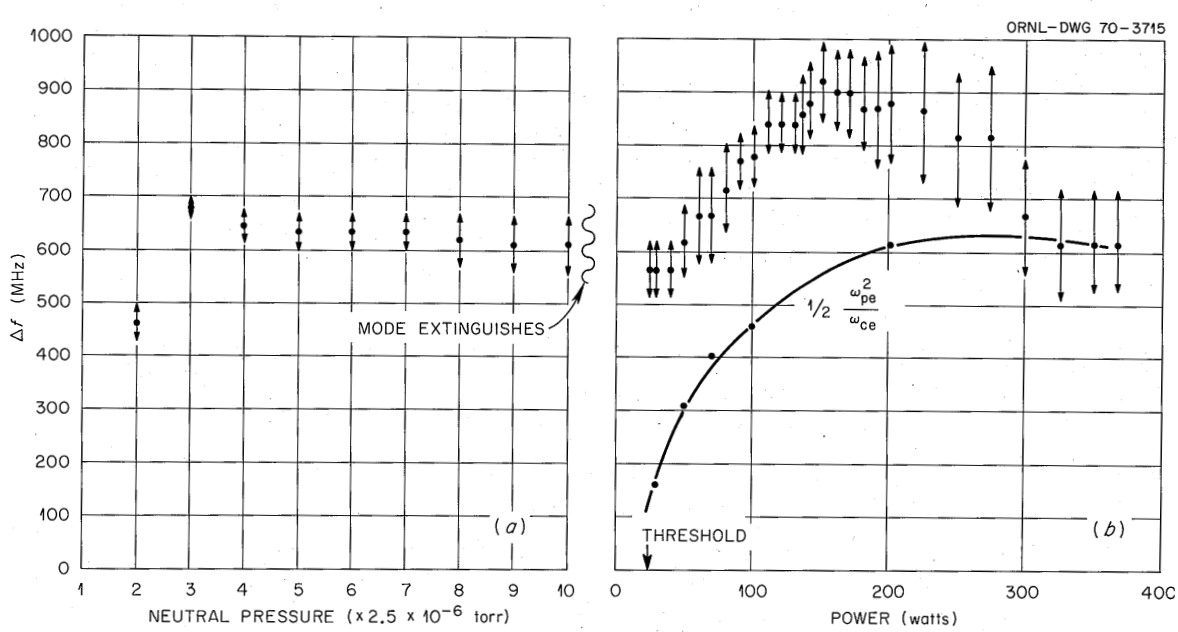


**Fig. 2.8. Frequency Observed at Nominal Field.** (*a*) As a function of pressure; (*b*) as a function of heating power. Also shown is $\Delta\omega = \frac{1}{2}\omega_{pe}^2(\text{cold})/\omega_{ce}$ for the same conditions.

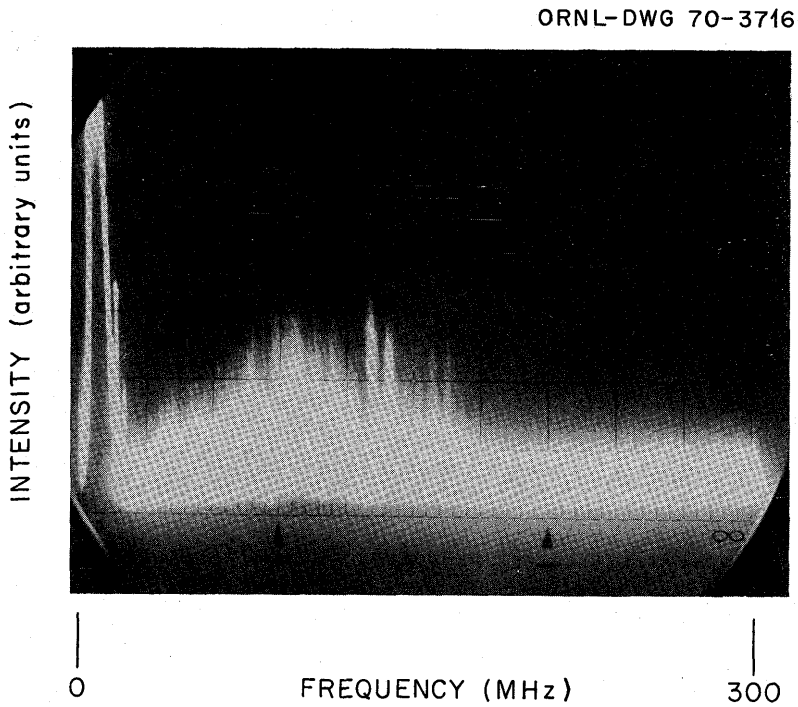


**Fig. 2.9. Frequency Spectrum Observed when Strong Beam-Plasma Interaction Occurs.** $I_{beam} \cong 250$ mA; $V_{beam} \cong 1$ kV.

rather intense peak near 100 to 150 MHz (Fig. 2.9), and the stored energy in the energetic electron plasma drops below a measurable amount (<0.5 J). The decay of the remaining plasma indicates a density of $\sim 10^{11}$ cm$^{-3}$ with a decay time of ~5 msec. The neutral density during these experiments was $5 \times 10^{10}$ cm$^{-3}$.

The source of the observed frequency peak must still be considered obscure. It is tempting to attribute it to lower hybrid or ion plasma oscillations (e.g., if $\omega = \omega_{pi}$, $n_i = 4 \times 10^{11}$ cm$^{-3}$), since such fluctuations could result in ion heating. However, from the ion currents detected during decay the energetic ion density cannot be as high as $3 \times 10^9$ cm$^{-3}$. A secondary emission detector was used to look for fast charge-exchange neutrals, but, again, no detectable current attributable to fast particles was found.

## 2.3 IMP

W. B. Ard
R. J. Colchin
J. S. Culver
J. L. Dunlap
R. S. Edwards
D. P. Hammond[12]
L. A. Massengill
T. F. Rayburn
R. G. Reinhardt
E. R. Wells
O. C. Yonts

### 2.3.1 Introduction

In this report period, IMP phase I (with mirror coils only) was assembled and made fully operational. The sections below review certain engineering features of the apparatus and diagnostics, detail this work, and describe preliminary observations of the electron cyclotron plasma (ECP). There follow some results of detailed computations of hot-ion and neutral densities in an ideal target plasma (high $n_t$ and large $n_t/n_0$).

Work toward completing the mirror-quadrupole trap (phase II) is summarized in Sect. 10.6.

### 2.3.2 Descriptions of the Apparatus and Diagnostics

Figure 2.10 is an overall view of the experimental apparatus before installation of lead walls for radiation shielding. In this photograph, the coil system is contained within the large vacuum tank, the 20-keV $H^0$ injector is on the right, and the beam burial section is on the left. A cutaway view of the gear within the vacuum tank is given in Fig. 2.11, and a photograph of this is provided as Fig. 2.12. The heart of the system is the superconducting coil system, previously described.[13] The coils are mounted in the cans for liquid

[12] On leave from Culham Laboratory, England.

[13] *Thermonuclear Div. Semiann. Progr. Rept. Oct. 31, 1967*, ORNL-4238, sect. 8.7, pp. 143–45; *Thermonuclear Div. Ann. Progr. Rept. Dec. 31, 1968*, ORNL-4401, pp. 197–99.

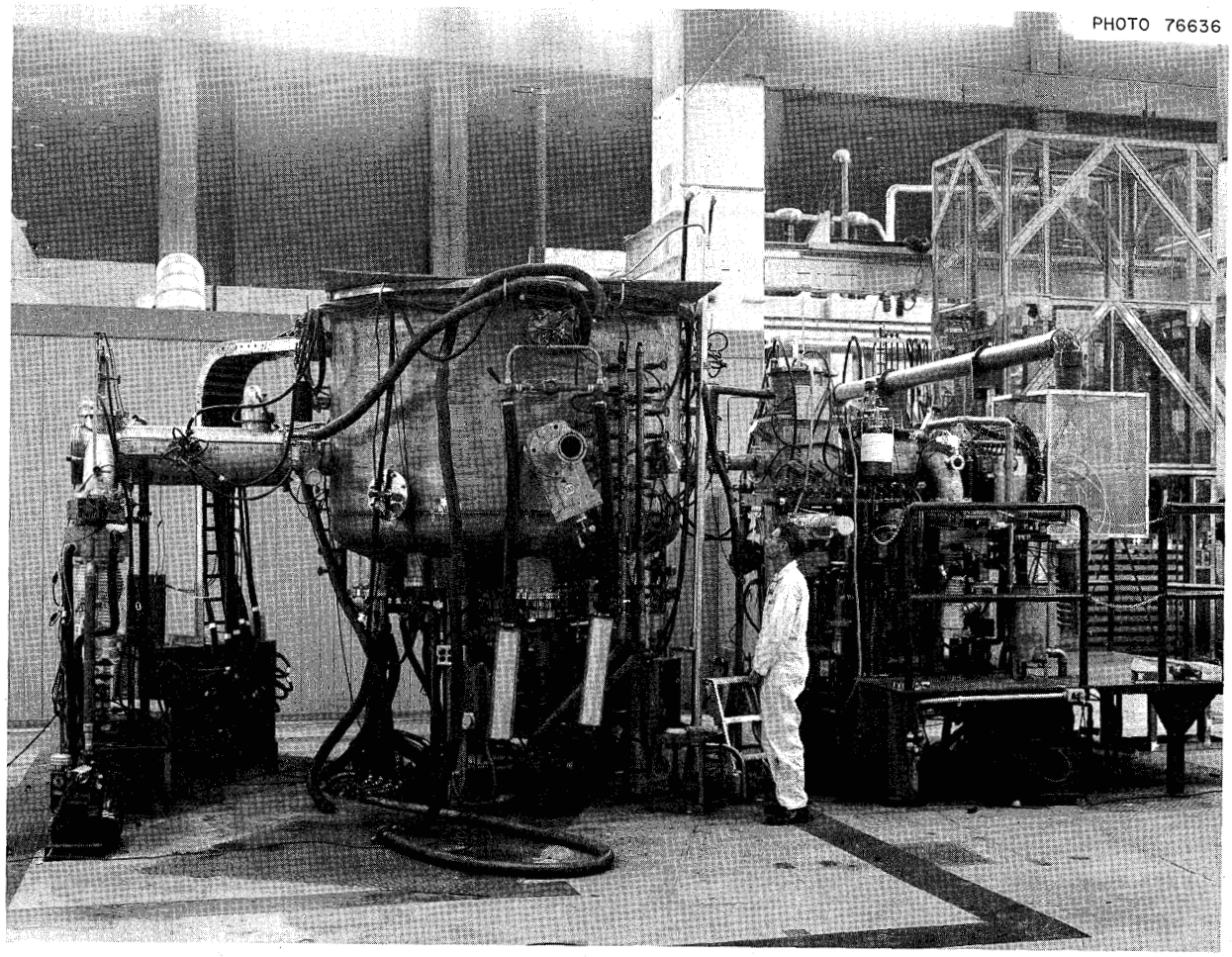


**Fig. 2.10. Overall Photograph of the IMP Facility.**

helium. These are suspended from the top lid of the main vacuum tank along with the copper microwave cavity. This cavity, which contains the plasma, separates the two cans and extends through the bore of each coil. It is liquid-nitrogen cooled. Thermal conduction to the 4.2°K elements is minimized by a mechanical suspension system that uses thin-wall stainless steel tubing. The injected neutral beam passes through the cavity in the median plane, centered on the coil axis, as is customary in injection devices of this general type. Four probe ports are available; the two vertical cavity extensions give access to the median plane, and the two bore extensions give access along the coil axis. A separate attachment to the cavity gives conductance to an externally mounted ion gage for monitoring the neutral pressure within the cavity.

The cavity is closed against microwave leakage at the probe locations by rotary cam locks that force each probe into contact with a knife-edge seal. The beam entrance and exit ports are sealed by honeycomb grids of tungsten, electric discharge machined to cutoff dimensions for the microwave power.

The components shown in Fig. 2.12 are surrounded by a close-fitted radiation shield, liquid-nitrogen cooled. A second radiation shield, also liquid-nitrogen cooled, is positioned just within the walls of the main vacuum tank. A number of titanium evaporators are located in the space between the two radiation shields.

The beam injector is basically that used in the DCX-1.5 experiments. It consists of a duoplasmatron ion source operated for optimum $H_2^+$ production, a water vapor neutralizer to produce $H^0$, a deflection magnet for diverting the residual charged beam, and, finally, a burial target which is monitored both calorimetrically and electrically. It provides up to 35 mA of

ORNL-DWG 69-3332A

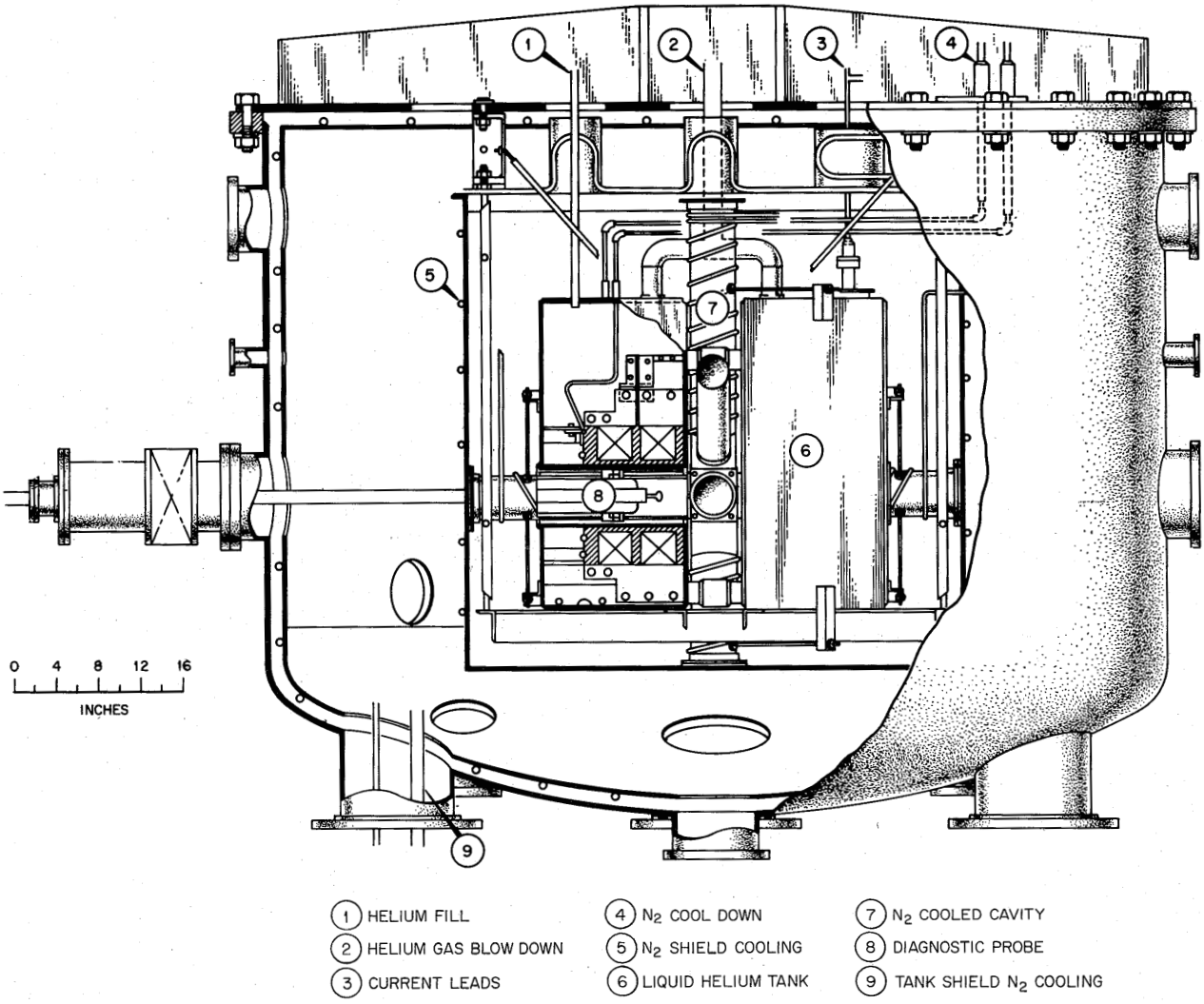


**Fig. 2.11. Cutaway View, Showing Components Within the Main Vacuum Tank.**

20-keV $H^0$ to the trapping region with a thermal neutral streaming component $<1 \times 10^{-7}$ torr.

The cooldown process initially uses liquid nitrogen for the helium system as well as for the cavity and radiation shields. In the helium system, the nitrogen is confined to copper tubes spot-welded at intervals to the coil cans and to the walls of the helium vessels. At ~80°K these lines are blown dry and sealed. The cooldown is completed with liquid helium. We presently use Dewar storage for the liquid helium; a 50-W helium refrigerator is scheduled for delivery during the first quarter of the next report period. During cooldown and filling, the helium gas is vented directly to the atmosphere. Afterward this vent is sealed (against gas pressure up to 3 psig), and the cold gas is routed to provide vapor cooling of the coil current leads. If pressure in the helium cans exceeds 3 psig, as in the event of leak into the main vacuum tank or transition to normal state in the coils, the larger vent automatically opens to prevent a dangerous buildup of pressure.

We have available the diagnostics that are by now considered standard for the work with ECP. Two 100-turn diamagnetic loops provide a measure of the

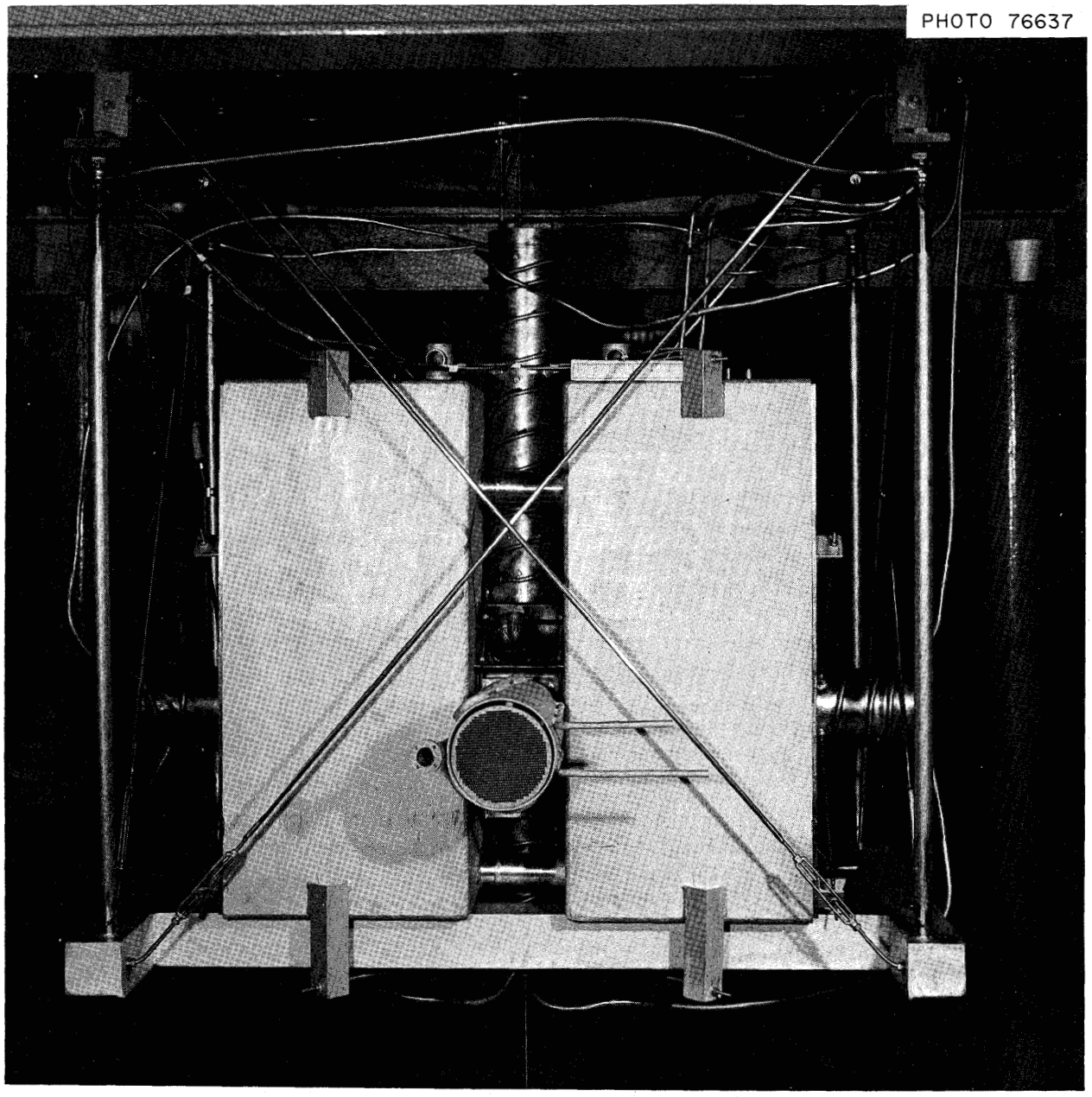


**Fig. 2.12. A View of the Suspended Package, Without Radiation Shield.**

total energy stored in the plasma, with compensation for variation of coil current; bremsstrahlung measurements provide electron temperature; and cold plasma collectors at the end of the plasma monitor ionization currents and charged-particle energies.

In addition to these, there are diagnostics for an injected hot-ion plasma. These consist of both secondary emission detectors and foil-covered Faraday cups for collection of fast charge-exchange neutrals, $\dot{B}_z$ and $\dot{B}_\theta$ rf loops, electrostatic rf probes, and a radial clipper for the plasma. With the exception of the secondary emission detector, these items are constructed with an ECP environment in mind; that is, the probe designs take into account the high levels of microwave field and of x-ray and ultraviolet photon fluxes expected for a dense ECP.

### 2.3.3 Assembly and Checkout

The phase I component with the longest lead time was the microwave cavity. It arrived from the shops in January, and work on assembly was begun. In April a partial assembly was ready for cooldown test to 77°K. The object of this work was to establish that the assembly was free of thermal shorts to the liquid-helium containers and to measure contractions so that the cavity could be positioned accurately with respect to the beam line. To facilitate the former, the cavity was electrically insulated from the helium cans.

A thermal short developed in the first of these tests. This was cleared up by retensioning of the cavity support rods. For additional insurance, some clearance dimensions that were unnecessarily close were also increased. The second of these tests proceeded without problems, and work to complete assembly was resumed.

The facility was ready for helium transfer and coil operation in July. The transfer proceeded well; it required only about 3 h to cool from 77 to 4.2°K and fill with liquid helium. An additional 24 h was needed to reach thermal equilibrium, and then helium consumption was at the calculated level, 3 to 4 liters/h. Coil tests to 10% over rated current (to 44 kG throat field) were also uneventful. Pressure in the main vacuum tank was somewhat high ($\sim 2 \times 10^{-6}$ torr, gage), and mass spectrometer runs showed the leak to be helium.

August and September were spent fixing the leak from the helium system (finally sealed with Stycast 2850 FT epoxy), replacing temporary liquid-nitrogen plumbing with a permanent arrangement, erecting a lead wall for radiation shielding, and installing the microwave power source. This last item is a 1-kW, 35-GHz klystron, remotely powered and controlled from the ELMO facility.

The facility became fully operational in October. Most of the engineering features have proved satisfactory; in a few instances improvements are desirable and will be incorporated in the mirror-quadrupole system. Diagnostic checks are presently in progress and for the most part have been concentrated on the ECP. Results of these studies are summarized in the following section.

### 2.3.4 Mirror Plasma in IMP

Preliminary studies have been made of the hot electron plasma produced in the simple mirror configuration of IMP. Measurements that have been made on the plasma include diamagnetic measurement of total stored energy, bremsstrahlung spectra measurement of the electron energy distribution, and total ion and neutral density measurements by means of neutral injection and trapping.

Although qualitatively the behavior of the plasma in IMP is similar to that in other simple mirror experiments,[14,15] such as ELMO, PTF, and INTEREM, major differences are observed in such plasma parameters as hot electron density and stored energy. At neutral background pressures above $6 \times 10^{-6}$ torr, a quiescent plasma can be obtained with a few hundred watts of microwave heating power. One does not obtain stable plasmas at lower pressure; experience with other mirror machines[16] indicates that this is because the cold plasma component is not sufficient to produce enough line tying to the cavity ends to stabilize flutes.

The maximum stored energy observed so far is about 1 J. Under these conditions, the bremsstrahlung measurements indicate a mean hot electron energy of about 150 keV. These measurements imply a density of a few times $10^{10}$ for the hot electron density. This density is considerably less than that obtained in some other ECH plasmas.[14,15] A possible explanation for this might be that the magnetic field is quite flat over the region between the cavity throats (see Fig. 2.13). If the magnetic field is set so that cyclotron resonance occurs just at the edge of the cavity throats, the ratio of $B_{res}$ to $B_0$ is only 1:1. If the resonant field is moved into the cavity throats, the mean electron energy and total stored energy fall to considerably lower values.

The total plasma density, as determined by the neutral beam injection, has been observed to be as large as $2 \times 10^{11}$ cm$^{-3}$. This is apparently mostly cold plasma and is about the same density as that observed in the other experiments under similar conditions.

### 2.3.5 Trapping Calculations

In dense mirror-confined plasmas, the plasma interior is shielded against neutral particles impinging from outside. Impinging atoms are ionized and trapped on field lines near the plasma periphery. Impinging molecules undergo a more complicated ionization-dissociation-ionization sequence which allows neutral atom penetration deep into the plasma. In spite of the obvious importance of these effects, only rather super-

---

[14] *Thermonuclear Div. Semiann. Progr. Rept. Oct. 31, 1965,* ORNL-3908, sect. 3.1.

[15] *Thermonuclear Div. Ann. Progr. Rept. Dec. 31, 1968,* ORNL-4401, sect. 5.1.

[16] *Thermonuclear Div. Semiann. Progr. Rept. Apr. 30, 1966,* ORNL-3989, sect. 3.3.

ORNL-DWG 70-979

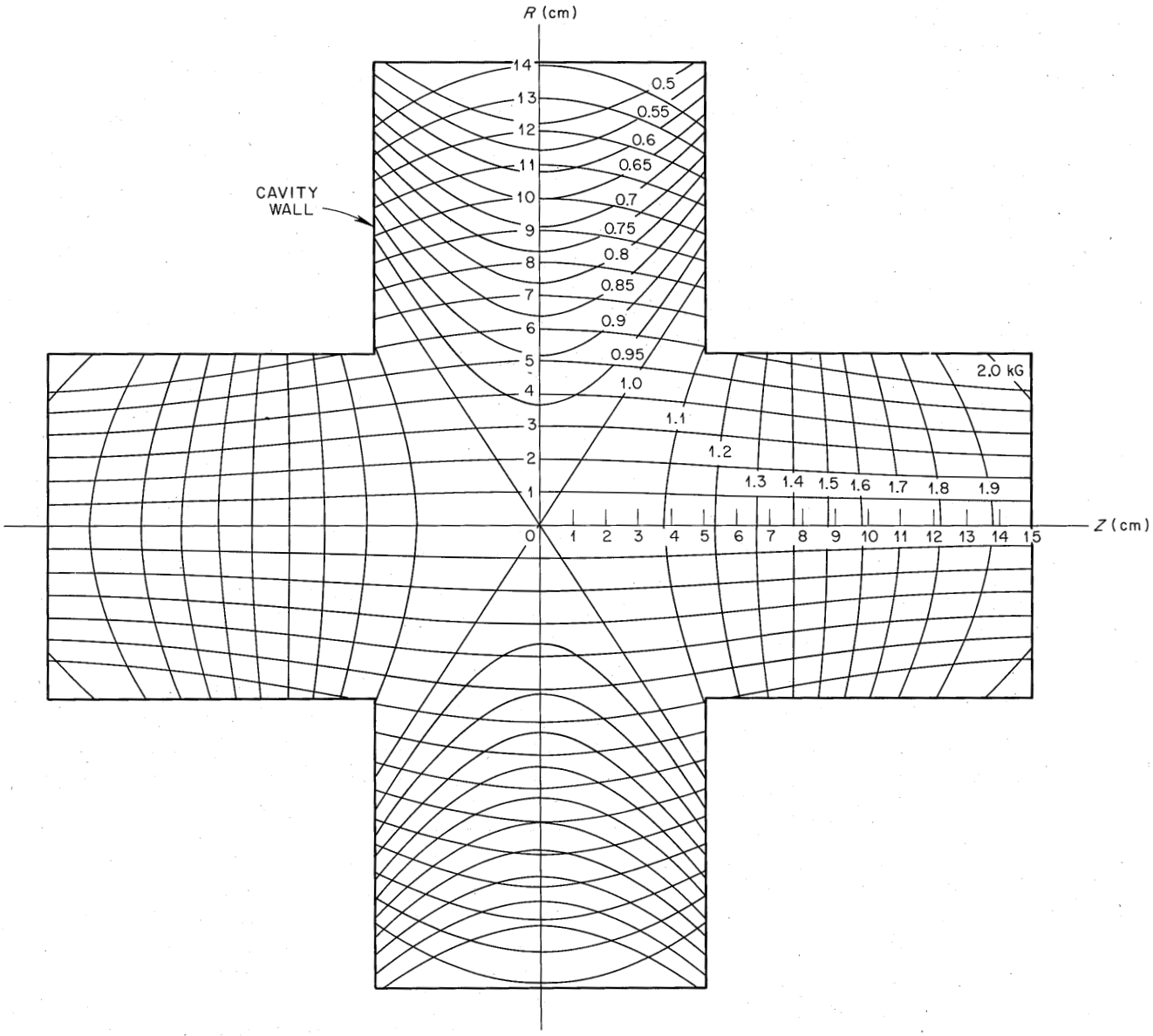


**Fig. 2.13. Field Lines and $|B|$ Contours for IMP (Mirror Configuration).**

ficial treatments have appeared.[17,18] The calculation of this section is an attempt to rectify many of the earlier deficiencies. However, an exact physical description remains analytically intractable.

In IMP, the electron-cyclotron-heated (ECH) plasma is expected to be of order $10^{13}$ particles/cm$^3$. The resulting mean free path for $H_2{}^0$ ionization is much less than the plasma radius, so that considerable shielding should accrue. In order to quantitatively demonstrate these ideas, calculations have been performed for a magnetic configuration of spherical geometry. Plasma components include both a uniform ECH plasma of hot electrons and cold ions, and beam-injected fast ions.

**2.3.5.1 Continuity Relations.** – In the following, it is assumed that a diatomic background gas is present. A monatomic gas is then a special case of this more general treatment. Specifically, the background gas treated is hydrogen.

[17] A. Simon, *J. Nucl. Energy: Pt C: Plasma Phys.* **1**, 215 (1960).

[18] R. J. Mackin, Jr., *Nucl. Fusion* **1**, 131 (1961).

At a given radius, the fast ion equilibrium density is determined by a balance between gain from injection and loss by either charge exchange (CX) or scattering. At a given point, this balance can be written as

$$\begin{aligned}\frac{dn_{II}}{dt} = 0 = &(\text{gain from CX on } n_{CI})\\ &+ (\text{gain from ionization on trapped } n_{II})\\ &- (\text{loss from CX on } n_{FC})\\ &- (\text{loss from CX on } n_{TN})\\ &- (\text{loss from CX on } n_{H2O})\\ &- (\text{loss from scattering on } n_{CI})\\ &- (\text{loss from self-scattering}) ,\end{aligned} \tag{1}$$

where

$n_{II}$ = injected fast ion density,

$n_{CI}$ = cold ion density associated with the ECH plasma,

$n_{FC}$ = density of dissociation or "Franck-Condon" neutrals,

$n_{TN}$ = target neutral density,

$n_{H2O}$ = $H_2{}^0$ neutral density.

Equation (1) may be written more explicitly as

$$\begin{aligned}0 = &n_{CI}\sigma_{CX}\left[I(R)\frac{\Delta l}{\Delta V}\right] + n_{II}(R)\,\sigma_{ION}\left[I(R)\frac{\Delta l}{\Delta V}\right]\\ &- n_{II}(R)\,n_{FC}(R)\,\langle\sigma_{CX}v\rangle_1 - n_{II}(R)\,n_{TN}(R)\,\langle\sigma_{CX}v\rangle_2\\ &- n_{II}(R)\,n_{H2O}(R)\,\langle\sigma_{CX}v\rangle_3 - n_{II}(R)\,n_{CI}\,\langle\sigma_{COUL}v\rangle_4\\ &- n_{II}(R)\,n_{II}(R)\,\langle\sigma_{COUL}v\rangle_5 ,\end{aligned} \tag{2}$$

where the $\langle\sigma v\rangle$'s are appropriately averaged corresponding to the loss processes listed in Eq. (1) and $\Delta l$ is the trapping length in trapping volume $\Delta V$ located at radius $R$.

Neutral particle densities are calculated from separate gain-loss equations. Because the ECH plasma can act as a very effective plasma pump, it is expedient to deal in particle flux. The equilibrium molecular hydrogen flux passing through volume $V_1$ is

$$\begin{aligned}\frac{d[n_{H2O}(R)\,V_1]}{dt} = 0 = &(\text{number into } V_1)\\ &- (\text{number out of } V_1) = F_{H2O}(R, n_{II})\\ &- n_{H2O}(R)\,v_{H2O}\frac{V_1}{\langle R_1\rangle} ,\end{aligned} \tag{3}$$

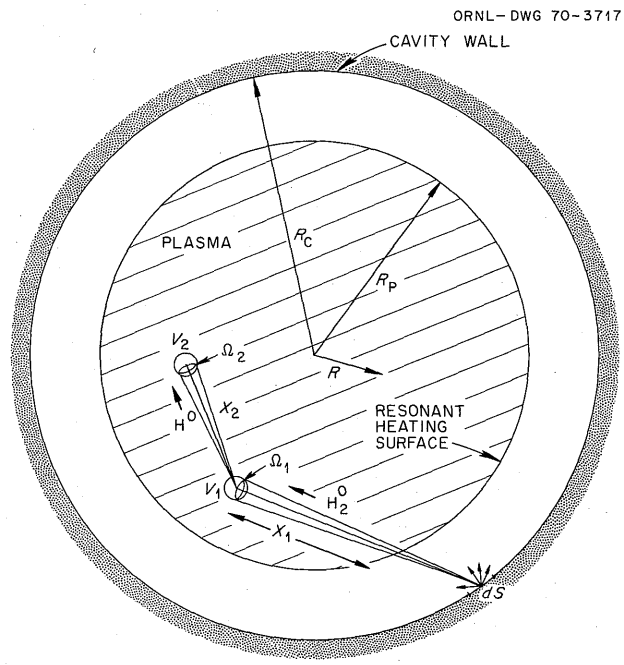


**Fig. 2.14. Spherical Geometry Used in Calculating the Flux of $H_2{}^0$ and Franck-Condon Neutrals as a Function of Radius.**

where $\langle R_1\rangle$ is the average distance traveled by an $H_2{}^0$ neutral in passing through $V_1$ (see Fig. 2.14).

While in $V_1$ a number of the $H_2{}^0$ neutrals will be ionized either by trapped fast ions or by components of the ECH plasma. The resulting molecular ions are constrained to drift along field lines. They dissociate quickly, because the cross sections for dissociation are larger than for ionization, and an average particle cannot drift far in an atmosphere of dense electrons before breakup occurs. For mathematical simplicity, ionization and dissociation are assumed to be simultaneous.

The products of dissociation are either two protons or a proton and a neutral. For each $H_2{}^0$ ionized, on the average 0.9 of an $H^0$ particle will be produced, with a mean energy of 9 eV. Such neutrals are commonly called Franck-Condon neutrals and are assumed to be emitted isotropically (see Sect. 8.5). They are free to penetrate the magnetic field further until, for example, they reach $V_2$ (shown in Fig. 2.14). A flux balance similar to Eq. (3) can be written

$$\begin{aligned}\frac{d[n_{FC}(R)\,V_2]}{dt} = 0 = &(\text{number into } V_2)\\ &- (\text{number out of } V_2) = F_{FC}(R, n_{II})\\ &- n_{FC}v_{FC}\frac{V_2}{\langle R_2\rangle} ,\end{aligned} \tag{4}$$

where $\langle R_2 \rangle$ is the average path length of a Franck-Condon neutral in $V_2$.

There is a third, independent, source of neutrals. This is the charge exchange of neutrals in the beam with cold (ECH associated) protons. These so-called "target neutrals" are assumed to be created isotropically. Their number flow in $V_3$ is

$$\frac{d[n_{TN}(R)\, V_3]}{dt} = 0 = (\text{number into } V_3) - (\text{number out of } V_3) = F_{TN}(R, n_{II}) - n_{TN}(R)\, v_{TN} \frac{V_3}{\langle R_3 \rangle} . \quad (5)$$

Solving Eqs. (3)–(5) for $n_{H2O}$, $n_{FC}$, and $n_{TN}$ and substituting into Eq. (2) results in a relation for $n_{II}(R)$. It is nonlinear because of the exponential dependence of $F_{H2O}$, $F_{FC}$, and $F_{TN}$ on $n_{II}$, as specified below.

**2.3.5.2 Injection and Shielding Geometry.** – Injection is basically a cylindrical process, and the assumed cylindrical geometry is shown in Fig. 2.15 to the left of the $X$ axis. Guiding center particles, ionized within a trapping length $\Delta l$ between $R$ and $R + \Delta R$, precess on circular drift surfaces. Although the drift surfaces in simple mirror devices are circles, mirror-quadrupole fields may have circular symmetry only in the midplane. The farther a particle wanders from the midplane, the more the drift surface becomes distorted and the more approximate this geometry becomes.

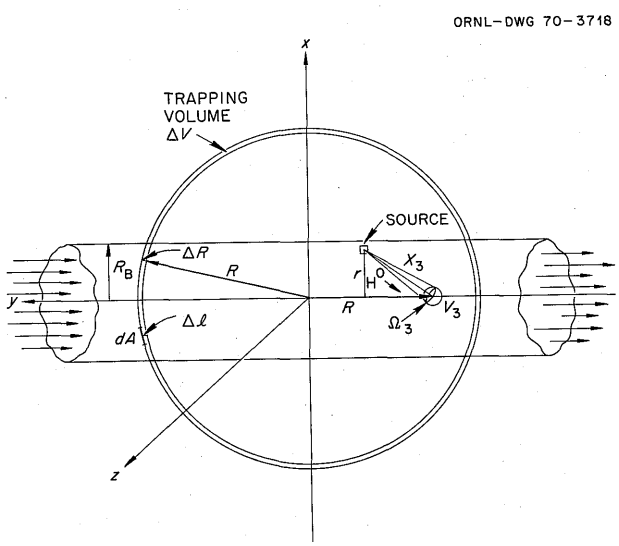


**Fig. 2.15. Cylindrical Geometries of the Trapping and Target Neutral Calculations.** The beam trapping geometry is shown to the left of the $X$ axis, while target neutral flux parameters are illustrated on the right.

The number of particles trapped in $\Delta V$ per second is

$$\left[ I(R) \frac{\Delta l}{\Delta V} \right] = \frac{1}{\Delta V} \int \Delta l\, J \cdot dA , \quad (6)$$

where $J(X, Z)$ is the beam current per unit area and all other quantities are shown in Fig. 2.15. In this calculation the beam was considered to have a Gaussian $X$-$Y$ dependence, closely approximating the IMP beam.

Of course, fast ions do not stay fixed at their injection point but move along field lines between reflection points. Dense ECH plasmas, such as are expected in IMP, provide sufficient shielding that scattering and charge-exchange times are comparable. This gives rise to an axial density spreading, with fast ions scattering toward the periphery, where shielding becomes negligible and charge-exchange times are very short. Thus fast ions tend to fill out the ECH volume. Such spreading is included in the calculation, and for the purpose of fast-ion shielding, it is assumed that the trapped proton density symmetrically fills the ECH volume.

Another cylindrical process is that of "target neutral" formation. These neutrals are formed by beam atoms charge-exchanging with the cold proton component of the ECP (here taken as 5 eV), the resulting cold neutrals then being free to leave the plasma. However, on their way out they may charge-exchange with fast protons, causing loss of $n_{II}$.

Because the beam is not symmetric with respect to either the ECH or fast-ion plasmas, it is rather difficult to calculate the flux of target neutrals. However, it is possible to place an upper limit to these neutrals by finding their flux along the beam path (as shown in Fig. 2.15 to the right of the $X$ axis). This overestimates the target neutral effect at radii greater than that of the beam, $R_B$. The target neutral flux at $R$ is then given by

$$F_{TN}(R, n_{II}) = \left[ I(R) \frac{\Delta l}{\Delta V} \right] \sigma_{CX} n_{CI} \int i(r) e^{-X_3/\lambda_3} \times \Omega_3\, dV_3 , \quad (7)$$

where $i(r)$ is the beam shape factor (Gaussian in IMP), $\Omega_3$ is the solid angle at $V_3$ subtended from the source point a distance $X_3$ away, and $\lambda_3(n_{II})$ is the mean free path length for fast-ion and ECP attenuation, averaged along $X_3$.

There remains the task of writing down expressions for penetration of neutrals impinging from the walls. Fortunately, this situation is one of near spherical symmetry, which lends itself to easy calculation.

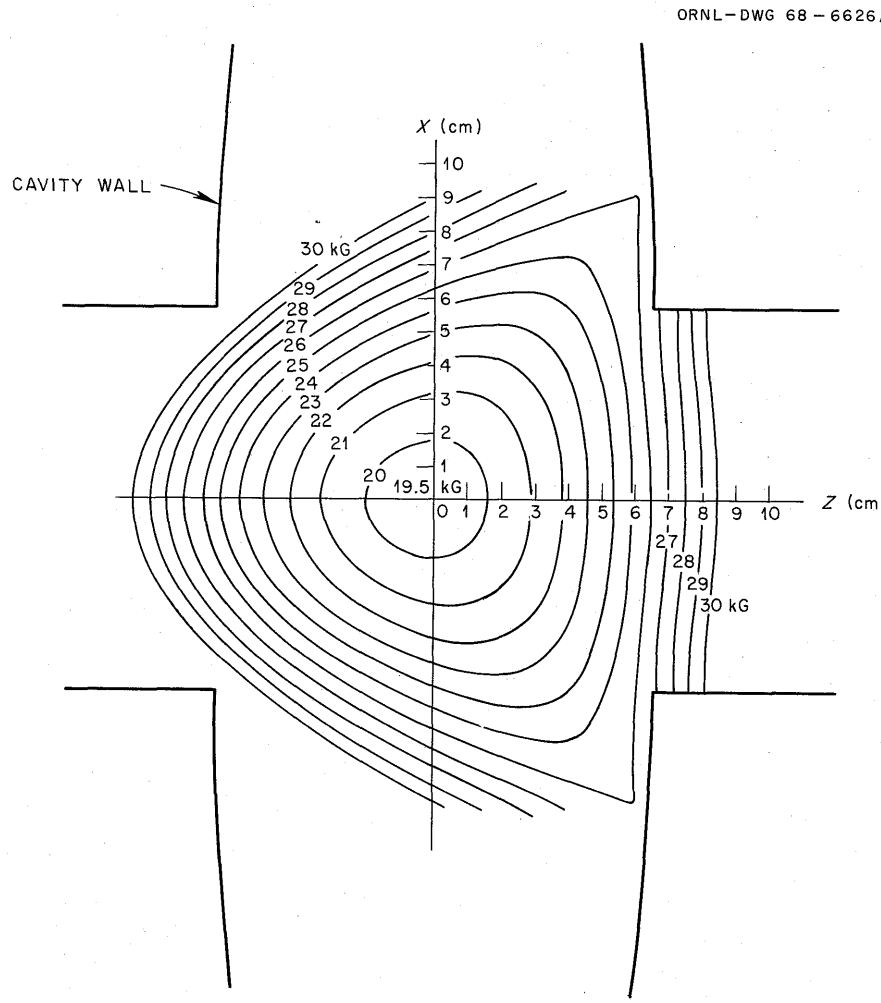


**Fig. 2.16. Constant $|B|$ Contours of the IMP Mirror-Quadrupole System in a Plane Between the Ioffe Bars.** Compensation ratio 1.7.

The reason for spherical symmetry lies in the shape of the $|B|$ contours, as shown for IMP in Fig. 2.16. The ECH plasma fills the volume inside the closed $|B|$ surface at which resonant heating takes place. Carrying this symmetry still further, it is assumed that the cavity is spherical (Fig. 2.14) and that $H_2{}^0$ molecules evolve uniformly from the walls, simulating either outgassing or a distributed feed. These molecules evolve isotropically with a temperature equal to that of the cavity. The flux of such particles into volume $V_1$ is

$$F_{H20}(R, n_{II}) = \frac{F_C A_C}{V_1} \int \Omega_1 e^{-X_1/\lambda_1} \, dS , \qquad (8)$$

where $dS$, $X_1$, and $\Omega_1$ are shown in Fig. 2.14, $F_C$ is the flux of particles evolving from the cavity wall, $A_C$ is the area of the cavity wall, and $\lambda_1(n_{II})$ is the average mean free path along $X_1$ for attenuation of $H_2{}^0$'s by ionization and charge exchange. Implicit in this formulation is the assumption that neutrals can reach the plasma unattenuated, as will be the case for most injection devices.

While passing through $V_1$, a number of the $H_2{}^0$'s will be ionized and dissociated. The $H^0$ atoms thus formed are then free to penetrate to $V_2$, and their flux is

$$F_{FC}(R, n_{II}) = P_{ION} \int F_{H20}(R, n_{II}) \, \Omega_2 e^{-X_2/\lambda_2} \, dV_1 , \qquad (9)$$

where $P_{ION}$ is the probability of an $H^0$ ion being formed in $V_1$ and $\lambda_2(n_{II})$ is the average mean free path along $X_2$ for attenuation of Franck-Condon neutrals by ionization and charge exchange.

Equations (2)–(9) complete the specification of $n_{II}(R)$. Because they form a rather complicated system, iterative computer techniques have been employed for their solution. Different size test volumes $V_1$, $V_2$, and $V_3$ have little effect on the results, except for small variations in the Franck-Condon neutral component. In any case, as $V_1$, $V_2$, and $V_3$ are made smaller, their size cancels out of the problem, leaving the calculation invariant.

**2.3.5.3 Solutions for IMP.** – Solutions for IMP parameters are shown in Figs. 2.17 and 2.18. The cavity was assumed to have a 12-cm radius, with an input flux of $F_C = 5 \times 10^{15}$ neutrals cm$^{-2}$ sec$^{-1}$. Injected atoms of 20 keV were assumed to be trapped in a field of 10 kG. Radii of the test volumes were $R_1 = R_2 = R_3 = 0.1$ cm. The various cross sections[19] used are as follows: From Eq. (2),

$$\sigma_{CX} = 5 \times 10^{-16} ,$$
$$\sigma_{ION} = 2 \times 10^{-16} ,$$
$$\langle \sigma_{CX} v \rangle_1 = \langle \sigma_{CX} v \rangle_2 = 5 \times 10^{-16} ,$$
$$\langle \sigma_{CX} v \rangle_3 = 6 \times 10^{-16} ,$$
$$\langle \sigma_{COUL} v \rangle_4 = \frac{\ln \Lambda}{2.50 \times 10^7 T^{3/2} \log R} ,$$
$$\langle \sigma_{COUL} v \rangle_5 = \frac{\ln \Lambda}{3.33 \times 10^7 T^{3/2} \log R} ,$$

where $\Lambda$ is the Debye length divided by the distance of closest approach, $T$ is the injected ion energy in electron volts, and $R$ is the mirror ratio. Other cross sections needed in the evaluation of mean free paths are:

| | |
|---|---|
| $\langle \sigma_{ION} v \rangle = 3.6 \times 10^{-8}$ | Ionization of Franck-Condon and target neutrals by injected ions |
| $\langle \sigma_{ION} v \rangle = 3 \times 10^{-8}$ | Ionization of $H_2{}^0$'s by injected ions |
| $\langle \sigma_{ION} v \rangle = 1 \times 10^{-8}$ | Ionization of Franck-Condon and target neutrals by ECP electrons |
| $\langle \sigma_{ION} v \rangle = 1.5 \times 10^{-8}$ | Ionization of $H_2{}^0$'s by ECP electrons |

with all dimensions in centimeters and seconds.

A few general conclusions can be drawn from studying Figs. 2.17 and 2.18. The $H_2{}^0$ neutrals are rapidly attenuated by several orders of magnitude. This leaves the Franck-Condons as the main source of charge-exchange centers at small radii. The Franck-Condon neutrals have a relatively long mean free path and suffer very little attenuation. However, they are much more energetic than the $H_2{}^0$'s and so leave the plasma more quickly, with the result that their density is lower. The same is true of target neutrals. Although not of major importance in the examples taken here, target neutral density increases linearly with input beam current and so could become more important than the Franck-Condons at higher beams.

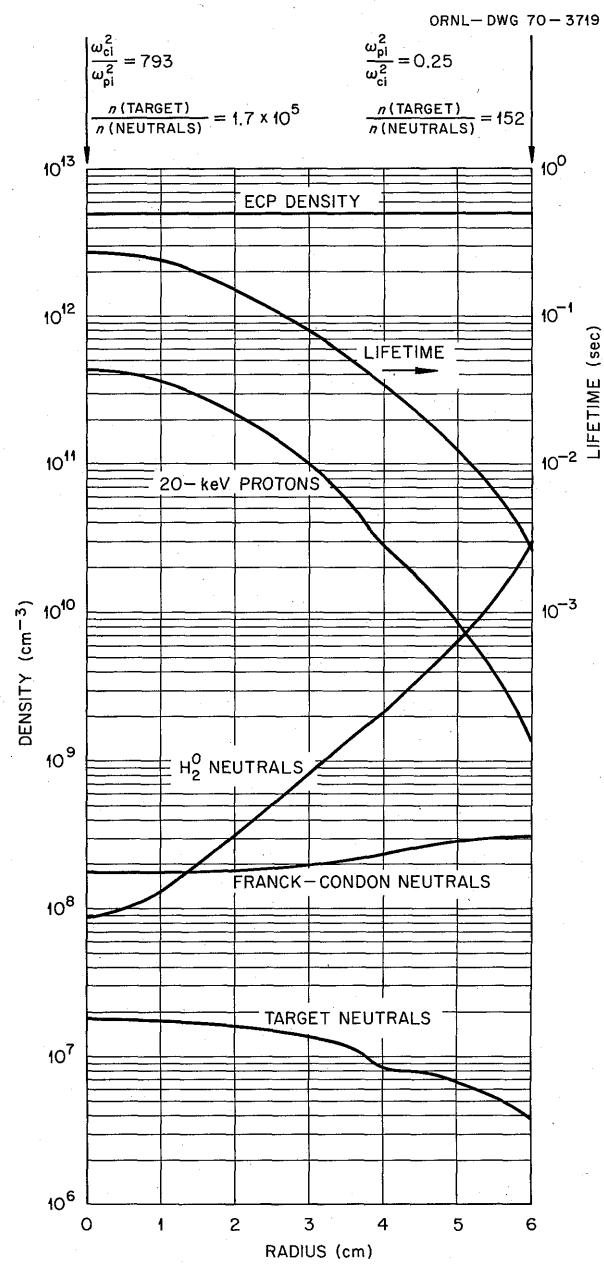


**Fig. 2.17. IMP Equilibrium Calculation for an ECP of 5 × $10^{12}$ particles/cm$^3$ and an Injected Current of 50 mA (Equivalent) $H^0$'s.**

[19]For Coulomb scattering formulas, see T. K. Fowler and M. Rankin, *J. Nucl. Energy: Pt C: Plasma Phys.* 8, 121 (1966).

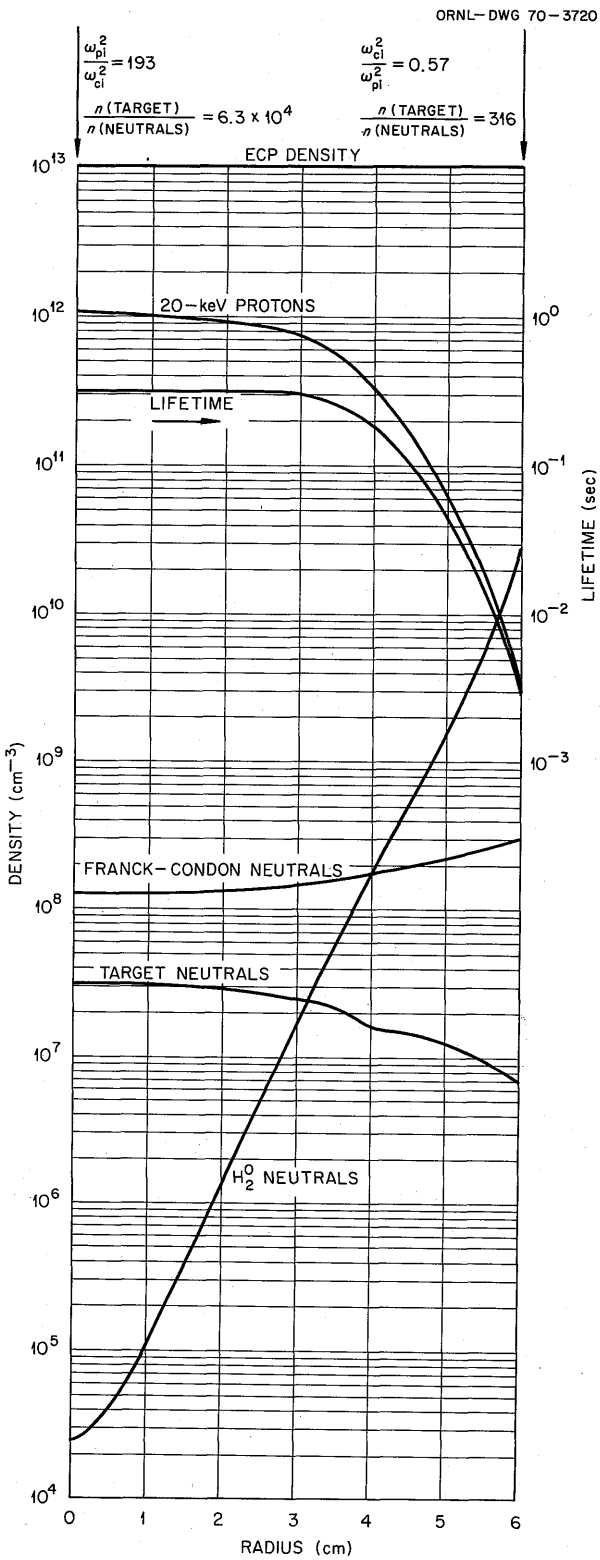


**Fig. 2.18. IMP Equilibrium Calculation for an ECP of $10^{13}$ particles/cm$^3$ and an Injected Current of 50 mA (Equivalent) $H^0$'s.**

Under the conditions of Fig. 2.18, the combination of $H_2{}^0$ shielding and a large number of ECP scattering centers gives rise to a near scatter-dominated plasma. Shielding has an effect in increasing the central ($R = 0$) target quality $n_{\text{TARGET}}/n_{\text{NEUTRAL}}$ by 300 times and the fast-ion scaled density $\omega_{pi}^2/\omega_{ci}^2$ by 87 times as compared with these values at the outside ($R_p$, 6 cm).

### 2.3.6 Acknowledgments

Members of the Magnetics and Superconductivity Group, under the direction of W. F. Gauster, made very significant contributions to the engineering aspects of this work. D. L. Coffey had primary responsibility for superconductor selection and test, and contributed in many other areas as well; K. R. Efferson designed the cryogenic system (including helium level detectors, vapor-cooled current leads, and the high-current feed-through insulators for operation at 4.2°K in a vacuum) and established the cooldown and transfer procedures; R. L. Brown devised the winding techniques and supervised the coil winding; J. L. Horton contributed in the areas of force computation, instrumentation, and regulation of the coil current supply; and J. N. Luton designed the charged-beam deflection magnet.

R. A. Dandl and H. O. Eason coordinated the installation of the microwave power source and gave instruction in its operation and advice in a number of matters relating to ECP in general. They are also in charge of most of the engineering toward the 55-GHz microwave package for IMP. Discussions on general matters relating to ECP with N. H. Lazar and G. E. Guest were helpful. Magnetic field and force calculations were carried out by C. E. Parker. E. A. Ferguson was responsible for coding the integrals described in Sect. 2.3.5.2.

## 2.4 SCATTER EXPERIMENTS

W. B. Ard W. A. Hogan[20]
R. F. Stetson[21]

The following is an abstract of a paper, "Time Dependence of the Energy Distribution of a Hot Electron Plasma Decaying in a Magnetic Mirror," to be submitted to *Physics of Fluids.*

The energy distribution of energetic electrons in a decaying electron-cyclotron-heated plasma has been measured as a function of time. The distribution

[20] Florida Atlantic University, Boca Raton, Fla.

[21] Instrumentation and Controls Division.

function is obtained by analysis of bremsstrahlung spectra taken at different times during the decay. The measured distributions are compared with results of a simple computer simulation based on a model for the plasma in which electrons are cooled by inelastic collisions with neutrals and lost from the mirror by multiple small-angle collisions with charged particles and neutrals. This comparison allows the experiment to yield values for the effective cross sections for both energy loss and scattering.

# 3. Toroidal Confinement

## 3.1 INTRODUCTION

Work on experiments using closed magnetic confinement schemes began here with the toroidal multipole experiments of Roberts and Alexeff using inductively levitated rings. This work, reported below, has been terminated, but further experiments using an identical system are being performed by M. Lubin at the University of Rochester in collaboration with ORNL.[1]

In May of this year (1969) it was decided that we should consider the advisability of beginning a TOKAMAK program at Oak Ridge, in view of the Russian success with this device. There resulted a machine concept and a program of research which have been approved. The major components of the design are finished, and work is under way. This work has superseded the toroidal multipole and DCX-2 projects.

In addition to this experimental program, called ORMAK, there is a computer study being made of TOKAMAK plasma equilibria. It is being conducted by R. Dory and is reported in detail in Sect. 1.

## 3.2 ORMAK

| | |
|---|---|
| J. F. Clarke | G. G. Kelley |
| S. M. DeCamp | M. Murakami |
| J. C. Ezell | M. Roberts |
| W. Halchin | R. F. Stratton |

The ORMAK design has the advantages with respect to present and proposed Russian TOKAMAK of increased symmetry and a wider range of geometrical configurations. (The aspect ratio, major radius/minor radius, can be about a third of that in present major Russian devices.) Details of the design are given in a separate report.[2]

The immediate program first duplicates the plasma geometry of one Russian experiment (TM-3) but with the advantage of greater symmetry, better control and greater range of parameters, and more extensive diagnostics. This phase is called ORMAK I. It probably will last for several months after completion of the device – expected in January 1971. In spite of the Russian work to date, there is still much to be learned from this kind of device.

Conversion to ORMAK II will exploit the ability to produce a plasma of low aspect ratio. The changeover should require a shutdown of less than two months.

The experiments with both devices are expected to answer the major questions concerned with the extrapolation of the TOKAMAK concept to a test of its feasibility for controlled fusion power. If the answers are favorable, future work in the program very likely will involve the design of a considerably larger device. Preliminary consideration of the problems of such a device is in progress.

## 3.3 TOROIDAL MULTIPOLE

| | |
|---|---|
| I. Alexeff | M. Roberts |
| W. Halchin | W. L. Stirling |

The final phase of the toroidal multipole work at ORNL dealt with three topics: realization of the potentially high magnetic field in the quadrupole, initial experiments on the magnetic energy storage properties of copper for production of (short)-time-invariant induction magnetic fields, and preliminary measurements of the effect of the resistive hoop voltage on plasma parameters. Details of these three topics are given in a separate report.[3]

---

[1] M. J. Lubin *et al.*, "Plasma Confinement in the University of Rochester–ORNL Toroidal Quadrupole," *Proceedings of the International Symposium on Closed Confinement Systems* (Dubna, U.S.S.R., Sept. 29–Oct. 3, 1969).

[2] G. G. Kelley, M. Roberts, and J. F. Clarke, *Conceptual Design of ORMAK Facility*, ORNL-TM-2821 (December 1969).

[3] M. Roberts *et al.*, *Proc. Symp. Engineering Problems of Fusion Research, Los Alamos Scientific Laboratory, April 8–11, 1969*, LASL report LA-4250, paper A-2.

# 4. High-Beta Plasma

## 4.1 OFF-RESONANT HEATING

W. B. Ard
R. A. Dandl[1]
H. O. Eason
P. H. Edmonds
A. C. England
R. L. Livesey
M. W. McGuffin
S. T. Nolan[2]

### 4.1.1 Introduction

Previous electron-cyclotron heating experiments have pointed to an effective off-resonant heating of electrons. Energetic plasmas were formed even when resonant heating coupled only to a small class of the electron population. However, the previous experiments did not permit the separation of nonresonant from resonant heating. The theory of Grawe[3] supported the observations and indicated through numerical calculations that relativistic electrons continued to gain energy at a significant rate. Significant heating rates were observed even when the electron gyrofrequencies differed markedly from the cold electron gyrofrequency.

Experiments have now been performed with independent nonresonant heating sources, both well above and well below gyroresonance. A resonant power source is required to break down the gas. This power source heats some electrons to a temperature sufficient for good mirror confinement. Their confinement time is increased to the point where the slower nonresonant heating can take over and form a hot plasma. The nonresonant microwave source was at a frequency either above or below the cold electron gyrofrequency everywhere in the cavity.

Because of the very different results in the two cases the investigations have taken two paths. One path involves heating at frequencies far above the gyrofrequency in the plasma region. The results of this investigation are covered in Sect. 4.2. The other path involves heating frequencies lower than the cold electron gyrofrequency, and the results will be discussed in Sect. 4.3.

## 4.2 OFF-RESONANT HEATING WITH $\omega > \omega_{ce}$

The study of the effect of off-resonant heating in the ELMO machine has been continued. In addition to the previous millimeter sources, the experiments have been extended by the addition of a 3-cm, 3-kW microwave source. This now permits operation with a 3-cm resonance, with power at 8 and 5 mm available for off-resonant heating in addition to the previously reported experiments with 8-mm resonance and 5-mm off-resonant heating.[4] As mentioned above, the results obtained with lower frequency off-resonant heating ($\omega < \omega_{ce}$) will be discussed in Sect. 4.3.

Figure 4.1 demonstrates the effect of off-resonant heating on the stored energy and temperature of the

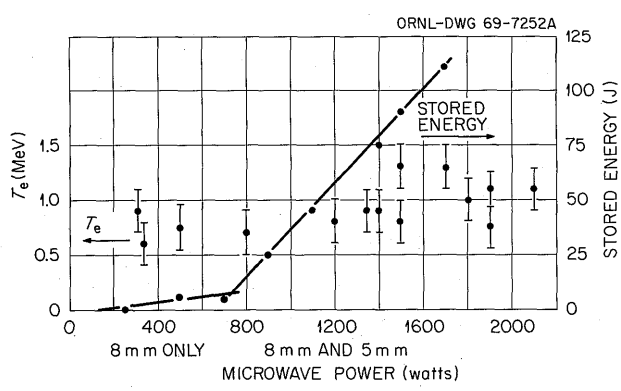


**Fig. 4.1. Electron Temperature and Stored Energy as a Function of Applied Resonant and Off-Resonant Microwave Power.**

[1] Instrumentation and Controls Division.

[2] Summer Research Participant from the University of South Alabama.

[3] H. Grawe, *Plasma Phys.* 11, 151 (1969).

[4] *Thermonuclear Div. Ann. Progr. Rept. Dec. 31, 1968,* ORNL-4401, p. 93.

plasma for 8-mm resonance and 5-mm off-resonant heating. The resonant power was increased to 700 W, with no off-resonant power, and then held constant and the off-resonant power increased. The greater efficiency of the off-resonant power is attributed to the higher electric field for this frequency due to the absence of any heavily damping fundamental resonance. The electron temperature is measured from bremsstrahlung, the stored energy from a diamagnetic loop encircling the axis of the device.

The most significant feature is the relative constancy of the electron temperature as the applied power is varied. That the temperature is almost constant can also be seen from Fig. 4.2, where the neutron count rate, a sensitive function of temperature, is seen to be proportional to the stored energy.

The electron temperature is usually between 500 keV and 1 MeV in these measurements, in qualitative agreement with Grawe's results.[3] In some experiments the total amount of stored energy has reached 400 J. The neutrons are believed to result largely from the Coulomb dissociation of deuterium by electrons with energies greater than the 2.22-MeV threshold.

Three distinct instability modes have been observed in the plasma. They have been tentatively identified as the mirror instability, the double-distribution instability, and the flute instability. All are controllable by various techniques. One of the most effective of these techniques in the case of the first two mentioned is off-resonant heating with $\omega > \omega_{ce}$. These instabilities are discussed further in Sect. 4.4. Much of the success with off-resonant heating is probably due to the successful suppression of these instabilities.

As has been mentioned in previous reports, the hot electron plasma is in the shape of an annulus near the midplane of the mirror. Figure 4.3 shows results obtained three years ago,[5] indicating roughly the radial position of the annular region. The figure indicates the change in the diamagnetic signal due to the removal of plasma by radial probes inserted from the outside and inside. The radial probes interrupt the outer and inner drift surfaces respectively. The data were obtained with 8-mm heating alone and some of the 8-mm power supplying the off-resonant effect.

The mean radii of the two profiles are separated by about a Larmor diameter for the energetic electrons making up the energetic plasma in the center of the annulus. Naturally, since the probes exert such a major disturbance, the curves do not give a true measure of the undisturbed inner and outer plasma radii.

Figure 4.4 shows a profile taken with 3-cm resonance heating and 8-mm off-resonance heating. As in the case with 8 mm and 5 mm together, the higher frequency nowhere supplies a resonant heating in the plasma region.

[5] *Thermonuclear Div. Ann. Progr. Rept. Dec. 31, 1968,* ORNL-4401, p. 87.

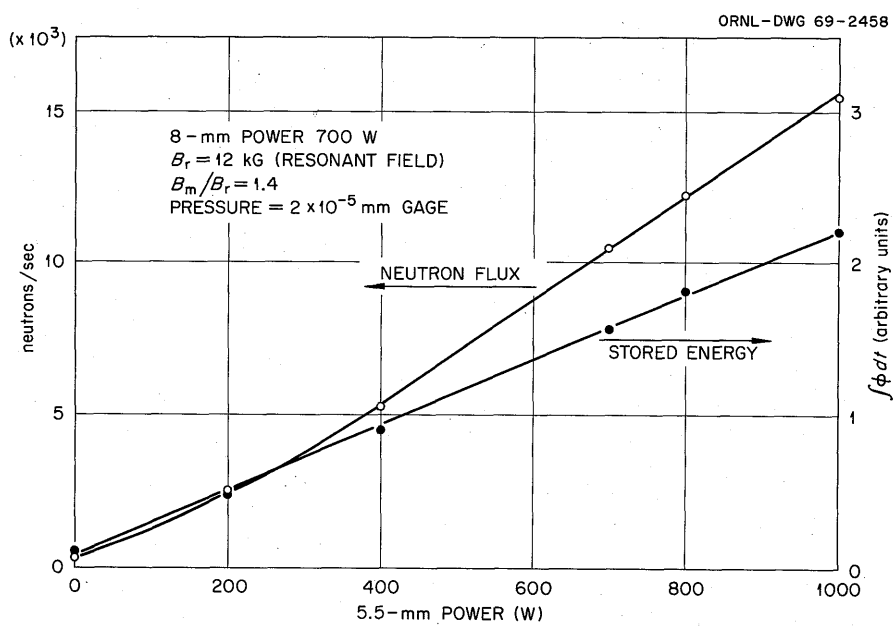


**Fig. 4.2. Stored Energy and Neutron Flux as a Function of the Applied Off-Resonant Power.**

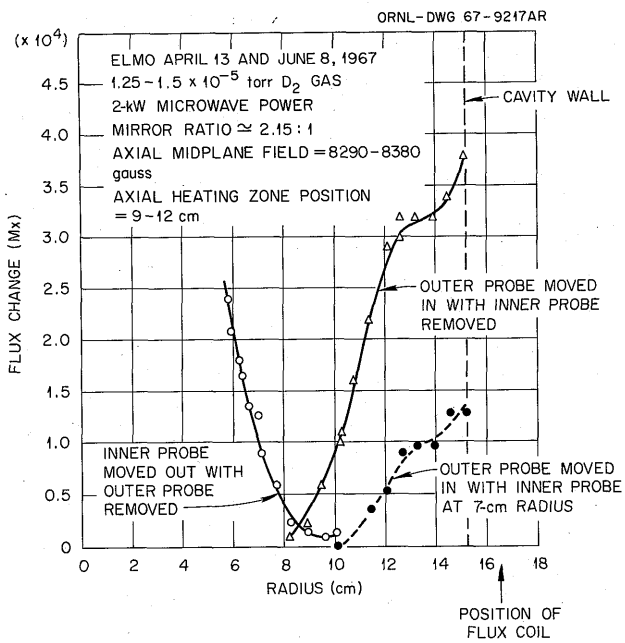


**Fig. 4.3. Diamagnetic Signal as a Function of Probe Position with Only Resonant Heating at 8 mm.**

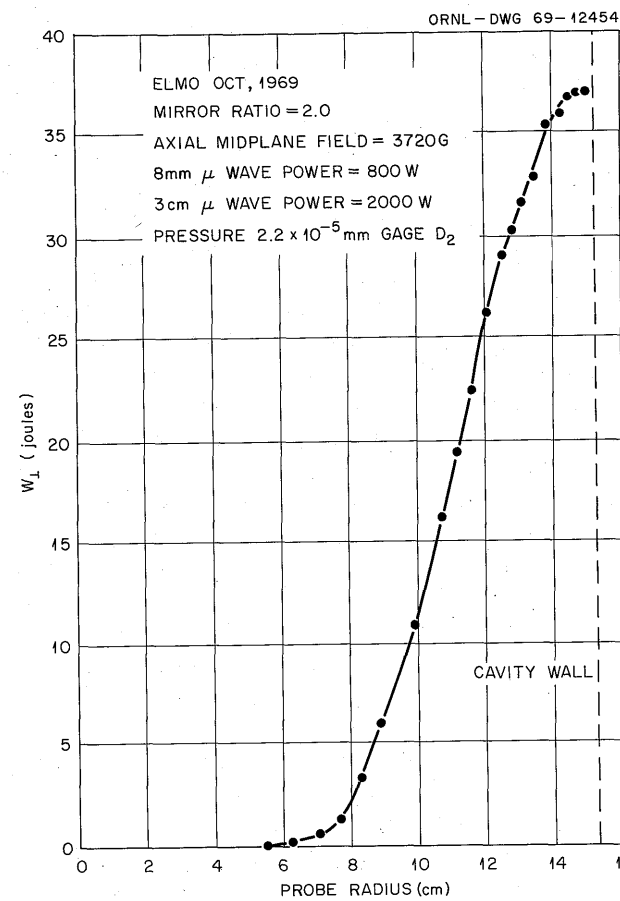


**Fig. 4.4. Stored Energy as a Function of Radial Probe Position with Resonant Heating at 3 cm and Off-Resonant Heating at 8 mm.**

The great similarity between the radial inward limiter profiles in both figures is striking. All the external conditions such as resonant heating frequency, off-resonant frequency, magnetic field, and resonance heating zone position were different with the exception that the experiments were done in the same cavity.

It is not clear that the cavity geometry is actually responsible for the annular characteristic of the plasma. Some evidence suggests that while line tying to the metallic end walls is responsible for the stability, there is no identifiable association with any particular geometric feature in the cavity. It may be that the annular plasma merely represents a particularly stable equilibrium condition.

## 4.3 DRIVEN LOSSES WITH LOW-FREQUENCY MICROWAVE POWER

As mentioned in the last section, off-resonant heating at short wavelengths ($\omega > \omega_{ce}$) is very effective in plasma heating. Based on this knowledge, the logical alternative was attempted: plasma heating at long wavelengths ($\omega < \omega_{ce}$). An incentive is that low-frequency microwave power is relatively cheap and readily available. Also, the microwave technology at shorter wavelengths is extremely difficult compared with that at longer wavelengths. A conveniently available 3-cm source of nominally 5-kW continuous wave was used for the off-resonance frequency, and the 8-mm source was used for resonance breakdown and the production of a moderate-$\beta$ plasma. The 3-cm power was added through an axial guide into the cavity. It was believed that whistler mode propagation would occur when the plasma density was high enough so that the ordinary mode was cut off.

The machine was operated with up to 800 W of 8-mm microwave radiation, and the magnetic field was adjusted for fundamental resonance in the mirror throats at this frequency. A plasma with a $\beta \cong 5\%$ was produced with the gas near the critical pressure for stability. The 3-cm power could be operated in the pulsed mode or steady state.

### 4.3.1 Perpendicular Energy Measurements

Upon the application of the subresonant 3-cm power, the plasma diamagnetic signal was observed to drop dramatically, indicating plasma loss. Figure 4.5 shows the drop of perpendicular stored energy vs applied 3-cm power. It is apparent that the stored energy drops approximately linearly with power until all but a small fraction of the stored energy is removed.

A waveguide port in the opposite end of the cavity showed a power transmission rise time approximately equal to the plasma energy decay time, indicating that the power is transmitted only as the energetic plasma is driven out. In addition, the reflected power shows an initial maximum which drops to a minimum near the time when the diamagnetic signal has dropped to its minimum.

Large bursts of x rays were observed with the application of the 3-cm power. Both radial and axial losses were observed, the radial losses to radial probes inserted on the midplane and the axial losses to the end walls. A burst of neutrons was also observed. These neutrons were found to be due in part to the deuterium gas and in part to $(\gamma,n)$ processes on copper requiring ~10-MeV photons. These effects will be discussed later.

Because of the nonsymmetrical arrangement of power introduction, one possible reason for the loss might have been radiation pressure from the end-feed microwave power. Subsequent experiments with balanced feed from both ends showed agreement between energy-loss measurements within a few percent, thus ruling out asymmetric radiation pressure.

The background cold plasma, as indicated by visible light intensity and probe current, showed no observable disturbance as a result of this loss process. The low-level diamagnetic signal remaining probably represented this cold plasma.

The decay time of the perpendicular diamagnetic signal is shown in Fig. 4.6. At low 3-cm power, the decay time is approximately constant and equal to the decay time of the stored energy with 8-mm power turnoff (i.e., no 3-cm power). At high 3-cm power, the decay time goes inversely as the 3-cm power.

Empirical relationships could be derived by assuming that the diamagnetic signal changes were exponential in time, a reasonably good assumption. For the low-power case, that is, $P_3/P_8 < 1/3$, where $P_3$ and $P_8$ are the 3-cm and 8-mm power, respectively, we have found (as mentioned above) that the decay time $\tau \cong$ constant $= 1/k_2$ and that the stored energy $\epsilon_\perp$ obeyed the relation

$$\epsilon_\perp(t) \approx \frac{k_1}{k_2} P_8 - \frac{k_3 P_3}{k_2} (1 - e^{-k_2 t}) , \qquad (1)$$

where $k_1$ and $k_3$ are constants of proportionality. Hence the differential equation for the process is

$$d\epsilon_\perp/dt \cong k_1 P_8 - k_3 P_3 - k_2 \epsilon_\perp . \qquad (2)$$

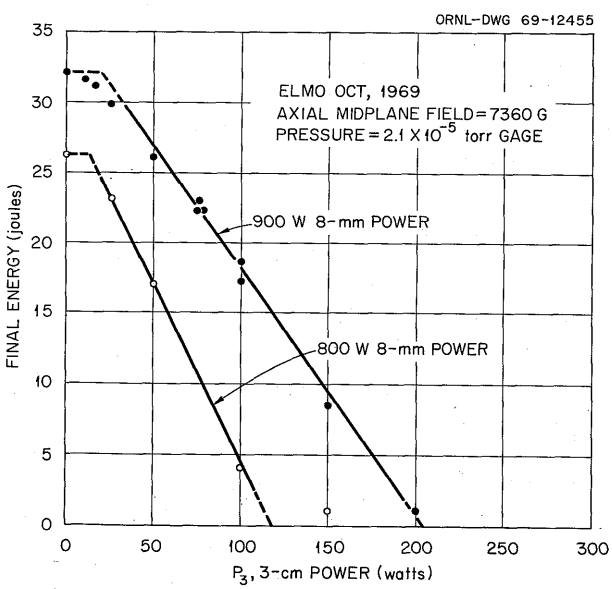


**Fig. 4.5. Final Stored Energy vs 3-cm Power.**

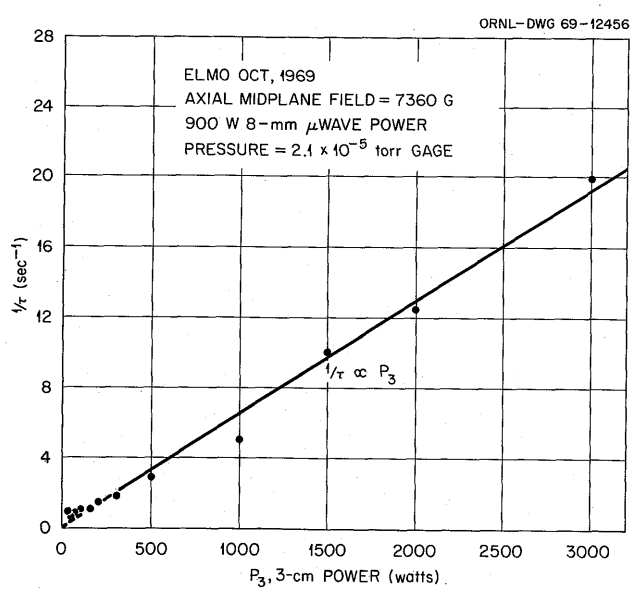


**Fig. 4.6. Decay Time of the Diamagnetic Energy vs 3-cm Power.**

We interpret the first term as a linear heating term due to the 8-mm power, the second term as a linear loss term due to the 3-cm power, and the third term due to the normal collisional losses of the plasma electrons out the mirror. In the absence of the second term (i.e., $P_3 = 0$) we would have an equation for the normal buildup and decay of the 8-mm plasma. Hence the 3-cm power represents an additional collisional loss process in its effect.

In the long time limit the relationship describing the coefficient of perpendicular velocity space diffusion,[6] $B_\perp$, is

$$\langle V_\perp^2 \rangle = 4B_\perp t \ ,$$

where $V_\perp$ is the perpendicular electron velocity. Differentiating by $t$ and assuming $B_\perp$ is not a function of $t$, we have

$$4B_\perp = \frac{d}{dt}\langle V_\perp^2 \rangle = \frac{1}{\gamma}\frac{2}{m_e}\frac{d\langle E_\perp \rangle}{dt}$$

or

$$2\gamma m_e B_\perp = \frac{d}{dt}\langle E_\perp \rangle \ ,$$

where $m_e$ is the electron mass. Hence the rate of change of perpendicular energy is proportional to the coefficient of velocity space diffusion.

Assuming constant 8-mm power, we have from Eq. (2),

$$\left.\frac{d\epsilon_\perp}{dt}\right]_{\text{3-cm effect}} = -k_3 P_3 = 2\gamma m_e B_\perp n_e \overline{V} \ .$$

Thus we have found a direct measurement of $B_\perp$. In the stochastic heating theory of Grawe,[3] for an individual particle,

$$d\epsilon/dt \propto E^2 \ ,$$

where $E$ is the average electric field in the plasma region. Here $P_3 \propto \langle E \rangle^2$ by Poynting's theorem. Hence our technique offers a direct measurement of $B_\perp$ and a positive check on the correct parametric dependence of the heating rate on the electric field. However, a detailed comparison with Grawe[3] is not possible because of the lack of fundamental resonance in the cavity.

Assuming that other loss processes can be neglected, we can calculate the coefficient of perpendicular velocity diffusion as

$$B_\perp \cong 2.25 \times 10^{20} \ \text{cm}^2/\text{sec}^3 \ .$$

Evidence is presented below (Sect. 4.3.5) that the perpendicular spatial diffusion is not appreciably affected by the microwave power, so that the assumption that the process is governed by $B_\perp$ may be good.

For higher power, that is, $P_3/P_8 \gtrsim 1/3$, we observed that the decay time $\tau \cong 1/k_4 P_3$, where $k_4$ is a constant of proportionality. The perpendicular stored energy followed roughly the equation

$$\epsilon_\perp(t) \cong \frac{k_1}{k_2} P_8 e^{-k_4 P_3 t} + \epsilon_0 \ , \tag{3}$$

where $\epsilon_0$ was the small residual stored energy remaining as long as the 8-mm power was left on. The differential equation for this process is then

$$d\epsilon_\perp/dt \cong -k_4 P_3 \epsilon_\perp \ . \tag{4}$$

Here we have a nonlinear process involving the product of the 3-cm power and the stored energy. As in the lower-power case, $d\epsilon_\perp/dt \propto \langle E \rangle^2$. However, this would appear to be a different nonlinear process than that seen in the low-power case.

### 4.3.2 Wall X-Ray Energies

Several more experiments were done on the driven losses. In one set, the "characteristic" energy of the particles striking radial and axial obstructions was measured as a function of the 3-cm power level. These characteristic energies were measured by an absorber transmission technique, because the burst of x rays was too intense to be handled by a pulse-height analyzer. Figure 4.7 shows the result. Again for low power, $P_3/P_8 \lesssim 1/3$, the characteristic energy of the lost particles is the same radially and axially and has the same characteristic energy as the temperature determined from the free-free bremsstrahlung, ~700 to 800 keV. However, at higher 3-cm power, $P_3/P_8 \gtrsim 1/3$, the characteristic energy of the axially lost particles increases. Because of the nonreproducibility of the measurements, it could not be precisely measured, but it clearly rose to a value 1.5 to 2 times larger than the

[6] O. Eldridge, Sect. 1.4.4, this report.

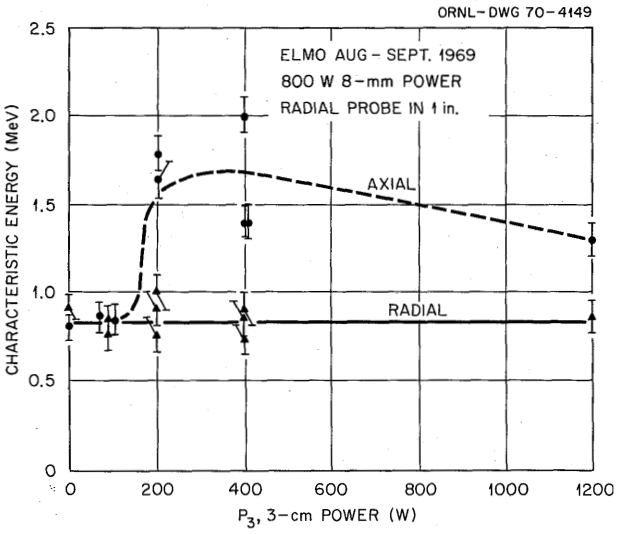


**Fig. 4.7. Characteristic Energy of X Rays vs 3-cm Power. The characteristic energy is defined by the *e*-folding depth of the x rays in lead produced by the driven losses.**

low-power value. The radial characteristic energy did not change an observable amount at high 3-cm power levels.

### 4.3.3 Time Dependence of Wall X Rays

As shown in Fig. 4.8, there were differences in the time dependence of the wall x-ray radiation burst produced by the 3-cm power. The axial loss showed a slow buildup after the application of 3-cm power, whereas the radial loss showed a prompt loss immediately on application of the power. Occasionally, the radial loss burst would have two or more peaks. However, energy analysis showed no energy change for any of these peaks. It would appear, then, that the 3-cm power was affecting the energy of the axially lost particles, but not that of the radially lost particles. This could either be a heating process, a selection process, or both: for example, particles were either actually absorbing energy from the 3-cm power, and/or particles in a certain energy range above the plasma temperature would find their diffusion rate into the loss cone suddenly increased.

### 4.3.4 Effect of Low-Frequency Microwave Power on the Electron Distribution in ELMO

In order to gain some information about how the 3-cm radiation was interacting with plasma, measure-

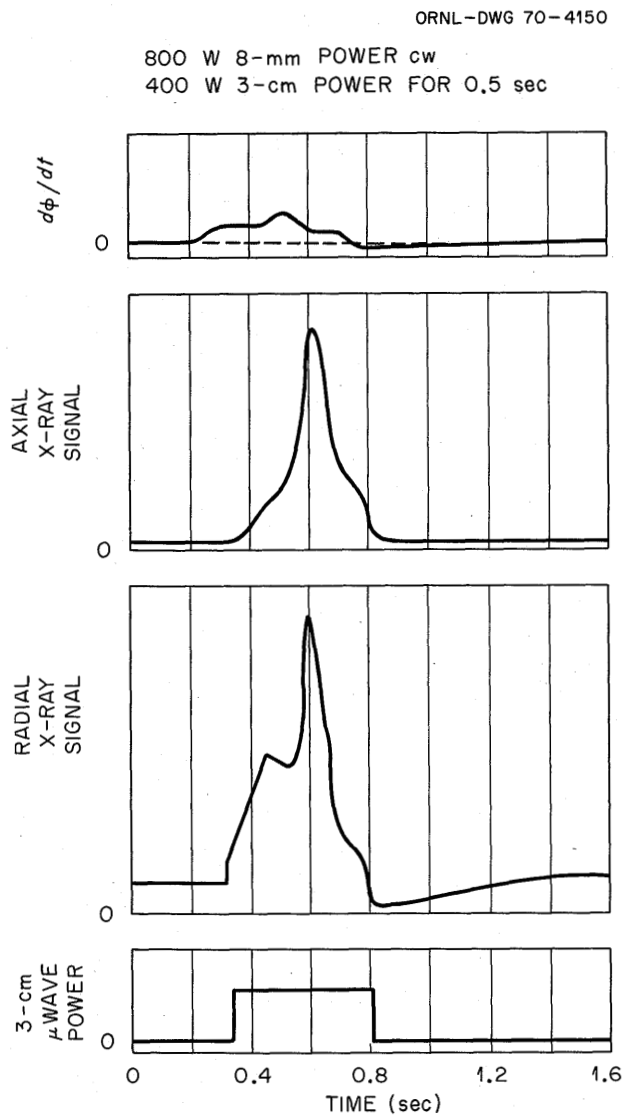


**Fig. 4.8. Time Dependence of Radial and Axial X-Ray Bursts Driven by the 3-cm Power. Also shown is the diamagnetic voltage and the 3-cm power gate pulse.**

ments of the free-free bremsstrahlung were made to determine which part of the electron distribution was interacting with the radiation. The distribution function was measured by unfolding the x-ray bremsstrahlung spectra from the plasma taken during various time intervals before and after the 3-cm power was applied. In order to accumulate enough x-ray counts to obtain the distribution, each spectrum was accumulated over a period of 5 min. This was done by gating the analyzer on for a period of 0.2 sec at four different times relative to the time when the 3-cm power was on. The spectrum

at each time interval was stored in a different quadrant of the memory. The four time intervals started at 0.2 sec before the 3-cm power was turned on, immediately after turnoff, 0.4 sec after turnoff, and 0.8 sec after turnoff. The distribution functions were obtained from the accumulation of 1500 turnoffs.

The total stored energy calculated from the distribution function showed a time behavior similar to that obtained from monitoring the diamagnetism of the plasma. The diamagnetism indicated a linear decrease in stored energy during the time the 3-cm power was on and then a continued decrease, but at a slower rate after the power was turned off. The minimum stored energy was reached some 300 or 400 msec after turnoff of the 3-cm power. Several seconds were required for the energy to rise to its initial value.

Figure 4.9 is a plot of the distribution obtained from the x-ray spectra at three time intervals. Curve *B*, taken immediately after the 3-cm power was applied, shows

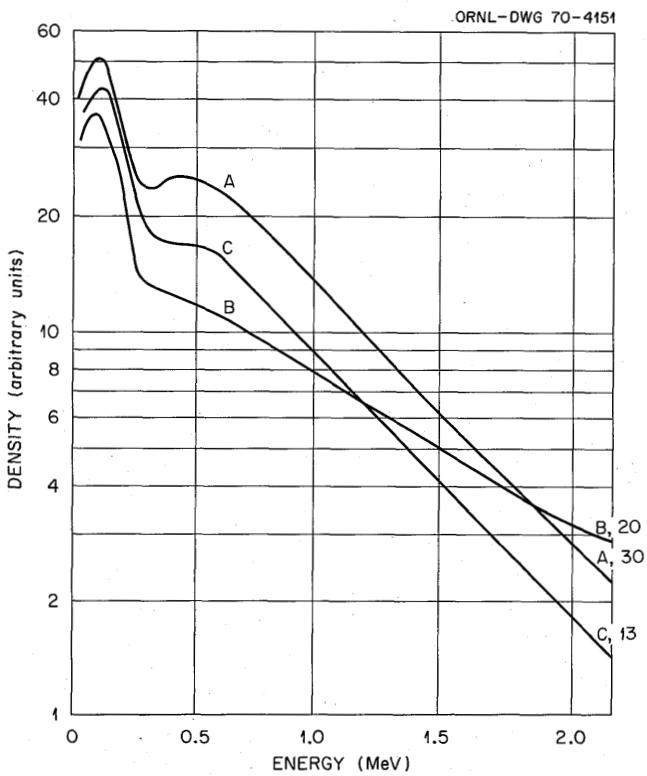


**Fig. 4.9. Energy Distribution in ELMO at Various Times Relative to Application of 1 kW of 3-cm Microwave Power for 50 msec.** Curve *A* is just previous to application of power, curve *B* is taken between 0 and 200 msec after turnoff of power, and curve *C* is between 400 and 600 msec after turnoff of power. Numbers at right end of curves are relative intensity of the spectrum at 2 MeV, which is related to the total number of electrons with energies above 2 MeV.

that the distribution has been greatly depleted at the lower energies, while at very high energies the density has actually increased. The distribution recovers toward the equilibrium distribution (curve *A*) by first recovering the very low energy part of the distribution. However, the intermediate energy part of the distribution is still small, and the heating rate of the 8-mm power is apparently not sufficient to maintain the density at high energy, and this part of the distribution is still decreasing. Since the higher energy electrons account for a large part of the total stored energy, this accounts for the observed continued decrease in stored energy after 3-cm power is turned off. Curve *C* shows that recovery toward equilibrium proceeds by the rather slow heating to high energy of the electrons at lower energies.

The mechanism for the interaction of the plasma with the 3-cm power is not understood at this point. However, it is apparent that the nature of the interaction depends on electron energy, since at low energies the enhanced loss of electrons is dominant. There must also be heating, at least at high energies, since the density above 1-MeV energy is actually higher than before the application of 3-cm power. In a relativistic plasma the cyclotron resonance is energy dependent. This suggests that the difference in the behavior of the high and low energy electrons might be due to the fact that the 3-cm microwaves are below resonance for low energy electrons and above resonance for electrons above about 700 keV. This is consistent with the observation that the addition of 5-mm power to the plasma results in a general heating of the plasma. In this case the 5-mm power is above resonance for all the electrons.

### 4.3.5 Spatial Diffusion

A probe was built that could be inserted radially and then be rapidly extracted a distance of ~1 cm in ~10 msec. The x-ray signal from this probe was measured by a collimated NaI crystal and phototube detector. The probe could be moved some milliseconds before the 3-cm microwave power was pulsed on. The time of the x-ray signal peak was measured while the probe was first held stationary during the microwave pulse and then moved just prior to the microwave pulse. The delay in occurrence of this peak after the probe was withdrawn indicated the radial diffusion velocity of the plasma electrons to the probe. Figure 4.10 shows the time dependence of the x-ray signals. The average measured values of the diffusion velocity were from 4 to 8 cm/sec. When the probe was moved but the

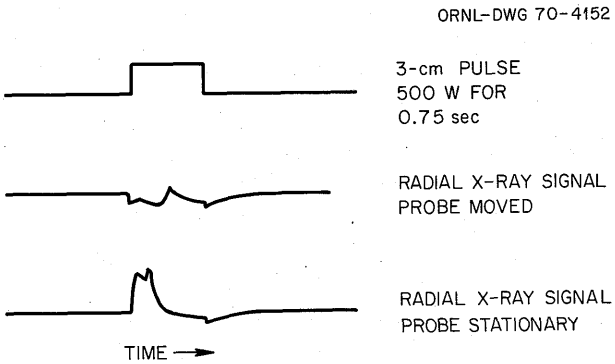


**Fig. 4.10. Time Dependence of Radial X-Ray Signal With and Without Radial Probe Motion.**

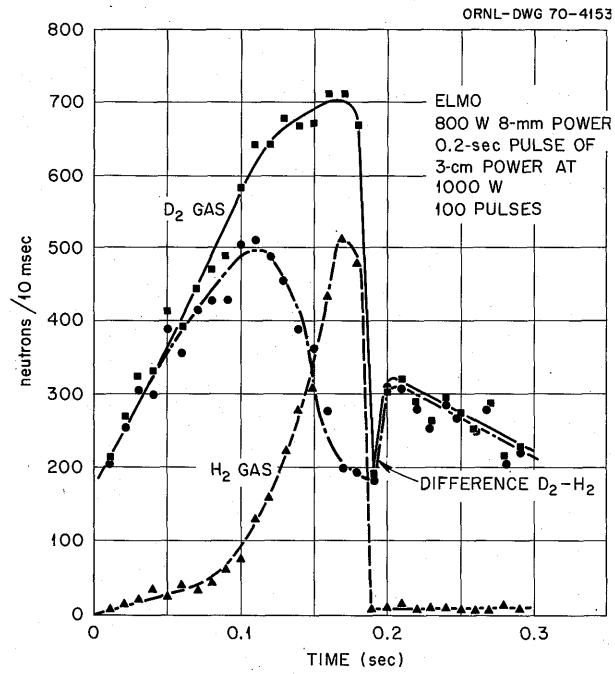


**Fig. 4.11. Neutrons as a Function of Time with 3-cm Power. A sum over 100 3-cm power pulses has been made to improve statistics. The 3-cm pulse period is 3 sec.**

microwave power not pulsed, the x-ray signal dropped and then rose exponentially to a new equilibrium level. The *e*-folding time for this rise associated with the ~1-cm probe motion indicated a normal radial diffusion velocity of ~4 cm/sec. We would conclude from this that the radial diffusion velocity might be increased by as much as a factor of 2 by the 3-cm microwave power, but was not increased by an order of magnitude. In the long time limit, the spatial perpendicular diffusion coefficient[6] is given by $\langle r^2 \rangle = 4D_\perp t$. Taking $t$ as the *e*-folding time and $\sqrt{\langle r^2 \rangle}$ as the distance the probe moved, we find $D_\perp \cong 1$ cm$^2$/sec for the nondriven perpendicular motion and $D_\perp \cong 2$ cm$^2$/sec for the driven loss. Since the value of $D_\perp$ is not affected strongly by the 3-cm power, our assumption of $B_\perp$ being the dominant process may be reasonable.

### 4.3.6 Neutrons

The neutron burst resulting from the 3-cm power pulses was analyzed by a pulse-height analyzer in the time mode. In order to accumulate a sufficiently high count for good statistics, a large number of pulses (~100) were used to trigger the time mode. The neutrons were counted in 10-msec channel intervals. Figure 4.11 shows one of the counts made by operating with $D_2$ gas and then subsequently operating with $H_2$ gas after a long baking process to remove the wall-embedded $D_2$. The $D_2$-$H_2$ difference curve should accurately represent the $D_2$ gas effect alone, since all other parameters have been held constant.

With the $D_2$ gas, a prompt buildup of the neutron count is observed with a buildup time of ~80 msec. With $H_2$ gas, this prompt buildup is missing, but a later peak occurs after an apparent delay of ~80 msec and a buildup time of ~50 msec. A series of runs has shown that these buildup and delay times are all roughly proportional to $P_3^{-1}$, in qualitative agreement with Grawe's heating theory.[3] However, because of the difficulty in averaging over the electron energy distribution and the neutron production cross sections, no quantitative agreement can be calculated.

The neutrons with $H_2$ gas can only be accounted for by wall processes, and the most reasonable explanation is $(\gamma,n)$ processes on copper. These require photon energies of $\gtrsim$10 MeV and imply either a selective loss of particles above this energy by the 3-cm radiation or a heating of particles to these energies by the 3-cm radiation. The long delay is indicative of a long heating time needed for electrons to gain many MeV. It would appear that some heating is occurring, since the buildup of the neutron count rate in the $D_2$-$H_2$ difference curve can best be accounted for by an increase in electrons over 2.22 MeV rather than an increase in cold plasma ions. As mentioned earlier, cold plasma current to probes does not change during a 3-cm pulse. Also, there is a tail on the neutron pulse after the 3-cm power pulse ends, implying that some electrons have been heated and are relaxing back to an equilibrium. The decay time of this tail is ~100 msec, which is too long to be

accounted for by a gas equilibrium time alone. The sharp discontinuity in the count rate at the end of the microwave pulse may be due to a gas burst from the walls but is not well understood.

The $H_2$ gas neutron count rate is reduced by a factor of ~3 when a radial probe is inserted by about 1 in. If there is an acceleration process occurring, this would mean that it is near the wall, and it is disturbed by a radially inserted obstruction. Copper probes show an approximately 10-min positron half-life after operation, indicating that some energetic (>10 MeV) electrons are striking the probe and producing $^{62}$Cu activity. This activity is not seen in the absence of 3-cm power. When operating with $D_2$ gas, boron-coated probes show no 20-min activity. A positive indication would imply *(d,n)* processes with deuteron energies of tens to hundreds of keV.[7] Hence there is no evidence for the creation of a large space charge or resonant rf fields by this process.

### 4.3.7 Calorimetric Measurements

Calorimetric probes were constructed to measure the energy content of the plasma striking them. One probe was inserted radially into the cavity. The probe was equipped with a copper tip of sufficient radial extent to intercept almost all of the large orbit particles lost radially during a burst. The sensitive element was a thermistor whose resistance change indicated the temperature rise of the copper tip and hence the energy input. A long time constant thermal leak to the demineralized water system provided an equilibrium temperature. The probe was calibrated with a resistor thermally connected to the front surface. A correction was made for both the increased thermal capacity of the resistor and for the long thermal transmission time from the resistor to the thermistor.

For a given input of 3-cm power (pulsed in 1-sec bursts for convenience), Fig. 4.12 shows that the total amount of energy deposited on the probe amounted to ~10% of the stored energy measured diamagnetically. There was no apparent absorption of the 3-cm energy by those plasma electrons which struck the radial probe. Although up to 3 kJ of 3-cm energy was injected, only a fraction of the plasma energy already present was deposited on the probe.

Normal (nondriven) flutelike instabilities were also measured with this probe. As shown in Fig. 4.12, about half of the energy lost (as measured by the diamagnetic drop) appeared on the radial probe. This energy loss was always higher than that obtained by the 3-cm power pulse.

Figure 4.13 shows the amount of energy deposited on the probe as a function of 3-cm power. It is clear that there is a saturation value independent of the input 3-cm energy. The amount of energy appears to increase monotonically (perhaps linearly) with 3-cm power up to a value near this saturation value.

[7] J. B. Marion *et al.*, *Phys. Rev.* **100**, 847 (1955).

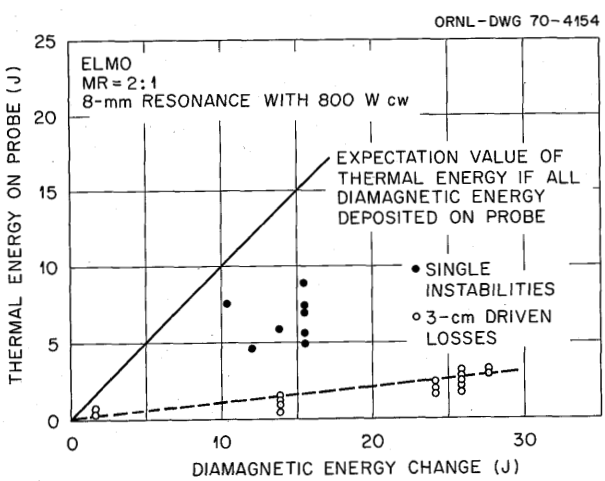


**Fig. 4.12. Thermally Measured Joules on a Radial Probe vs Diamagnetically Measured Joules Stored in Machine.**

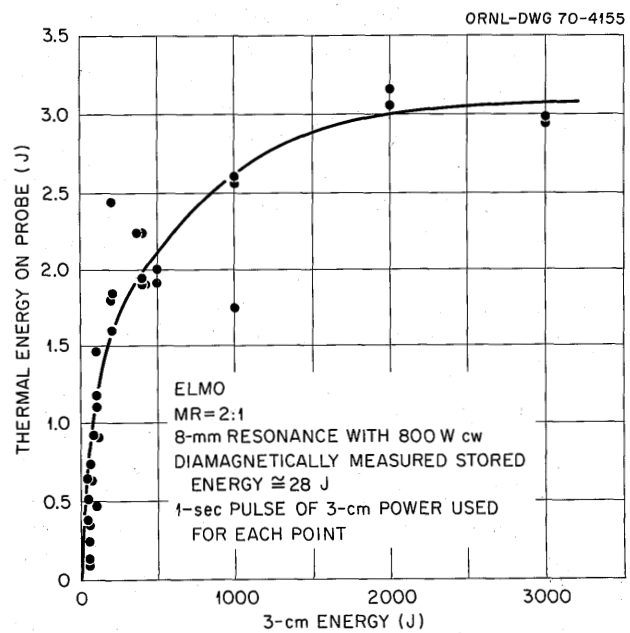


**Fig. 4.13. Thermally Measured Joules on a Radial Probe vs 3-cm Energy in Microwave Pulse Injected in Machine.**

Corresponding measurements made on the axial losses show some 3-cm energy absorption by the axially lost particles. An off-axis probe so situated as to intercept particles lost from the annular region showed the larger energy input. When averaged over the annular region where the plasma energy should be dumped, more energy was inferred than had been stored in the annulus (as determined from the diamagnetic measurements). A probe on the axis showed very little energy input, in agreement with our knowledge that the energetic plasma is annular. The probes were not movable and could not be used to map the radial distribution of the axially lost energy, so that a full energy balance could not be made. Reasonable estimates, however, give a maximum 3-cm energy absorption by the axially lost electrons of ~60% and a minimum absorption of ~3%.

All measurements are averaged over the pulse length (1 sec) and hence do not see the temporal behavior. It is possible that the energy absorption with time can reach very high values during the initial period of rapid energy loss and later drop to very low values.

These data have given further evidence that the main plasma loss is not radial spatial diffusion.

## 4.4 INSTABILITY STUDIES

### 4.4.1 Near Gyrofrequency Instability

A characteristic instability is seen that gives bursts of radiation in a band of several hundred megahertz width which always lies in the range between 5.5 and 8 GHz. The instability frequency varies with the cold plasma density and can be stabilized by the addition of a small amount of off-resonant ($\omega > \omega_{ce}$) heating. There are two major candidates: double distribution instability modes[8] and anisotropy-driven half-harmonic electron gyrofrequency instabilities.[9] The former gives frequencies above the gyrofrequency for that component of the plasma undergoing the instability, while the latter gives frequencies lower than the gyrofrequency. One difficulty lies in determining the gyrofrequency of the relativistic electrons undergoing the instability, and another lies in the indeterminancy of the measured frequencies (band spectra are observed, since the plasma samples an inhomogeneous magnetic field). The instability suppression might be the result of the separation of the energy peaks in the case of the double distribution modes, or it might be the result of a decrease in the anisotropy in the case of the unstable Timofeev modes. Detailed investigations of these modes are under way.

### 4.4.2 Mirror Instability

The mirror instability has previously been experimentally identified in a moderate-$\beta$ hot electron plasma.[10] This instability has been the subject of numerous theoretical studies.

In the theoretical description of this instability, an anisotropic plasma in a magnetic mirror field undergoes a collapse toward the midplane. This occurs when the plasma pressure and anisotropy are sufficient to make $\beta(T_\perp/T_\parallel) > 1$. In some theories the threshold criterion is even more anisotropic.

In the one-frequency ECH plasmas, the energetic component tends to be confined between the surfaces at which cold electron resonance occurs. Hence

$$\left(\frac{T_\perp}{T_\parallel}\right)_0 \cong \frac{1}{R_\mu - 1},$$

where $R_\mu$ is the mirror ratio at the resonant surface. In the past, stability has only been observed for $R_\mu > 1.2$. When off-resonant heating is used to suppress the microinstability mentioned in Sect. 4.4.1, it is possible to stably heat near the midplane. In this heating configuration, electrons gain energy at a much higher rate, and consequently a larger fraction of the cold throughput is trapped. These cases have exhibited the highest values of $\beta$ yet measured without being limited by the mirror instability. A reasonable conjecture is that the enhanced stability results from the modification of the vacuum mirror field by the plasma field. The effective mirror ratio becomes, then,

$$R_\mu \cong R_{\mu_0}/\sqrt{1-\beta}\,.$$

If we combine this with the stability criterion and the anisotropic heating criterion, we obtain, for stability,

$$R_{\mu_0} \geqslant (\beta + 1)\sqrt{1-\beta}\,.$$

The stability boundary determined by $R_{\mu_0}$ and the critical $\beta$, $\beta_c$, is shown in Fig. 4.14. Note that at high values of $\beta_c$ a stable condition with $R_{\mu_0} < 1$ is possible.

We have not yet determined if the experimental stability boundary agrees with this analysis, so this

[8] L. S. Hall *et al.*, *Phys. Rev.* **139**, A1117 (1965).

[9] A. V. Timofeev, *Soviet Phys. JETP* **12**, 281(1961).

[10] H. P. Furth, *Phys. Fluids* **6**, 48 (1963); W. B. Ard *et al.*, *Phys. Fluids* **9**, 1498 (1966).

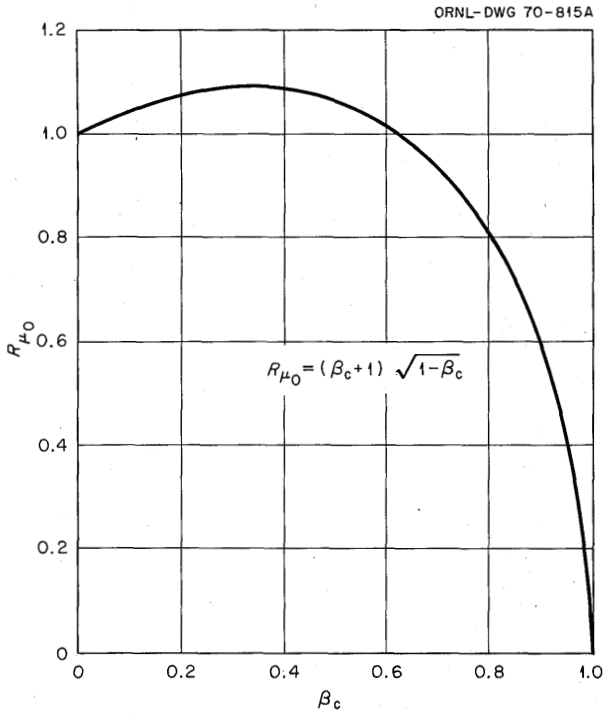


**Fig. 4.14. Mirror Ratio as a Function of the Critical $\beta$ for Finite-$\beta$ Stabilization.**

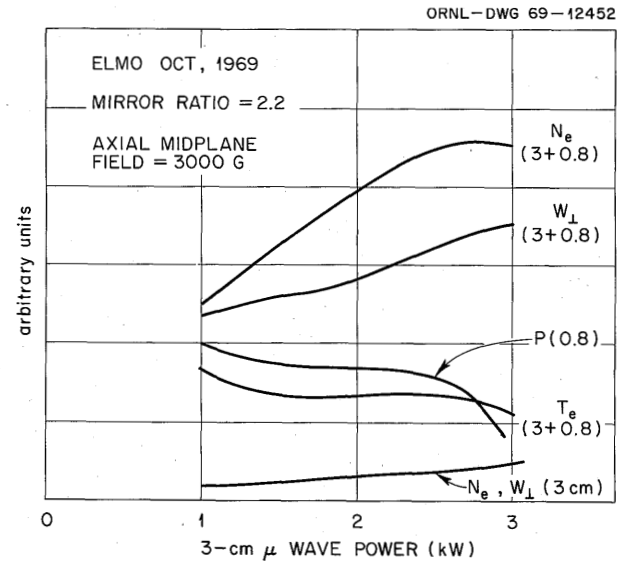


**Fig. 4.15. Dependence of Various Plasma Parameters on the Amount of Cold Plasma as Determined by the Resonant 3-cm Microwaves.** The amount of 8-mm power shown is that required for finite-$\beta$ stabilization. The bottom curve applies for no 8-mm off-resonant heating.

formulation must be regarded as conjectural. However, we have some concrete evidence of the control of the mirror instability through finite $\beta$ effects.

Figure 4.15 shows the stabilizing effect of finite $\beta$ achieved through off-resonant heating. The lower curve shows the electron density, $n_e$, or the stored energy, $W_\perp$, as a function of 3-cm power alone. All the upper curves indicate various parameters as resulting from the addition of 8-mm off-resonant power. The 8-mm power level is also shown as it varies with 3-cm power. The amount of 8-mm power is that required to control the instability at each 3-cm power level. Note that the stored energy, $W_\perp$, and density, $n_e$, are increased more than a factor of 10 over the level achieved with 3-cm heating. The temperature shows little change during the run, indicating that the change in stored energy is almost entirely due to an electron density increase.

### 4.4.3 Flute Modes

A third instability has a low frequency, ~11 to 12 MHz, and is controllable by cold plasma. The most logical choice at present is the ordinary magnetohydrodynamic flute. The amount of cold plasma required for stabilization is much larger (a factor of $\sim 10^3$) than that required by considerations of line tying.[11] It appears that other considerations such as particle balance and control of the space potential by cold plasma play a major role.

## 4.5 ION HYBRID HEATING

Two techniques will be explored for heating the cold ions of the electron-cyclotron plasma ELMO at the hybrid frequency. The first method is to inject an electron beam axially down the field lines of the device and to modulate the beam at the hybrid frequency. Various interaction mechanisms have been suggested for dissipating the energy into the ions. One possibility is that the radial oscillating electric field will launch an ion acoustic wave which will propagate out until the density falls to where the ion hybrid frequency equals the modulating frequency; at this radius the ion wave is heavily damped and the energy is transferred to the ions. A schematic of the electron gun system is shown in Fig. 4.16. Presently a beam of 500 mA at 2.5 kV is available; this can be modulated at frequencies up to 200 MHz.

[11] G. E. Guest and C. O. Beasley, *Phys. Fluids* 9, 1798 (1966).

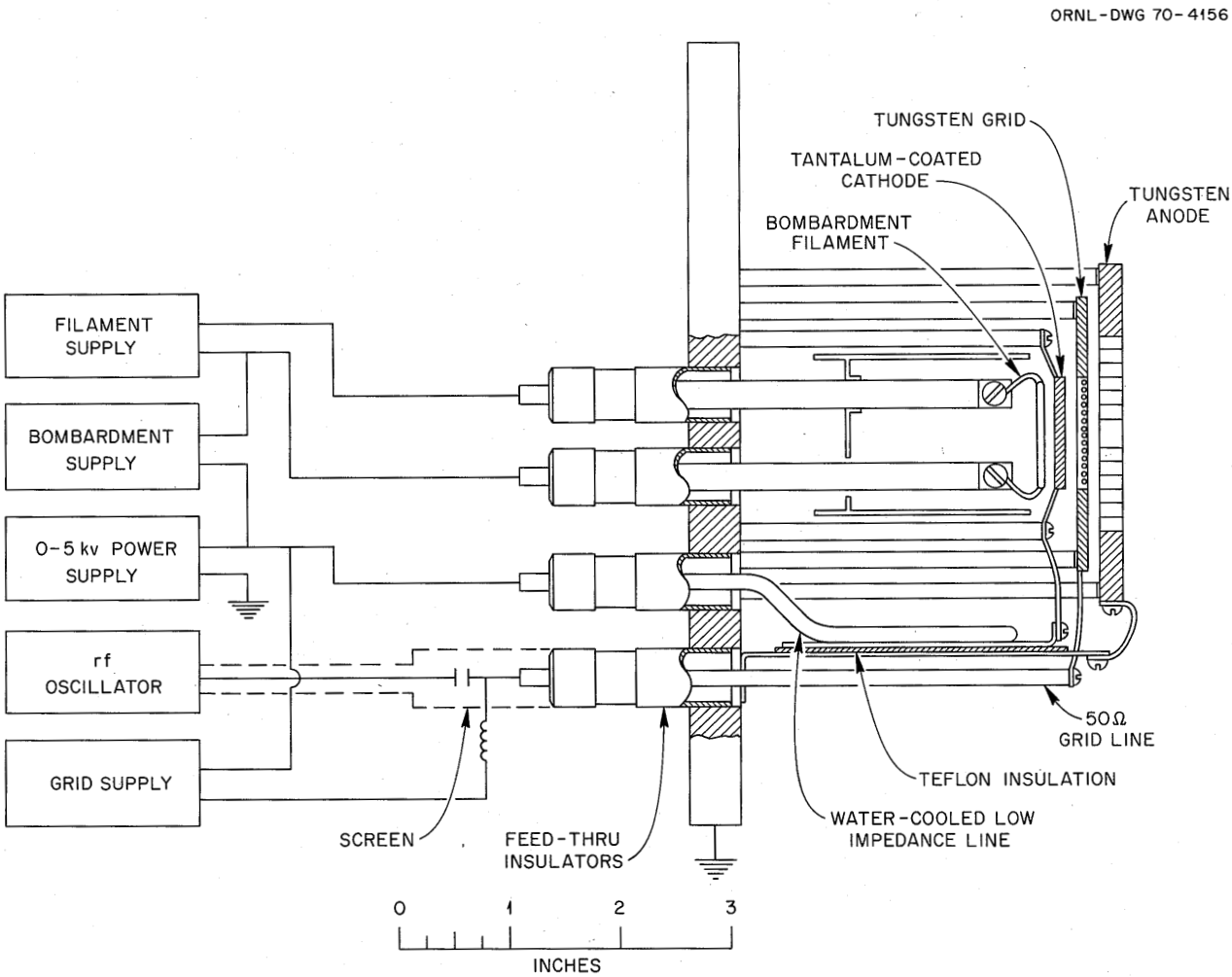


**Fig. 4.16. Schematic of the Modulated Electron Gun.**

The second approach under study is to construct a resonant cavity for the ion hybrid frequency, using the plasma surface as one cavity wall. Then, as rf power in the relevant range is readily available, even very inefficient coupling into the plasma becomes acceptable. The configuration of the experiment is shown in Fig. 4.17. The coupling system allows separate adjustment of both the resonant frequency and of the degree of coupling into the cavity. The maximum power on hand is 1 kW over the range 400 to 1000 MHz, with the possibility of operating at lower frequencies with reduced power.

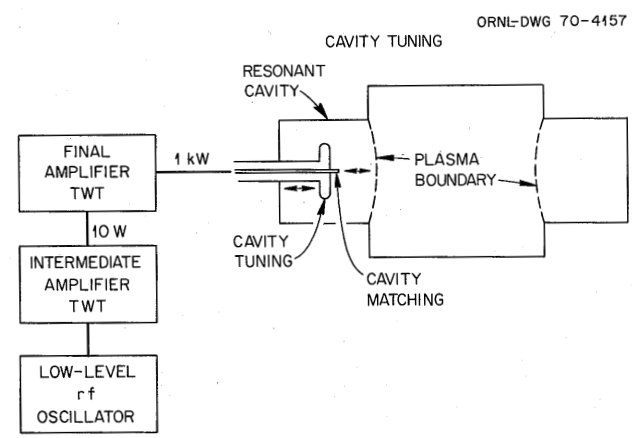


**Fig. 4.17. Experimental Configuration for the RF Heating Experiment.**

## 4.6 SUMMARY

Heating studies have shown that large increases in stored plasma energy are produced by high-frequency

($\omega > \omega_{ce}$) microwave power. This is in sharp contrast to the effect of low-frequency ($\omega < \omega_{ce}$) power, which reduces the stored plasma energy.

The high-frequency effect is attributed to off-resonant stochastic heating and control of instabilities through changes in the electron distribution function. One explanation for the low-frequency effects is that relativistic electrons are resonant with the 3-cm power at low field regions in the cavity. The higher the electron energy, the higher the field at which resonance occurs, since the field at resonance for a relativistic particle is equal to $\gamma B_{\text{resonance}}$, where

$$\gamma = \frac{1}{\sqrt{1 - v^2/c^2}}.$$

With high-frequency off-resonant power, energy is absorbed by the electrons. With low-frequency off-resonant power, some energy is absorbed by a few electrons, but the main effect appears to be enhanced diffusion in velocity space into the loss cone.

# 5. Turbulent Heating

## 5.1 THEORETICAL MODELS

### 5.1.1 Introduction

I. Alexeff R. V. Neidigh

One electron-heating model and six ion-heating models are presented here in an attempt to understand heating mechanisms. Each is unique in detail, but most have a similar dependence on magnetic field, namely, that $\omega_{ce} < \omega_{pe}$ for electron heating and that $\omega_{ce} > \omega_{pe}$ for ion heating. Turbulent heating of the sort found in our experiments must certainly be complicated and must involve more than one or possibly all of these models. For clarity, however, each is discussed in turn.

### 5.1.2 Limitations on Beam-Plasma Heating of Electrons and Ions

I. Alexeff

During the period over which beam-plasma interactions have been studied, some striking limitations have been observed. First, electron heating does not occur for high plasma densities ($n_e > 10^{11}$ cm$^{-3}$) or high magnetic fields; second, ion heating takes place only at high plasma densities such that $\omega_{ce} > \omega_{pe} > \omega_{pi} > \omega_{ci}$; third, ion and electron heating seem to be mutually exclusive in a given machine. A consistent but not yet completely clear picture of where the above-mentioned limitations originate is now evolving.

Consider the first point, the failure to produce a hot-electron plasma at high electron densities or high magnetic fields. This limitation prevented us from reaching high hot-electron densities in our small mirror machines, prevented Will Stirling[1] from reaching interesting densities in his hot-electron blanket machine, and resulted in the electrons in Burnout V being relatively cool. The reason for the limitation now seems to be simple. We assume, as both theory and experiment suggest, that electron heating is caused by the incident electron beam producing intense plasma electron oscillations at $\omega_{pe}$. If the electron cyclotron frequency, $\omega_{ce}$, is of the same order of magnitude as $\omega_{pe}$, the electron plasma oscillations heat the electrons by electron cyclotron resonance. (The equations also predict a lower heating rate for higher $B$.) Thus $\omega_{ce} \approx \omega_{pe}$, and consequently electron heating at high plasma densities is equivalent to heating at high magnetic fields.

Given the above model, the limitations on heating both at high plasma densities and at high magnetic fields are easily understood. Consider the $e$-folding distance $x_0$ in which the growth of plasma electron oscillations occurs along an electron beam. We find

$$x_0 = \frac{1}{k_i} \approx \frac{v_{\text{beam}}}{\omega_{pe}},$$

where $k_i$ is the imaginary part of the wave number, $v_{\text{beam}}$ is the velocity of the incident electron beam, and $\omega_{pe}$ is the angular plasma electron frequency [$\approx 6 \times 10^4 (n_e)^{1/2}$]. At 30 keV, $v_{\text{beam}} \approx 10^{10}$ cm/sec, and for $10^{11}$ electrons/cm$^3$ ($\omega_{pe} \approx 2 \times 10^{10}$), we see that $x_0$, the $e$-folding distance for plasma oscillation growth, is about 0.5 cm. Thus, to bring the plasma oscillations up from noise to levels capable of stopping the beam and providing intense electron heating in the middle of our small mirror machines requires perhaps ten $e$-folding distances (1/3 V noise to 30 kV rf), which corresponds approximately to 5 cm (from the electron gun to the midplane of the machine). This value is consistent with the size of our small machines. Also, we note that in our small machines the rf in the midplane has ceased to grow – the fluctuating voltage is on the order of the beam voltage, and also no growth is observed by axial probe correlation studies.

In the case of higher plasma densities or, equivalently, higher magnetic fields, the heating limitation probably occurs because at higher $\omega_{pe}$ the $e$-folding growth

[1] W. L. Stirling and I. Alexeff, *A Turbulently Heated Electron Plasma*, ORNL-TM-2631 (1969) (to be published in *Plasma Physics*).

distance becomes very short. In Burnout V, this distance is about 0.5 mm. Thus the oscillations are produced in the electron gun, outside the mirrors, where electron cyclotron resonance cannot result in trapped hot electrons. Instead we get arcing in the gun, a quite reasonable result.

By reducing the magnetic field in the gun region with the aid of a local bucking magnetic field, Will Stirling[1] was able to heat electrons in a machine with higher overall field. This result presumably means that both $\omega_{ce}$ and $\omega_{pe}$ were reduced and that the growth distance for waves in the gun region became large enough so that breakdown was avoided. The heating rate is also increased since $B$ is reduced.

This short growth distance for the instability can possibly be overcome by increasing the beam voltage. We could increase v to $\approx c$, giving it three times the growth distance for a given plasma density and simultaneously increasing the number of $e$-folding distances necessary to provide disruption of the beam. Alternatively, we can use a different electron-gun design placed between the mirrors. In any case, the electron density limitation in electron heating probably can be overcome.

The third possibility, pointed out to us by S. J. Buchsbaum and L. C. Hebel[2] and calculated out by Owen Eldridge[3] and Akira Hirose,[4] is to use a relativistic electron beam. The growth distance increases as $\gamma^{3/2}$, where $\gamma = [1 - (v/c)^2]^{-1/2}$. Thus, as the electron beam's velocity approaches the velocity of light, the growth distance becomes infinite. As a consequence, we can probably do beam-plasma heating at arbitrarily high plasma densities and magnetic fields by using relativistic electron beams.

One interesting problem for electron plasma heating that was discussed before, and was recently brought out by Alan Ware,[5] is that a low-frequency instability must be present in the electron-heating case. The electron heating has a PIG configuration, and we find that the observed rf fields near $10^9$ Hz, if nonresonant, are completely inadequate to account for the radial current flow to the anodes. One requires an azimuthal **E** field comparable with that supplied radially by the power supply across the anode gap. The **E** field must be almost dc and perhaps is an azimuthal instability that rotates with the electrons. This low-frequency instability has been studied further (see Sect. 5.1.3).

[2] S. J. Buchsbaum and L. C. Hebel, private communication.

[3] O. Eldridge, private communication.

[4] A. Hirose, private communication.

[5] A. Ware, private communication.

We know that the beam-plasma interaction cannot produce hot electrons in the midplane of the Burnout V in-heating apparatus, since the electron density is too high, and we find that none are observed. We find as a consequence of having cold electrons that the **E** fields of what appear to be the ion-heating modes near $\omega_{pi}$ are perpendicular to **B**. Assuming that **E** is perpendicular to **B** and that $\omega_{pe}$ is less than $\omega_{ce}$, we can predict that one fundamental mode of oscillation of the plasma is at $\omega_{pi}$, which is the dominant frequency that is observed. Finally, if we assume azimuthally streaming overlapping ion beams of different velocities (presumably driven by radial $E$ fields), one finds the rate of growth of this instability to increase as $\omega_{pi}$.

Thus, to have ions heated at $\omega_{pi}$ requires first, that $\omega_{pe} < \omega_{ce}$ [the inverse inequality produces oscillations at $\sqrt{\omega_{ce}\omega_{ci}}$ (also the order of growth rate) and, we suspect, loss of confinement] and second, a high value of $\omega_{pi}$ to get a rapid rate of growth.

These two conditions are not compatible with electron heating – the first results in no transfer of rf energy from plasma electron oscillations to electron cyclotron rotation, and the second results in plasma electron oscillations being restricted to the region of the electron gun. This incompatibility of electron heating with ion heating agrees with our experimental observations.

To summarize, we think that electron heating is due to a beam-plasma interaction along **B**; the ion heating is due to an ion-plasma oscillation driven by current across **B**. Our experiments seem to support the above models.

### 5.1.3 Turbulent Heating Mechanisms

I. Alexeff

In a survey report[6] we suggested the idea that ion heating in Burnout V is due to a radial electric field. This excites electrostatic waves traveling perpendicular to the magnetic field, causing intense heating at frequencies near $\omega_{pi}$. These conclusions are derived from experimental results.

In this section, we derive a dispersion relation that predicts an instability conforming to the experimentally derived model above. We first show that in any device in which the electric field is perpendicular to the magnetic field and which possesses cylindrical symmetry, the electrons drift azimuthally with a different

[6] I. Alexeff, *A Survey of Recent Results from the Turbulent Heating Group at ORNL,* Plasma Studies Tech. Memo No. 40, Oct. 21, 1969.

average velocity than the ions do. We then demonstrate, under certain assumed approximations, that the relative streaming energy of electrons and ions is converted into oscillations near $\omega_{pi}$ by means of a magnetron-type instability. (Increasing the radial $E$ field on the electrons increases their rate of precession and reduces their local density.)

*Relative motion of electrons and ions.* Let $v_D$ be the drift velocity of a particle (small orbital motion averages out). The equation of motion is

$$eE = \frac{e}{c} v_D B + m v_D^2 / r .$$

Thus, in cylindrical geometry, the precessional velocity depends on the mass. In Burnout V, the precessional velocities of ions and electrons can differ by a factor of 2.

*The instability calculation.* We make the following assumptions:

1. The cylindrical system is approximated by a slab geometry.
2. The ions are assumed to oscillate radially and freely across magnetic field lines ($\omega > \omega_{ci}$).
3. Electrons stream with a velocity $v_D = CE/B$ across field lines in a direction perpendicular to the ion motion. (We ignore in this approximation electron motion parallel to $E$; it will appear in a later version and is important.)

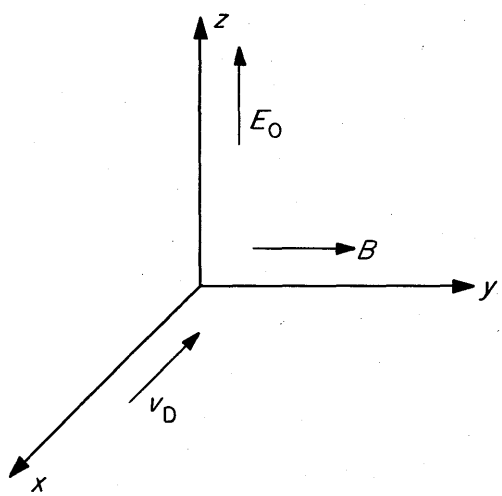


We get five linearized equations of motion. Subscripts 0 and 1 indicate unperturbed and perturbation terms respectively.

Ion momentum conservation:

$$\frac{\partial v_{1i}}{\partial t} = \frac{e}{m_i} E_1 . \tag{1}$$

Ion particle conservation:

$$\frac{\partial n_{1i}}{\partial t} + n_{0i} \frac{\partial v_{1i}}{\partial t} = 0 . \tag{2}$$

Electron momentum conservation as modified by the electric and magnetic fields:

$$-v_{1D} = \frac{C}{B} E_1 . \tag{3}$$

Electron particle conservation:

$$n_{1e} v_{0D} + n_{0e} v_{1D} = 0 . \tag{4}$$

Poisson's equation:

$$\frac{\partial E_1}{\partial z} = 4\pi e (n_{1i} - n_{1e}) . \tag{5}$$

Next, we assume a solution of the form $e^{i(kz - \omega t)}$. The equations now appear as follows:

$$-i\omega v_{1i} = \frac{e}{m_i} E_1 , \tag{1a}$$

$$-i\omega n_{1i} + ik v_{1i} n_{0i} = 0 , \tag{2a}$$

$$-v_{1D} = \frac{C}{B} E_1 , \tag{3a}$$

$$n_{1e} = -\frac{n_{0e}}{v_{0D}} v_{1D} , \tag{4a}$$

$$ikE_1 = 4\pi e (n_{1i} - n_{1e}) . \tag{5a}$$

Equations (1*a*) and (2*a*) give

$$n_{1i} = \frac{iekn_{0i}E_1}{m_i \omega^2} . \tag{1b}$$

Equations (3*a*) and (4*a*) give

$$n_{1e} = +\frac{n_{0e}}{v_{0D}} \frac{C}{B} E_1 . \tag{2b}$$

Place (1*b*) and (2*b*) into (5*a*) to get

$$ikE_1 = ikE_1 \frac{4\pi n_{0i} e^2}{m_i} \frac{1}{\omega^2} - \frac{4\pi n_{0e} e}{v_{0D}} \frac{C}{B} E_1 . \tag{3b}$$

The second term can be rewritten as

$$-\frac{ik}{ik}\frac{4\pi n_{0e}e^2}{m_e}\frac{Cm_e}{eB}\frac{E_1}{v_{0D}}.$$

We thus get

$$ikE_1 = ikE_1\frac{\omega_{pi}^2}{\omega^2} - \frac{ik_1}{ik_1}\frac{\omega_{pe}^2}{\omega_{ce}}\frac{E_1}{v_{0D}}.$$

Factor out $ikE_1$ to get our dispersion relation

$$1 = \frac{\omega_{pi}^2}{\omega^2} - \frac{1}{ik}\frac{\omega_{pe}^2}{\omega_{ce}}\frac{1}{v_{0D}}. \tag{5a}$$

Note that the factor $i$ means that either $k$ or $\omega$ is always complex – the system is always unstable.

Solve for $k$ to find a resonance at $\omega \approx \omega_{pi}$:

$$k = \frac{+i\omega_{pe}^2/\omega_{ce}v_{0D}}{1-(\omega_{pi}^2/\omega^2)}. \tag{6a}$$

If we solve for real $k$ and complex $\omega$, we also find a resonance at $\omega \approx \omega_{pi}$. Thus we also theoretically predict the major frequency that appears experimentally. A more complete analysis is being written.

### 5.1.4 Electron and Ion Heating in Beam-Created Plasmas

I. Alexeff A. Hirose

In this section we clarify heating mechanisms of electrons and ions in plasmas created by an electron beam. As summarized in Sect. 5.1.2, there exist several severe experimental limitations for effective heating to occur. For example, (1) electron heating does not occur for high plasma densities or high magnetic fields; (2) the maximum plasma density so far achieved is on the order of $10^{11}$ cm$^{-3}$, and the magnetic field is a few kilogauss; (3) in Burnout V, the electron cyclotron frequency must be commensurate with or higher than the electron plasma frequency for ion heating to occur; and (4) the electrons in Burnout V remain relatively cool (a few electron volts).

We wish to explain the above limitations in terms of electrostatic instabilities produced by beam-plasma interactions. Heating rates for electrons and ions are derived and qualitatively compared with experimental results.

**5.1.4.1 Electron Heating.** – We conjecture that electrons absorb energy from electric fields created by beam-plasma interactions through cyclotron resonance as suggested by Alexeff *et al.*[7] and Stix.[8] For effective absorption to occur, we must have

$$\omega_{pe} \cong \omega_{ce}, \tag{7}$$

since the fastest growth occurs at $\omega_{pe}$.

The intensity of the electric field associated with the beam-plasma two-stream instability should be limited at some maximum value because of the hydrodynamic nature of the instability. We have shown that the saturated electric field $E$ is given by

$$\frac{E^2}{8\pi} \cong mu^2 n_b\left(\frac{n_b}{n_p}\right)^{1/3}, \tag{8}$$

where $m$ is the electron mass, $u$ is the beam velocity, $n_b$ is the beam electron density, and $n_p$ is the plasma electron density. The above equation already shows an interesting limitation: The plasma density must be relatively low for the turbulence to be strong. Also, Eq. (8) estimates the highest plasma electron temperature available through nonlinear hydrodynamic heating. For a plasma with $n_p = 10^{11}$ cm$^{-3}$ and an electron beam with $mu^2 = 10$ keV and $n_b = 10^8$ cm$^{-3}$, the electron temperature is on the order of 1 eV. Thus, it is not possible to explain the $T_e \cong 100$ keV experimentally observed in terms of a hydrodynamic heating process.

Below, we show the results of the calculation for heating rate made under the assumption that electrons absorb energy from the saturated electric field through cyclotron resonance. The energy absorption rate is given by

$$\frac{d\epsilon_\perp}{dt} = \frac{E^2}{2}\,[R_e(\sigma)]_{\omega=\omega_{ce}}, \tag{9}$$

where $R_e(\sigma)$ is the real part of the conductivity, which can be approximately given by

$$\frac{1}{16\sqrt{\pi}}\frac{\omega_{pe}^2 k_\perp^2}{k_\parallel^3\beta_e}, \tag{10}$$

where $\omega_{pe}$ is the electron plasma frequency, $k_\parallel$ and $k_\perp$ are, respectively, wave numbers parallel and perpendicular to the magnetic field, $\beta_e$ is the electron thermal velocity, and $\omega_{ce}$ is the electron cyclotron frequency.

From Eqs. (8) and (10) we obtain

$$\frac{dT_e}{dt} = \frac{\sqrt{\pi}}{4}mu^2\left(\frac{n_b}{n_p}\right)^{1/3}\frac{\omega_{pb}^2 k_\perp^2}{\beta_e k_\parallel^3}, \tag{11}$$

[7] I. Alexeff *et al.*, *Phys. Rev. Letters* **10**, 273 (1963).

[8] T. H. Stix, *Phys. Fluids* **7**, 1960 (1964).

where $\omega_{pb}$ is the plasma frequency of the beam electrons. Thus, the scaling law for the energy density $n_p T_e$ becomes

$$n_p T_e \propto (mu^2)^{5/2} .$$

The exponent $5/2$ agrees well with the experimental results reported by Plakhov *et al.*[9] We also observe that the heating rate decreases as the magnetic field increases, since we must have the condition given by Eq. (7). However, comparison with experimental results might be difficult since the lifetime of the electrons could strongly depend on magnetic fields.

**5.1.4.2 Ion Heating.** – A strong radial (perpendicular to an external magnetic field) electric field characterizes the Burnout V machine. This immediately leads us to the conjecture that ion motion perpendicular to the magnetic field is responsible for the rapid ion heating ($T_i$ is a few kilo-electron volts and the lifetime is 40 $\mu$sec) observed in the machine.

It has been shown[10] that the characteristic frequency of the ion motion perpendicular to a magnetic field is given by

$$\omega = \begin{cases} \sqrt{\omega_{ce}\omega_{ci}} & (\omega_{pe} \cong \omega_{pe}) \\ \omega_{pi} & (\omega_{ce} \gg \omega_{pe}) \end{cases} ,$$

and the growth rate of the instability driven by currents perpendicular to the magnetic field can be of the same order as the frequency. In fact, a strong oscillation has been observed in Burnout V with confirmation that the oscillation is associated with electric fields perpendicular to the magnetic field.[11] The observed frequency is close to the ion plasma frequency.

The ion heating rate was estimated in a similar manner to Eq. (11):

$$\frac{dT_i}{dt} = mu^2 \left(\frac{n_b}{n_p}\right)^{4/3} \left(\frac{k_\perp}{k_\parallel}\right)^2 \times \begin{cases} \sqrt{\omega_{ce}\omega_{ci}} & (\omega_{ce} \cong \omega_{pe}) \\ \omega_{pi} & (\omega_{ce} \gg \omega_{pe}) \end{cases}$$

$$\propto \begin{cases} BW_B^{10/3} & (\omega_{ce} \sim \omega_{pe}) \\ W_B^{10/3} & (\omega_{ce} \gg \omega_{pe}) \end{cases} , \qquad (12)$$

where $B$ is the magnetic field and $W_B$ is the beam energy. The experimentally observed scaling law[12] is

$$T_i \propto W_B^{3.0} ,$$

in agreement with the above estimate. Again, the ion lifetime could strongly depend on the magnetic field, which would prevent us from obtaining the magnetic field dependence of the ion temperature. However, in a series of Burnout experiments, it has been established qualitatively that higher ion temperatures can be achieved at higher magnetic fields.

### 5.1.5 Limitations of the Beam-Plasma Facility Hot-Electron Plasma

W. L. Stirling V. J. Meece

The beam-plasma facility (BPF) generated a hot-electron plasma that reached an apparent density limit of a few times $10^{11}$ cm$^{-3}$ at $T_e \approx 2$ keV. By reducing the local magnetic field in the anode region it was shown that the overall magnetic field could be increased (by a factor of ~4), but the density of hot electrons produced in the arc column remained constant. Theoretical considerations lead us to believe that two conditions must be satisfied for electron heating: The electron cyclotron frequency $\omega_{ce}$ must be of the same order of magnitude as the electron plasma frequency $\omega_{pe}$,

$$\omega_{ce} \approx \omega_{pe} , \qquad \text{(I)}$$

and the $e$-folding distance for wave growth $x_0$ is such that

$$x_0 \approx \frac{v_b}{\omega_{pe}} , \qquad \text{(II)}$$

where $v_b$ is the velocity of the beam. Thus as $\omega_{ce}$ and $\omega_{pe}$ increase, due to an increase of $B$ or $n_e$, $x_0$ decreases, and the instability may grow to a maximum in a very short distance in the anode or mirror throat. Above some critical $\omega$ the beam energy is dissipated in the anode channel itself, causing a local electrical breakdown of the arc. Such an effect was observed in the BPF when increasing $B$ or $n_e$. By reducing the local magnetic field in the anode, it was possible to produce electron heating with increased $B$ in the midplane. Due to condition I, one would not expect the density to

[9] A. G. Plakhov *et al.*, Plasma Physics and Controlled Nuclear Fusion Research Conf. Proc. – English Translations of the Russian Papers – Novosibirsk, 1–7 August 1968, *Nuclear Fusion*, Special Supplement 1969, IAEA, Vienna, p. 243.

[10] A. Hirose and I. Alexeff, *Ion Beam Instability in Burnout V*, Plasma Studies Tech. Memo. No. 47, Dec. 10, 1969.

[11] I. Alexeff *et al.*, *Proc. 9th Intern. Conf. Phenomena in Ionized Gases*, ed by G. Musa, I. Ghica, A. Popescu, and L. Nastase (Institute of Physics, Academy of the Socialist Republic of Romania, Bucharest, Romania, 1969), p. 575.

[12] R. V. Neidigh, private communication.

increase. Consistent with condition II, increasing the beam energy by a factor of 2 (to 40 keV) had no significant effect on $n_e$.

We have considered the possibility of increasing the plasma density by letting the hot-electron plasma, produced as in the BPF, drift via $\nabla B$ to a region in which the drift is then canceled. (Slanting the mirror coils might be effective.) From rough calculations using Liouville's theorem we estimate an increase by two orders of magnitude. Assuming plasma is lost by scattering into the mirror loss cone, we find that a plasma volume of 5 liters can be filled to a maximum density of $\sim 5 \times 10^{13}$ electrons/cm$^3$.

### 5.1.6 Stochastic Electric Pumping

F. R. Scott[13]

One possible mechanism for ion heating in Burnout V which appears to satisfy most observations is "stochastic electric pumping." By this we mean the impulse transferred to the ions from fluctuating fine-grain regions of high electrostatic energy density near the edge of the electron beam. These large electrostatic energy regions are the result of the nonlinear growth of longitudinal electrostatic oscillations at $\omega_{pe}$. The modulation or growth time of these energy density regions is taken as $\omega_{pi}$, which is observed on the constant-impedance probes. The reason for selection of this mechanism is the difficulty encountered with heating ions with an electric field oscillating at $\omega_{pe}$, which is the frequency of the intense fields observed in the plasma beam. This mechanism is essentially momentum transfer by radiation pressure. Thus

$$F(\text{the body force}) = -\nabla\left(\frac{\epsilon E^2}{2}\right)$$

using mks units. If we assume that this force is applied for only $\tau = 10^{-9}$ sec (take envelope of the electron oscillations, or the ion plasma period) to ions only (electrons are adiabatic since $\omega_{ce} > \omega_{pe}$), that the fluctuating energy density is limited to a region of the order of the Debye length $\lambda_0 = 3 \times 10^{-6}$ m ($T_e \sim 1$ eV, $n = 3 \times 10^{13}$ cm$^{-3}$), and that the electric field is $10^6$ V/m (we measure $1.4 \times 10^6$ V/m), then we will have a momentum increment to the deuterium ions of

$$\rho\, \Delta v \cong \frac{E^2}{2\lambda_D} \times \tau = 1.4 \times 10^{-3}\ \text{N sec}^{-1}\ \text{m}^{-3}\ ,$$

or for our density of deuterium ions

$$\Delta v = 1.5 \times 10^6\ \text{cm/sec}\ .$$

This means that in approximately 20 positive momentum impulses a cold deuteron will be heated to 1 keV. This gives a heating rate that is too optimistic. Assuming that deuterons receive equal positive and negative momentum impulses, it can be shown that the net increase of energy per pair of collisions will be $E_+ - E_- = 2nv\,\Delta v$. This will lengthen the heating time to several hundred impulses (approximately 0.5 $\mu$sec). From this it can also be seen that the heating rate goes up with the energy of the ion.

There are several problems connected with this process. First, the efficiency must be high in order to account for the final ion energy density and containment time. Second, the localized region of the fields will slow up the heating rate for deuterons outside of this region.

There are several attractive features to this mechanism. It is compatible with the observed exponential rise in mean ion energy with beam power (essentially beam voltage). It avoids the incompatibility of 60-Gc high-amplitude electric fields with heating ions.

Obviously, this notion is not yet in satisfactory shape; it is only presented for consideration along with all the other possibilities for proposed mechanisms for heating ions in Burnout V.

### 5.1.7 Possible Ion-Heating Mechanism

J. R. McNally, Jr.

We present here an alternative possibility for the rapid heating of ions in the Burnout V plasma. If there is a highly negative dc potential well due to the hot-electron beam in the core of the Burnout V plasma (an unneutralized electron beam of $\Delta n_e = 3 \times 10^9$ electrons/cm$^3$ would give 3 kV/cm at $r = 1$ cm), the $D^+$ and $Cu^+$ ions would be strongly heated in the core region by $E_r \times B_Z$. Thus, if $E_r \sim 3$ kV/cm the average energy of the deuterons would be about ⅓ keV in this region, and some near-resonance cyclotron mixing with the colder, lower-density deuterons at larger $r$ would produce hot deuterons at $T_+ \sim 100$ eV. Actually, since $D^+$ can only be detected spectroscopically via a charge-exchange or recombination process, the exact radial dependence of the $D^+$ energy cannot be determined (this is also partly due to delayed emission via cascade effects). This $E \times B$ heating of $D^+$ ions is thus insufficient to produce the $D^+$ energies directly.

[13] Consultant, University of Tennessee, Knoxville.

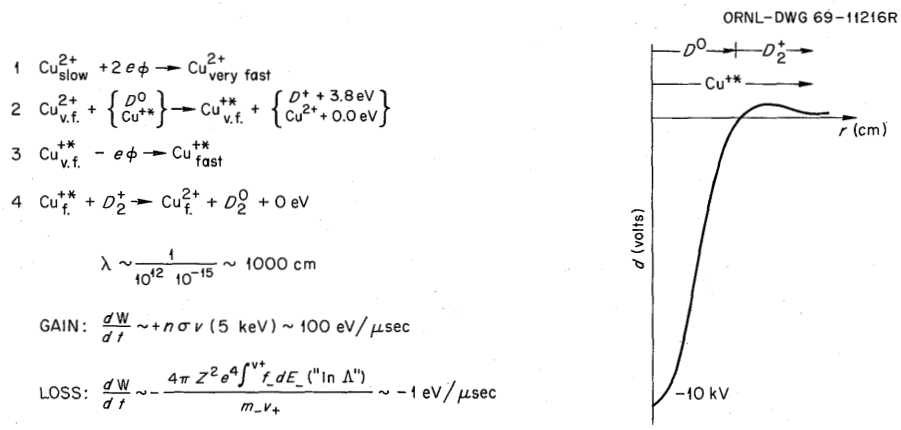


**Fig. 5.1. Rapid Potential Well Heating by Selective Resonance Charge Exchanges.**

The $E \times B$ heating of $Cu^+$ in the core would be ~60 keV. The $E \times B$ heating of $D^+$ ions would be this large if $E_r$ extended over a large distance; however, the Larmor orbit size of the $Cu^+$ ion is so large and the core region ($r \sim 1$ to 2 cm) so small that the ion can gain, at most, the energy of the potential well (~5 keV). However, $Cu^{2+}$ ions would gain twice this potential well energy; if, in addition, a charge-exchange capture process involving $Cu^{2+}$ occurs near the bottom of the well, the resulting $Cu^+$ can leave the well with a net energy gain of order 5 keV (see Fig. 5.1). Ion cyclotron mixing of the hot ions with colder ions of lower density may then occur very rapidly,[14] and a mean energy for $Cu^+$ of order 3 keV might be expected. Rapid heating of $Ar^+$ and $He^+$ in a hot-proton plasma (produced by proton cyclotron resonance heating) has been reported.[15]

## 5.2 BURNOUT V

### 5.2.1 Introduction

R. V. Neidigh

The objective of the Burnout series of experiments is to create a dense hot-deuterium plasma in a mirror machine, using beam-plasma interactions of a dc axially injected electron beam, and to contain the resulting plasma. This year, the experiments stressed increased understanding of the ion-heating mechanism, so that in application we might be guided better in our parameter changes.

In this report period we have adjusted parameters to yield increased ion temperature and density, have improved the measurement of containment time, and have developed diagnostic experiments which give an insight into the mechanism responsible for the ion heating. We compare data from the new plasma modes with the old data and describe the parameter changes responsible. Then we describe successively some new diagnostic techniques which give a better qualitative picture of the mechanisms.

### 5.2.2 Four Ion-Heating Modes

R. V. Neidigh V. J. Meece

Besides the relatively cold-ion discharge coincident with a minimum cathode-emission-limited beam (mode I), there are to date three other separately identifiable and tractable plasma modes obtainable with higher beam power (Fig. 5.2). Since mode II has been with us the longest, most of the analysis has been done on it. A summary of ion temperature and plasma density measurements is embodied in Fig. 5.3. The laser measurement, made in this report period, measures $\int n_e\, dl$, and therefore depends on another distribution (in this case spectral light radius) for the limiting values given, $3.3 \times 10^{12}$ to $5.0 \times 10^{12}$ $cm^{-3}$. Ion heating in the first three modes increases exponentially with beam power (Fig. 5.4). In mode IV the ambient gas pressure is reduced and the greatest ion temperature is obtained

[14] *Thermonuclear Div. Ann. Progr. Rept. Dec. 31, 1968,* ORNL-4401, p. 62; J. F. Clarke and G. G. Kelley, *Phys. Rev. Letters* **21**, 1041 (1968).

[15] V. T. Tolok (Kharkov) during June 1969 visit of U.S.S.R. fusion delegation to ORNL.

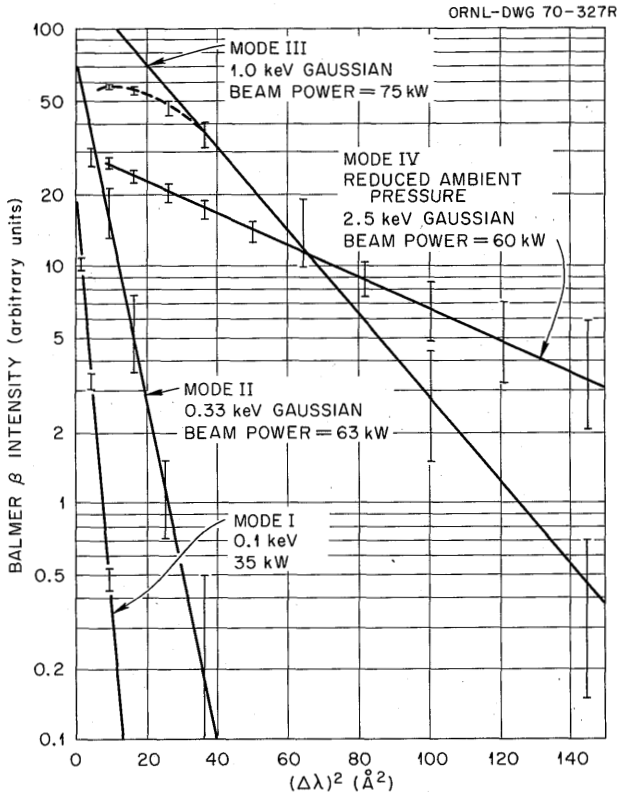


**Fig. 5.2. Doppler Broadening of the Balmer $\beta_2$ Spectral Line.** Log of the radiance is plotted against $\Delta\lambda$ showing the reasonably good fit (the error bars) to a Gaussian (the straight lines) in this plot. Note that the maximum radiance is reduced in the fourth mode.

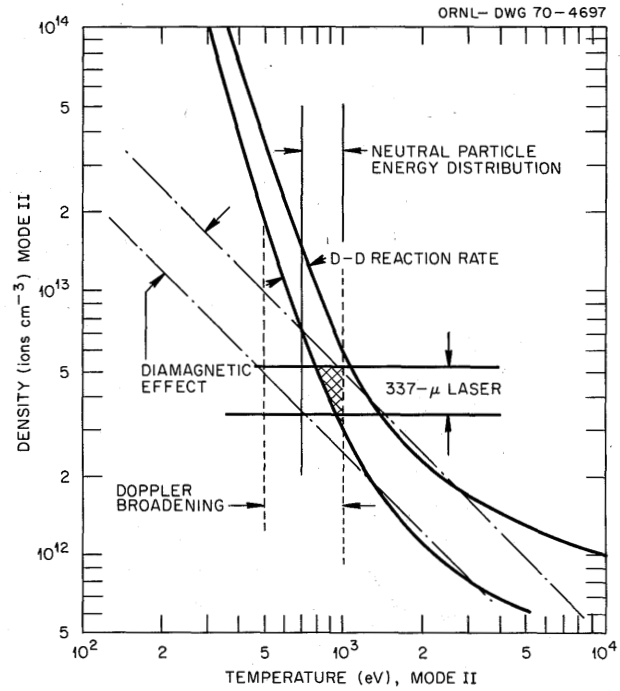


**Fig. 5.3. Summary of Temperature and Density Measurements on the Mode II Plasma.** The Doppler-broadened Balmer lines indicated a temperature between the limits shown by the vertical dashes. D-D reaction rates, determined by 3-MeV proton emission from the plasma, place limits on the temperature-density product, indicated by the heavy solid lines. Diamagnetic effect (long dashes) also gives a temperature-density product. Energy distribution of neutral emission (vertical solid lines) gives the best temperature resolution. Laser-measured density (horizontal lines) gives the best density resolution.

with a beam power somewhat lower than that for mode III. To obtain mode IV, ambient pressure is reduced to one-half of the mode III value by opening the midplane to the vacuum chamber and locating the gas feed in the mirror throats. The ion temperature appears to increase by a factor of at least 2. This is shown by the neutral-particle analyzer curves of Fig. 5.5. The increase in temperature was also noted by broader Balmer lines. Reduced radiance and repeatable structures also begin to show on the usually smooth Gaussian curves when run at the higher ambient pressure (Fig. 5.6). This is obviously an area for further investigation.

### 5.2.3 Ion Energy-Density Distribution from Neutral-Particle Flux

R. V. Neidigh V. J. Meece

We have collected both spectroscopic data (Fig. 5.6) and data (Fig. 5.5) from an energy analyzer which is depicted in Fig. 5.7. Both methods show that ion heating has taken place and that an average perpendicular ion energy greater than 1 keV exists. We also find the dense portion of the plasma confined within the beam profile and a measurable neutral flux from this region in the 0-to-10-keV energy range. The neutral flux observed by the analyzer and that seen spectroscopically must both have been the result of the same charge-transfer process and therefore subject to the same values for the charge-transfer ($\sigma_{10}$) cross section. However, there is considerable uncertainty in the value to be assigned to the cross section in this instance since the composition of the plasma is not accurately known. Further, the relative density of charge-exchange centers in the plasma appears to be a function of radius.

Beyond this, similarities in the measurements cease. The spectral intensity of a Balmer line as a function of

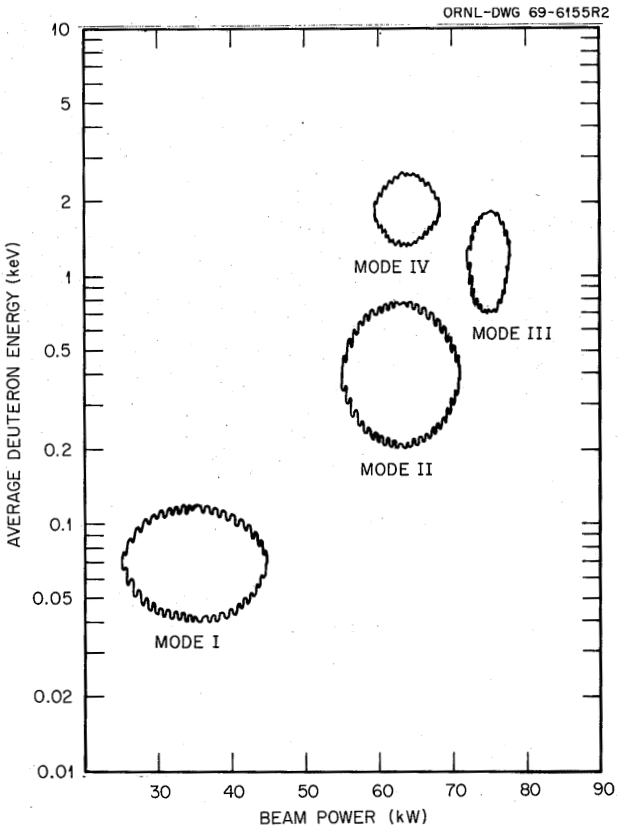


Fig. 5.4. **Average Deuteron Energy vs Beam Power.** Mode IV is obtained by a reduction in ambient gas pressure.

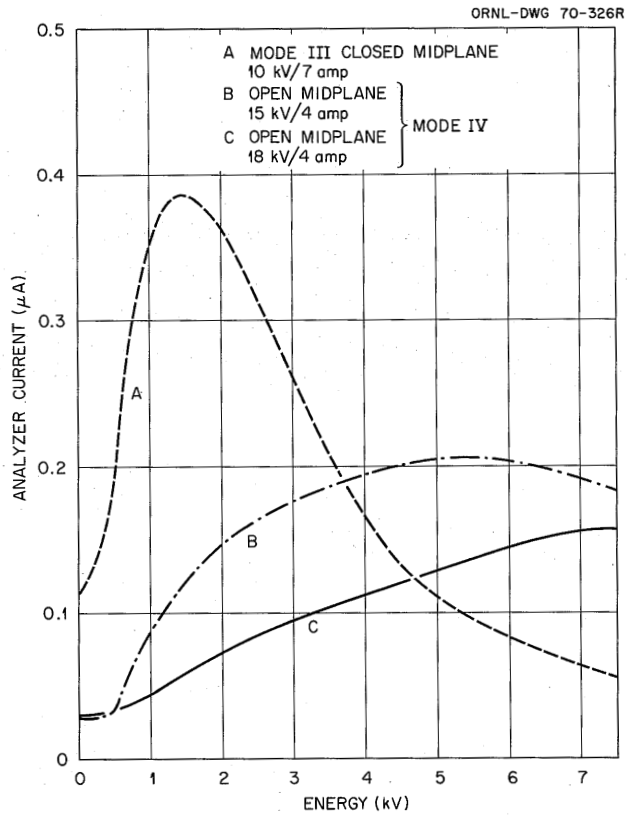


Fig. 5.5. **Raw Velocity Selector Data.** Note the change in energy distribution with reduction in midplane ambient pressure.

radius is not a reliable indication of the density distribution, because the spectral distribution is altered by delayed cascading. That is, neutral transit time across the plasma is comparable with the time required for the neutral to cascade from its level of excitation (the result of charge exchange) to the upper level of the transition being observed. Transit time and therefore what is observed change with the physical dimensions of the liner. Spectral light from the neutral originates from places other than where its charge transfer took place.

There are some excitation levels that are sufficiently stable so that excited neutrals as well as ground-state neutrals reach the gas cell of the analyzer, 23 cm from the plasma. This may not be a large fraction or affect the value of the stripping cross section greatly, but it is mentioned in contrast to the spectroscopic technique, where no such dependence on a stripping cross section exists. These uncertainties can be resolved only by the calibration in situ of whatever type of analyzer is used, a difficult procedure that has so far not been done.

In lieu of exact analysis we have presented the raw data showing relative effects (Fig. 5.5) and the reduced data showing limits in the energy density (Fig. 5.8). Changes in operating parameters responsible for the apparent temperature increases have been described above.

### 5.2.4 Plasma Structure

R. V. Neidigh V. J. Meece

There is considerable evidence for spatial inhomogeneity in the plasma density. In the previous report period[16] we discussed correlation measurements made in the plasma. The probe data indicated practically no correlation between probes displaced azimuthally. Regions of constant potential appeared to be radial segments smaller than 6°. Probe signals have since been

[16] *Thermonuclear Div. Ann. Progr. Rept. Dec. 31, 1968,* ORNL-4401, p. 107.

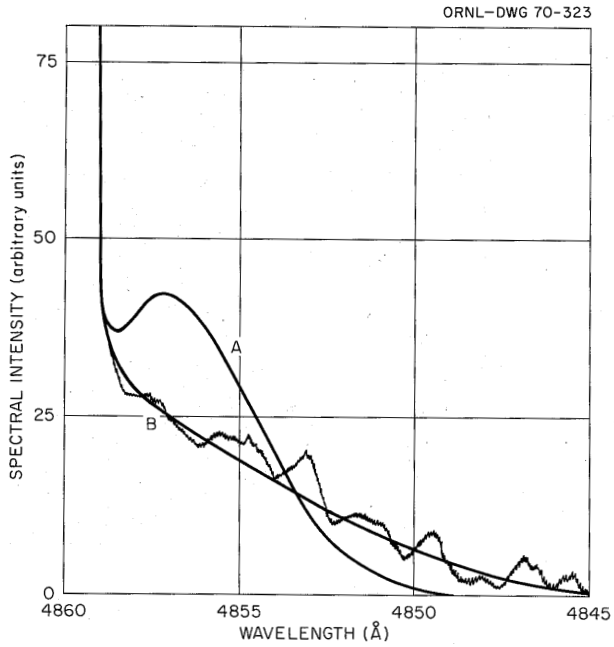


**Fig. 5.6. Doppler-Broadened Balmer $\beta$ Lines of Deuterium.** Reduced ambient pressure produced curve $B$ and is compared with a closed midplane region which produced curve $A$. Note the structure in curve $B$. The smooth curve $B$ was drawn in, arbitrarily smoothing the data.

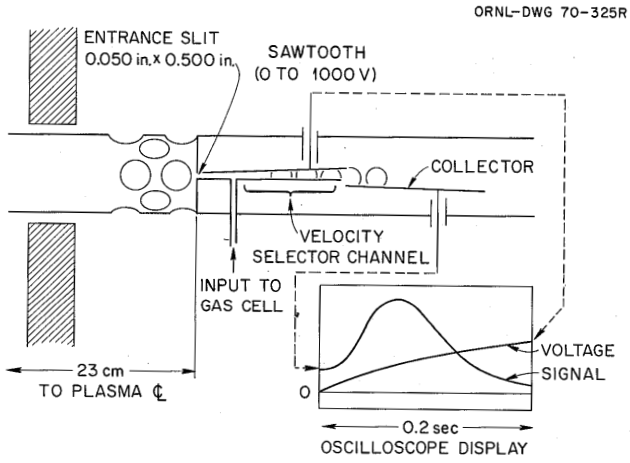


**Fig. 5.7. Velocity Selector Analyzer (Schematic).** The velocity selecting channel is tapered to accommodate magnetic field falloff with increased radius. Field strength at entrance slit is about 6000 G.

recorded on a traveling-wave oscilloscope using a single trace of 30-nsec duration, traces 3 and 4 of Fig. 5.9. The potential fluctuations resemble step functions

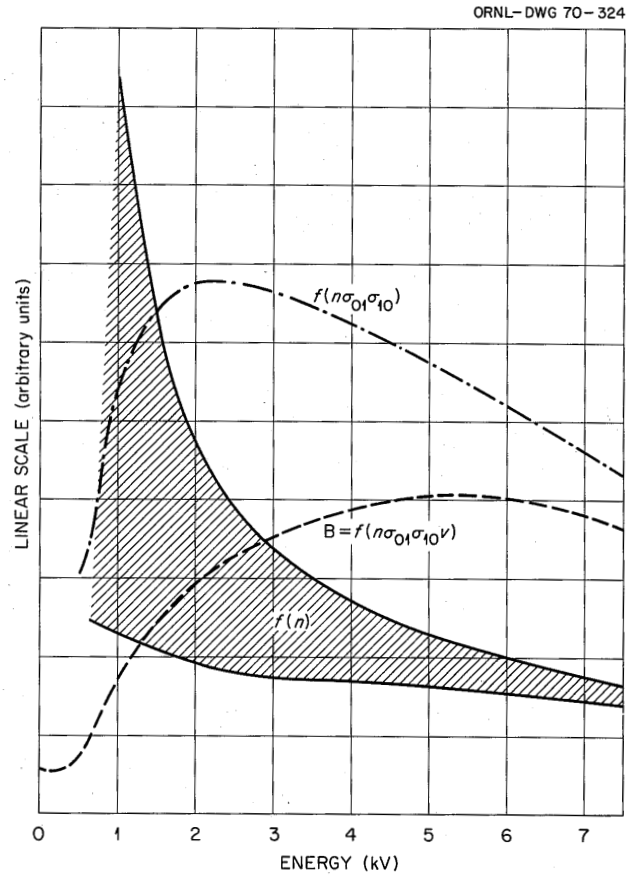


**Fig. 5.8. Reduced Velocity Selector Data.** Curve $B$ is the raw data and is adjusted for velocity in curve $f(n\sigma_{10}\sigma_{01})$. The limits of $f(n)$, the energy-density distribution, are determined by assuming $\sigma_{10}$, the charge-transfer cross section, to be that for a plasma consisting of either all atomic deuterium or all molecular deuterium and impurities. Note that below 1 keV the distribution becomes relatively obscure.

which appear to remain constant for up to 1 nsec. By electrostatic pickup the neutral-particle detector shows similar stepwise bursts modulating its signal (traces 1 and 2 of the same figure). Perhaps additional evidence for structure is obtained when we measure $n_iT_i$ by using cellulose nitrate to detect tritons, a D-D reaction product; there we have observed that in addition to a background of triton tracks (from which the plasma profile and reaction rate can be estimated)[17] there are many clusters of tracks. Figure 5.10 is a sample which indicates plasma regions of greater $n_iT_i$ with azimuthal dimensions as small as $10^{-3}$ to $10^{-2}$ cm at the beam-plasma interface ($r \approx 1$ cm). Since the detecting

[17] *Thermonuclear Div. Semiann. Progr. Rept. Apr. 30, 1966,* ORNL-3989, p. 47.

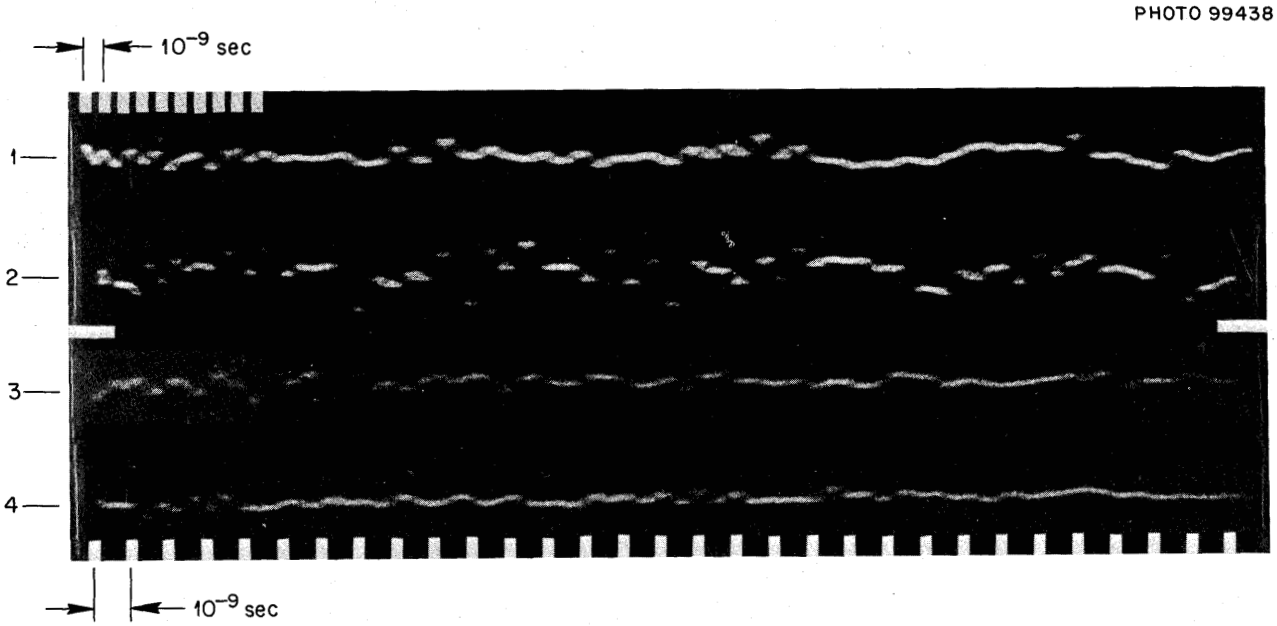


**Fig. 5.9. Potential Fluctuations vs Time.** A Tektronix 519 traveling-wave oscilloscope records the plasma potential fluctuation picked up on (1.2), the neutral-particle analyzer collector, and (3.4), a plasma probe. Signal amplitude is about 1 V.

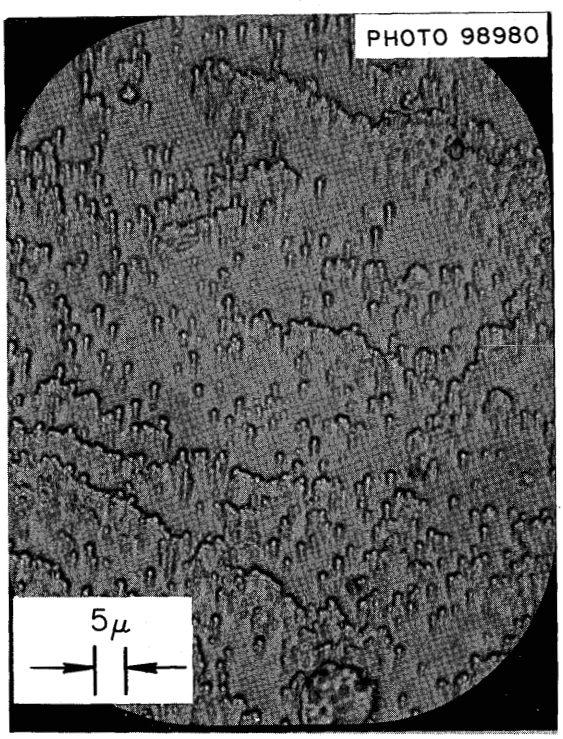


**Fig. 5.10. Tritons from D-D Reactions Recorded in Cellulose Nitrate.** Since the tritons pass through a pinhole in the liner wall, the clusters may image similar cells of maximum $n_i T_i$ in the plasma.

material integrates over the total exposure, no conclusions from the cluster-to-cluster proximity may be drawn, but it appears probable that there are submillimeter regions of plasma where D-D reactions are more abundant and that this "structure" is revealed in the triton tracks as well as in the probe signals.

### 5.2.5 Use of Forbidden Spectra to Measure Large High-Frequency Fields

F. R. Scott[13]

Intense high-frequency electrostatic oscillations have been measured by observing the forbidden satellite of the $^3P - {}^3D$ (4471 Å) transition in helium. By Abel inversion the field intensity was found as a function of radius. Peak electrostatic fields greater than 10 kV/cm were found near the edge of the 1-cm-radius electron beam (the beam-plasma interface). These fields decrease to zero on axis and to less than 3 kV/cm at a radius of 2 cm. The satellite spectral line shift indicates a frequency of 60 GHz (approximately the electron plasma frequency) for these strong electrostatic oscillations.

Recent experiments[18,19] reported successful measurement of large electric fields either externally applied

[18] H. J. Kunze and H. R. Griem, *Phys. Rev. Letters* **21**, 1048 (1968).

[19] W. S. Cooper III and H. Ringler, *Phys. Rev.* **179**, 226 (1969).

or internally produced in helium plasmas by observing the forbidden two-quantum transitions in neutral helium as suggested by Baranger and Mozer.[20] Considering second-order time-dependent perturbation theory, they proposed that a measurement of the intensity of selected forbidden lines relative to their corresponding allowed transitions would yield a mean value of the energy in the fluctuating electric field. By measuring the frequency shift from the expected position of the forbidden line due to a static electric field, the frequency of the fluctuating field could be found. Cooper and Ringler's[19] measurements, using an externally applied field, have essentially verified the method. Observations by Kunze and Griem[18] indicate that for larger fields the theory may need refinement, since they observe only the weaker, far satellite in their plasma. Our measurements seem to substantiate their contention.

After surveying the emission spectra from λ 3600 Å to λ 6000 Å we selected the λ 4471 Å triplet transition $^3P - {}^3D,F$ for careful study. Unfortunately the more comparable singlet transition at λ 4921 Å was too close to a $Cu^+$ impurity line, thus making accurate intensity ratios difficult. The usual oxygen impurity line near λ 4471 Å was not present in our experiment.

Figure 5.11 shows the emission of λ 4471 Å and its corresponding forbidden transition as observed along a diameter through the plasma. No spatial corrections are included in this figure. The wavelength shift 1.44 Å in the field-free case is indicated.[21] No near satellite is observed. The far satellite (mean displacement = 1.85 Å) shows a splitting which we believe is due to a Zeeman effect.[22] This is demonstrated in Fig. 5.12, which shows the same spectral region under similar conditions with the addition of a polarizer. In Fig. 5.12*a* the polarizer was aligned to observe emission with the *E* vector perpendicular to *B*, and in Fig. 5.12*b* the alignment permitted only emission with *E* parallel to *B*. The allowed line shows the normal Zeeman splitting expected. The forbidden line shows a much stronger degree of polarization than is predicted from the two-quantum transition. We feel that this is due primarily to combined Zeeman and Stark effects. Since the σ components are absent from the perpendicular emission of the satellite, this suggests that the high-frequency *E* field is aligned mostly along the magnetic field, excluding the $\Delta m = \pm 1$ transitions.

[20] M. Baranger and B. Mozer, *Phys. Rev.* **123**, 25 (1961).

[21] W. C. Martin, *J. Res. Natl. Bur. Std.* **64**, 19 (1960).

[22] J. S. Foster, *Proc. Roy. Soc.* **A124**, 133 (1931).

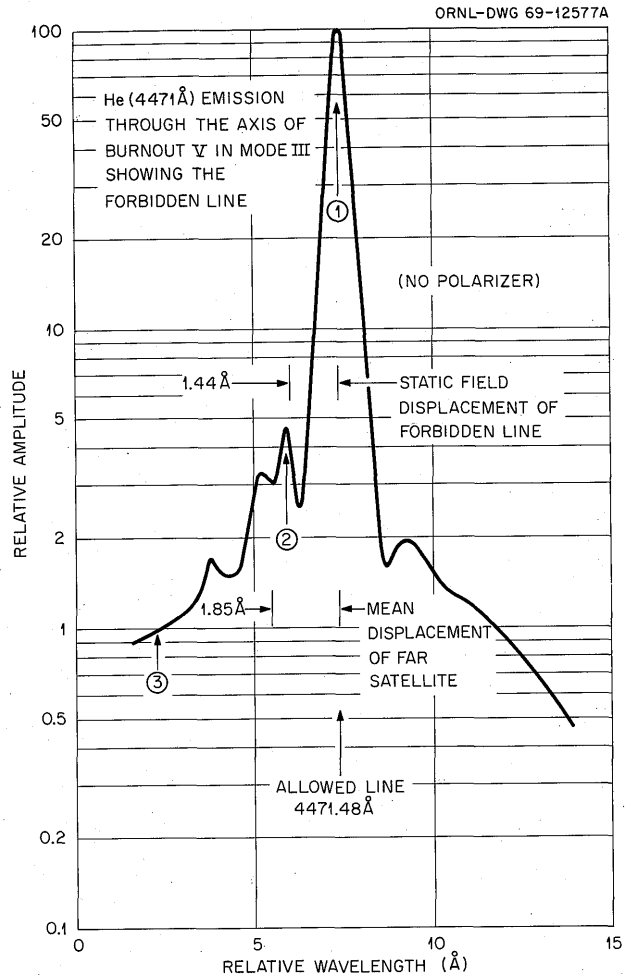


**Fig. 5.11. Profiles of the λ 4471 Å ($2^3P - 4^3D$) Line of He I as Observed Through the Axis of Burnout V in Mode III Showing the Satellite ($2^3P - 4^3F$) with Mean Displacement of 1.85 Å.** Intensity of the lines at 3.5 and 9 Å is independent of ion heating.

The steady-state nature of the Burnout V experiment and its axial symmetry permitted radial sector scans of (1) the central peak of the allowed line, (2) the forbidden line, and (3) the background as indicated in Fig. 5.11 by arrows 1, 2, and 3. No polarizer was used. These scans were then Abel-inverted and adjusted for the line profile, and the electric field was calculated from the ratio of the forbidden satellite intensity to the allowed line intensity. Both the Abel-inverted amplitude ratio and the resulting mean electric field are shown in Fig. 5.13. This field is obtained from the expressions used by Baranger and Mozer.[20]

The static shift of the forbidden line is 1.4 Å. In Fig. 5.11 the mean shift of the forbidden line is 1.85 Å,

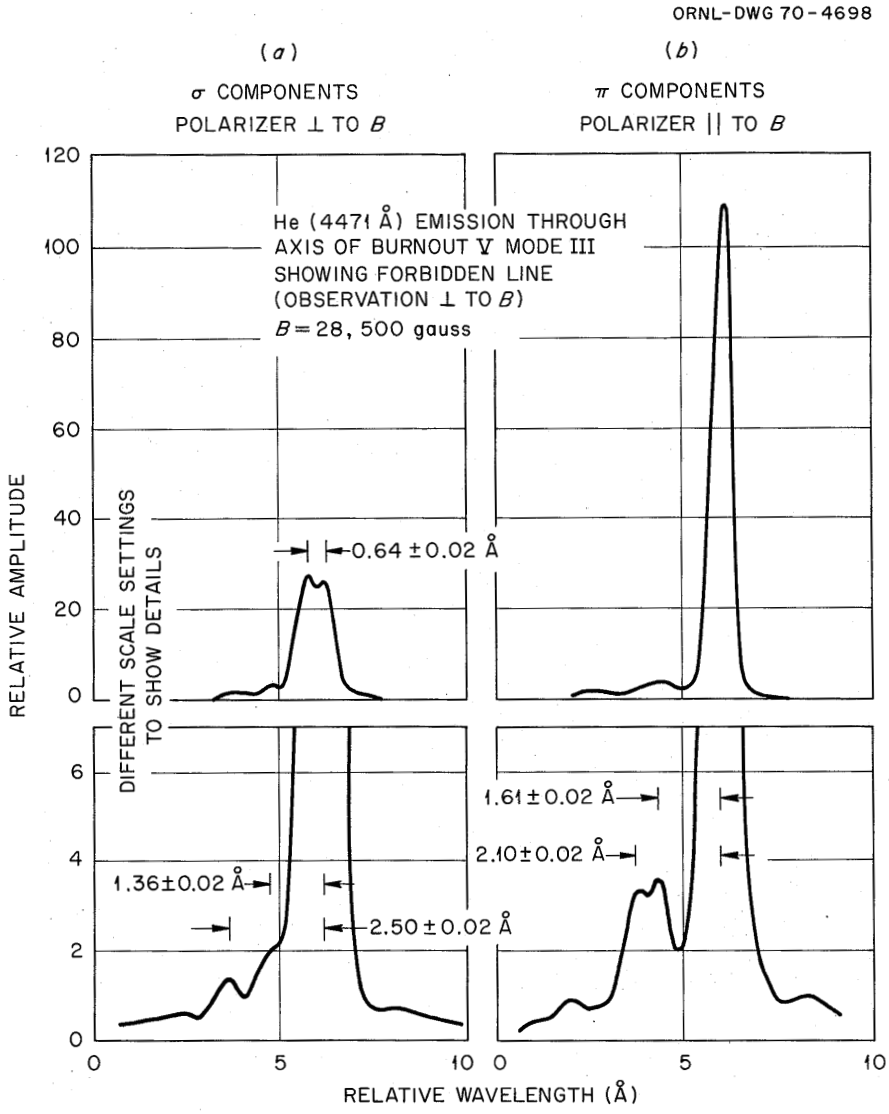


**Fig. 5.12. Profile of the λ 4471 Å Line of He I as Observed Perpendicular to the Axis of Burnout V.** (*a*) Using a polarizer set perpendicular to the magnetic field, (*b*) using a polarizer set parallel to the magnetic field ($B$ = 28,500 G). Upper and lower curves have different scale settings to show details.

corresponding to an oscillating frequency of $60 \times 10^9$ Hz. This line shift was observed to be nearly independent of radius.

Recently Kunze and Griem[23] have developed the perturbation theory to higher order and find that under our conditions the near satellite would be of the order of 10% of its Baranger and Mozer value, while the far satellite would be increased by about 5%. Our observations indicate that the near satellite must be less than 1% of its Baranger and Mozer value. However, the Zeeman effects have not been included theoretically, so this discrepancy may be meaningless.

In conclusion, we report spatially resolved measurement of collective electric fields greater than 10 kV/cm with a frequency in the range of the electron plasma frequency. This electric field appears to be aligned with the magnetic field, indicating a strong nonlinear longitudinal electrostatic plasma oscillation. The peak intensity occurs near the boundary of the electron beam or at the beam-plasma interface. Assuming the availability of pertinent optical transitions and

[23] H. J. Kunze and H. R. Griem, private communication.

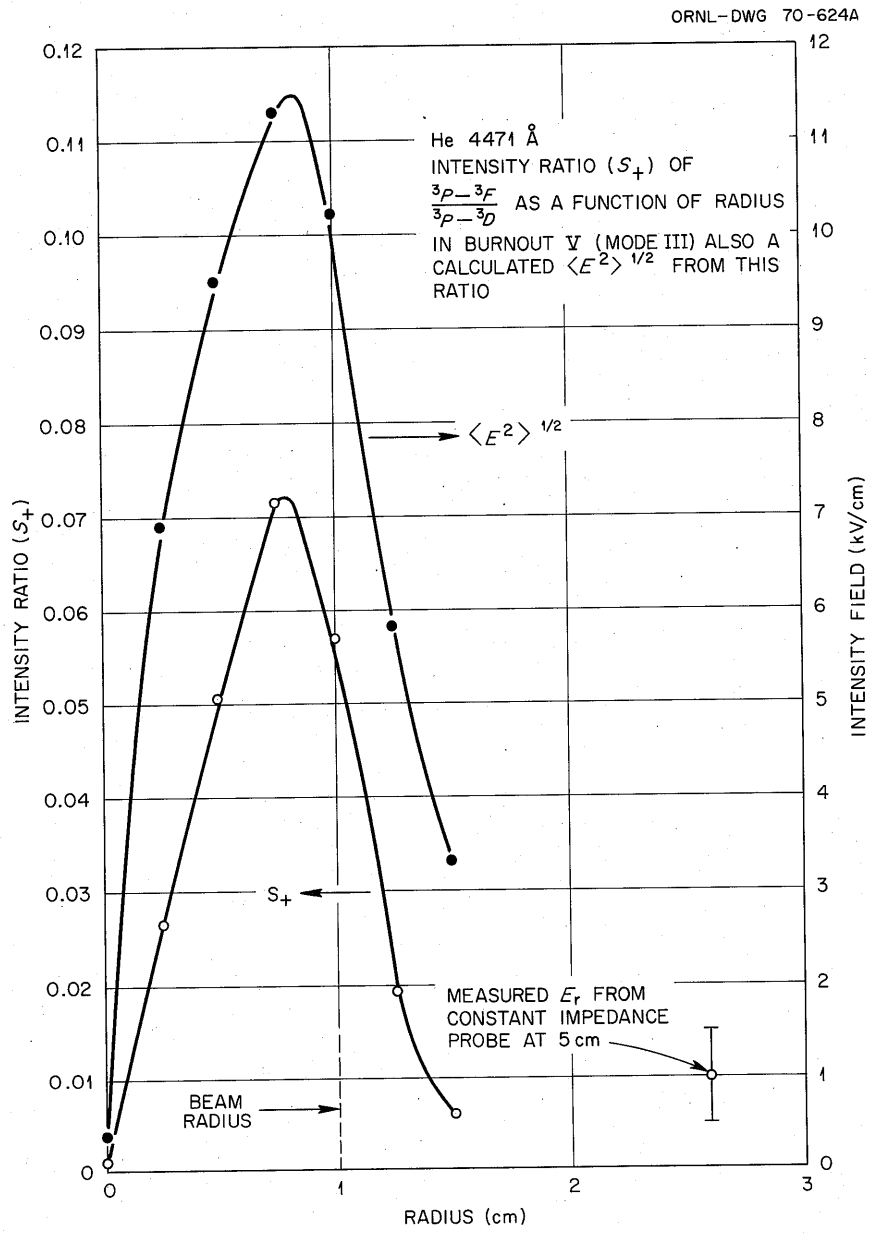


**Fig. 5.13. Amplitude Ratio of the Far Satellite to the Allowed Transition as a Function of Radius After Abel Inversion (Left-Hand Scale).** Also included are the derived $\langle E^2 \rangle^{1/2}$ field values using the formula given by Baranger and Mozer[20] (right-hand scale). Constant-impedance probe data are from ref. 2.

appropriate theory, this method of observation extends our ability to probe turbulent plasmas with essentially no interference.

### 5.2.6 Plasma Impurity Reduction

J. R. McNally, Jr. R. V. Neidigh
V. J. Meece

Preliminary tests using niobium liner material in the mirrors resulted in a tenfold reduction in the spectral intensity of CuD and neutral Cu, but not $Cu^+$. The neutral diatomic molecule of CuD has now been positively identified. It may be produced as a result of chemical sputtering at the copper walls and throats of the apparatus or as a result of sputtered copper reacting with background deuterium molecules $D_2^0$ or $D_2^+$.

Jeppeson[24] produced the CuD spectra using a 3-amp arc between an anode of bismuth-copper alloy and a cathode of pure copper in $D_2$ at 40 torrs. Exposure time on a high-resolution Johns Hopkins University spectrograph was 24 h, indicating the relative weakness of this spectrum under his experimental conditions.

Several bands of CuD (the $^1\Sigma^* - {}^1\Sigma$ band system) have been positively identified in the wavelength region λ 4000 Å to λ 5000 Å. Bands of the 1–0 branch starting at λ 4178 Å (band head), 0–0 *R* at λ 4281 Å, 0–1 *R* at λ 4541 Å, 0–0 *P* at λ 4287 Å, and 1–1 *P* at λ 4321 Å have all been identified (see Fig. 5.14 for λ 4280 rotational structure). The band head of the 0–0 *R* branch at λ 4280.9 Å is of intensity comparable with the intensities of the Balmer γ line of deuterium at λ 4339.29 Å, of $Cu^0$ at λ 4275.1 Å, and of $Cu^+$ at λ 4506 Å, thus indicating that CuD spectra are quite prominent in the emitted radiation. The excitation potential of the $^1\Sigma^* - {}^1\Sigma$ system of CuD is only 2.9 eV, compared with 7.7 eV for λ 4275 Å $Cu^0$ and 11.0 eV for λ 4506 Å $Cu^+$.

The ions $Cu^+$ and $D^+$ exhibit ion energies of about 2 keV from Doppler-broadening studies ($D^0$ from charge exchange of $D^+$),[25] making this a truly unusual plasma having apparently cold electrons and very hot ions, plus a trace of 5-keV beam electrons ($n_{e\,hot} \sim 2 \times 10^9$ electrons/cm$^3$, $n_{e\,cold} \sim 10^{13}$ electrons/cm$^3$).

It may prove necessary to replace the midplane section of the liner, which still remains copper, with a low-sputtering metal or ceramic to suppress the remaining impurities.

[24] M. A. Jeppeson, *Phys. Rev.* **50**, 445 (1936).

[25] I. Alexeff *et al.*, *Phys. Rev. Letters* **23**, 281 (1969).

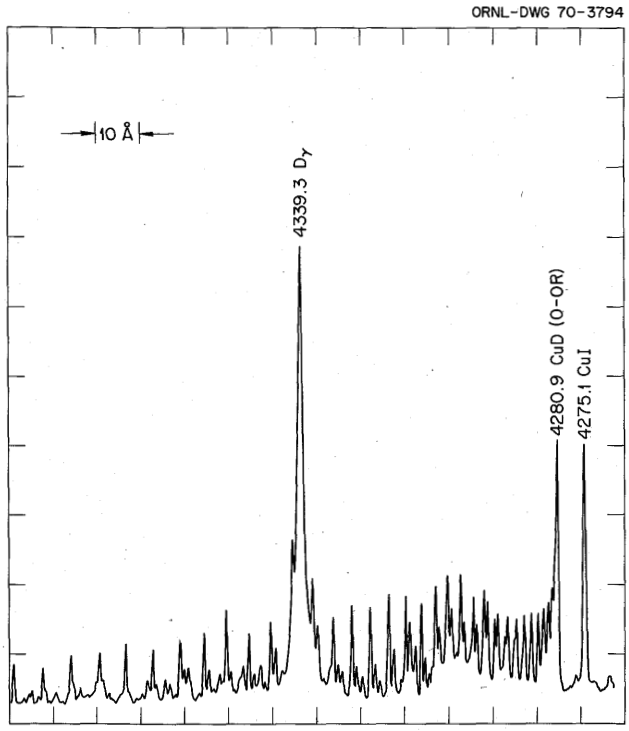


**Fig. 5.14. Spectrum of Burnout V Showing CuD Rotational Band Structure.** Also shows the Balmer γ line of deuterium (λ 4339.3 Å), Cu I (λ 4275.1 Å), and the 0-0 *R* band head of CuD at λ 4280.9 Å. View along diameter and perpendicular to magnetic field (28,000 Oe). 15 kV, 3 A source conditions. Pip marks indicate 5-Å markers. Overlapping from 0-0 *P* branch, 1-1 *R* branch, and 1-1 *P* branch is also present.

### 5.2.7 Soft X-Ray Emission

W. L. Stirling V. J. Meece

X-ray emission from Burnout V operating in mode II was investigated with a krypton-filled proportional counter. The proportional counter was operated at a gain of 150 eV per channel and was used to look at the soft x-ray emission from the arc column.

Figure 5.15 shows the intensity distribution of the bremsstrahlung produced in the center of the electron beam. This was taken with a 5-mil beryllium window on the detector through a 1-mil Mylar vacuum-to-air window. Absorption corrections for the Mylar, air, and beryllium have been made, as have the necessary background corrections. As shown, the applied voltage is 11.5 kV. However, the beam is about 4.5 keV and is spread to ~60% (FWHM) of the mean value. Assuming that the intensity is constant below 2 keV, the x-ray flux corresponds to a beam current in the plasma of about one-half that registered by the power supply. We

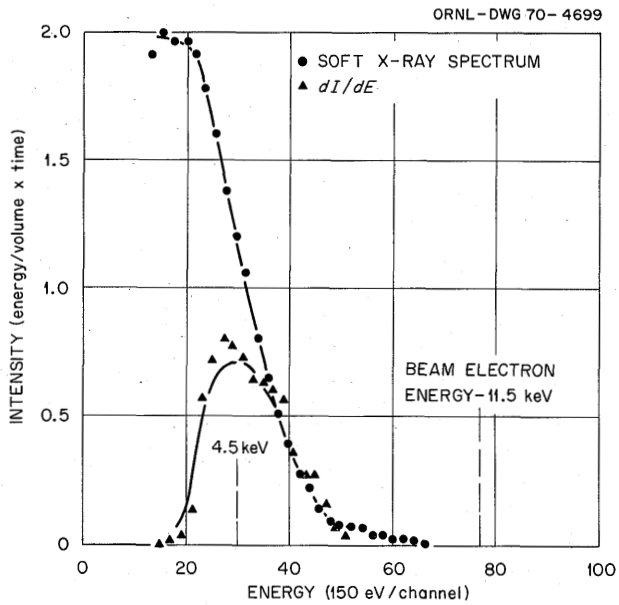


**Fig. 5.15. X-Ray Intensity vs Energy.** Note that the average beam energy has been degraded to less than half its input value.

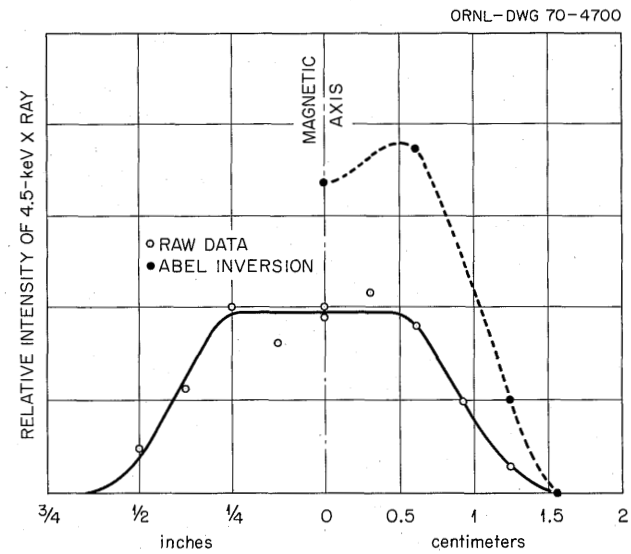


**Fig. 5.16. Radial Profile of Soft (4.5 keV) X Rays.**

have then a beam strongly degraded in energy making a single pass at a velocity of $4 \times 10^9$ cm/sec through a background plasma of $3 \times 10^{12}$ $cm^{-3}$ density. The density of the beam is calculated to be $3 \times 10^9$ $cm^{-3}$.

Figure 5.16 shows a radial scan of the beam. The beam is well defined with an *e*-folding distance of 1 ± 0.2 cm. Abel inversion of the data shows a beam density falloff in the center.

### 5.2.8 Plasma Lifetime

W. L. Stirling V. J. Meece

Our first attempt to measure the plasma lifetime directly employed a calcium washer gun to see if a dynamic value of $\tau$ could be obtained, that is, a value with arc on and heating. The idea was to inject neutral calcium into the plasma and measure the decay in its spectral light intensity. Calcium was chosen because of its very low ionization potential (~6 eV) and the even lower excitation potential (~3 eV) of both $Ca^0$ and $Ca^+$, and because it would be easily distinguishable from the deuterium and copper spectra.

The calcium gun had no effect on the arc heating, as evidenced by a constant output of the neutral-particle analyzer. However, the $Ca^+$ and $Ca^0$ lifetimes were the same within experimental error and equal to about 100 μsec. Since no calcium light is present in the center with arc off and since the time delay from gun firing to onset of light signal is consistent with cold calcium (a few tenths of an electron volt) filling the system, we interpreted a 100-μsec duration of the calcium spectra as an input or filling of the system, and therefore no dynamic lifetime measurement was possible using this technique.

A deuterium gun caused about a 30% reduction in the neutral-particle analyzer signal, which recovered to full value in about 10 to 15 msec. This recovery time is within a factor of 2 of that calculated for pumpout of the midplane region. The signal decay for the Balmer $\beta$ line of deuterium is also about 100 μsec, the same as that obtained for calcium. It may be that the deuterium gas emitted by the gun increases the plasma density, resulting in violation of the requirement that $\omega_{ce} \cong \omega_{pe}$ (see Sect. 5.1.4) and thus a reduction in heating of the plasma. The gun experiments give at best an upper limit to the plasma lifetime of about 100 μsec.

In arc turnoff experiments, rapid turnoff of the arc is achieved by shorting the high-voltage terminal. In order to reduce the noise originating in the resultant spark, a shorting switch developed on the beam-plasma facility was used. This switch is electrically operated, immersed in oil, and enclosed in a grounded metal container. With this switch, photomultiplier signals from the optical spectrometer on the order of a few millivolts are easily observed.

Light decay measurements of $D_\beta$ and several Cu I and II spectral lines were made at the arc turnoff of mode

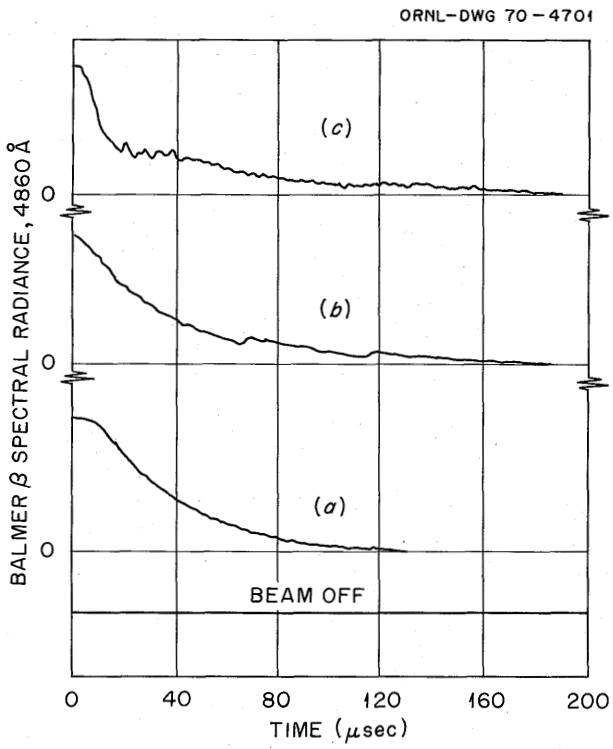


**Fig. 5.17. Decay of Balmer β Spectral Radiance, 4860 Å, After Beam Turnoff.** (*a*) Mode II, (*b,c*) mode IV.

II. The lifetime ranged between 40 and 50 μsec (Fig 5.17*a*). The calculated charge-exchange lifetime is also about 40 μsec. We conclude, therefore, that the plasma lifetime may be charge-exchange limited.

With a factor of 2 reduction in the ambient neutral pressure in the system (mode IV), some neutral particles are detected having energies above 10 keV. In this mode there is a two-component decay of about 10 μsec followed by a 60-μsec decay (Fig. 5.17*b,c*). The instrumental time constant was 5 μsec. There is reduced light output and radial expansion of the plasma in the midplane region as compared with mode II. The short time may be the escape of low-energy ions and is followed by the slower decay of trapped energetic ones, or the fast decay may be due to the energetic beam electrons, which disappear rapidly at turnoff.

### 5.2.9 Doppler Studies on Copper Impurity Spectral Lines

J. R. McNally, Jr. R. V. Neidigh

Strong spectra of neutral copper (Cu I) and singly ionized copper (Cu II) have been observed in mode III. The neutral lines are generally overlapped by a weak but broad structure which shifts as the angle of view through the discharge varies. For different plasma sectors the broadening and shift follow the trend observed for Cu II spectra and hence are attributed to hot Cu II ions which charge-exchange or recombine with electrons to give Cu I and then radiate while still possessing a large velocity component of motion. This weaker structure is therefore Doppler related.

Doppler-broadening studies on the strong Cu II lines give a mean ion energy of about 3500 eV (Fig. 5.18), which, after correction for instrumental broadening, is about 3200 eV. The line shape is not quite Gaussian; the wings are broader than for a $T_+$ of 3200 eV, suggesting the presence of an overabundance of ions hotter than a Maxwellian distribution would predict. Thus, the copper ions exhibit a somewhat higher "temperature" than the deuterons (1000 eV), which were observed indirectly as in earlier spectroscopic experiments.

Doppler shifts of the Cu II lines as one moves the view direction across the plasma are very pronounced (Fig. 5.18). There are several potential sources of such shifts:

1. $E \times B$ drifts. For $v_d \sim 1.3 \times 10^7$ cm/sec ($\Delta\lambda = 1.9$ Å for $\gamma = 4506$ Å or $r = 6$ cm), the required electric

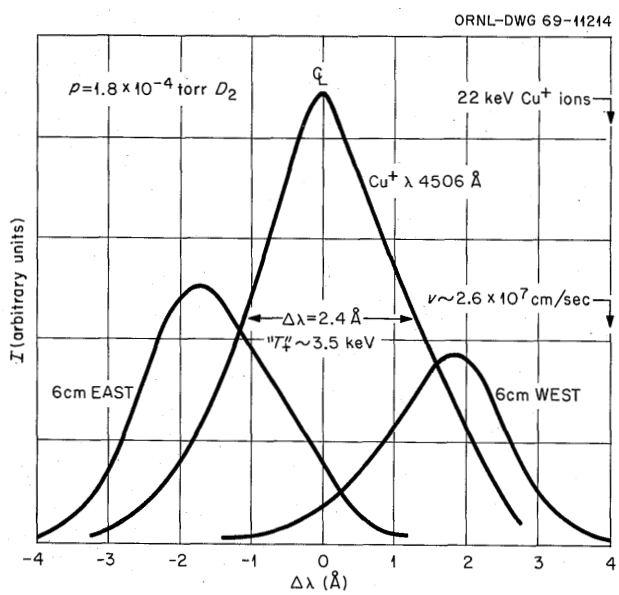


**Fig. 5.18. Line Profiles of λ 4506 Å $Cu^+$ Spectral Line for Different Sectors Through the Burnout V Mode III Plasma.** East and west views are at 10 times the sensitivity level of the central view.

field at $r$ = 6 cm is about 4000 V/cm and would require a positive plasma potential with the gradient increasing in magnitude radially at least to $r$ = 9 cm ($\Delta\lambda$ = 2.2 Å) from the axis. At large $r$ (~6 cm) the plasma potential, based on probe measurements, is only slightly positive (~100 V) and decreases as one penetrates the plasma. Thus, it does not appear likely that $E \times B$ drifts

$$(v_d = \frac{cE \times B}{B^2} = c\,\Delta\lambda/\lambda)$$

can produce the large shifts observed; they seem to be too small by a factor of 50 or more.

2. $\nabla B/B^2$ drifts. The radial gradient of the magnetic field is quite small (few percent), and it is not sufficiently large to produce the magnitude of the shift.
3. $\nabla T$ drifts. The magnitude of Doppler broadening remains approximately the same for different $r$, suggesting that $T$ does not change appreciably and certainly insufficiently to produce the observed Doppler shift.
4. $\nabla n$ drift. The drift here is

$$v_d = \frac{ckT}{eB}\frac{\nabla n}{n}$$

and requires a $\nabla n/n$ of 0.8 cm$^{-1}$. Since the $e$-fold distance for density falloff is about 1.3 cm, as measured by Abel-inverted intensity studies, there appears to be a logical explanation of the unusually large shifts (Fig. 5.19).

Examination of the intensity of the emission spectra of $Cu^+$ lines indicates a very low excitation temperature (~1 eV); however, in view of the presence of very hot ions and the expected large excitation cross sections for such energetic ions, no firm estimate of the electron temperature can be obtained. No definite indication of $Cu^{2+}$ spectra has been found (it is probably more likely to charge-exchange than be excited in heavy-ion–ion or ion-neutral collisions). Examination of the spectra of helium-doped (47% He) plasmas from λ 3850 Å to λ 5900 Å showed only spectra of $D^0$, $D_2{}^0$, $Cu^0$, $Cu^+$, and $He^0$ (no $He^+$ was observed, but the excitation potential of λ 4686 Å of He II is 51 eV). The maximum excitation potential for all observed lines was only 21 eV for He and 17 eV for $Cu^+$, indicating a low electron temperature (~3 eV) and a weak excitation mechanism by hot ions. There is a class of high-energy electrons in the core of the discharge ($T \sim 4.5$ keV and $n_{ehot} \sim 3 \times 10^9$ electrons/cm$^3$), but this apparently has negligible effect on the excitation.

ORNL-DWG 69-11215

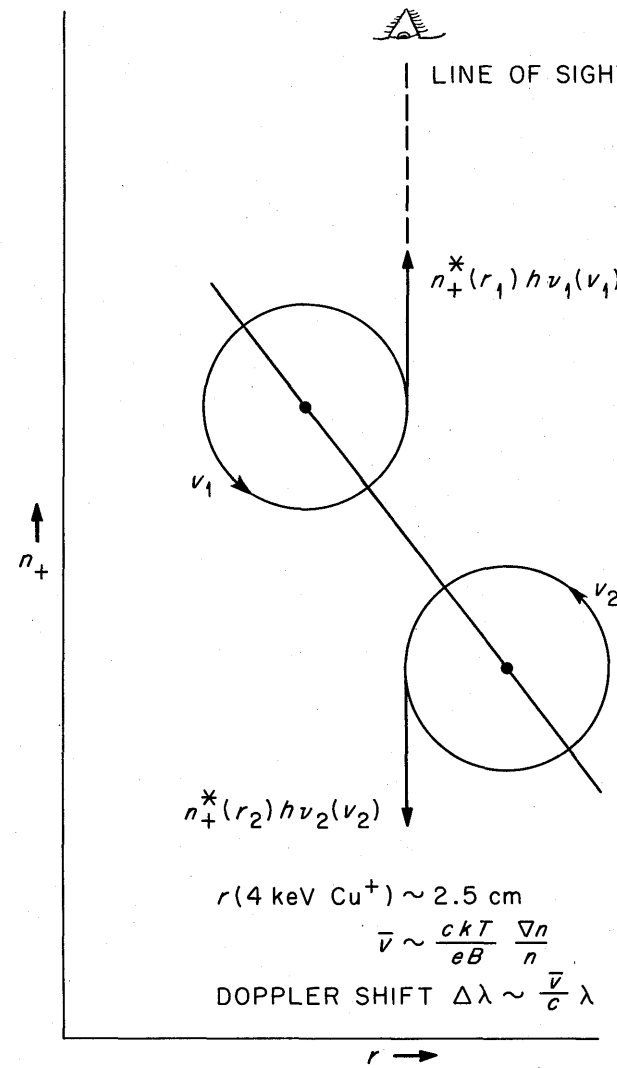


**Fig. 5.19. Schematic Illustrating Apparent Drift Due to Density Gradient of $Cu^+$ Ions in Burnout V Mode III Plasma.**

### 5.2.10 Radio-Frequency Spectrum

R. V. Neidigh V. J. Meece

The spectrum of radio frequencies radiated from and found within the plasma is very complicated and is not known in detail. The behavior of its distribution with different heating modes is under study. A further complication due to the very broad-band feature of the radiation arises from the frequency-selective nature of signal receiving networks. In spite of these problems some pertinent observations have been made.

The inequality

$$\omega_{ce} >_1 \omega_{pe} >_2 \omega_{pi} >_3 \omega_{ci} ,$$

where

$>_1 = 1.6$ to 3.2,

$>_2 \approx 60$,

$>_3 = 36$ to 18,

conveniently describes density and magnetic field relationships compatible with ion heating. It does not mean that only the frequencies designated by the $\omega$'s are present in the plasma. We have detected all frequencies up to $>\omega_{pe}$ but $<\omega_{ce}$ in a random noise spectrum having maximum amplitudes at about $\omega_{ci}$, $\omega_{pi}$, and $\omega_{pe}$. Antennas external to the plasma, internal high-frequency probes, and the displacement of satellites of visible spectral lines, techniques sensitive in the $\omega_{ci}$, $\omega_{pi}$, and $\omega_{pe}$ regions, respectively, have been used as detectors. Each technique examined electric field strengths successively deeper into the plasma. At the radial beam-plasma interface, electric field strengths as great as 10 kV/cm are implied from spectral satellite displacement.

We feel that the key to understanding the heating process lies in this expression of inequalities. It has persisted in all of the Burnout experiments, as shown in Fig. 5.20. The magnitude of the first and the second inequality establishes the magnitude of the third; that is,

$$\frac{\omega_{ce}}{\omega_{pe}} \times \frac{\omega_{pi}}{\omega_{ci}} = \frac{\omega_{pe}}{\omega_{pi}} .$$

The annoying result is that if $\omega_{ce}$ is set approximately equal to $\omega_{pe}$ to increase the possibility of resonant energy transfer from electron cyclotron oscillations to electron plasma oscillations, then $\omega_{pi} \gg \omega_{ci}$, and energy flow from ion plasma oscillations to ion cyclotron oscillations is hindered, and conversely. By reducing the plasma density or increasing the magnetic field, we can set $\omega_{pi} \approx \omega_{ci}$. This would further restrict electrons, improve stochastic acceleration efficiency, and greatly increase the ion heating as has been demonstrated by operation in mode IV, that is, with reduced density. To approach plasmas of thermonuclear interest, however, higher magnetic field strengths, not lower densities, are dictated.

## 5.3 BASIC TURBULENCE EXPERIMENTS

### 5.3.1 Introduction

W. D. Jones

In our attempts to understand mechanisms responsible for turbulence, four experiments, one of which is a computer simulation experiment, have been performed. In the first, observations have been made of anomalously high resistivity in a steady-state non-magnetically-supported discharge plasma. The observed resistivity can be explained only by the presence of

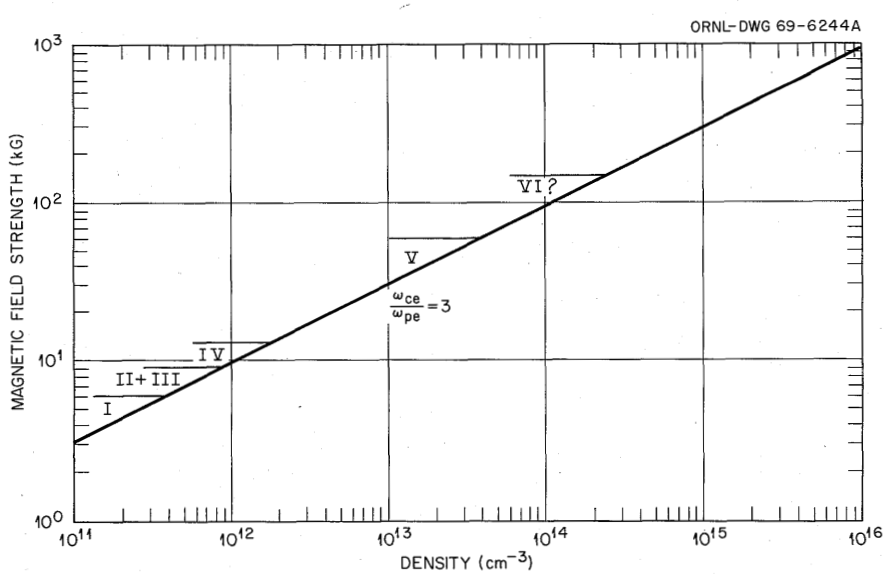


**Fig. 5.20. Basic Requirement for Ion Heating.** This is the relation of magnetic field strength to density when ion heating is experienced in the Burnout series of experiments. Note that for a density of $10^{14}$ cm$^{-3}$ a magnetic field strength of 100 kG will be needed.

electrostatic instabilities such as the ion-acoustic-wave and two-stream instabilities. In the second experiment, in a continuation of our efforts to understand the basic heating mechanism in the mode II beam-plasma pressure-gradient arc, a (geometrical) parametric study has been made of a standing wave in the main plasma column. Preliminary results suggest that the wave is due to an interaction between a slow space-charge wave on the beam and a space-charge wave in the plasma. In the third experiment, the possibility of reducing the molecular neutral density in the Burnout experiments by use of a ceramic liner has been tested in a small unit having a Pyrex glass liner. Preliminary results do not indicate that this will be a useful technique. Finally, a technique has been found for direct numerical integration of the Vlasov equation. The technique has been tested by simulating the behavior of the ions in the vicinity of a transparent grid in a plasma during and after a short negative voltage pulse on the grid.

### 5.3.2 Anomalous Resistivity in a Steady-State Plasma

I. Alexeff A. Hirose
W. D. Jones

Observations of anomalously low electrical conductivity in plasmas have been reported by several authors.[26] The conductivity observed is much too low to be the classical value and can be explained only by the presence of electrostatic instabilities such as the ion-acoustic-wave[27] or two-stream instability.[28] These instabilities provide electrons with effective collisions and give rise to low conductivity. If we denote the effective collision frequency by $\nu_{\text{eff}}$, the conductivity is given by

$$\sigma = \frac{\omega_{pe}^2}{4\pi} \frac{1}{\nu_{\text{eff}}},$$

where $\omega_{pe}$ is the electron plasma frequency. Thus, conductivity measurements give the value of $\nu_{\text{eff}}$, which is a measure of degree of turbulence.

In the experiment to observe these effects, a dc discharge is operated in a cylindrical glass discharge tube which has a constricted region in its central part (Fig. 5.21). The object of constricting the center of the tube is to increase the ratio of electron drift velocity to electron thermal velocity in this region relative to their ratio in the rest of the discharge. This results in any velocity-driven instability being constrained to the constricted region, thereby avoiding the regions near the electrodes. The increase in velocity ratio arises from the increased radial loss rate of plasma in the constricted region relative to the loss rate in the rest of the tube.

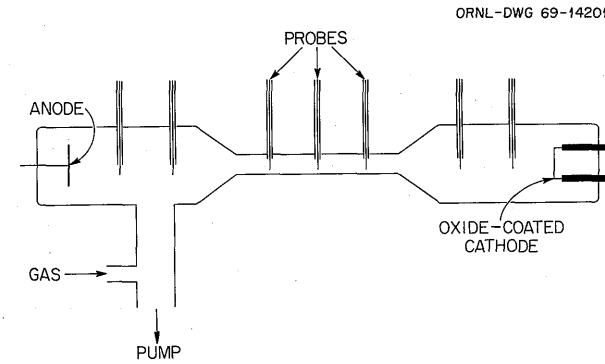


**Fig. 5.21. Schematic of the Discharge Tube.** The diameter of the constricted region is either 5 or 12 mm, as compared with a diameter of 50 mm for the end sections. The cathode is a directly heated coiled oxide-coated tungsten wire.

The electric field along the plasma column was obtained by measuring the floating potential of each of several small closely spaced probes placed in the plasma column. The maximum electric field measured in the experiment was about 400 V/cm, being much higher than Dreicer's critical field (~1 V/cm).[29] The conductivity can be simply calculated from the electric field and the current density by the relationship

$$\sigma = \frac{I}{ES},$$

where $I$ is the discharge current and $S$ is the cross-sectional area of the constricted region.

In Fig. 5.22 an example of the conductivity measurements is shown for an argon discharge. (Similar results have been obtained for a helium discharge.) As is seen from the figure, the conductivity has three distinct regions. The saturation at the lower electric fields ($E \lesssim 0.7$ V/cm) can be attributed to electron-neutral collisions. The conductivity in this region is roughly

[26] S. D. Fanchenko *et al.*, *Soviet Phys. JETP* (English Transl.) **19**, 337 (1964); S. M. Hamberger and M. Friedman, *Phys. Rev. Letters* **21**, 674 (1968).

[27] E. F. Field and B. D. Fried, *Phys. Fluids* **7**, 1937 (1964); L. M. Kovrizhnykh, *Soviet Phys. JETP* (English Transl.) **24**, 1210 (1967).

[28] O. Buneman, *Phys. Rev.* **115**, 503 (1959); V. D. Shapiro, *Soviet Phys. – Tech Phys.* (English Transl.) **6**, 376 (1961).

[29] H. Dreicer, *Phys. Rev.* **115**, 238 (1959).

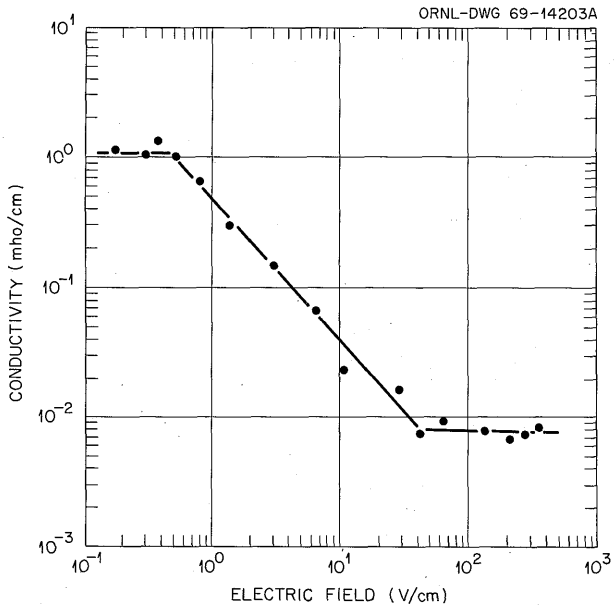


**Fig. 5.22. Conductivity vs Applied dc Electric Field.** The plasma density is normalized at $5 \times 10^9 \text{cm}^{-3}$, which was the density at the higher electric fields ($E \gtrsim 100$ V/cm). The gas pressure was varied to achieve the high electric fields.

proportional to $1/P$, where $P$ is the gas pressure. For $1 \lesssim E \lesssim 50$ V/cm, it is seen that

$$\sigma \propto \frac{1}{E};$$

that is, the current does not depend on the electric field. In this region, the plasma is strongly turbulent, continuously emitting strong low-frequency ($\lesssim 1$ MHz) oscillations (presumably ion acoustic waves) and an oscillation around 200 to 300 MHz, which has been identified as the electron plasma oscillation in a bounded plasma. The observed frequency roughly satisfies

$$\omega \cong \omega_{pe} \frac{a}{l},$$

where $a$ is the plasma radius and $l$ is the plasma length. For further increases in the electric field, the conductivity saturates at a value of ~0.01 mho/cm, which is on the order of the Buneman-Shapiro conductivity[28] but is an order of magnitude lower than that which has been reported for a transiently turbulent plasma.[26] In this high-resistivity region, the plasma is even more turbulent, and its rf spectrum is characterized by the appearance of an additional strong oscillation with frequency in the range 0.5 GHz $< f <$ 2.0 GHz (Fig. 5.23). This frequency is tentatively identified as the electron plasma frequency, since the observed frequency is roughly proportional to $(I_d)^{1/2}$ and since the electron density obtained from the Langmuir probe measurements at the mildly turbulent state agrees well with the density calculated from the observed frequency. We have not, however, been able to observe any rf emission in the vicinity of the Buneman frequency,[28]

$$\omega = \left(\frac{m}{M}\right)^{1/3} \omega_{pe} .$$

The $1/E$ dependence of the conductivity in the range $1 \lesssim E \lesssim 50$ V/cm qualitatively agrees with theory on the ion-acoustic instability.[27] However, the electron drift velocity determined from the current and the plasma density is already on the order of the electron thermal velocity, being much higher than the critical drift velocity required for the onset of the ion-acoustic instability. Further study will be required to resolve this apparent contradiction.

For higher electric fields ($E \gtrsim 50$ V/cm), we have an additional means to determine the drift velocity since we have the resonance condition

$$\omega_{pe} \cong k V_d ,$$

where $\omega_{pe}$ and $k$ are measurable (Fig. 5.23). The drift velocity at $E$ = 50 V/cm, for example, is $7 \times 10^8$ cm/sec when estimated from $\omega_{pe}/k$ and $8 \times 10^8$ cm/sec when calculated from the current density. The two values are in good agreement. Being different from transient turbulence, in which the instability ceases to grow after a relatively short interval of time, the electron drift velocity is expected to saturate at some critical value for the onset of the turbulence. It is known that the critical velocity for the two-stream instability is on the order of the electron thermal velocity. Thus we can estimate the electron temperature from the drift velocity. The value $7 \times 10^8$ cm/sec, for example, gives $T_e \cong 100$ eV.

An upper limit on the ion temperature has been established spectroscopically, being that $T_i \lesssim 1$ eV. Initially, we had anticipated that in such a strongly turbulent plasma the ions might be heated significantly. Since the electron-ion collision time is extremely long, however, compared with the ambipolar diffusion time (which also, of course, limits the electron temperature), the ions escape from the plasma before thermalization takes place, so that the observed lack of ion heating is,

ORNL-DWG 69-14204

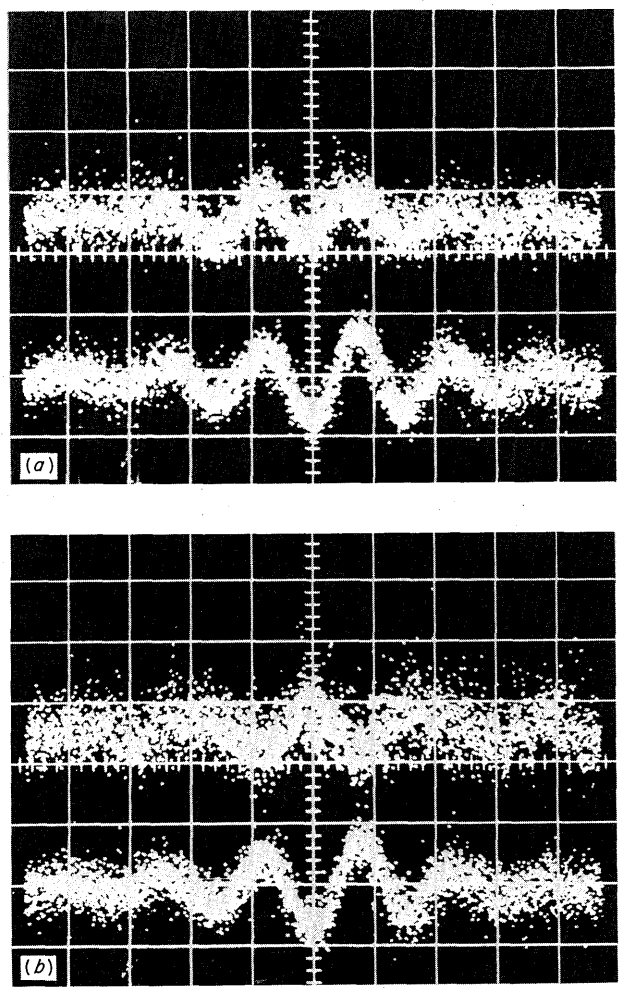


**Fig. 5.23. High-Frequency Oscillations Observed in a Strongly Turbulent Regime.** Note the phase shift ($\sim\pi$) as the probe separation is varied (relative distance change $\cong$0.5 cm). This gives a wavelength of 1 cm, which gives a phase velocity of $6.7 \times 10^8$ cm/sec. This value is in good agreement with the drift velocity. The wave propagation is in the direction of the electron drift, that is, from the cathode side to the anode side.

perhaps, not too surprising. The addition of an axial $B$ field to provide better confinement may increase the ion heating.

We estimate the intensity of rf oscillation at the electron plasma frequency to be on the order of 100 V/cm, or larger. That is, the turbulent electric fields are on the order of the applied dc field, which is, presumably, an upper limit for the turbulent fields. To reach an electric field greater than 100 V/cm at the surface of the discharge tube requires that essentially *all* of the electrons are removed from the plasma by the rf; that is, $\Delta N_e/N_e \approx 1$, which implies that this is the largest level of electrostatic turbulence possible.

Since the effective collision frequency $\nu_{\text{eff}}$ is approximately given by

$$\nu_{\text{eff}} \cong \omega_{pe} \frac{E^2}{8\pi n T_e} ,$$

where $E$ is the turbulent electric field, $n$ is the plasma density, and $T_e$ is the electron temperature, we find the degree of turbulence

$$\frac{E^2}{8\pi n T_e} \cong 0.05$$

or

$$E \cong 400 \text{ V/cm}$$

at our highest turbulent regime. This also supports the above estimate.

In summary, we have measured the conductivity of a steady-state plasma in which the degree of turbulence can be varied over a wide range. For the nonturbulent case, the observed conductivity is just the conductivity due to electron-neutral collisions. As the relative ion-electron drift velocity becomes comparable with the electron thermal velocity, the plasma develops strong turbulence, and the conductivity is greatly reduced, exhibiting a $1/E$ dependence in qualitative agreement with the prediction for the ion-acoustic-wave instability. For applied dc electric fields $\gtrsim$50 V/cm, the conductivity saturates at the Buneman-Shapiro value, being about an order of magnitude less than that reported earlier for a transiently turbulent plasma. For the strongly turbulent case, the electron temperature is inferred to be ~100 eV – about 100 times its initial value – whereas the ions do not seem to be significantly heated. The electric fields in the strongly turbulent plasma at the electron plasma frequency appear to be comparable with the applied dc electric fields.

The help of J. R. McNally with the spectroscopic measurements is greatly appreciated.

### 5.3.3 Finite Plasma Effects in a Reflex Discharge

W. L. Stirling

The Burnout series of experiments has developed a very potent means of converting the directed energy of beam electrons into random energy of plasma ions: namely, $T_i \approx 1$ keV, $n_i \approx 10^{13}$ cm$^{-3}$, and $\tau_i \approx 50$ $\mu$sec.

The present work represents a continuation of our effort (see Sect. 5.1 also) to understand the basic interaction mechanism in these devices. Earlier work showed the presence of intense Langmuir oscillations along the magnetic field inside the plasma-filled hollow anode of the present device.[30] We describe a parametric study of standing waves found outside the anode, which shows that the frequency depends on the geometry (length) of the plasma column.

A phenomenological model proposed by G. Guest suggests a two-step process: (1) self-modulation of the electron beam and (2) stochastic ion heating in the field of this beam. It is with the concept of self-modulation or beam bunching that we are concerned. The argument for beam bunching in Burnout V is based upon the observation of a wide band of rf in the vicinity of 1 GHz, the ion plasma frequency $\omega_{pi}$. Heating in this device is thought to be related to uncorrelated axial filaments of current (bunching) which live a time $\tau$ on the order of $2\pi/\omega_{pi}$ and which produce a stochastic azimuthal $E$ field. However, recent measurements of beam-produced x rays indicate that the entire beam density must be quenched in order to produce the observed electric fields (on the order of $10^4$ V/cm). Thus the relevance of beam bunching to ion heating is not clear.

The purpose of the experiment described herein is to test the first part of the phenomenological model and the influence of the system geometry on the frequency spectrum observed. To be applicable to the Burnout experiments, the argon-gas-fed reflex discharge of Fig. 5.24 was used.

In the model to be tested, it is assumed that

$$v_b \gtrsim \frac{\omega}{k_{\|}}, \tag{1}$$

$$L_s = \frac{n\pi}{k_{\|}}, \quad n = 1, 2, \ldots, \tag{2}$$

where $v_b$ is the beam velocity, $\omega$ is the oscillation frequency, $k$ is the wave number for propagation parallel to the magnetic field, and $L_s$ is a characteristic length of the system which determines a standing-wave pattern.

Eliminating $k_{\|}$,

$$f \lesssim \frac{n v_b}{2} \times \frac{1}{L_s}. \tag{3}$$

Equations (1) and (2) yield no information about the particular interaction mode of the beam-plasma system. In applying the parametric study suggested by Eq. (3), that is, $f$ vs $1/L_s$, one must be careful to ascertain that a particular mode of interaction is maintained throughout. To this end, our operation was adjusted to give rf signals as shown in the two traces of Fig. 5.25*a*. The top trace is probe No. 1, and the bottom is probe No. 2. This was taken on a sampling oscilloscope at a sweep speed of 0.5 $\mu$sec/cm. By expanding the sweep, it is seen

[30] Igor Alexeff and Wm. Denver Jones, *Basic Interaction Producing Heating in the ORNL Mode II Pressure Gradient Arc*, ORNL-TM-2661 (June 1969).

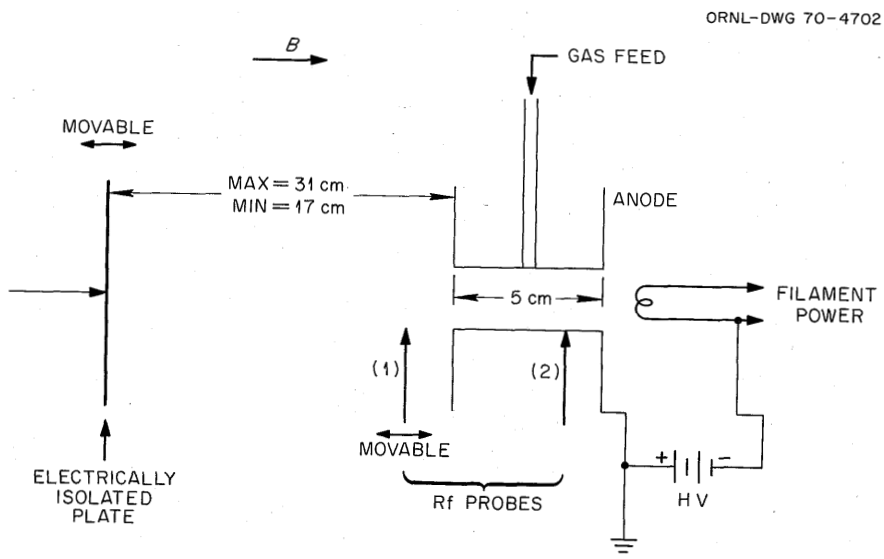


**Fig. 5.24. Reflex Discharge Schematic.**

PHOTO 98981

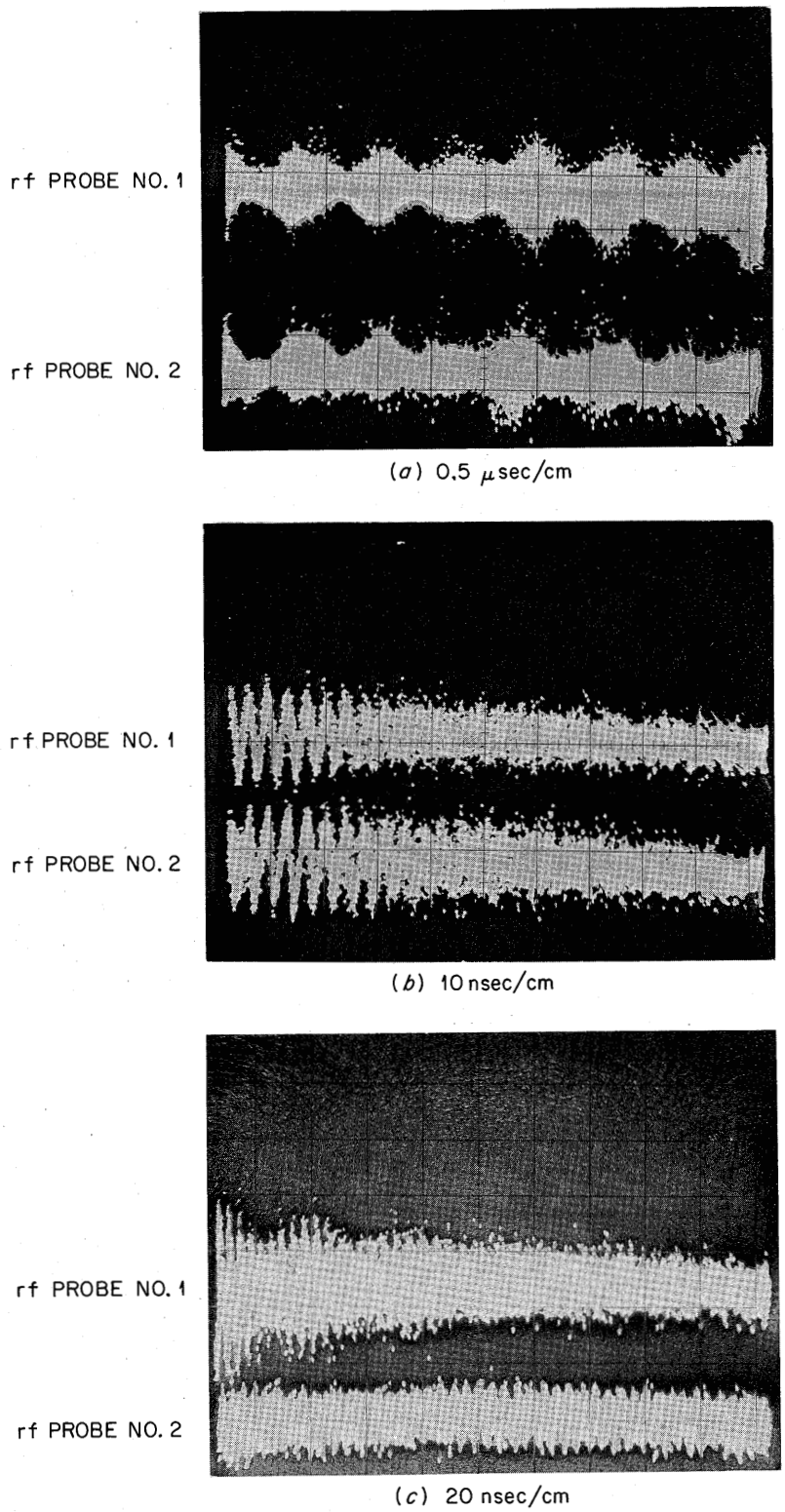


**Fig. 5.25. Typical RF Probe Signals.**

that the 1.3-MHz peaks in Fig. 5.25*a* are periodic chopping of the rf emission. The high-frequency rf is shown in the 250-Hz oscillations of Fig. 5.25*b*, which lose their coherence in about six cycles. The behavior depicted in Fig. 5.25*a* is defined as beam bunching. The current delivered by the arc high-voltage supply also shows a modulation in phase with the rf bunching.

A somewhat similar experiment has been reported by Apel.[31] In his experiment, a pulsed beam was used, and wave reflections were purposely minimized in order to measure the spatial growth rate of the waves. The similarity of arc operating parameters and observed frequencies suggests that the interaction seen here is the same as that identified by Apel: slow space-charge wave on the beam interacting with the space-charge wave in the plasma. Both this experiment (Fig. 5.25*c*) and Apel's exhibit a 30- to 50-MHz modulation of the high frequency under certain conditions. Apel designates this modulation frequency, which is equal to the ion plasma frequency in his experiment, as either (1) a participation of the ions in what is fundamentally an electronic plasma oscillation or (2) mixing of adjacent electron wave modes. Since this experiment uses argon gas and Apel used helium, there is a factor of 3 difference in ion plasma frequency, the densities being equal. Since the modulation frequencies are the same, this experiment favors the latter explanation. The electron mode mixing comes about from reflections which provide a positive feedback to the wave origin. Such an effect has also been seen by Simpson and Dunn.[32] The mode spacing of these waves is $\Delta f \approx v_b/2L \approx 70$ MHz, within a factor of 2 of that observed.

Figure 5.26 shows a plot of observed frequency vs $(L_s)^{-1}$, where $L_s$ is the anode-to-reflector spacing. The arc voltage and current were held fixed at 4 kV and 125 mA, respectively, except for two points indicated by open circles, at which the current is 200 mA. The fundamental frequency recorded on probe No. 1 is plotted; a lower-amplitude second harmonic was seen in many instances. The minimum value of $n$ shown is calculated from Eq. (3) and holds for all points at a given frequency. The bunching frequency stayed constant with $L_s$ except for the largest spacing. The higher frequencies seen with the higher beam currents are most likely due to higher plasma density.

The results shown in Fig. 5.26 clearly indicate that the system geometry is a dominant factor in determining the oscillatory mode, as are the beam current and voltage (the voltage effects are not shown). Assuming that the oscillation frequency is equal to the electron plasma frequency, as discussed above, the density at 500 MHz is about $10^9$ cm$^{-3}$ with $n = 4$. The $n$ values will be checked through use of the movable probe.

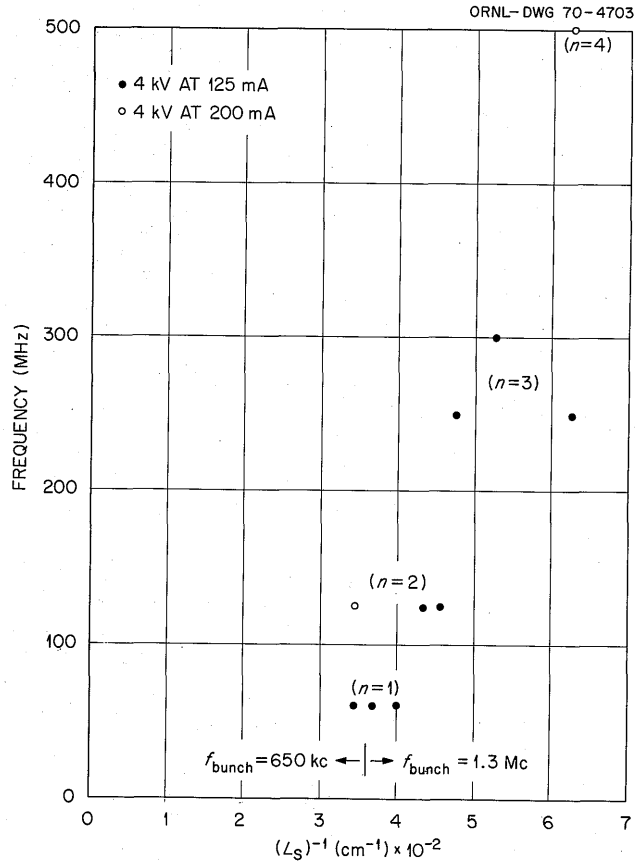


**Fig. 5.26. Characteristic Frequency as a Function of Arc Length.**

One attempt has been made with a gridded probe to detect ions with energies as low as 100 eV – resulting, for example, from the bunching. None have been seen. This is possibly due to the fact that there is no resonance between characteristic ion frequencies and the observed frequencies:

$$\left.\begin{array}{l} f \sim 60 \text{ to } 500 \text{ MHz} \\ f_{\text{modulation}} \sim 30 \text{ to } 50 \text{ MHz} \\ f_{\text{bunch}} \sim 650 \text{ kHz or } 1.3 \text{ MHz} \end{array}\right\} \text{observed}$$

$$f_{ci} \sim 10^5 \text{ Hz/sec}$$

$$f_{pi} \sim 2 \times 10^6 \text{ Hz/sec}$$

[31] J. R. Apel, *Phys. Fluids* **12**, 291 (1969).

[32] J. E. Simpson and D. A. Dunn, *J. Appl. Phys.* **37**, 4201 (1966).

By changing ion species and/or density, an attempt will be made to make an observed frequency equal to a characteristic frequency, for example,

$$f_{pi} \approx f_{\text{bunch}} \cdot$$

To this end helium will be more useful than argon.

### 5.3.4 Investigation of a Glass Liner in a Small Burnout Unit

I. Alexeff W. D. Jones

High ambient gas pressures limit plasma lifetime in the Burnout plasmas. Even for large dense plasmas, Franck-Condon neutrals resulting from dissociation of the hydrogen molecules penetrate the plasma and limit the plasma lifetime by charge exchange. It was recently proposed that perhaps the molecular density in such a machine could be effectively reduced by making the liner of the machine out of a ceramic material, thereby eliminating atom-atom recombination at the wall.[33] We have recently made some preliminary experiments to investigate this idea. The results to date indicate that in the small-scale burnout machine tested a Pyrex glass liner does not result in an appreciable reduction of the molecular gas $H_2$ vs H at the center of the plasma, when compared with that present in the same machine under approximately the same conditions but with a mostly metal liner.

In the experiment a grating spectrometer was used to make radial scans of the plasma column to measure the relative intensities of the excited atomic radiation at ~4861 Å and the excited molecular radiation at ~4634 Å. To permit radiation from the mostly metal liner experiment to be observed, a narrow section of the cylindrical liner at the midplane was made of glass. Thus far, comparisons have been made of the data only for the light emission when the spectrometer was scanning the central region of the plasma. These comparisons indicate, perhaps, a slight decrease in the absolute magnitudes of the $H^0$ and $H_2{}^0$ light when the glass liner is used; however, the ratio of $H^0$ to $H_2{}^0$, perhaps a more meaningful quantity, seems to be somewhat less for the glass liner. A perhaps relevant observation is that the glass liner becomes rather quickly uniformly discolored, except at the midplane region, which is kept clean by energetic ion bombardment, by a brownish, as-yet-unidentified nonmetallic substance. Whether this substance may be leading to a reversal of the empirically known non-catalytic effect of clean Pyrex glass for atom-atom recombination at its surface is not presently known. These preliminary results, however, make it seem doubtful that Pyrex glass liners in the burnout machine are going to be extremely helpful in solving the neutral-gas problem.

[33] I. Alexeff, *Thermonuclear Div. Ann. Progr. Rept. Dec. 31, 1968,* ORNL-4401, p. 112.

### 5.3.5 Computer Simulation of Ion Sheath Formation and Ion Bursts by Numerical Solution of the Vlasov Equation

K. Estabrook[34] I. Alexeff
M. Widner W. D. Jones

The ion distribution function was solved by numerical integration of the Vlasov equation using the "forward-backward" difference method[35] self-consistently with Poisson's equation. We scaled

$$\frac{\partial f}{\partial t} + \mathrm{v}\frac{\partial f}{\partial x} - \frac{e}{m}\frac{\partial \phi}{\partial x}\frac{\partial f}{\partial \mathrm{v}} = 0$$

to dimensionless quantities by $x = \hat{x}\lambda_D$, $\mathrm{v} = \hat{\mathrm{v}}\mathrm{v}_a$, $\phi = \hat{\phi}kT_e/e$,

$$t = \hat{t}/\omega_{pi} ,$$

and we assumed that for each time step the electron distribution function becomes a Maxwellian under a potential:

$$f_e = n_0 \sqrt{\frac{m_e}{2\pi kT_e}}\, e^{-(m_e \mathrm{v}_e^2/2kT_e)-(e\phi/kT_e)} .$$

We check the accuracy by the second moment of the Vlasov equation and by conservation of ion, electron, and electrostatic energy. We find that the accuracy is better than 1% in both checks.

Computer experiments thus far have examined sheath formation around a grid, collapse of the sheath producing an ion burst, and termination of the pulse producing a burst.[36,37] The burst has a velocity corresponding in

[34] ORAU Graduate Fellow, University of Tennessee, Knoxville.

[35] R. D. Richtmyer and K. W. Morton, *Difference Methods for Initial Value Problems,* Wiley, Interscience, New York, 1967.

[36] I. Alexeff *et al., Phys. Fluids* **12,** 345 (1969).

[37] I. Alexeff, W. D. Jones, and K. Lonngren, *Phys. Rev. Letters,* **21,** 878 (1968).

energy to the exciting potential with a spread in energy that is in qualitative agreement with low-energy bursts observed in the laboratory. Due to the low energy of the burst ($2kT_e$) we have not seen the multiple bursts upon sampling the ion density as a function of time, but we do notice four humps[38] in the distribution function in the vicinity of the grid at time about $0.5\nu_{pi}^{-1}$.

At time $t = 0$ the ion distribution function is initialized a Maxwellian. At time $t = 0+$ a negative pulse ($-2kT_e/e$) is placed on the grid. According to the electron model where $n_e = n_0 e^{-\phi/kT_e}$, the electrons are immediately blown out before the ions move, creating a transient sheath. The ions now react to the potential and move toward the grid. The ions oscillate in $x$ space and swirl in phase space with a frequency and amplitude depending on the initial positions of the ions. When the pulse is released, the energetic ions are ejected by the then positive potential and the ion kinetic energy.

Figure 5.27 shows contours of the ion distribution function in phase space for one-dimensional infinite sheets of plasma surrounding a negatively pulsed grid. The time is 0.25 ion plasma period; the edge of the swirl is about 2 Debye lengths in $x$ space and about 2.5 $v_a$ lengths in velocity space, where

$$v_a = \sqrt{\frac{kT_e}{m_i}}.$$

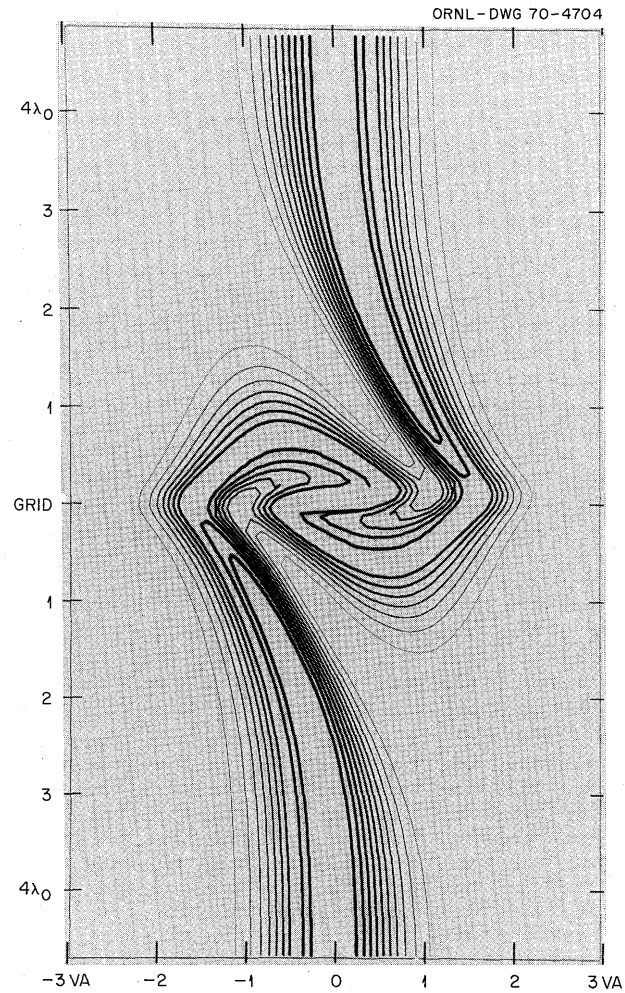


**Fig. 5.27. Diagram of Contours of the Ion Distribution Function in Phase Space for One-Dimensional Infinite Sheets of Plasma Surrounding a Negatively Pulsed Grid.** Positive $x(I\,\Delta x)$ is downward and positive $v_x(-v_0 + J\,\Delta v_x)$ is to the right.

## 5.4 DIAGNOSTICS

### 5.4.1 Introduction

R. V. Neidigh

Two diagnostic techniques with general application are described: (1) a correlator with auto- and cross-correlation capabilities useful for describing the power spectrum up to 50 GHz in what would otherwise appear to be random noise; (2) an HCN laser, 337 $\mu$, for measuring $\int n\,dl$ for plasma densities as low as $10^{12}$ $cm^{-3}$ over a path length of a few centimeters.

### 5.4.2 Correlators

W. R. Wing[39]

As is well known, a random process may be equally well described by its characteristic function or by its probability density function.

Thus, given the probability density function of, say, the electric field in a turbulent plasma, we would have as much information about the electric field as is allowed by statistics. Since in general we are completely unable to measure any of the joint probability densities, we must be satisfied with less.

What we can measure are the moments of the joint probability densities:

$$\alpha_{ij\ldots n}(t_1, t_2, \ldots) = \iint\ldots\int\int\ldots\int x_1^i x_2^j \,,$$
$$\ldots P_{x_1 x_2 \ldots}(x_1 t_1, x_2 t_2, \ldots, x_n t_n)\, dx_1\, dx_2 \ldots dx_n$$

at times $t_1, t_2, \ldots, t_n$. For example (say the field strength again), in one dimension the first moment,

[38] I. Alexeff, W. D. Jones, and M. Widner, *Multiple Pseudo-waves Produced by a Single Voltage Pulse,* ORNL-TM-2656 (July 22, 1969).

[39] Student guest, University of Iowa, Iowa City.

$$\alpha_1 = \int E\,P(E)\,dE\,,$$

is the mean value, and the second moment,

$$\alpha_2 = \int E^2\,P(E)\,dE\,,$$

is the mean square, and so on. Of particular importance are the second-order joint moments at the instants $t_1$ and $t_2$:

$$\alpha_{ij}(t_1, t_2) = \int\int E_1{}^i E_2{}^j\,P_{E_1E_2}\,(E_1t_1, E_2t_2)\,dE_1\,dE_2\,,$$

the cross-correlation function, and $\alpha_{ii}$, the autocorrelation function.

A correlator also has immediate practical diagnostic applications. For instance, a correlator can sort out the frequencies and wave numbers of an almost arbitrarily large number of waves which may be present in a plasma. This is immediately obvious if one thinks in terms of frequencies and phase velocities. If a wave with velocity v is moving past a set of probes spaced a distance $x$ apart, the cross correlation of the signals from these probes will have its maximum at a time $\tau$ equal to $x/v$. In practice, when there are many signals present, the sorting is done on a computer by taking the two-dimensional Fourier transform of the correlation function. The correlation function of $x$ and $\tau$ is thus converted to a power spectrum of $k$ and $\omega$, and the desired information is then available.

As another application, we consider the well-known technique of measuring the impulse response of a system, while it is in operation, by injecting low-level noise and correlating the input and output signals. The technique can be directly applied to measuring lifetimes of ions in steady-state machines by measuring density fluctuations in the input gas or ion beam and correlating it with the signal from an analyzer monitoring the escaping plasma. By making the output analyzer energy selective one can directly measure lifetime as a function of energy. Thus the machine can be monitored continuously while other parameters are varied.

Starting in the summer of 1968 the first instrument capable of computing $\alpha_{ij}$ with a time resolution $(t_1 - t_2)$ of the order of $10^{-9}$ sec was built by the Basic Physics Group.[40] It demonstrated the principles involved but was limited by signal-to-noise ratio and needed to be refined.

[40] I. Alexeff, R. V. Neidigh, and W. R. Wing, *Intern. J. Eng. Sci.* 7, 531 (1969).

In October 1969 work was resumed with the intention of improving the time resolution, the signal-to-noise ratio, and the data handling ability and possibly of extending the machine to higher-order moments $\alpha_{ijk}$ and $\alpha_{ijkl}$. (The fourth order probably represents a practical limit.)

Figure 5.28 illustrates the improvement in signal-to-noise ratio achieved from the summer of 1968 (Fig. 5.28*a*) to November 1969 (Fig. 5.28*b*).

### 5.4.3 Far-Infrared Laser-Interferometer

J. N. Olsen[41] C. E. Nielsen[42]
R. V. Neidigh

An HCN laser, emitting at a wavelength of 337 $\mu$, has been developed and coupled with a Michelson interferometer for electron density measurement on Burnout V. The intrinsic interest in this laser is that its useful density range bridges those of 4-mm microwaves at the lower and the $CO_2$ laser at the higher densities. The resulting density measurement has the advantage of being direct and therefore temperature-independent (see Fig. 5.3).

Since the electrons are cold ($T_e \cong 2$ eV) and the electron cyclotron frequency is small, the index of refraction at this wavelength is given simply by

$$n = (1 \text{ to } 1.015 \times 10^{-16}\,n_e)^{1/2}\,,$$

where $n_e$ is in $\text{cm}^{-3}$. For densities $n_e \ll 10^{16}\ \text{cm}^{-3}$, the single-pass phase shift is

$$\phi_p = (5.45 \times 10^{-13}\ \text{degree cm}^2)\,n_e\,dl\,.$$

We first consider the essential details of the laser-interferometer and then consider the results from its application to the Burnout V plasma.

**5.4.3.1 The HCN Laser.** – The laser is substantially unchanged from the previous report;[43] however, several aspects of its performance have been investigated, such as power with various gas mixtures, polarization characteristics, and modes of operation.

Several gas mixtures were tested for continuous wave operation. Methane-nitrogen-hydrogen and *n*-propyl amine–nitrogen–hydrogen (see Fig. 5.29) mixtures were each found to give the same power as the earlier

[41] NSF Trainee and ORAU Graduate Fellow, Ohio State University, Columbus.

[42] Consultant, Ohio State University, Columbus.

[43] *Thermonuclear Div. Ann. Progr. Rept. Dec. 31, 1968,* ORNL-4401, pp. 138–41.

PHOTO 98982

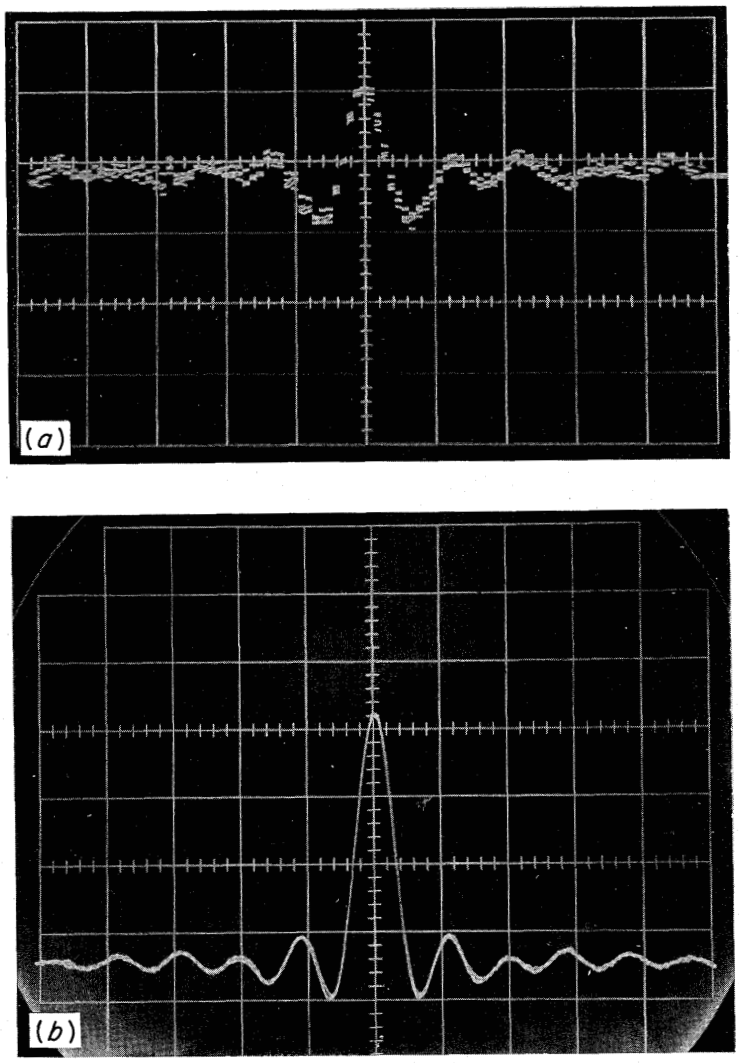


**Fig. 5.28. Typical Correlation Functions.** (*a*) Measured in August 1968; (*b*) measured in November 1969. Note improved resolution and signal-to-noise ratio. The vertical axis in both pictures is signal amplitude in arbitrary units, and the horizontal axis is $\tau$. For signals from Burnout V, $\tau$ typically varies from 50 nsec/div to 100 psec/div. Note that $\tau = 0$ is placed at the center of both photographs.

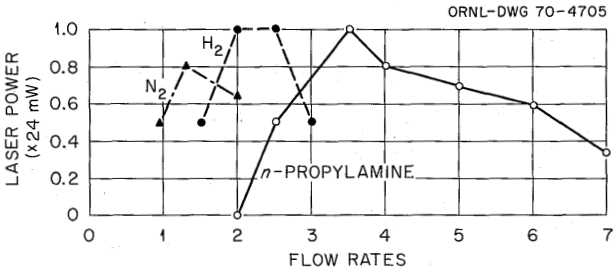


**Fig. 5.29. Laser Power as Each Gas Flow Rate Is Varied Separately.**

methyl cyanide–hydrogen fill. Ether-nitrogen-hydrogen failed to lase, while the addition of helium to the $CH_3CN$-$H_2$ mixture resulted in up to 35% power increases. For ease of operation and adjustment of power the two-gas, $CH_3CN$-$H_2$, fuel is preferable.

Polarization of various modes was measured with a rotating gold grating polarizer (1000 lines per inch on a Mylar backing). Different modes showed 50 to 100% polarization, vertical or horizontal, depending upon the particular mode. An internal horizontal 3-mil copper wire results in 80 to 100% vertical polarization accompanied by 50% power decrease. Since the plasma

electron cyclotron frequency is only 8% of the laser frequency, the laser was used unpolarized for higher power.

The importance of single-mode operation for high power is seen in Fig. 5.30, where the laser tuning mirror moves through several resonances and modes of each line. The power increase in the 337-$\mu$ emission is clearly seen as the 311-$\mu$ line falls off coincident resonance. This feature allows easy identification of single-mode 337-$\mu$ operation.

**5.4.3.2 The Interferometer.** – The basic laser-interferometer schematic is shown in Fig. 5.31. The total laser-to-detector distance is about 8 m with the laser power focused to the waveguide leading to the detector. Alternatively the laser may be focused to the plasma, the planar mirrors and waveguide replaced by concave

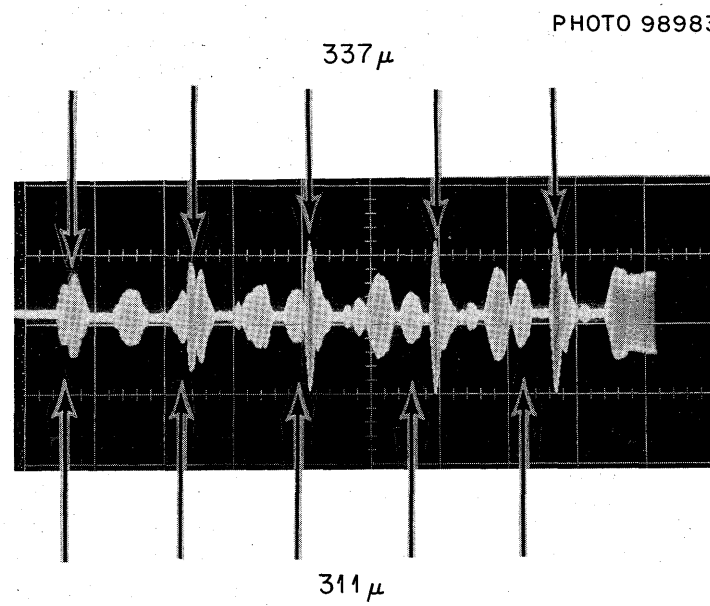


**Fig. 5.30. Laser Power as Tuning Mirror Travels Through Cavity Resonances.**

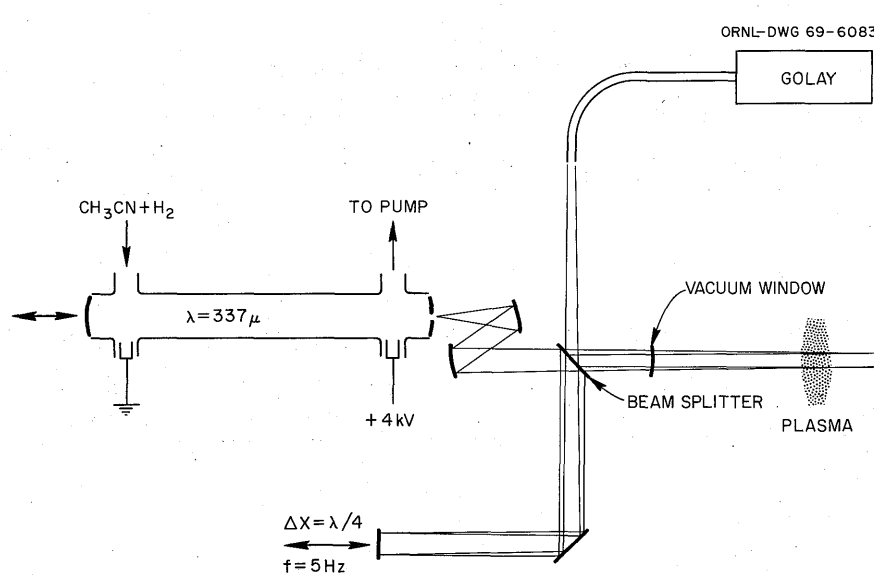


**Fig. 5.31. Laser-Interferometer Schematic.** Shown here focused to detector.

reflectors. The beam splitter and vacuum window are 2- and 7.5-mil Mylar respectively.

The reference path mirror is driven at 5 Hz by an eccentric wheel whose axle is $\Delta \approx \lambda/4$ off center. The resulting interferometer signal power is

$$P = \tfrac{1}{2} + \cos 2(\phi_p + kx) \sum_{\text{even}} (-1)^{n/2} \sigma_n J_n(2k\Delta)$$

$$\times \cos 2\pi n 5t + \sin 2(\phi_p + kx) \sum_{\text{odd}} (-1)^{(n+1)/2}$$

$$\times J_n(2k\Delta) \cos 2\pi n 5t ,$$

$$\sigma_n = \begin{cases} \tfrac{1}{2}, n = 0 \\ 1, n > 0 \end{cases},$$

where $\phi_p$ is the single-pass plasma phase shift and $kx$ is the phase difference between mirrors. Thus changes in $\phi_p$ or $x$ vary the relative magnitudes of even and odd harmonics. Fourier analysis of the interferometer signal with and without plasma leads to the phase shift and an averaged density line integral. Given a radial density scale length, this last quantity is converted into a central density.

The difference in sensitivity between the planar mirror and the focusing mirror interferometer depends upon the size of the laser beam relative to the plasma column. As the plasma becomes smaller than the laser beam, the radial averaging of the density line integral results in loss of sensitivity. For Burnout modes I and II, spectroscopic profiles predict no loss; however, the constricted mode III is sampled with only 40% of full sensitivity by the planar interferometer. The focused version should sense close to 100% of the maximum line integral.

It is possible to avoid Fourier analysis of the signal by mechanically translating the oscillating mirror in such a way as to compensate for the absence of plasma after turnoff. The difference between the micrometer readings gives a direct value for the phase shift. For simplicity the micrometer is set to obtain pure even harmonics with plasma and then is moved to re-null the odd harmonics after turnoff.

**5.4.3.3 Results.** – Table 5.1 shows the phase shifts, averaged line integrals of density, and inferred central densities for the several modes of plasma and laser-interferometer operation. Figure 5.32 shows a typical plasma on-off corresponding to 18° phase shift.

The mode II results for planar and focusing mirrors show good agreement, while the mode III values reflect the difference in sensitivity. The mechanical re-null was found to be direct but tedious at the time of data taking, whereas Fourier analyzing was very easy experimentally but time-consuming in the analysis process. An improved data system will remove the latter problem.

Future work will center on improving the statistics of the laser-interferometer for reliable data and on performing radial scans. Sensitivity of the laser-interferometer for reliable data appears to be about $1/40$ of a fringe; however, null results can place an upper limit on plasma density as low as $1/100$ of a fringe.

**Table 5.1. Summary of Laser-Interferometer Measurements on Burnout V**

| Burnout V Mode | Phase Shift | | $\langle \int n_e\, dl \rangle$ (cm$^{-2}$) | $n_e(0)$ (cm$^{-3}$) |
|---|---|---|---|---|
| | Planar | Focused | | |
| I | 34.4° | | $3.2 \times 10^{13}$ | |
| II | | | | |
| Warm | 17.2° | | $1.6 \times 10^{13}$ | $5.3 \times 10^{12}$ |
| Warm | 19° (re-null) | | $1.7 \times 10^{13}$ | $5.5 \times 10^{12}$ |
| Hot | 11.3° | 11.1° | $1.0 \times 10^{13}$ | $3.3 \times 10^{12}$ |
| III | | | | |
| 4.2 A | 4.6° | | $4.0 \times 10^{12}$ | $1.0 \times 10^{13}$ |
| 6.3 A | | 23.3° | $2.1 \times 10^{13}$ | $2.1 \times 10^{13}$ |

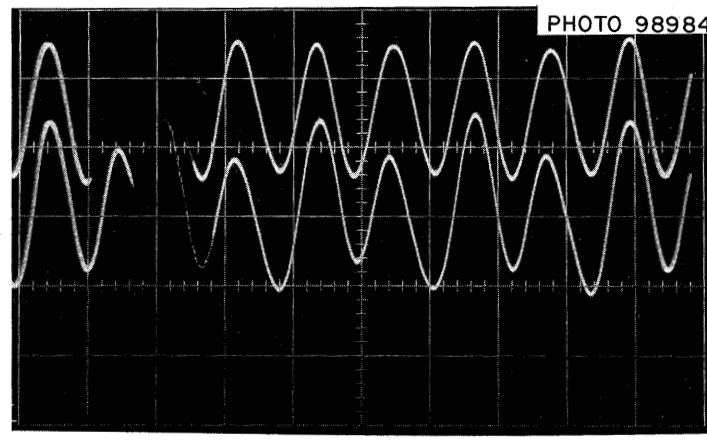


**Fig. 5.32. Laser-Interferometer Response to Plasma Turnoff.** Top trace: mode II plasma on; bottom trace: after plasma is turned off (0.1 sec/cm horizontal sweep).

# 6. Plasma Physics

## 6.1 WAVE STUDIES IN A UNIFORM MAGNETIC FIELD

### 6.1.1 Introduction

Two studies of ion acoustic waves, one of drift waves and one of an as-yet-unidentified slow wave, have been made in a plasma supported by a uniform magnetic field. Electron Landau damping of ion acoustic waves ($\omega \gg \omega_{ci}$) has been investigated, both as a function of frequency and as a function of propagation angle with respect to the magnetic field, and excellent agreement with theory is found. In another experiment, it is found that a negatively pulsed wire probe perpendicular to the magnetic field instantaneously creates an ion-rich sheet along the entire length of the plasma column; ion acoustic waves which propagate perpendicularly to the magnetic field are simultaneously excited at all points on the ion-rich sheet. The phase velocity of drift waves excited via a grid in a magnetically supported plasma column and propagating across the column has been measured as a function of frequency for $\omega < \omega_{ci}$. Both the observed frequency dependence and frequency cutoff are in good agreement with theory. Finally, an as-yet-unidentified slow wave propagating perpendicular to the magnetic field with a velocity which varies directly as $\omega_{ci}$ has been observed.

### 6.1.2 Electron Landau Damping of Ion Acoustic Waves in a Uniform Magnetic Field

A. Hirose I. Alexeff W. D. Jones

The effect of a weak magnetic field ($\omega \gg \omega_{ci}$) on the electron Landau damping of ion acoustic waves has been experimentally investigated.[1] In earlier works,[2] we demonstrated that ion acoustic waves can propagate at an arbitrary angle with respect to an external magnetic field with no dispersion in velocity if the wave frequency is well above the ion cyclotron frequency. The Landau damping due to electrons, however, should be modified by the presence of the magnetic field as[3]

$$k_i = \pi^{3/2} \frac{f}{\beta_e \cos\theta}, \tag{1}$$

where $k_i$ is the spatial damping factor, $f$ is the wave frequency, $\beta_e$ is the electron thermal velocity, and $\theta$ is the propagation angle.

We followed the experimental procedures used in the contaminant Landau damping experiment of ion acoustic waves in a magnetic field.[2] The results are shown in Fig. 6.1. Except for the uppermost one, the theoretical curves were calculated from Eq. (1) for each propagation angle used in the experiment, with no adjustable parameters. The angle 88.5°, however, was *chosen* as the best fit for "perpendicular" propagation, since finite probe size, etc., make it impossible to resolve the exact angle of propagation to within better than about ±2°. The 88.5° data are of the correct order of magnitude and show the correct frequency dependence. For the other data, good agreement between experiment and theory is observed for both the angular and the frequency dependence.

### 6.1.3 Ion Acoustic Wave Excitation in a Weak Magnetic Field by a Virtual Transmitter

A. Hirose I. Alexeff W. D. Jones

We have experimentally demonstrated that the ion acoustic wave can propagate without velocity dispersion in a magnetic field if the wave frequency is well above the ion cyclotron frequency. In the present paper, we

---

[1] A. Hirose, I. Alexeff, and W. D. Jones, *Landau Damping of Ion Acoustic Waves in a Uniform Magnetic Field,* ORNL-TM-2678 (August 1969); *Phys. Fluids* **13,** 1290(1970).

[2] A. Hirose, I. Alexeff, and W. D. Jones, *Thermonuclear Div. Ann. Progr. Rept. Dec. 1968,* ORNL-4401, p. 120; *Dispersion Measurements of Electrostatic Ion Waves in a Uniform Magnetic Field,* ORNL-TM-2761 (December 1969); *Phys. Fluids* **13,** 1414(1970).

[3] K. N. Stepanov, *Soviet Phys. JETP* 8, 808 (1959).

demonstrate that a single wire exciter placed perpendicular to the magnetic field can excite the ion acoustic wave in two directions at once: one is directly from the exciter probe to the receiver probe, along $d_r$ (see Fig. 6.2), and the other is perpendicular to the magnetic field, along $d_\perp$.

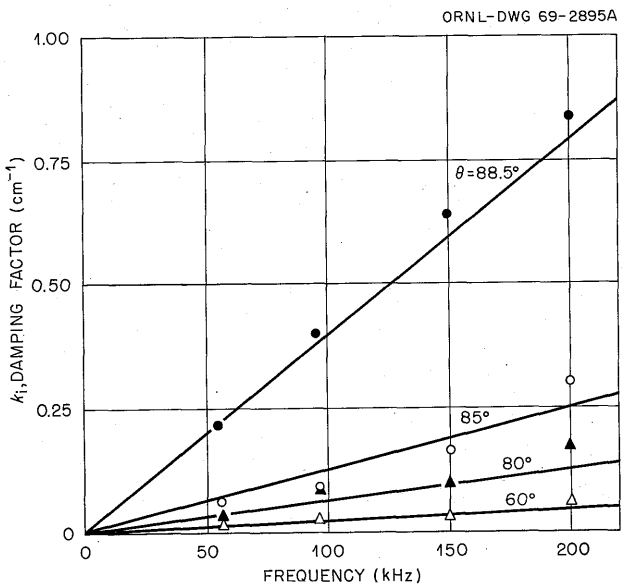


**Fig. 6.1. Damping Factor Plotted as a Function of Wave Frequency.** The solid lines are theoretical curves predicted by Eq. (1), while the points show the experimental values.

A xenon plasma with a diameter of 6 cm was used in the experiment. The electron temperature is 0.8 eV, and the electron density is on the order of $10^9$ cm$^{-3}$. The magnetic field was 400 G. A negative voltage pulse with a width of 4 $\mu$sec was applied to the exciter probe. Signals received are shown in Fig. 6.3. We notice that two signals ($B$ and $C$) are received at different times. The propagation time of signal $B$ depends only on the perpendicular distance $d_\perp$ between the two probes, $d_\perp = d_r \sin\theta$. The propagation velocity was found to be 7.8 $\times 10^4$ cm/sec.

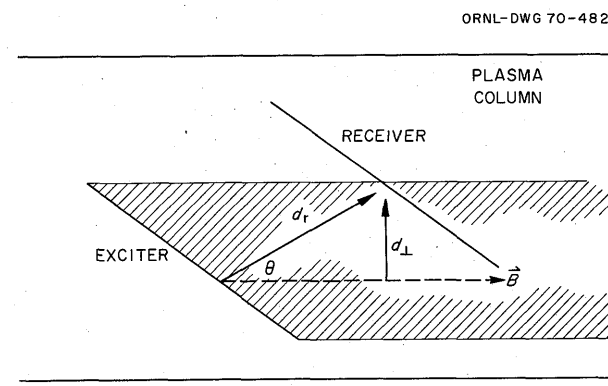


**Fig. 6.2. Schematic of Exciter and Receiver System.** Both wire probes are perpendicular to the magnetic field. $d_r$ is the direct distance between the two probes and $d_\perp$ is the perpendicular distance ($d_r \sin\theta$).

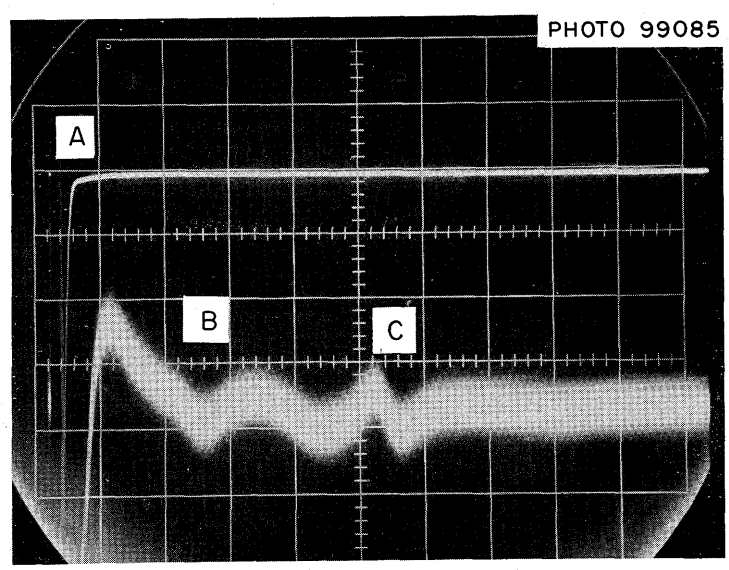


**Fig. 6.3. Propagation of Two Ion Acoustic Waves.** Signal $A$ is the exciting signal. Signal $B$ is due to the wave propagating over the perpendicular distance $d_\perp$ = 3.5 cm. Signal $C$ is due to the wave propagating over $d_r$ = 7.8 cm. Time scale is 20 $\mu$sec/cm.

The propagation time of signal $C$ depends on the distance $d_r$ from the exciter to the receiver, and the velocity was found to be $7.6 \times 10^4$ cm/sec.

Since the pulse width is much shorter than $\omega_{ci}^{-1}$ (ion gyration time), the ion acoustic wave can propagate isotropically (signal $C$).[2] The perpendicular propagation needs some explanation. Even though the magnetic field is weak, so that ions are almost free, electrons are completely bound to the field lines. Thus electrons can move only along the field lines, and the parallel electron pressure provides the waves with the restoring force. When a negative pulse is applied to the exciter, an ion-rich sheet is formed along the magnetic field. Since ions are not bound to field lines, the sheet acts as a virtual transmitter for the ion acoustic wave observed propagating perpendicularly to the magnetic field.

### 6.1.4 Dispersion Measurements of Externally Excited Drift Waves

A. Hirose W. D. Jones
I. Alexeff K. E. Lonngren[4]

The phase velocity of externally excited drift waves propagating perpendicularly to a uniform magnetic field has been measured as a function of the wave frequency ($<\omega_{ci}$).[5] The experimental results show good agreement with the simple dispersion relation[6]

$$\omega = \frac{\omega_*}{1 + k^2\rho^2}, \tag{2}$$

where $\omega_*$ is the drift frequency ($cT_e k_\perp / eBr_0$, where $c$ is the speed of light and $r_0$ is the $e$-folding distance for density decrease, i.e., the density-gradient constant), $k_\perp$ is the wave number perpendicular to the magnetic field, and $\rho_i = C_s/\omega_{ci}$, where $C_s$ is the ion acoustic velocity. In our experimental condition (xenon plasma, $T_e \cong 1$ eV, density gradient constant $\cong 1.2$ cm$^{-1}$), the cutoff frequency predicted by Eq. (2) becomes ~10 kHz, while the cutoff frequency experimentally found is about 9 kHz, being almost independent of the magnetic field up to 5 kG, as also predicted.

In Fig. 6.4, the phase velocity normalized by the drift velocity is shown as a function of the wave frequency for two different magnetic fields ($B$ = 3 kG and 4 kG). The theoretical curve is calculated from Eq. (2), using the experimental conditions. The agreement between experiment and theory is seen to be quite good.

### 6.1.5 Observation of Slow Waves Propagating Across a Uniform Magnetic Field

A. Hirose

Propagation of very slow unidentified waves in a magnetically supported plasma (Fig. 6.5) has been observed. A typical propagation pattern is shown in Fig. 6.6. The waves have the following distinct features:

1. Propagation is perpendicular to the magnetic field. ($k_\perp \gg k_\parallel$). No phase change was observed for variation of the distance between exciter and receiver along the magnetic field or the variation of the plasma length. The linear dependence of the propagation time on the distance between exciter and receiver implies that the propagation is perpendicular to the grid plane (i.e., no azimuthal component).

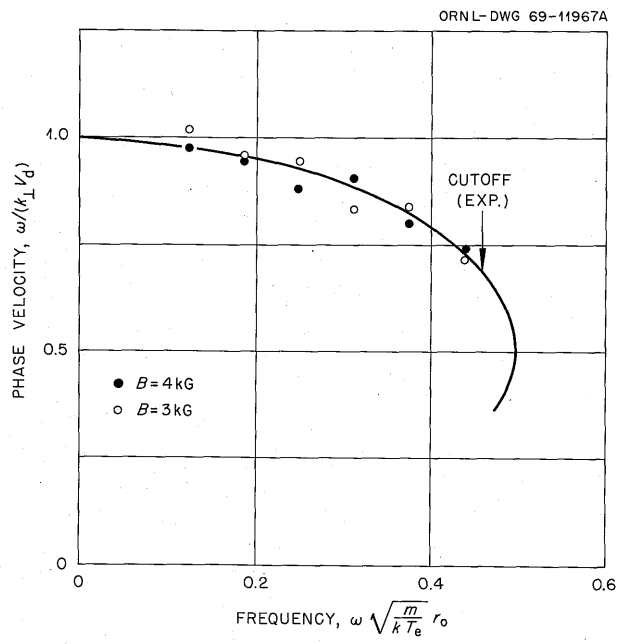


**Fig. 6.4. Phase Velocity vs Wave Frequency.** The phase velocity is normalized by the drift velocity, and the wave frequency is normalized by $r_0^{-1}\sqrt{T_e/m}$ (ion acoustic velocity times density gradient constant). The cutoff is observed to be approximately independent of magnetic field strength, as expected.

---

[4] Electrical Engineering Department, University of Iowa, Iowa City.

[5] A. Hirose and Karl Lonngren, *Bull. Am. Phys. Soc.* **14**, 1042 (1969).

[6] A. B. Mikhailovskii, *Reviews of Plasma Physics*, vol. 3, p. 182, ed. by M. A. Leontovich, Consultants Bureau, New York, 1967.

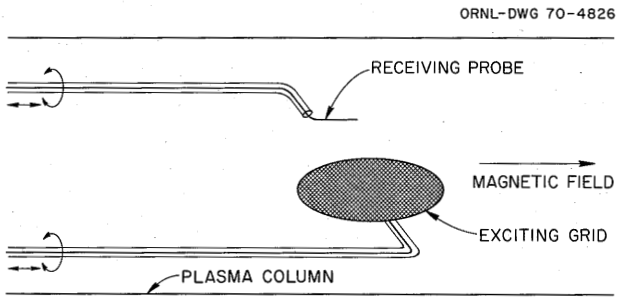


**Fig. 6.5. Schematic of the Apparatus Used in the Study of Unidentified Slow Waves.** The diameter of the plasma column is about 6 cm. The transmitter is a 6-cm-diam 100-mesh tungsten grid. The receiver is a 2-cm-long, 0.2-mm-diam tungsten wire.

2. The phase velocity is directly proportional to the magnetic field (Fig. 6.7).
3. The phase velocity seems to be inversely proportional to the atomic mass, although we have used only two different gases, xenon and argon (Fig. 6.7).
4. The wave does not appear to propagate for frequencies $\gtrsim 0.2\omega_{ci}$.
5. The propagation is fairly nondispersive, that is, the phase velocity does not depend on the wave frequency.
6. The phase velocity appears to be independent of plasma density.

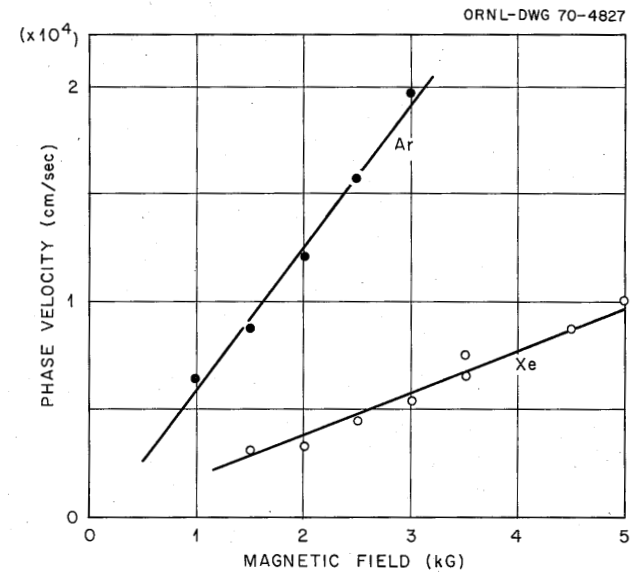


**Fig. 6.7. Phase Velocity vs Magnetic Field.** The wave frequency for the xenon measurement was 4 kHz and for the argon measurement was 8 kHz.

The empirically found dispersion relation is given by

$$\frac{\omega}{k_\perp} = A\omega_{ci} , \tag{3}$$

where $A \cong 3 \times 10^{-2}$ cm. We notice that the quantity $A$ has the dimension of length and is on the order of the

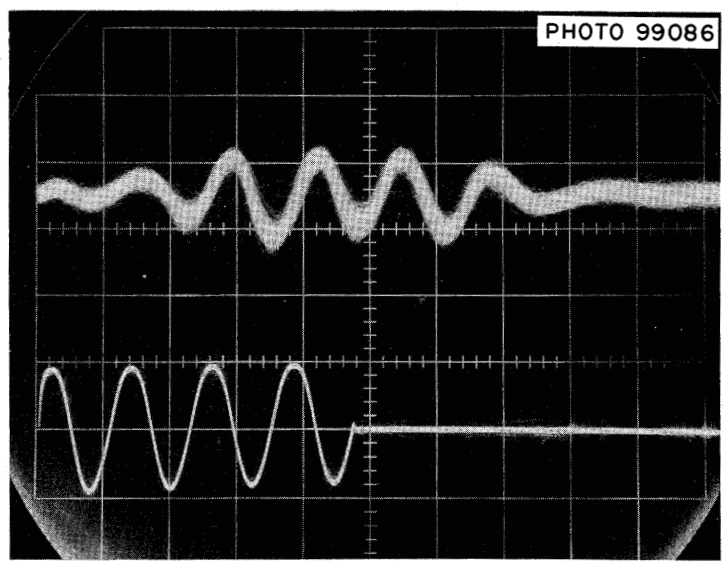


**Fig. 6.6. Typical Slow-Wave Propagation in Xenon Plasma.** The lower trace shows the transmitting signal (2 V/cm), while the upper trace shows the received signal (50 mV/cm). $B$ = 2.5 kG, $f$ = 4 kHz, probe separation = 2 cm, and time scale = 0.2 msec/cm.

Debye radius in our experimental condition ($T_e \cong 1$ eV, $n = 10^9$ cm$^{-3}$); however, as noted above in feature 6, $A$ is not density dependent. Further investigation is required to identify this wave.

## 6.2 COMPUTER SIMULATION STUDIES OF LOW-FREQUENCY NONLINEAR PLASMA BEHAVIOR

### 6.2.1 Introduction

W. D. Jones

Three computer simulation studies of low-frequency nonlinear plasma behavior have been made, all three being based on a model of cold fluid ions and hot background electrons in equilibrium. In the first study the evolution of the ion sheath around negatively biased cylindrical and spherical electrodes in a plasma is investigated. After the rapid establishment of an ion space-charge sheath near the electrode, a rarefying density disturbance propagates into the plasma at the ion acoustic wave speed. Within a short time the density disturbance becomes completely separated from the sheath region and propagates in the plasma, exhibiting all the characteristics associated with experimentally studied ion acoustic waves. In the second study an ion acoustic wave generated at an interior position in a plasma is allowed to propagate into a steady-state ion sheath at a planar boundary of the plasma. The simulation shows that the wave-sheath interaction produces a modification in the bulk plasma which resembles a dispersed phase-inverted reflection and which may be relevant to standing waves in discharge tubes under some conditions. In the third study the expansion of a plasma into a vacuum is computed. Except for a small group of ions which are quickly accelerated to a velocity of about $3(kT_e/m_i)^{1/2}$ and which lead the expanding plasma, the expansion takes place in a manner which was predicted analytically several years ago. In the analytic work, charge neutrality was required, whereas here it was not.

### 6.2.2 Ion Acoustic Wave Excitation and Ion Sheath Evolution

M. Widner W. D. Jones
I. Alexeff K. Lonngren[4]

A series of computer simulations and experiments have been performed to investigate the time evolution of an ion space-charge sheath on a negatively biased solid electrode in a plasma of cold ions and hot electrons. For a planar electrode we found that a rarefying disturbance was generated and propagated into the plasma at the ion acoustic wave speed; however, this density disturbance was always tied to the ion space-charge sheath on the electrode.[7]

We have now modified the planar computer model to allow for cylindrical and spherical electrodes and find that for a collisionless plasma the propagating density perturbation completely separates from the space-charge sheath and propagates out into the plasma as an ion acoustic wave.[8] Figure 6.8 shows the results for a spherical electrode ten Debye lengths in radius. In the figure the lower trace of each pair of traces represents the electron density. As the accentuated last trace shows, the density has regrown between the propagating disturbance and the space-charge sheath, representing the generation of an ion acoustic wave. The regrowth of the density is due to the geometrical convergence of the ions being accelerated toward the electrode. From the computer solutions we have calculated the coupling efficiency of the applied voltage in the wave-generation process, the main spectral components of the wave, the wave potential, and the so-called electron adiabatic compression coefficient $\gamma_e$

[7] *Thermonuclear Div. Ann. Progr. Rept. Dec. 31, 1968,* ORNL-4401, p. 134.

[8] Melvin M. Widner, *Computer Simulation of Fluid Motion in Plasmas,* Ph.D. thesis, University of Iowa, August 1969; M. Widner, I. Alexeff, and W. D. Jones, *Ion Acoustic Wave Excitation and Ion Sheath Evolution,* ORNL-TM-2754 (Oct. 9, 1969).

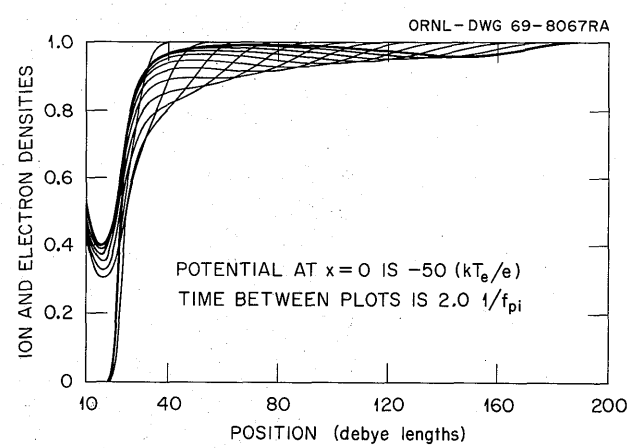


**Fig. 6.8. Computer Simulation of Ion Sheath Evolution Around a Negatively Pulsed Spherical Electrode.** As is shown by the accentuated last trace, a quasi-charge-neutral sheath is generated and a density disturbance propagates into the plasma as an ion acoustic wave.

and have found good agreement in all respects with experimental results.[7–11]

The addition of ion-neutral collisions as a drag force in the equation of motion of the computer model for cylindrical and spherical electrodes shows that the ion-neutral collisions interfere with the regrowth of the plasma density between the ion space-charge sheath and the propagating density disturbance, so that no separation occurs.

### 6.2.3 Interaction Between Ion Acoustic Wave and Sheath

M. Widner I. Alexeff W. D. Jones

Computer simulation of the nonlinear interaction of an ion acoustic wave with a Langmuir sheath shows that the motion of the wave in the sheath produces a modification in the bulk plasma which resembles a dispersed phase-inverted reflection. The model we use is similar to one previously used to study ion wave excitation,[7] with ion production added to match the steady-state boundary losses.[12] Initially a wave is launched at a steady-state ion space-charge sheath. The ion wave propagates to the sheath and is absorbed there, producing no reflection in the usual sense. There is, however, a distorted "reflection-like" response due to the disturbance of the steady-state production-loss balance of the plasma by the wave. This process is demonstrated in Fig. 6.9. We feel that this reflection-like process may be a mechanism which permits standing waves in discharge tubes under some conditions.

### 6.2.4 Expanding Plasma into a Vacuum

M. Widner I. Alexeff W. D. Jones

The expansion of a plasma into a vacuum was studied by computer simulation.[12] The model is similar to that previously used to study ion wave excitation: cold fluid ions and hot background electrons in thermal equilibrium.[7] The electron pressure couples electrostatically with the ions and accelerates them into the vacuum.

[9] I. Alexeff and W. D. Jones, *Phys. Rev. Letters* **15**, 286 (1965).

[10] H. Doucet, I. Alexeff, and W. D. Jones, *Phys. Fluids* **11**, 2451 (1968).

[11] M. Widner, I. Alexeff, and W. D. Jones, to be published.

[12] *Ibid.;* Melvin M. Widner, *Computer Simulation of Fluid Motion in Plasmas,* Ph.D. thesis, University of Iowa, August 1969.

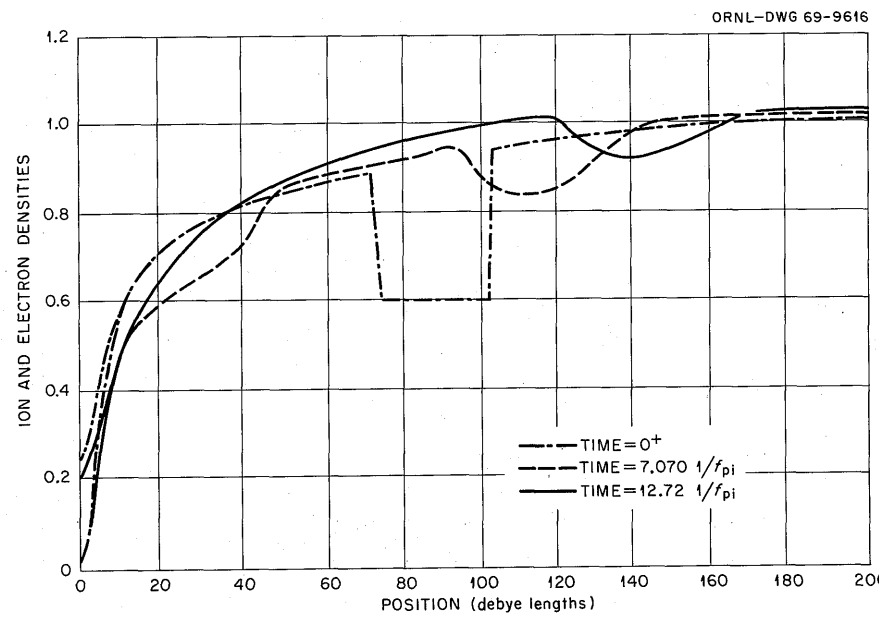


**Fig. 6.9. Computer Simulation of Ion and Electron Densities vs Distance at Several Different Times Relative to the Generation of Propagating Ion Acoustic Waves in the Plasma.** Each pair of traces represents the density profile at a particular time, with the electron density the lower trace of each pair. Three stages of the wave-sheath interaction are shown. Note that the interior plasma density rises above its steady-state value as the ion wave propagates into the sheath, representing a kind of phase-inverted "reflection."

At time = 0, a semi-infinite, one-dimensional, uniform charge-neutral plasma exists for $x \leqslant 0$, while there is a vacuum for $x > 0$. For the purposes of the simulation, a finite region of this space including the density discontinuity is used. As before, Poisson's equation is solved at each time step, allowing the electron density to adjust to the potential while the ions remain fixed. The potential is assumed zero at the plasma boundary, which is located at some point in the plasma far removed from the plasma-vacuum interface, while the electric field is zero at the vacuum boundary. The electric field obtained advances the ion velocity in time through the equation of motion, and the continuity equation advances the ion density in time. This sequence is iterated, advancing the quantities as far in time as desired.

This same model was used in an analytic description given by Gurevich *et al.*,[13] who obtained a self-similar solution:

$$n_e = n_i = 1 \text{ for } \frac{x}{t} < -1 \,,$$

$$n_e = n_i = \exp\left(-\frac{x}{t} - 1\right) \text{ for } \frac{x}{t} \geqslant -1 \,. \qquad (4)$$

[13] A. V. Gurevich, L. V. Pariiskaya, and L. P. Pitaevskii, *Sov. Phys. JETP* 22, 449 (1966).

Their solution handles some of the nonlinear aspects of the problems, although charge neutrality was assumed throughout. We treat essentially the same problem without assuming charge neutrality.

The solution we obtain is shown in Fig. 6.10. There is an initial acceleration of the leading edge of the plasma to a velocity of about $3\sqrt{kT_e/m_i}$. Charge neutrality breaks down at the leading edge, and a group of ions precedes the charge-neutral plasma flow. Except for the initial acceleration, our solution has the essential characteristics of a self-similar solution. The solution we obtain agrees almost exactly with the self-similar solution of Gurevich *et al.* for the charge-neutral regions.

## 6.3 PSEUDOWAVES

### 6.3.1 Introduction

W. D. Jones

Two studies of pseudowaves have been made. In the first, involving the "single" ion burst which is generated when a long negative voltage pulse is placed on a grid in a plasma, the pseudowave was found to exhibit reflection during the course of being energy analyzed. The maximum energy of the reflected ions varies approximately as the voltage on the positive grid of the energy analyzer up to the maximum energy possessed by the

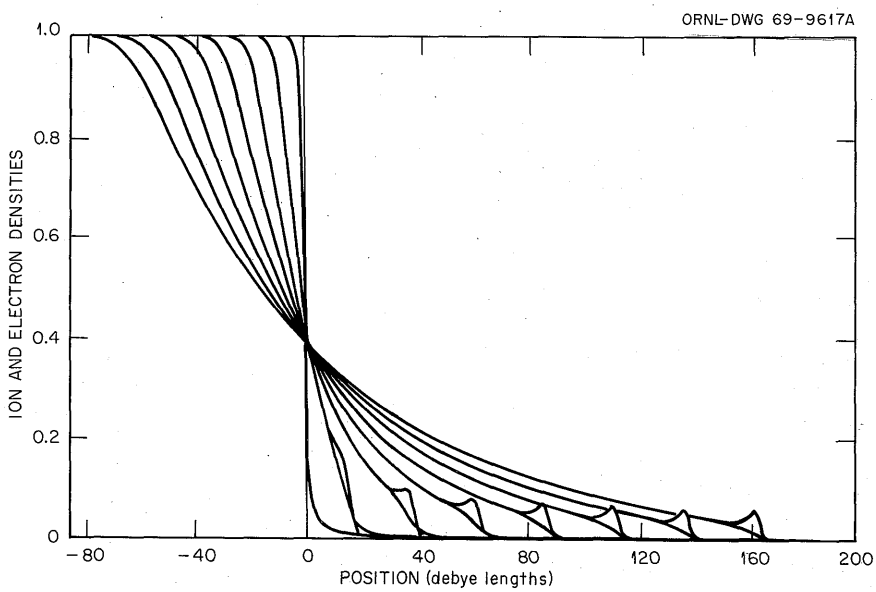


**Fig. 6.10. Computer Simulation of Plasma Expanding into a Vacuum.** The electron and ion densities vs distance are superimposed at several times. There is initially a step discontinuity in the ion density. The electron density leads the ion density into the vacuum, followed by a "bump" of unshielded ions. Following this group of ions is a flow of charge-neutral plasma. Meanwhile a rarefaction wave propagates back into the plasma at precisely the ion acoustic speed. The unshielded ion group is accelerated to a velocity of about $3\sqrt{kT_e/m_i}$. The time interval between plots is $1.4/f_{pi}$.

incident ions. In the second study of pseudowaves it was discovered that, if a sufficiently short negative voltage pulse is placed on a grid in a plasma, several ion bursts, each having a separate velocity, are created. These "multiple" pseudowaves have been explained in terms of ions trapped and oscillating in the ion sheath around the grid due to the negative voltage pulse. Quantitative agreement is found between the measured velocities of the separate ion bursts and a theory based on single-particle motion in a potential well surrounding a transparent grid.

### 6.3.2 Reflection of Pseudowaves

K. Estabrook[14] W. D. Jones
I. Alexeff K. Lonngren[4]

While using an ion energy analyzer[15] in a rare-gas discharge plasma[9,16,17] to analyze the energy of ion bursts,[18,19] we discovered that some ions were being reflected[20] by the analyzer. We describe here the salient features of a brief study made of these reflections.

The measurements were made in a quiescent xenon plasma with $T_e \approx 1.7$ eV, $T_i \approx 1/30$ eV, $N_e \approx 10^9$ cm$^{-3}$, and background pressure of about 0.1 $\mu$. The plasma was generated by an electron gun spraying 100-eV electrons into neutral xenon in a tubular glass cross. The burst[18] was generated by a 1-$\mu$sec pulse on a 90%-transparent fine-mesh grid. The pseudowave detector was a small positively biased wire probe[21] located between the transmitter grid and the energy analyzer.

The energy analyzer consisted of two grids and a plate enclosed in a boron nitride cylinder. The outer grid was biased −22.5 V to repel electrons. The next grid was the ion energy analyzer (or barrier) and was biased positively from 22.5 to 180 V. The collector plate was a flat copper plate.

Figure 6.11 shows six multiple exposures with the positions of the transmitter, detector, and reflector all fixed in space. The potential here is varied from 50 to 100 V in 10-V intervals. For the 100-V barrier, virtually all detectable ion current to the collector is gone, as shown by arrow $A$ at the top of Fig. 6.11. The reflected current peak is composed of the most energetic ions in the incident burst and is the first to arrive at the detector probe, as identified by $A$ on the bottom trace. For the 50-V barrier, most of the ions go across the barrier and appear as current on the collector (current trace $B$). The reflected ions in the pulse corresponding to the lowest barrier are the least energetic and are the last to arrive on the detector probe (trace $B$).

The maximum energy of the reflected ions increases roughly as the voltage of the potential barrier up to the maximum energy possessed by the incident ions.

In all cases the energy of the ions was measured by the free-streaming velocity of the current peak detected. Without the analyzer we made several measurements of the difference in velocity of the peak and the leading edge of the burst and found empirically that the velocity of the leading edge exceeds the velocity of the peak by the ion acoustic velocity within about an error of 5%, independent of the average energy of the pulse. This effect, which is just due to a thermally driven expansion of the burst,[22] allows pseudowaves to be used as a rough diagnostic for measuring plasma electron temperature, since ion acoustic velocity and electron temperature are related by

$$v_{\text{ion wave}} = v_{\text{leading edge}} - v_{\text{peak}} = (kT_e/m_i)^{1/2} .$$

The range of $T_e$ over which this relationship is valid has not been checked; in the present experiment, $T_e \sim 1$ eV. Almost certainly, however, $T_e$ must not be larger than approximately $eV_{\text{pulse}}/k$; otherwise the pseudowave would spread too rapidly for meaningful velocity measurements to be made.

### 6.3.3 Multiple Pseudowaves

I. Alexeff W. D. Jones M. Widner

A multiple pseudowave, or series of fast ion bursts (see Fig. 6.12), is generated when a short negative voltage pulse is placed on a transparent grid immersed in a plasma.[23] We show, using a single-particle model,

[14] ORAU Graduate Fellow from the University of Tennessee.

[15] H. Ikezi and R. J. Taylor, UCLA report R-42 (February 1969).

[16] W. D. Jones and I. Alexeff, *Proc. VIIth Intern. Conf. on Phenomena in Ionized Gases*, II, ed. by B. Perovic and D. Tosic, p. 330, Gradevinska Knjiga Publishing House, Belgrade, 1966.

[17] K. Lonngren *et al.*, *Phys. Letters* **25A**, 629 (1967).

[18] I. Alexeff, W. D. Jones, and K. Lonngren, *Phys. Rev. Letters* **21**, 878 (1968).

[19] I. Alexeff *et al.*, *Phys. Fluids* **12**, 345 (1969).

[20] J. R. Proni *et al.*, *Bull. Am. Phys. Soc.* **14**, 1042 (1969).

[21] I. Alexeff and W. D. Jones, *Phys. Letters* **20**, 269 (1966).

[22] Theory by I. Alexeff (unpublished).

[23] I. Alexeff, W. D. Jones, and M. Widner, *Multiple Pseudowaves Produced by a Single Voltage Pulse*, ORNL-TM-2656 (July 22, 1969); *Phys. Fluids* **13**, 1519(1970).

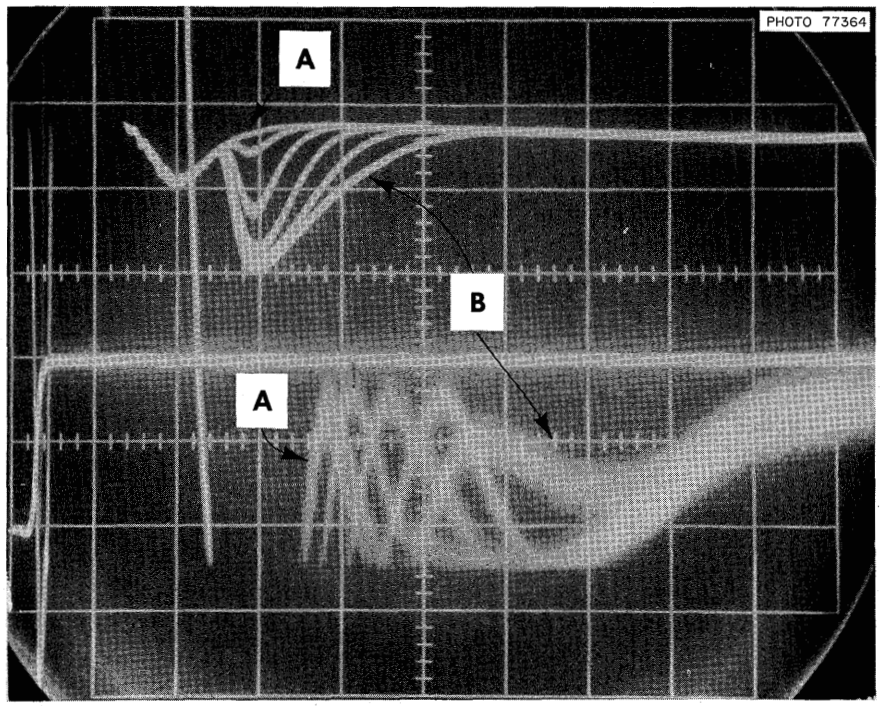


**Fig. 6.11. Oscilloscope Traces Showing Ion Burst Reflection as a Function of the Height of the Positive Potential Barrier.** Trace *A* shows the analyzer current for a potential barrier of 100 V (top) and the corresponding reflected burst (bottom); *B* shows the results for a potential barrier of 50 V. Note that the collector current increases as the reflected burst becomes slower. As the potential barrier is lowered, the reflected burst energy also lowers. Note also the long tail on the low-barrier collector current *B*, showing the wide distribution in velocity of the ions in the burst. Transmitter-reflector separation ~2.5 cm, with detector for reflected signal located at an intermediate position ~1 cm from reflector. Time scale = 1 μsec/cm. Vertical scale = 50 V/cm for center trace (pulse on transmitter) and 1 mV/cm for all other traces.

that multiple pseudowaves can be explained in terms of ions trapped and oscillating in the sheath formed around the grid by the negative voltage pulse. The theory gives

$$v_n = v_{max} \tanh\left(\frac{\omega_{pi}}{2n-1}\right)\tau\,, \tag{5}$$

where $v_{max} = \sqrt{2eV_0/m_i}$ ($V_0$ = amplitude of the negative voltage pulse), $\omega_{pi}$ refers to the ion density in the vicinity of the grid, $\tau$ is the width of the negative voltage pulse on the grid, and $n$ is the order in appearance of the ion bursts at the detector probe.

Figure 6.13 shows a quantitative comparison between the velocities predicted by Eq. (5) and the ion burst velocities measured experimentally. Since $\omega_{pi}$ refers to the density inside the ion sheath around the grid, we have allowed this to be a free parameter and have chosen the value which optimizes the overall agreement of experiment and theory. The value chosen gave a density approximately a factor of 2 less than that measured just outside the sheath by an ordinary Langmuir probe. Considering the fact that the simple model does not include collective effects or grid absorption, the agreement between experiment and theory is reasonably good.

Allowing $\omega_{pi}$ to be a free parameter allows a gridded probe, used in the manner discussed here, to be used as a simple diagnostic tool for measuring plasma density. Under optimum conditions densities over the entire range of $10^6$ to $10^{11}$ cm$^{-3}$ can be measured. The technique should also work in magnetic fields by propagating the pseudowaves along the field.

PHOTO 76779A

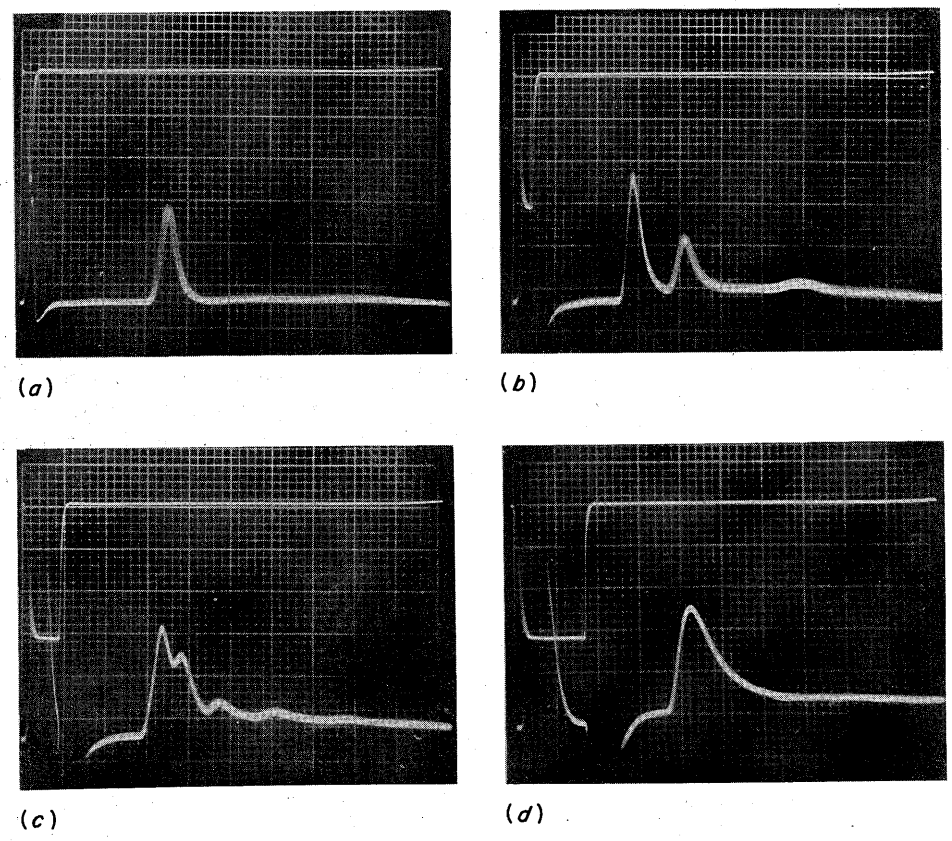


**Fig. 6.12. Detection by an Ion-Sensitive Probe of Energetic Ion Bursts (Lower Traces) Accelerated into the Plasma by a Negatively Pulsed Grid.** Only the width of the −160-V pulse (upper traces) was varied in this sequence of photographs. Sweep scale is 2 μsec per large division; transmitter-receiver separation was 6 cm.

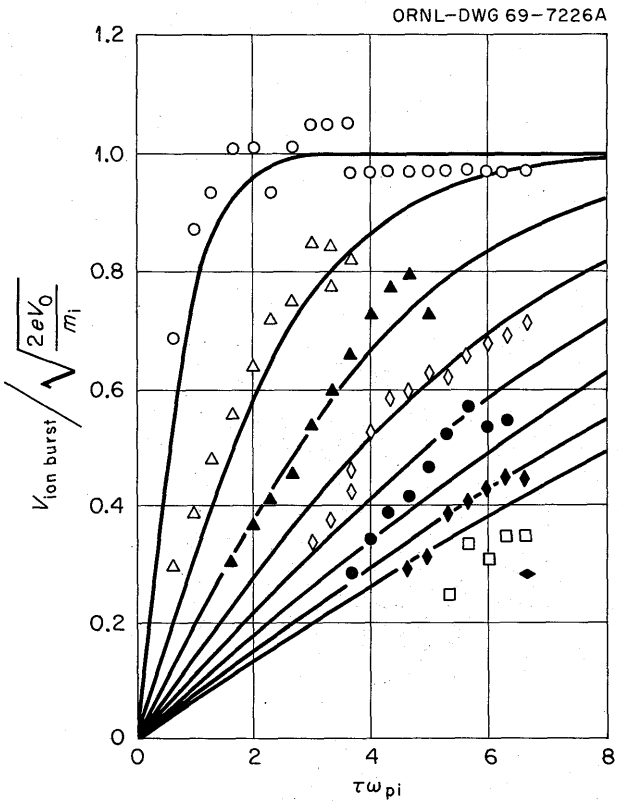


**Fig. 6.13. A Quantitative Comparison of the Experimentally Observed Variation of Multiple Pseudowave Velocities with Pulse Width and the Velocities Predicted by Eq. (5) for the Conditions of the Experiment.** The open circles correspond to the measured velocities of the first ion burst of the multiple pseudowave as a function of pulse width $\tau$, while the solid curve passing through these points shows the theoretically expected variation. The open triangles next to the open circles, and the accompanying solid curve, refer to the second ion burst, etc. Letting $\omega_{pi}$ be a free parameter, so as to optimize agreement of experiment and theory, allows a pulsed gridded probe to be used as a simple diagnostic for measuring plasma density.

## 6.4 DIAGNOSTIC TECHNIQUES

### 6.4.1 Introduction

W. D. Jones

Two techniques have been discovered for measuring plasma density; one of these seems to be valid for measuring electron temperature also. In the first technique, a negative pulse on a grid in a plasma causes pseudowaves to be generated. By studying the velocity properties of the pseudowaves, both the ion density and the electron temperature can be determined. By propagating the pseudowaves along field lines, this technique should also be applicable to magnetically supported plasmas. In the second technique, which has been successfully tested only in magnetically supported plasmas, a negatively biased grid parallel to the magnetic field lines is found to excite plasma oscillations near the grid plane at the ion plasma frequency. This oscillation, from which the ion density can be calculated, may be a cross-field ion instability which was just recently predicted theoretically.[24]

### 6.4.2 A Pulsed Grid for Measuring Plasma Ion Density and Electron Temperature

I. Alexeff W. D. Jones M. Widner

As was noted in Sect. 6.3.3 of this report and as is described more fully elsewhere,[23] a negatively pulsed grid can be used as a diagnostic tool for measuring plasma density. Not only is the technique valid at densities much lower than that at which Langmuir probe measurements become ambiguous,[25] but it can probably be used to measure ion densities in magnetically supported plasma of simple geometry by propagating the pseudowaves along field lines.

The limits of usefulness of the pulsed grid as a diagnostic tool for measuring plasma density depend upon the dimensions of the plasma, the grid mesh size, the plasma's characteristic shielding length for large potentials, and pulse technology.[23] Under optimum conditions we estimate that densities over the entire range of $10^6$ to $10^{11}$ cm$^{-3}$ can be measured. The probe is probably of limited use for plasmas having $T_e > 50$ eV or $T_i > 10$ to 20 eV.

As was noted in Sect. 6.3.2 of this report, it is found that the velocity of the leading edge of a pseudowave exceeds the velocity of the peak by about the ion acoustic wave velocity, thereby allowing pseudowaves to be used to estimate $T_e$. Thus, a pulsed gridded probe can be used to measure both $n_i$ and $T_e$ in a plasma. The range of $T_e$ over which the technique will yield accurate values of $T_e$ has not been measured, but almost certainly $T_e$ must not be larger than $eV_{\text{pulse}}/k$; otherwise the pseudowave would spread too rapidly for meaningful velocity measurements to be made.

[24] A. Hirose and I. Alexeff, "Ion Beam Instability in Burnout V," Plasma Studies Tech. Memo. No. 47 (Dec. 10, 1969).

[25] Igor Alexeff, W. D. Jones, and John Lohr, *Phys. Fluids* 9, 1403 (1966).

### 6.4.3 A Negatively Biased Grid for Exciting $\omega_{pi}$ in a Magnetic Field

A. Hirose

It was recently proposed that an ion beam instability at $\omega_{pi}$ involving ion motion perpendicular to the magnetic field can occur for the case when $\omega_{pe} \ll \omega_{ce}$.[24] It is now found in a xenon plasma that a negatively biased ($\sim -100$ V) grid placed parallel to the magnetic field gives rise to oscillations which appear to be at the ion plasma frequency. Preliminary results over a range of discharge current from ~15 to 300 mA show that the observed frequency varies quite accurately (0.2–0.9 mHz) as the square root of the current; also, the densities predicted by the observed frequencies seem to be quantitatively correct. The oscillation has been observed to occur only for magnetic field strengths greater than about 2 kG but is independent of field strengths up to our maximum field strength of about 5 kG.

# 7. Injection and Accumulation

## 7.1 NEUTRAL INJECTION EXPERIMENTS (DCX-1.5)

R. J. Colchin L. A. Massengill
J. L. Dunlap R. G. Reinhardt
R. S. Edwards W. J. Schill
E. R. Wells

The abstracts which follow constitute a summary of instability studies performed on DCX-1.5.

### 7.1.1 Evolution and Stabilization of Flutes in a Magnetic Mirror[1]

This paper deals with flutes as observed in a hot-ion, low-$\beta$ plasma. This plasma was established in an adiabatic simple mirror trap by Lorentz or gas-collisional ionization of an energetic $H^0$ beam. The studies emphasize (1) the detailed evolution of the flute mode and comparisons with linear theory and (2) the stabilizing effects of increased electrical connection of the plasma to conducting end walls (line tying). The evolution is traced as a function of density from a stable drift wave at low density to threshold for a growing, unstable wave which quickly exhibited nonlinear frequency behavior. Evolution of the stable drift wave is much as predicted by the linear theories. Instability threshold seems to occur at a somewhat higher density than that calculated, even from theories treating bounded plasmas. The line-tying experiments used movable end walls as a control on the electrical connection. Threshold was raised with end walls close to the hot plasma in a fashion that is in qualitative agreement with a recent calculation. Two possible explanations of the nonlinear frequency behavior of the unstable wave are proposed.

### 7.1.2 Harris Instabilities in a Plasma of Finite Length[2]

The experimental observations concern particular microinstability modes found in a short, highly anisotropic ($T_{\parallel}/T_{\perp} \approx 0.005$) hot ion plasma ($\omega_{pe} \gtrsim \omega_{ci} > \omega_{pi}$) formed by fast $H^0$ injection into a simple magnetic field. These modes are characterized by $\dot{B}_\theta$ probe signals at ion gyrofrequencies and also at discrete side bands of comparable amplitude about the gyrofrequencies. Side bands were related to mirror bounce motions of the ions by experiments using different magnetic field gradients. The presence of high-amplitude side bands and observations of an antisymmetric axial potential distribution associated with one of the oscillations indicated that the modes were those of Harris instability rather than of negative mass. Comparisons of observations with results of numerical studies of Harris instability in infinite media and with finite-length effects confirmed the assignment.

## 7.2 MULTIPLE-PASS EXPERIMENTS (DCX-2)

J. F. Clarke J. F. Lyon
S. M. DeCamp E. C. Moore
G. G. Kelley R. F. Stratton
J. P. Wood

### 7.2.1 Introduction

This is the final progress report on the high-energy ion-injection experiment DCX-2,[3–5] since DCX-2 ceased operation in June to provide funds and personnel for the new ORMAK experiment (described in Sect. 3.2). The turbulent heating experiments using the DCX-2 arc,

[1] R. J. Colchin, J. L. Dunlap, and H. Postma, *Phys. Fluids* **13**, 501 (1970).

[2] Abstract of paper by R. J. Colchin and J. L. Dunlap, accepted for publication in *Physics of Fluids.* Presently available as ORNL-TM-2767.

[3] J. F. Clarke *et al.*, p. 291 in *Plasma Physics and Controlled Nuclear Fusion Research* (Proc. IAEA Third Conf., Novosibirsk, U.S.S.R., Aug. 1–7, 1968), vol. II. IAEA, Vienna, 1969.

[4] P. R. Bell *et al.*, *Proceedings, International Conference on Plasma Confined in Open-Ended Geometry,* Gatlinburg, Tenn., CONF-671127 (1967).

[5] P. R. Bell *et al.*, p. 77 in *Plasma Physics and Controlled Nuclear Fusion Research* (Proc. Conf., Culham, England, Sept. 6–10, 1965), STI/PUB/111, vol II, IAEA, Vienna, 1966.

described in the last progress report,[6] continued into this report period but produced no essentially new results. The large plasma losses in the form of plasmoids and the lack of positive evidence of efficient ion heating and confinement were not encouraging, so this experiment was terminated in March in order to concentrate on the normal energetic plasma produced by ion beam injection into DCX-2.

The major features of the DCX-2 plasma behavior (the characteristics and mode identifications of the main instabilities, and the effects these instabilities have on the DCX-2 plasma) have been described in previous reports.[7,8] This report deals with the steady-state instability behavior at low plasma density (gas breakup operation) and the losses from the two distinct groups of energetic trapped protons. No attempt will be made here to summarize the overall results of the DCX-2 experiment, as this will soon be done elsewhere.[9]

The DCX-2 device and the energetic trapped plasma have been described in detail in previous reports. Briefly, a beam of 540-keV $H_2^+$ ions is injected into a large-volume, almost uniform magnetic field region where energetic (270 keV) protons are trapped from the $H_2^+$ beam by dissociation (breakup) on the gas background or a high-current arc. An instability (the modified negative mass instability)[7] occurs in the highly anisotropic group of beam dissociation protons (the side-lobe proton group), spreading their energy and creating a new group of energetic protons by near-resonant instability heating of background cold plasma. The instability-produced group of energetic protons (the central-peak proton group) has higher density, higher energies, longer lifetime, and greater stability than the injected (side lobe) proton group. These two separate groups of energetic protons can be seen in the steady-state pitch-angle distribution of the trapped energetic protons shown in Fig. 7.1. The central-peak proton group is characterized by very low axial energies $[(\overline{W}_{\parallel})_{CP} \lesssim 100$ eV] and high perpendicular energies $[(\overline{W}_{\perp})_{CP} \sim 400$ to 900 keV], whereas the counter-streaming side-lobe proton group is characterized by a parallel energy distribution corresponding to the axial velocity distribution of the injected $H_2^+$ beam $[(W_{\parallel})_{SL}$ $\sim 1.3$ to 5 keV] and perpendicular energies peaked about the initial (270 keV) energy. Figure 7.1 also shows the central magnetic field shape that produces a strong central-peak proton group, and the different axial extents of the two energetic proton groups trapped in this field.

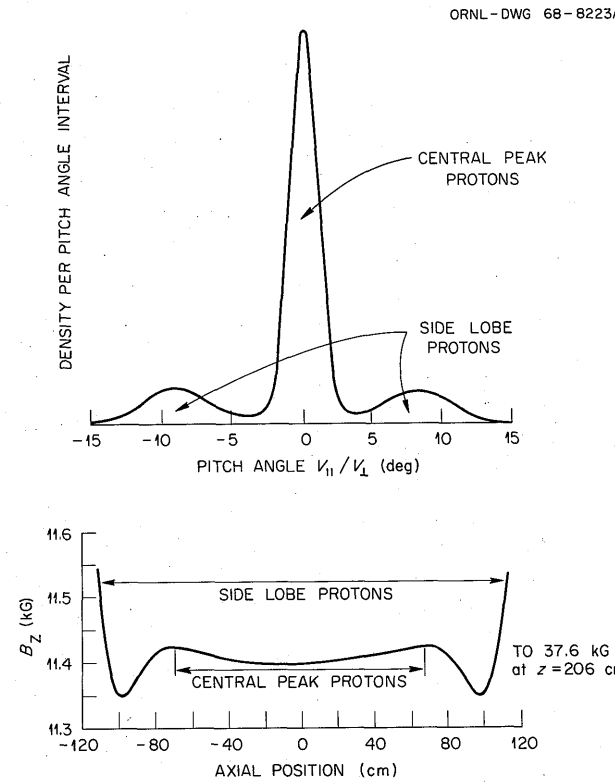


**Fig. 7.1. Pitch-Angle Distribution of the Energetic Charge-Exchange Neutrals ($W > 50$ keV) Seen from the Machine Midplane.** The measured magnetic field configuration that produces a strong central-peak proton group is also shown, along with the axial extents of the two energetic proton groups. The $H_2^+$ beam injector is located at an axial position of +107 cm.

### 7.2.2 Gas Breakup Instability Behavior

The dominant microinstabilities occurring in DCX-2 at the harmonics of the proton and $H_2^+$ ion cyclotron frequencies are Harris instabilities and the modified negative mass (MNM) instability. Harris instabilities occur in the $H_2^+$ beam under all conditions and in the two energetic proton components at the higher densities ($n_+ \gtrsim 10^8$ to $5 \times 10^9$ energetic protons/cm$^3$) obtained with arc breakup of the injected beam, while the modified negative mass instability is dominant at

[6] *Thermonuclear Div. Ann. Progr. Rept. Dec. 31, 1968,* ORNL-4401, pp. 74–78.

[7] *Thermonuclear Div. Ann. Progr. Rept. Dec. 31, 1968,* ORNL-4401, pp. 52–74.

[8] *Thermonuclear Div. Semiann. Progr. Rept. Oct. 31, 1967,* ORNL-4238, pp. 39–58.

[9] J. F. Lyon, Ph.D. dissertation, University of Tennessee, 1970 (to be published).

the lower side-lobe densities ($n_+ \lesssim 10^8$ energetic protons/cm$^3$) obtained with gas breakup operation.

In the previous report theoretical calculations and experimental observations on the high-frequency (ion cyclotron fundamental) modified negative mass instability and an associated low-frequency drift wave were presented, and a coupling between the two waves was inferred which produced instability of the drift wave. There is some doubt about the positive identification of such an unstable coupling in DCX-2.

There is no doubt now, however, about the existence of a low-frequency drift wave in the side-lobe plasma, although it has never been observed directly and has been observed indirectly (as an amplitude modulation of different plasma signals) only rather recently. In fact, the difficulty of detection led us to believe for a long time that DCX-2 did not have any low-frequency plasma disturbances. Since the radial electric and magnetic loop rf probes have a linear frequency response, they are much less sensitive (by a factor of $\omega_{ci}/\omega_{\text{drift}} \approx 2 \times 10^3$) to the fields of the drift wave than to those of ion cyclotron frequency instabilities. Our observations indicate, however, that the drift-wave fields must be at least an order of magnitude less intense in absolute magnitude than the ion cyclotron instability fields; otherwise they would be directly observable.

The low-frequency drift wave manifests itself as a low-frequency amplitude modulation of the MNM instability rf at the proton cyclotron fundamental, of the cold plasma current, and most recently, of the energetic proton charge-exchange current (see next section). Phase measurements on the steady-state amplitude modulation of the MNM signal had previously shown that it was in phase along the field (flutelike) and had an $m = 1$ azimuthal mode pattern rotating in the direction of ion mirror precession. The observed frequencies (8 to 10 kHz) were in the range of the hot proton mirror precession frequency and also of the frequency of plasma rotation in the radial electric field resulting from the large plasma potential found at pressures below $\sim 2 \times 10^{-6}$ torr.

Measurements using a short beam pulse had shown that the oscillations could be identified as the lower-frequency branch (electric field drift branch) of an ion drift wave with

$$\omega \approx \omega_E = \frac{E_r}{rB_z} \propto \Phi ,$$

where $\Phi$ is the plasma potential. For side-lobe densities below $\sim 3 \times 10^6$ energetic protons/cm$^3$, the amplitude-modulated MNM signal decayed stably with an $e$-folding time on the order of the average proton charge-exchange lifetime. Above $\sim 6 \times 10^6$ energetic protons/cm$^3$, there was evidence of large potential fluctuations and rapid loss of particles, suggesting that an instability threshold had been exceeded. Since drift waves were expected to be stable at these densities in DCX-2, and the low-frequency modulation of the cold plasma current and the plasma potential were correlated with the amplitude modulation of the MNM signal, it was concluded that the MNM instability was coupling to an otherwise-stable drift wave and driving the drift wave unstable. Support for this conclusion was also derived from the behavior of the cold plasma current (a large increase can occur) when the MNM instability rf grew to large amplitude.

We feel that this conclusion, that the MNM instability produces the observed low-frequency effects in DCX-2, may not be warranted for the following reasons.

1. The instability threshold for an ion drift wave in DCX-2 has been recalculated and found to be $\sim 2 \times 10^7$ energetic ions/cm$^3$ rather than the $8 \times 10^8$ energetic ions/cm$^3$ quoted in the last report. It is not as surprising, therefore, to find an unstable low-frequency behavior at $\sim 6 \times 10^6$ energetic ions/cm$^3$ as was initially thought.
2. The low-frequency behavior found preceding build-up of the MNM instability rf is not always significantly different from that found in steady state. Figure 7.2 shows the MNM instability rf and the cold ion current to probes located 24 cm from the axis obtained with low-pressure ($3 \times 10^{-7}$ torr) hydrogen gas breakup. The lower cold ion current, collected axially outside the energetic ion plasma, shows that two cold plasma oscillations occurred before the MNM instability grew to large amplitude and that no apparent change in the cold plasma oscillation occurred in the presence of the MNM instability. The upper cold ion current, collected in the machine midplane, probably reflects the increased ionization from the central-peak proton group that the MNM instability creates from background cold ions. The charge-exchange current from the side-lobe proton group also undergoes part of a low-frequency oscillation before the MNM instability grows to large amplitude. Of course, such initial low-frequency behavior cannot be caused by the MNM instability rf occurring at a later time.
3. Correlation between the amplitude modulation of the MNM instability rf and the other low-frequency plasma behavior does not by itself establish a causal relationship.

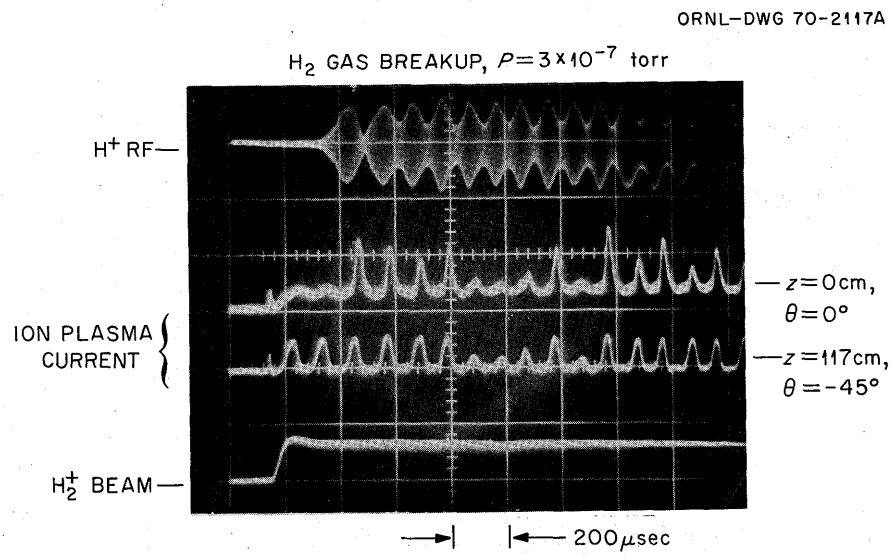


**Fig. 7.2. The Proton Cyclotron RF Activity and the Cold Plasma Current to Probes in the Machine Midplane and Axially Outside the Central-Peak Plasma.** The cold plasma pulses indicate a flute rotation in the $+\theta$ direction (direction of ion mirror precession).

We do not doubt that such a coupling[10] can exist between a high-frequency instability and a low-frequency stable drift wave, leading to instability of the drift wave. However, we feel that this mechanism has not yet been unambiguously identified in DCX-2.

There is some evidence that the steady-state behavior of the flute oscillation seen in DCX-2 may differ from that observed in the initial plasma buildup phase following beam turnon. It usually takes a few cycles for the amplitude modulation of the MNM signal to settle down to a stable, coherent oscillation, although the first few oscillations of the various plasma signals are generally about the same amplitude and frequency as the steady-state oscillations. With continuous injection, as contrasted with preparing a short burst of plasma, the oscillation frequency seen in the different plasma signals varies much less than the plasma potential, both during the plasma buildup phase, and during the steady state as the background gas pressure is varied.

### 7.2.3 Energetic Proton Plasma Behavior

Instabilities in DCX-2 have a strong effect on the behavior of the energetic trapped protons. The low-frequency oscillations observed cause enhanced losses of the side-lobe protons, while the MNM instability at the proton cyclotron fundamental creates the dominant central-peak proton group by near-resonant heating of cold protons and spreads the energy of both energetic proton groups. This behavior was treated in detail in the previous report, but some additional information has been obtained since and is included here for completeness.

The previous evidence for a flute rotation of the side-lobe plasma was an amplitude modulation of the MNM instability rf, modulation of the cold plasma current flowing out of the energetic proton region, and a radial power measurement showing that the side-lobe plasma extends radially beyond the edge of the beam injector on the side of the machine opposite the injector. The rf amplitude modulation can be assumed to result from the varying proximity of the plasma to the rf probe as the side-lobe plasma rotates. Assuming that the electric field from the $l = 1$ azimuthal mode of the MNM instability at the proton cyclotron fundamental varies as $1/r^2$, the plasma excursion corresponding to the rf amplitude modulation is $r_{max}/r_{min} = (E_{max}/E_{min})^{1/2}$. For typical modulation amplitudes, the plasma radial excursion found agrees roughly with that found from the radial plasma power measurement. The cold plasma current modulation, shown in Fig. 7.2 for probes at two axial and azimuthal locations, reflects either increased local ionization by the rotating energetic protons or a rotation of the cold plasma itself.

[10] J. F. Clarke, *Phys. Rev. Letters* 23, 1215 (1969).

Direct evidence for oscillations in the energetic proton plasma has been obtained since the last report, using collimated foil neutral detectors (FND's) to look at the charge-exchange current from the central-peak or side-lobe proton group and to exclude the energetic beam dissociation current. The acceptance range of pitch angles was narrowed to the point (~±2°) where the amount of dissociation current reaching the detectors was not significant.

Figure 7.3 shows the side-lobe and central-peak FND signals and the MNM rf at the proton cyclotron fundamental and second harmonic for three different pressures with hydrogen gas breakup of the injected beam. Since only protons with energies over ~50 keV can penetrate the detector foil and the charge-exchange loss rate is a rapidly decreasing function of proton energy, the FND current signals in Fig. 7.3 reflect the energetic proton density behavior in the energy range 50 keV to 100–150 keV. The top photo in this figure, a time exposure for ~100 beam pulses, shows that the same low-frequency modulation seen in the cold plasma current signals of Fig. 7.2 appears in the side-lobe and, to a lesser extent, central-peak FND signals. As the hydrogen background gas pressure is raised, the MNM fundamental rf becomes quite bursty, and higher frequencies are seen in the amplitude modulation of the

ORNL-DWG 70-2118A

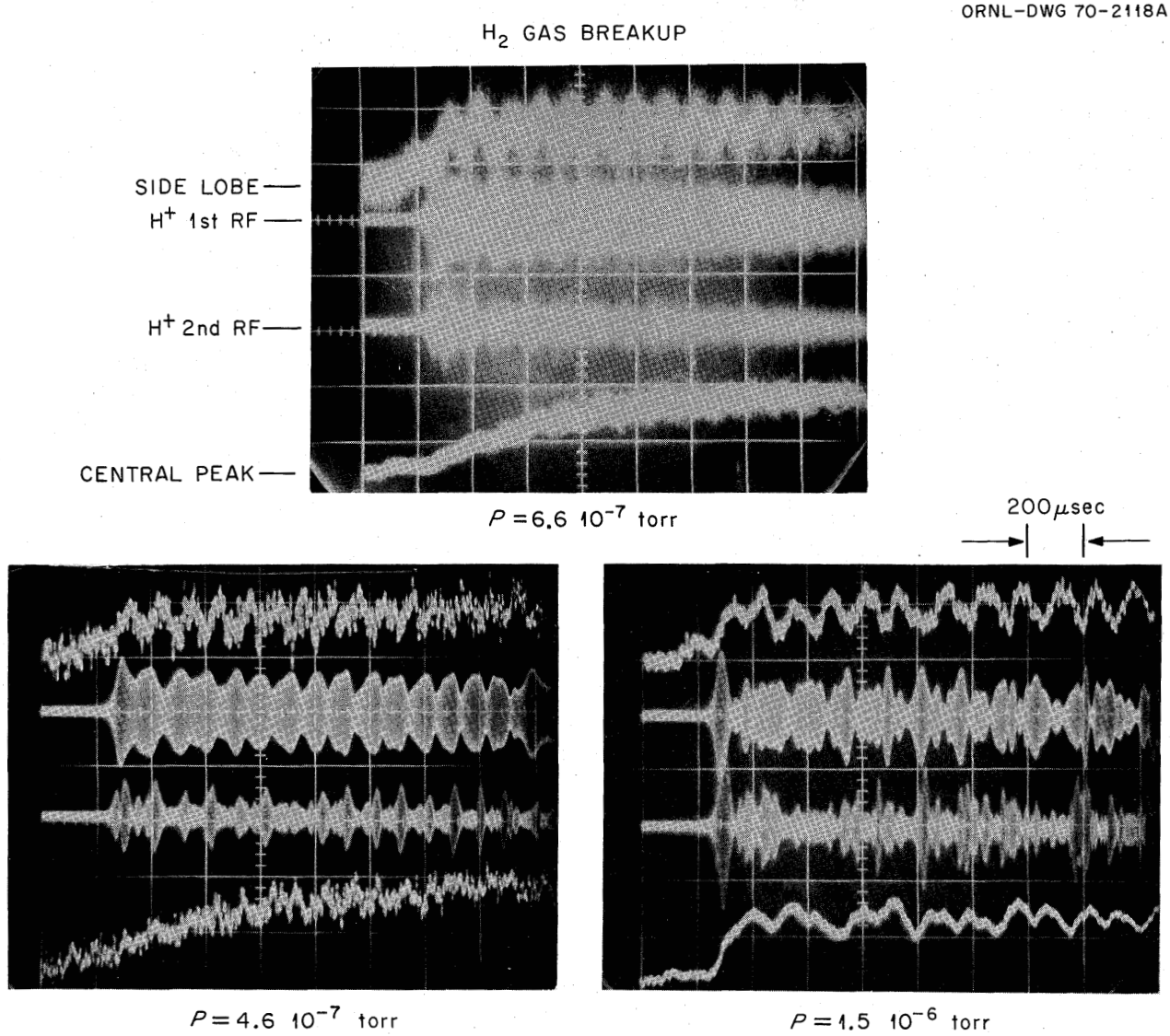


**Fig. 7.3. Correlation of the MNM Instability RF Activity at the Proton Cyclotron Fundamental and at the Second Harmonic with the Central-Peak and Side-Lobe Charge-Exchange Currents for Different Hydrogen Background Pressures.**

rf activity. The amplitude modulation of the side-lobe FND signal stays about the same percentage amplitude but falls slightly in frequency (from 9.5 to 7.5 kHz, roughly about half the average side-lobe mirror precession frequency) as the pressure is increased. The percent modulation of the central-peak FND signal is smaller than that of the side lobe and increases with pressure.

Figure 7.4 shows the results obtained at a higher hydrogen background pressure. Above a certain partial pressure of hydrogen, the cold proton density builds up to "cut off"[11] the proton cyclotron fundamental of the MNM instability. However, in this case the MNM fundamental does not stay "cut off" but reappears in bursts throughout the beam pulse. The amplitudes of the rf activity at the proton cyclotron fundamental and the second harmonic are seen to be strongly anticorrelated. The rf at the second harmonic increases in intensity when the fundamental decreases, and decreases when the fundamental increases, showing that the plasma is switching back and forth between the fundamental and the second harmonic MNM instability modes. The side-lobe FND signal decreases abruptly when the MNM fundamental is intense and recovers gradually after this rf activity ceases. The central-peak FND signal exhibits just the opposite behavior.

We interpret this behavior in the following way. Immediately following beam turnon, the side-lobe density starts to build up, and there is no rf activity at the proton cyclotron fundamental or second harmonic and no central-peak proton group. At a certain low-density threshold, the monoenergetic side-lobe proton group becomes unstable with respect to the MNM instability at the proton cyclotron fundamental. These near-cyclotron-resonant electric fields spread the energy of the side-lobe protons and create the central-peak proton group from the background cold plasma, which is steadily increasing in density. The plasma potential is high, as are the flute-driven side-lobe proton losses to the beam injector. When the cold plasma density reaches the "cutoff" density, the growth rate of the MNM instability in the side lobe at the proton cyclotron fundamental falls abruptly, and the previously unstable, though much weaker growth rate, MNM instability at the second harmonic is no longer suppressed and becomes dominant. The central-peak production rate (and hence the central-peak density) falls, the plasma potential decreases, the side-lobe flute losses decrease, and hence the side-lobe density increases. Since the increase in side-lobe density is usually not enough to offset the decrease in the central-peak density, the total energetic proton density decreases and with it the cold plasma density produced by

[11] The "cutoff density" calculated for the MNM instability is really an upper critical density above which the plasma is stable. It does not actually correspond to a cutoff of a plasma wave in the usual sense (W. P. Allis, S. J. Buchsbaum, and A. Bers, *Waves in Anisotropic Plasmas*, p. 13, Wiley, New York, 1963), that is, nonpropagation of a wave due to the phase velocity $\omega/k$ becoming infinite (the wavelength going to infinity).

ORNL-DWG 70-2116A

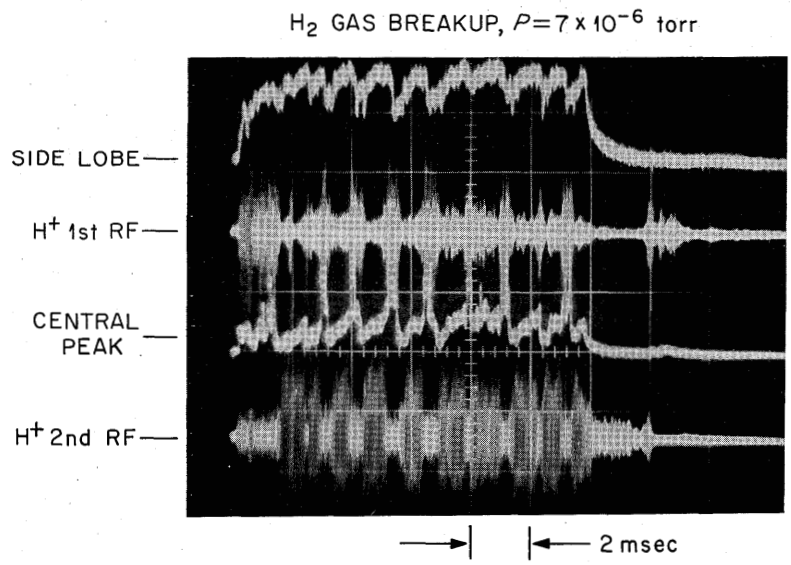


**Fig. 7.4. Long-Time Correlation of the MNM Instability RF with the Central-Peak and Side-Lobe Charge-Exchange Currents at a Hydrogen Background Pressure Above the Normal "Cutoff" Pressure for the MNM Instability Fundamental.**

energetic proton ionization of background gas. If the cold plasma density falls below the MNM "cutoff" density, the fundamental can become unstable again, and the cycle repeats.

The relation of the amplitude changes in the side-lobe and central-peak FND signals in Figs. 7.3 and 7.4 to the total density behavior of these two groups is not obvious, since the FND signals represent the density behavior in a rather limited energy range, ~50 to 100 keV wide, considerably removed from the maximum of the central-peak and side-lobe energy distributions. However, other measurements (beam-off FND integrals and beam-on and beam-off measurements with collimated scanning silicon barrier detectors) show that the total central-peak and side-lobe densities are correlated with the rf activity at the proton cyclotron fundamental and the second harmonic in the same manner as the FND signals shown in Fig. 7.4.

While the extent and cause of the steady-state side-lobe proton losses are well known, only rough estimates can be made of the extent of any non-charge-exchange steady-state losses from the central-peak proton group. With gas breakup of the injected beam, both the central-peak and side-lobe proton groups decay stably after beam turnoff, principally by classical charge-exchange loss. This conclusion comes from the good agreement obtained between beam-on and beam-off density measurements of the two energetic proton groups using collimated scanning silicon barrier detectors. The beam-off measurement collects only those energetic protons that are lost by charge exchange, while the beam-on measurement determines the actual density, independent of the actual proton loss mechanism, since it uses charge exchange to sample the energetic proton density.

With arc breakup of the injected beam, the beam-on and beam-off measurements of the central-peak and side-lobe proton densities no longer agree, and significant non-charge-exchange losses occur in both the central-peak and side-lobe proton groups after beam turnoff. In addition, sudden increases in the integral of the FND signal following beam turnoff correlated with rf bursts at the proton cyclotron fundamental are observed, also indicating additional losses. This type of behavior is not observed in the stable plasma decay following beam turnoff with gas breakup operation. Although presumably a significant non-charge-exchange loss of central-peak protons occurs after beam turnoff with arc breakup, nothing is known about the extent of any non-charge-exchange losses from the central-peak proton group in steady state. It is known, however, that the beam-on instability behavior (mode patterns and frequency spectrum) differs considerably from the beam-off instability behavior and that the steady-state instability-produced losses from the side-lobe proton group are less severe in arc breakup plasmas than with the lower-density gas-breakup-produced plasmas.

An indirect indication that significant non-charge-exchange losses of central-peak protons may be occurring with gas breakup during the beam-on time is obtained from measurement of the central-peak buildup time for different proton energy intervals. Figure 7.5 shows the measured central-peak buildup time [experimentally,

$$n_{CP}(W_1 - W_2) \approx n_+(\overline{W})\,(1 - e^{-t/\tau_{CP}(\overline{W})})]$$

and the calculated mean charge-exchange lifetime vs central-peak proton energy. If the current feed into the central peak at energy $W$ is assumed to have a buildup time $\tau_I(W)$, then the central-peak buildup time $\tau_{CP}(W)$ should be approximately $\tau_I$ if $\tau_I \gg \tau_{loss}$ and $\tau_{loss}$ if $\tau_I \ll$

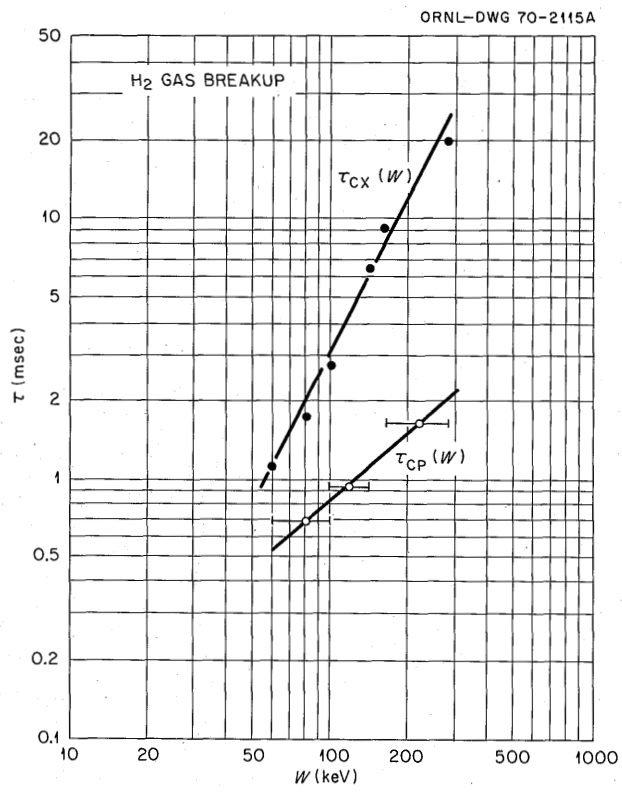


**Fig. 7.5. Comparison of the Buildup Time and Charge-Exchange Time for Central-Peak Protons of Different Energies.** In the absence of instability losses, the central-peak buildup time would be expected to be longer than the charge-exchange time.

$\tau_{loss}$, where $\tau_{loss}$ $(W)$ is the mean central-peak lifetime at energy $W$. In any event, we expect $\tau_{CP}(W) > \tau_{loss}(W)$. Since $\tau_{CP}(W) < \tau_{cx}(W)$, we conclude that $\tau_{loss}(W) < \tau_{cx}(W)$ and that non-charge-exchange losses from the central-peak proton group are significant, especially at higher energies. What physical mechanism is responsible for this additional loss is not known.

### 7.2.4 Discussion

Instabilities and enhanced losses of side-lobe protons occur over the entire density range explored in DCX-2 ($\sim 3 \times 10^6$ to $\sim 5 \times 10^9$ energetic protons/cm$^3$). The net result is that although the energetic plasma density is reduced from that expected if charge exchange were the only loss process, no limitation in trapped proton density is seen up to the highest input current available. Three methods were attempted this report period to increase the energetic trapped density: turbulent heating of the DCX-2 arc plasma, reduction of the side-lobe flute losses using electron-emitting end plates, and coupling of rf power through the electron-emitting end plates into increased ion cyclotron heating of the central-peak proton group. The turbulent heating experiments have already been described, and they produced no positive indication of cold ion heating. Preliminary experiments with segmented electron-emitting end plates just before the DCX-2 shutdown showed no effect on the plasma density, instability amplitude, or frequency spectrum. The reason for the null result is not known. The rf heating experiment was not performed due to lack of time, but an earlier experiment using a nonemitting conducting end plate that coupled $\sim$3 kW into the plasma had encouraged us to try a larger experiment.

# 8. Atomic and Molecular Physics

## 8.1 THE COULOMB LOGARITHM FOR ENERGETIC TEST IONS

J. Rand McNally, Jr.

Energy losses for energetic test ions in a plasma of slower electrons are proportional to the Coulomb logarithm,

$$\ln \Lambda = \ln \frac{b_{\max}}{b_{\min}} .$$

The energy loss is given by

$$\frac{dW}{dt} = \frac{-4\pi Z^2 e^4 \int_0^{v_+} f_- \, dE_-}{m v_+} \ln \Lambda .$$

Here, $b_{\max}$ is the maximum impact parameter (in the otherwise divergent integral) and is usually taken to be the Debye screening or shielding distance $\sqrt{kT_-/4\pi ne^2}$. The minimum parameter $b_{\min}$ is $Ze^2/mv_+^2$, which is usually approximated as $Ze^2/3kT_-$; $n$ is the number density of electrons, $v_+$ the ion velocity, and $T_-$ the electron temperature.

The latter approximation is generally quite poor, and $b_{\min}$ should be expressed as $Ze^2/mv_+^2$. This can be readily seen by considering the impulse-momentum approximation

$$\frac{Ze^2}{b^2}\frac{2b}{v_+} \cong mv_- \leqslant m(2v_+) ,$$

since the maximum velocity gained by a *slow* electron in a collision with a heavy fast ion is $2v_+$ (the test ions lose energy only to the slower electrons). Thus

$$b_{\min} = \frac{Ze^2}{mv_+^2} ,$$

where $m$ is the *electron* mass. Fermi[1] gives this same result for the close impact parameter to be used in stopping power calculations.

The question of

$$b_{\max} = \sqrt{kT_-/4\pi ne^2}$$

has also been examined. It appears that the collective electric field generated by the field electrons displaced by the heavy test ion must be of order of the individual Coulomb field acting on each electron by the test particle at the maximum impact distance. This can be seen by applying Gauss's law of electrostatics to a cylinder having impact radius $b$ with the electron population (of the otherwise neutralized cylinder) having been increased by $n(4\pi b^2)\Delta R$, where

$$\Delta R \cong \frac{1}{2m}\left(\frac{Ze^2}{b^2} - \frac{\xi e}{2}\right)\left(\frac{2b}{v_{\rm rel}}\right)^2 .$$

In order that the collective electric field be comparable with the Coulomb field we have

$$\xi = \frac{8\pi ne^2}{mv_{\rm rel}^2}\left(Ze - \frac{\xi b^2}{2}\right) \sim \frac{Ze}{b_{\max}^2}$$

or

$$\xi = \frac{8\pi nZe^3}{mv_{\rm rel}^2}\frac{1}{1 + 4\pi ne^2 b^2/mv_{\rm rel}^2} \sim \frac{Ze}{b_{\max}^2} ;$$

we obtain

$$b_{\max} = \sqrt{\frac{mv_{\rm rel}^2}{4\pi ne^2}} .$$

[1] E. Fermi, *Nuclear Physics*, University of Chicago Press, Chicago, 1951.

Thus, depending on the magnitude of the test ion velocity, we have

$$b_{\max} \cong \begin{cases} \sqrt{\dfrac{m\mathrm{v}^2}{4\pi n e^2}} & \text{for } \mathrm{v}_+ < \mathrm{v}_- \text{ thermal} \\ \sqrt{\dfrac{m\mathrm{v}^2}{4\pi n e^2}} & \text{for } \mathrm{v}_+ > \mathrm{v}_- \text{ thermal}. \end{cases}$$

Spitzer[2] discussed the arbitrariness of using the Debye cutoff distance for plasmas. Kihara and Aono[3] found that the Debye distance is not appropriate to the test ion case for very fast test ions. For most plasma cases ($\mathrm{v}_+ < \mathrm{v}_-$ thermal) the Debye distance is a good approximation to use for $b_{\max}$.

The revised expression for the effective Coulomb logarithm for ions slowing down on electrons is then

$$\text{“}\ln \Lambda\text{”} = \ln \frac{b_{\max}}{b_{\min}}$$

$$= \ln \sqrt{\frac{m^3 \mathrm{v}_+^6}{4\pi Z^2 n e^6}} \quad \text{for } \mathrm{v}_+ > \mathrm{v}_- \text{ thermal} \qquad (1)$$

$$= \ln \sqrt{\frac{m^3 \mathrm{v}_+^4 \mathrm{v}_-^2}{4\pi Z^2 n e^6}} \quad \text{for } \mathrm{v}_+ < \mathrm{v}_- \text{ thermal}, \qquad (2)$$

instead of $\ln \sqrt{9k^3 T_-^3 / 4\pi Z^2 n e^6}$. Expression (1) essentially agrees with that of Kihara and Aono.[3] Expression (2) reduces the expected stopping power on a test ion due to the electrons in a plasma and thus would permit a somewhat larger transfer of energy to heavy field ions, such as from reaction products to fuel ions in a thermonuclear plasma. In plasmas containing relatively slow ions ($\mathrm{v}_+ \sim 10^7$ cm/sec) the correction may be quite large,[4] with the result that the ion temperature is much higher than the electron temperature.

The above expression for “ln Λ” obviously breaks down when the density

$$n \sim \frac{m^3 \mathrm{v}_+^6}{4\pi Z^2 e^6}$$

(or

$$\frac{m^3 \mathrm{v}_+^4 \mathrm{v}_-^2}{4\pi Z^2 e^6}$$

for test ions slower than the electron thermal velocity). In such cases one must establish new conditions such as that of Fermi and Teller[5] for degenerate plasmas, or that of McNally *et al.*[6] for low-temperature (~1 keV) or high-density (i.e., large $n_Z^2$) plasmas.

These improvements in the Coulomb logarithm for heavy ions slowing down on electrons have implications for hot, dense plasmas having a thermonuclear energy source for the generation of fast ions. They indicate that, in dynamic equilibrium, the ion and electron “temperatures” will be different in such systems as fusion reactors, the core of the sun, or even novae and supernovae. This comes about principally because the ln Λ for *fast electrons* slowing down on *ions* is much larger and thus Fokker-Planck coefficients are grossly affected.

Thus we should expect in actual fusion plasmas $T_- < T_+$, since $\ln \Lambda_{ie} < \ln \Lambda_{ei}$. This suggests that for a given $\beta$ one can increase the nuclear reaction rate. In addition, the synchrotron radiation rate, which goes as $T_-$, and the ordinary bremsstrahlung rate, which goes as $\sqrt{T_-}$, should be somewhat reduced.

The question of the proper generalized form for the Coulomb logarithm is still open. Improved forms are suggested here, but in view of its importance to high-temperature plasmas it merits further study. Using Spitzer's expression for the Coulomb logarithm[2] (the integral in Eq. 5.12) but applying his treatment to test ions slowing down on electrons rather than electrons slowing down on heavy ions, one obtains

$$\text{“}\ln \Lambda\text{”} = \ln (1 + y^2)^{1/2} - \frac{0.5 y^2}{1 + y^2},$$

where

$$y = \frac{b_{\max} m \mathrm{v}_+^2}{Z e^2}.$$

For most plasmas (low-density cases) this reduces to the form given earlier ($\ln y$); however, for the high-density case this is probably the most satisfactory form for nonrelativistic plasmas. For small $y$, “ln Λ” approaches zero asymptotically; that is, the energy loss rate

[2] L. Spitzer, Jr., *Physics of Fully Ionized Gases*, Interscience, New York, 1962. See also L. Spitzer, Jr., and E. H. Scott, *Astrophys. J.* 158, 161 (1969).

[3] T. Kihara and O. Aono, *J. Phys. Soc. Japan* 18, 837 (1963); see also O. Aono, *J. Phys. Soc. Japan* 17, 853 (1962).

[4] J. R. McNally, Jr., *Plasma Phys.* 10, 903 (1968).

[5] E. Fermi and E. Teller, *Phys. Rev.* 72, 399 (1947).

[6] J. R. McNally, Jr., *et al.*, *Appl. Opt.* 5, 187 (1966).

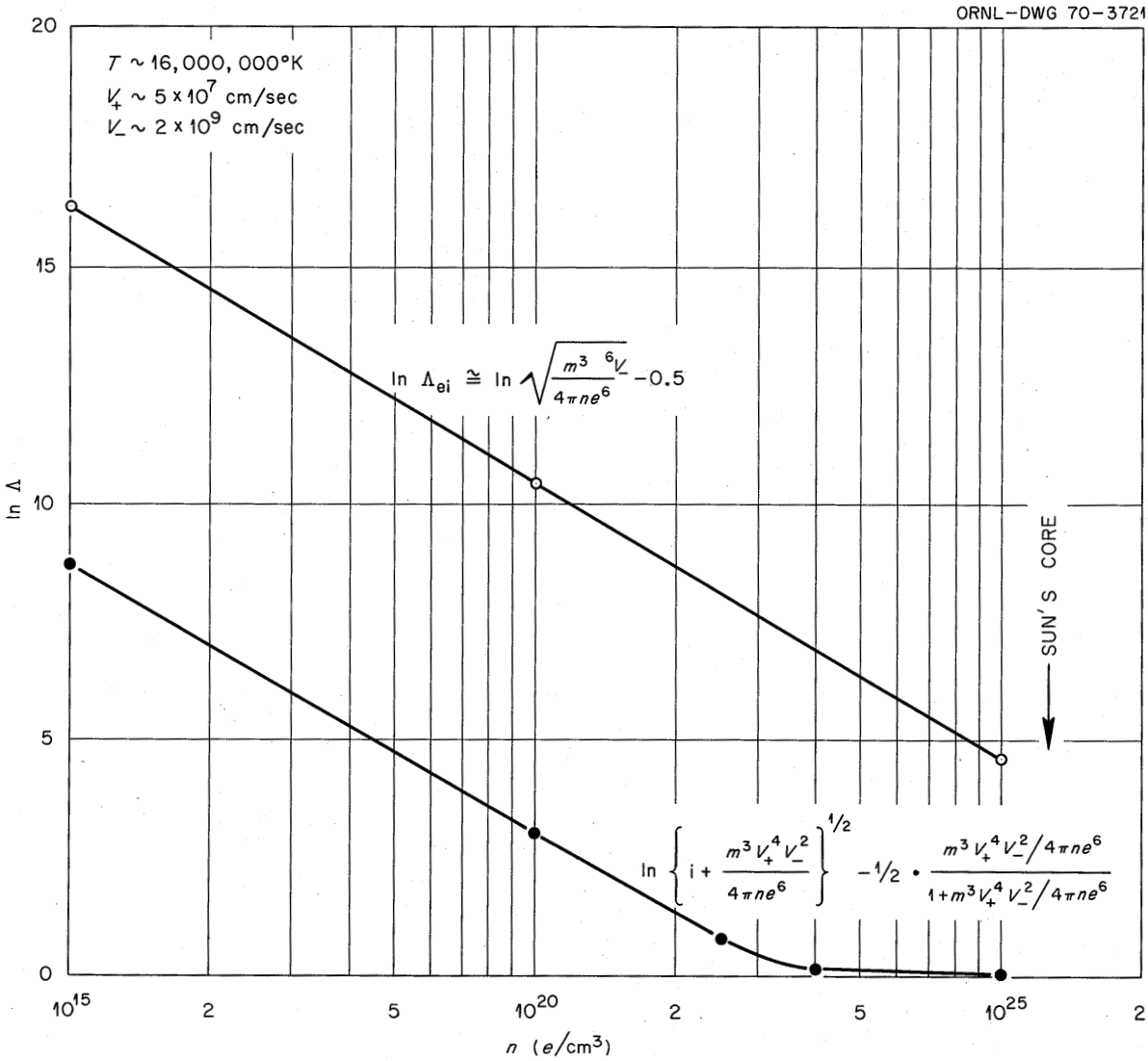


**Fig. 8.1. Variation of the Coulomb Logarithm for Ions Slowing Down on Electrons and for Electrons Slowing Down on Ions as a Function of Electron Density at Solar Temperatures.** For a controlled fusion plasma at $10^{15}$ $e/\text{cm}^3$ the ratio $\ln \Lambda_{ei}/\ln \Lambda_{ie}$ is of order 2.

becomes independent of electron density. Figure 8.1 shows the variation of the Coulomb logarithm for ions slowing down on electrons and for electrons slowing down on ions assuming an isothermal solar temperature case. It is uncertain whether this treatment is valid for $\ln \Lambda < 1$, but the figure does illustrate the tremendous disparity in the two Coulomb logarithms over a wide range of density.

## 8.2 ELECTRON AND ION SPECTROMETRY

Manfred O. Krause

An electrostatic analyzer has been designed and constructed for the purpose of measuring energy distributions of charged particles that are produced in atomic and molecular collision processes. The particles may be electrons, ions, or neutral species (after suitable conversion) and can be regarded as observables of a variety of processes, such as ionization by photons, electrons, or ions, autoionization following excitation, and charge transfer between ions and neutrals. Thus many processes in physics, astrophysics, and chemistry can be studied per se, or can be utilized for qualitative or quantitative analysis of matter in the gaseous or solid phase.

The instrument is shown schematically in Fig. 8.2. A condenser of accurately machined spherical sectors

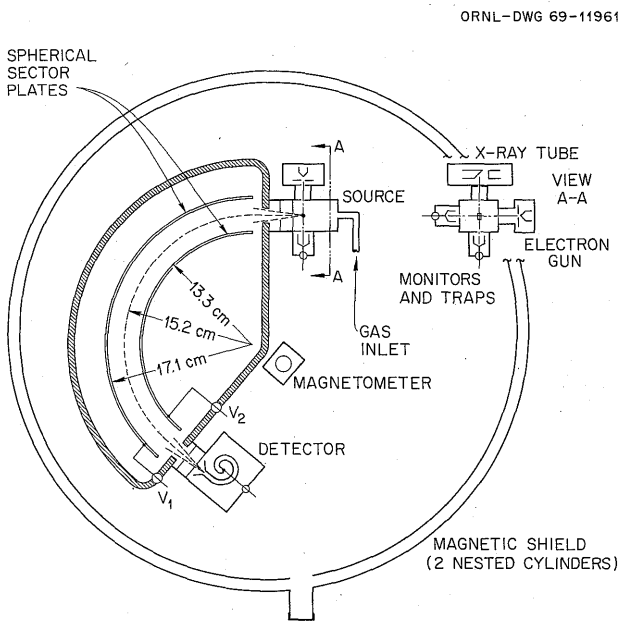


**Fig. 8.2. Schematic of 15-cm Electrostatic Energy Analyzer.** Fixed source volume shown can be replaced by a rotatable chamber for angular measurements. Sector plates are made of aluminum and subtend spherical sections of 140° by 60°. Accuracy of radii of plates is about 0.01 mm.

forms the dispersive element, a Mullard channel electron multiplier with an entrance funnel serves as single-particle detector in the pulse-counting mode, and the source of electrons or ions is described by the intersection of the incident ionizing beam with the bundles of electron-optical paths through the two entrance apertures. These two apertures, together with the exit aperture, determine the resolving power of the analyzer. Apertures are slits of typically 8 mm length and tenths of a millimeter width. The apparatus is completely enclosed in a double-layer magnetic shield to attenuate the earth's magnetic field and ambient stray magnetic fields. Under the present conditions a residual field of a few milligauss is present along the electron (ion) paths. The resolution $\Delta E/E$ of this 15-cm analyzer can be set to better than 0.1% (FWHM).

The instrument is operated in a manner similar to that used with an earlier, simpler electrostatic analyzer.[7] Briefly, the energy range of interest is scanned continuously by applying a repetitive sawtooth voltage to the condenser plates and by storing the detector signals in a multichannel memory core whose channels are advanced in synchronization with the sawtooth. Thus each particle detected is placed into a channel appropriate to the kinetic energy of the particle. Repetitive scanning of the same energy range not only affords the convenience of automatic operation but also minimizes spectral distortion by fluctuations and drifts of the particle flux. Typical scanning time is 50 msec for one pass.

In the course of testing the performance and potential of the instrument a great number of data were obtained. The following is an enumeration of the more significant results of investigation of basic processes in atomic and molecular collisions and of the application of electron and ion spectrometry to practical problems of qualitative and quantitative analysis.

Auger electron spectra contain a wealth of information on the dynamics of atomic and molecular systems. They have also become an important diagnostic tool for collision processes and for the investigation of surface phenomena.[8] In a study of multiple-excitation processes the range of validity of the electron shake-off theory was tested by observing the *K* Auger spectrum of neon. If the removal of an orbital electron occurs fast compared with characteristic periods of the bound electrons, multiple excitation (to bound and continuum states) is independent of the energy of the incident particle and of the excitation mode according to this theory. We verified the prediction for electron and photon impact,[9] and we can now predict[10] with confidence the probability of multiple excitation relative to single excitation for any combination of orbital electrons in any element under photon, electron, or heavy-particle impact. Figure 8.3 illustrates the results; that is, the probability of multiple excitation relative to single excitation (satellite intensities/*K-LL* line intensities) is identical for different excitation modes.

The theory of the Auger effect is still rather crude, as a comparison with experiment reveals (cf. Tables 8.1 and 8.2). Neither Hartree-Fock calculations nor relativistic calculations of transition energies yield very accurate values for argon *K-LL* lines. Failure of the independent-particle model to predict correctly relative intensities of neon *K-LL* lines indicates that configuration interaction as well as electron-electron correlation effects need to be incorporated into theory.

[7] M. O. Krause, *Phys. Rev.* **140**, A1845 (1965); *Phys. Letters* **19**, 14 (1965).

[8] See, for example, E. S. Parilis, *The Auger Effect*, ed. by U. A. Arifov, Academy of Sciences, U.S.S.R., Tashkent, 1969.

[9] See following abstract, and T. A. Carlson, W. E. Moddeman, and M. O. Krause, to appear in the *Physical Review* (1970).

[10] T. A. Carlson *et al.*, *Phys. Rev.* **169**, 27 (1968).

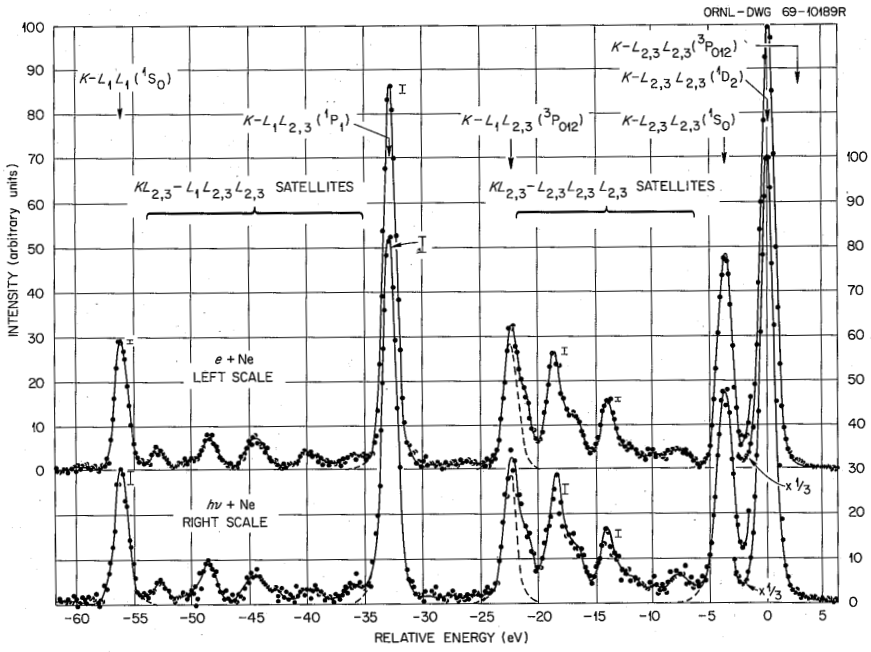


**Fig. 8.3. *K* Auger Spectrum of Neon Excited by Electrons (3.2 keV) and Photons (1.5 keV).** Resolution $\Delta E/E$ = 0.17% FWHM. Satellite structure is due to initial multiple ionization in *K* and *L* shells. Note similarity of spectra under both electron and photon impact.

**Table 8.1. Experimental Energies of *K-LL* Auger Transitions in Argon Compared with Hartree-Fock (HF) and Relativistic Hartree-Slater (RHS) Calculations**

Energies in electron volts

| Line | Experiment | | Theory[a] | | |
|---|---|---|---|---|---|
| | Absolute | Relative | Absolute (HF) | Relative (HF) | Absolute (RHS) |
| $1s-2p2p\ ^3P$ | | 8.1(4) | | 7.8 | |
| $^1D$ | 2660.8(4) | 0 | 2650.2 | 0 | 2670.1 |
| $^1S$ | | −9.9[b] | | −11.7 | |
| $1s-2s2p\ ^3P$ | | −61.3(3) | | −58.9 | |
| $^1P$ | | −85(2) | | −83.8 | |
| $1s-2s2s\ ^1S$ | | −151.6(4) | | −145.4 | |

[a]According to C. W. Nestor, Jr., Mathematics Division. For details, consult C. W. Nestor, Jr.

[b]Tentative; satellite lines interfere.

Figure 8.4 represents the high-resolution photoelectron spectrum of neon excited by Mg $K_\alpha$ x rays and shows an effect reported earlier,[11] namely, the promotion of a $2p$ electron into $np$ ($n \geqslant 3$) states concomitant with the ejection of a $1s$ electron.

Turning to the energy analysis of ions, we measured the kinetic energy distribution of protons from the much-studied dissociative ionization of $H_2$. A typical spectrum is shown in Fig. 8.5; similar spectra were obtained for electron energies of 300 eV, 1 keV, and

[11]M. O. Krause, T. A. Carlson, and R. D. Dismukes, *Phys. Rev.* **170**, 37 (1968).

**Table 8.2. Relative Intensities of *K-LL* Lines of Neon**

| Line | Experimental | Theory (HF)[a] |
|---|---|---|
| $1s-2s2s\ ^1S$ | 1.00 | 1.00 |
| $1s-2s2p\ ^1P$ | 2.90(4) | 1.67 |
| $^3P$ | 1.06(4) | 1.05 |
| $1s-2p2p\ ^1S$ | 1.5(1) | 0.45 |
| $^1D_2$ | 10.03(15) | 4.94 |
| $^3P$ | 0.01(3) | |

[a]E. J. Callan (private communication). See also *Bull. Am. Phys. Soc.* 14, 830 (1969).

2.3 keV. The experimental distribution is in satisfactory accord with the calculations of Kieffer and Dunn,[12] but only in moderate agreement with these authors' experiment. The larger experimental width as compared with the theoretical prediction – with $\Delta E/E = 0.2\%$ no instrumental broadening is introduced – is probably due to transitions to states other than the $2p\sigma_u$ state of $H_2^+$, which is the only state considered in the calculation. Following establishment of the *absolute* energy scale, perhaps within 0.1 eV, similar measurements can be carried out with great accuracy for dissociation of $D_2$ and other molecules (though without mass discrimination). Such studies are of value to our understanding of molecular dissociation and of phenomena in plasmas that are influenced by dissociative processes.

This instrument can also be used as an analytical device, especially since at least four different avenues are open requiring little or no physical change of the setup:

1. photoelectron lines using Mg $K_\alpha$ or other characteristic x rays,

[12]L. J. Kieffer and G. H. Dunn, *Phys. Rev.* 158, 61 (1967).

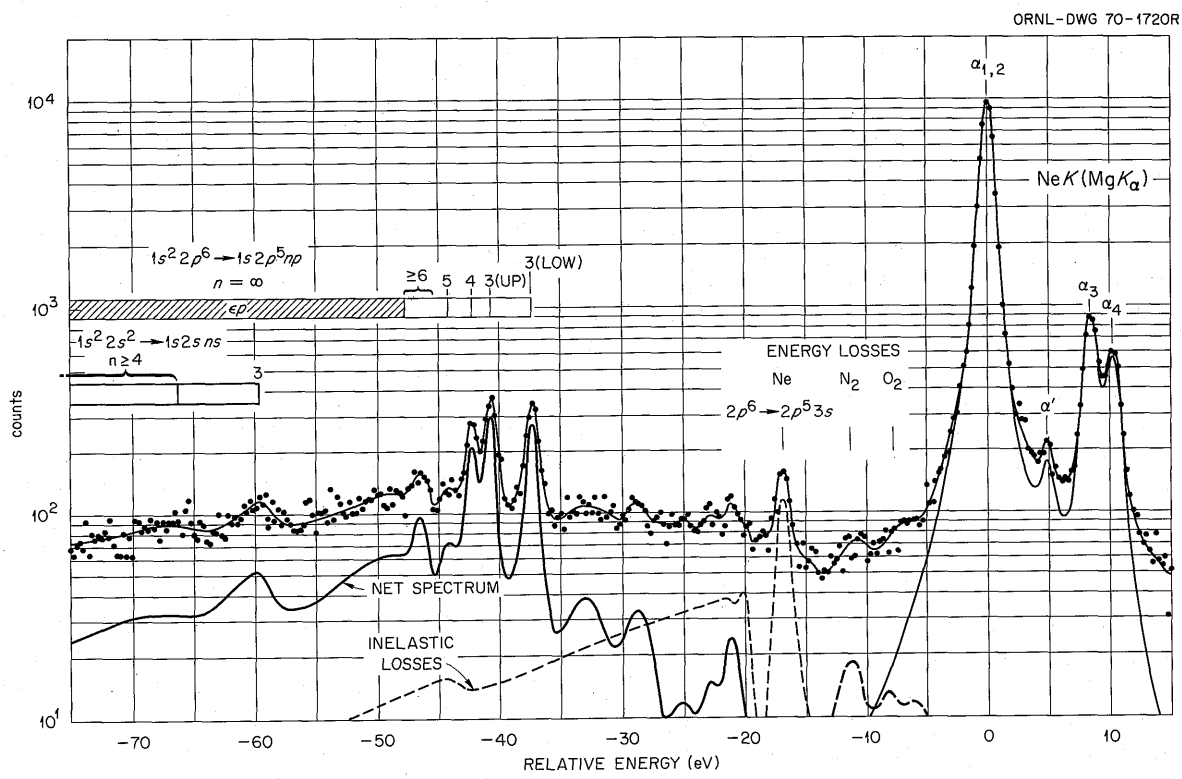


**Fig. 8.4. Spectrum of Photoelectrons Ejected from Neon by Mg $K\alpha$ X Rays.** Peaks near $\Delta E = -40$ eV are due to promotion of $2p$ electrons to $np$ ($n \geqslant 3$) states together with emission of $1s$ electron. At $\Delta E \sim -60$ eV, a $2s$ electron can be promoted to an $ns$ ($n = 3$) state.

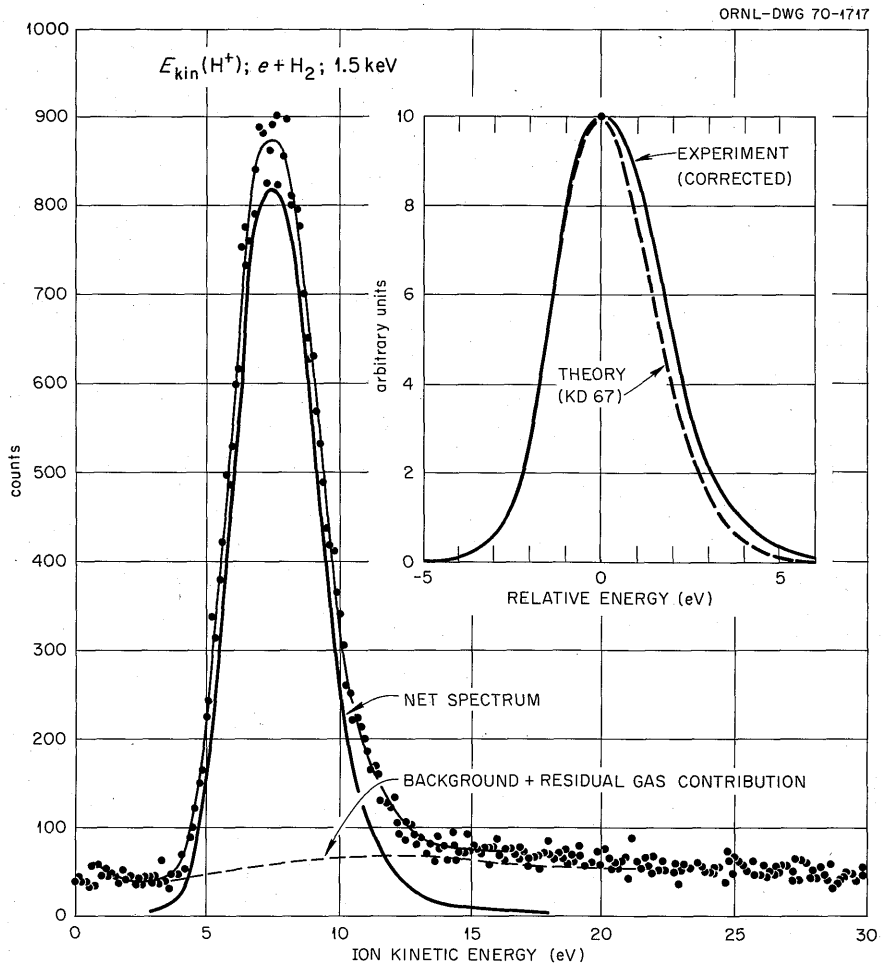


**Fig. 8.5. Kinetic Energy Distribution of Protons from Dissociative Ionization of $H_2$ by 1.5-keV Electrons.** Most of the ions come from the $2p\sigma_u$ state of $H_2^+$. Inset shows experimental spectrum, corrected for dispersion of instrument, compared with theory; distributions matched at maximum. Absolute energy scale is tentative, relative scale better than ±0.05 eV. $\Delta E/E = 0.2\%$.

2. photoelectron lines using ultraviolet radiation, such as the He 21.22-eV resonance line,
3. Auger electron spectra excited by electrons (or x rays),
4. characteristic electron energy loss spectra.

Figure 8.6 shows the elemental analysis of air by way of photoelectron lines; Fig. 8.7 shows the same analysis by way of Auger spectra; and Fig. 8.8 shows a number of energy loss spectra characteristic of the chosen sample compound. Though no attempt was made to demonstrate the capabilities of electron spectrometer and excitation sources at their best, the versatility and potential of this type of instrument[13] for analytical purposes can easily be recognized from Figs. 8.6–8.8.

In many instances it is desirable to know the angular distribution of ejected and scattered electrons, and of dissociative fragments. To this end a rotatable chamber has been constructed which is interchangeable with the fixed source shown in Fig. 8.2. An angular range from 0 to ±140° can be covered. The chamber is large enough to hold a second smaller (3.5 cm) analyzer of design similar to that of the larger 15-cm analyzer. Using both analyzers coincidence measurements of the type electron-electron, ion-ion, or electron-ion can be performed

[13]See also K. Siegbahn *et al.*, *ESCA Applied to Free Molecules*, North-Holland, Amsterdam, 1969; T. A. Carlson *et al.*, ORNL-4395 (1969); and J. A. Simpson and C. E. Kuyatt, NBS (private communication).

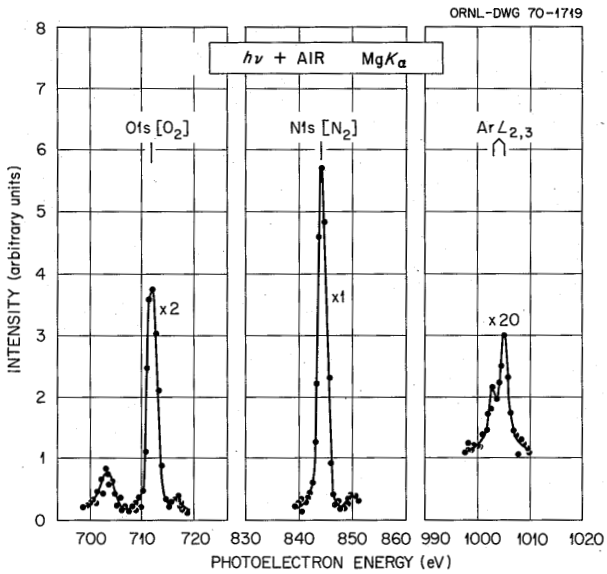


**Fig. 8.6. Photoelectron Spectrum of Air Excited by Mg $K\alpha$ X Rays.**

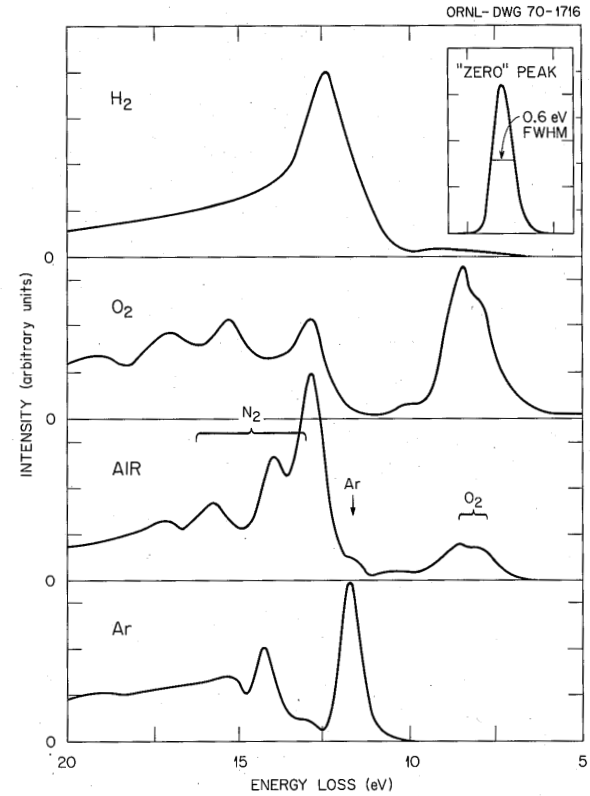


**Fig. 8.8. Electron Energy Loss Spectra of $H_2$, $O_2$, Air, and Ar, Obtained in Forward Direction.** Resolution is limited by energy width, about 0.4 eV, of primary beam of 400-eV electrons. Spectra can be used for diagnostic purposes or for determining excitation energies and probabilities of atoms and molecules.

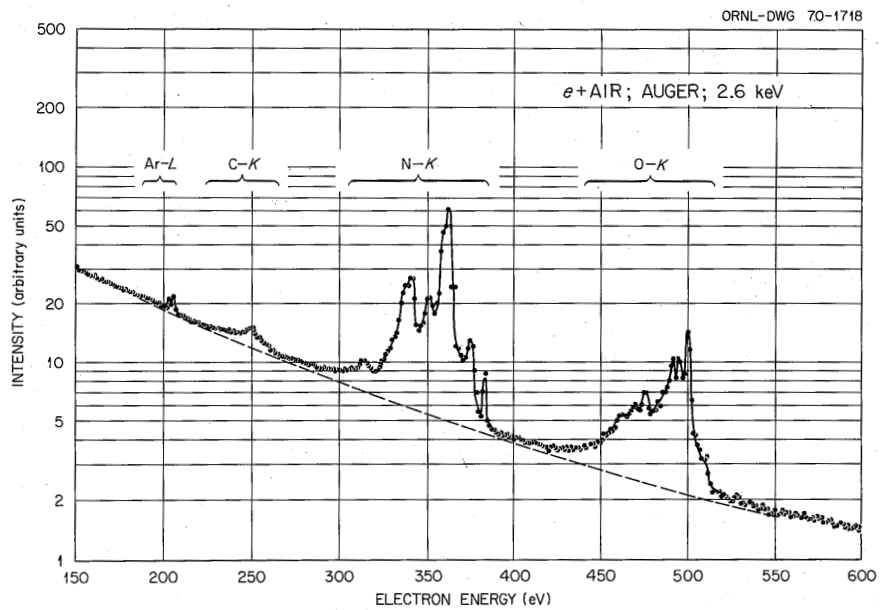


**Fig. 8.7. Auger Spectra of the Components of Air; Excited by 2.6-keV Electrons.** $\Delta E/E = 0.15\%$. Oxygen spectrum mostly due to $O_2$; minor $H_2O$ contribution. Most of carbon spectrum arises from residual gas.

which will allow us to further differentiate many of the processes described above. For example, protons from $H_2$ dissociation can be linked to a certain potential curve of $H_2^+$. In a preliminary experiment, $N^+$ ions have been correlated with a selected Auger electron line and thus with the $B\ ^3\Pi_g$ state of the doubly ionized molecular ion $N_2^{2+}$. One of the future goals is to introduce methods long known in nuclear physics to atomic physics, namely, angular $(e,2e)$ correlation studies [similar to nuclear $(p,2p)$ reactions]. Ionization processes such as $e$ + He, $e + H_2$, and ultimately $e$ + H can then be investigated in great detail.

## 8.3 MULTIPLE EXCITATION OF NEON BY PHOTON AND ELECTRON IMPACT[14]

Manfred O. Krause L. J. Lewis
F. A. Stevie T. A. Carlson
W. E. Moddeman

It is shown that the shake-off theory holds for both photon and electron excitation. Relative intensities are given for diagram and satellite lines of the $K$ Auger spectrum of neon.

## 8.4 ELECTRON ENERGY LEVELS IN FREE ATOMS FROM $Z = 1$ TO $Z = 60$[15]

Manfred O. Krause

A table of electron energy levels in free atoms from $Z = 1$ to $Z = 60$ has been prepared by converting the values of Bearden and Burr for bound atoms with the aid of Moore-Fisher's values of optical levels and theoretical values by Mann and by Froese-Fischer. With a few exceptions, present values are considered to be accurate within ±2 eV and often within ±1 eV.

## 8.5 SCATTERING FROM INELASTIC COLLISIONS

C. F. Barnett J. A. Ray
H. H. Fleishmann[16]

During the past decade a technique has been developed and used extensively in determining the ion energy distribution in a plasma. Neutral particles escaping the plasma via charge-exchange collisions are passed through a gas stripping cell, and the resulting ions are energy analyzed. Unfortunately, these efforts have often been semiquantitative, and geometrical parameters have not been optimized to obtain maximum information, particularly for plasma lifetimes in the range of microseconds or milliseconds. This condition stems from the lack of information concerning the stripping cross section of low-energy (<2 to 4 keV) hydrogen or deuterium atoms in various gases, and also the differential scattering cross section for such inelastic processes. We have started a series of measurements to fill in this gap in the low-energy region. Specifically, measurements are proceeding to measure the differential scattering cross section for the formation of $H^+$ or $D^+$ from stripping collisions and $H^-$ or $D^-$ from electron capture collisions. At the present time the scattering cross sections in target gases of $H_2$, He, $O_2$, $N_2$, Ne, Ar, Kr, $H_2O$, and $C_6H_6$ have been investigated in the energy range 1 to 10 keV with the exception of $N_2$, in which measurements have been extended down to 0.5 keV. Extension of the measurements to energies as low as 0.1 keV are now being carried out in an auxiliary low-energy accelerator.

Basically, the determination of the scattering cross section involves accelerating the proton or deuteron to the desired energy, passing the particle through a gas cell where electron capture collisions result in neutral particles, transmitting the neutral particles through a second gas cell where either the stripping collision or capture collisions result in scattering of the ion formed, and rotating a detector in a direction $\theta$ about the beam axis. In the experiment the count rate or beam intensity, $I(\theta)$, was measured as a function of the angle $\theta$. $I(\theta)$ contains both absolute calibration factors, such as gas pressure, stripping cross sections, detection efficiencies, etc., and the finite resolution of the aperture system. A schematic diagram of the aperture geometry is shown in Fig. 8.9. It can be shown that the angular resolution $\theta_B$ of the neutral beam is given by

$$\theta_B = \frac{d_2}{d + D_2} ,$$

where $d$ is the crossover point of the beam between the beam-defining aperture $d_0$ and the neutralizing cell entrance $d_1$, and $d_2$ is the entrance aperture of the stripping cell. Resolution determined by the detector aperture $d_3$ at position $D_3$ is simply

$$\theta_D = \frac{d_3}{D_3} .$$

Since the stripped ions are formed along the path length $l$ in the stripping cell, another resolution factor is introduced and is given by

[14] *Phys. Letters 31A*, 81 (1970).

[15] Abstract of paper to be issued as an ORNL-TM report.

[16] Summer consultant, Cornell University.

ORNL-DWG 70-3722

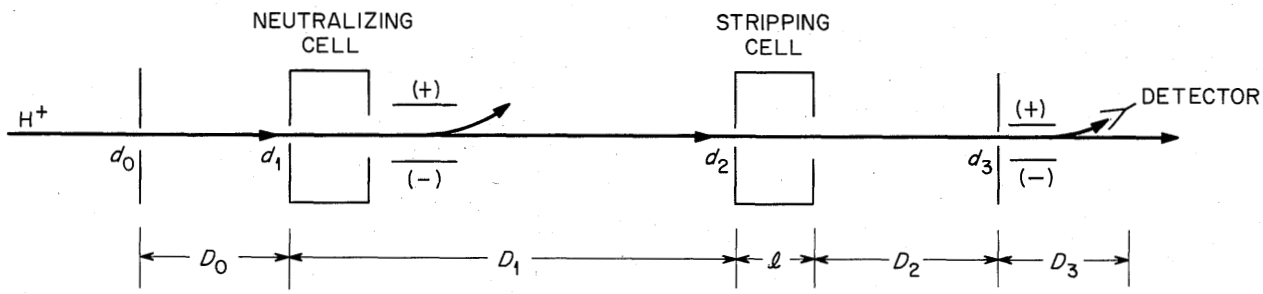


**Fig. 8.9. Schematic Diagram of the Aperture Geometry for Determining the Differential Scattering Cross Section of Hydrogen Atoms in Gases.**

$$\theta_l = \frac{1}{2}\left(\frac{l}{D_2}\right)\theta \ .$$

The total resolution can be characterized by $\theta_0$:

$$\theta_0 = \sqrt{\theta_B^2 + \theta_D^2 + \theta_l^2} \ .$$

During the measurements in the energy range 0.5 to 2 keV the following parameters were used: $d_0$ = 3 mm, $d_1$ = 1 mm, $d_2$ = 1 mm, $d_3$ = 1 mm, $D_0$ = 66 cm, $D_1$ = 100 cm, $l$ = 2.5 cm, $D_2$ = 54 cm; for measurement in the 2-to-10-keV range, $d_2$ and $d_3$ were decreased to 0.5 mm. For small angles, $\theta_l$ could be neglected, and the expected resolution was approximately 2 mrad (0.1°) for low energy and 1 mrad for energies of 2 to 10 keV. The expected resolution corresponds closely to the measured resolution of the neutral beam.

The absolute value of the differential scattering cross section $d\sigma/dr$ can be obtained by integrating $I(\theta)$ over the full space angle and comparing this integral with the total stripping cross section $\sigma_{10}$:

$$\frac{d\sigma}{dr} = A\, I(\theta) \ ,$$

where the calibration factor $A$ is determined from

$$\sigma_{10} = A\int I(\theta)\, dr = 2\pi A \int I(\theta) \sin\theta \, d\theta \ .$$

Thus to represent our present results as absolute cross sections we must in the future measure $\sigma_{10}$ for energies <2 to 4 keV.

For brevity, only results obtained for an $N_2$ stripping (except for one direct comparison) target will be presented in this annual report. Typical experimental results for the scattering resulting from stripping H in $N_2$ gas are shown in Fig. 8.10. Plotted is the counting rate $I(\theta)$ as a function of $\theta$ with the intensity of all curves normalized. Both + and − angles were scanned to assure scattering symmetry and to provide a convenient reference point for zero angle or beam center. The intensity is then multiplied by sin $\theta$, and relative differential scattering cross sections are obtained as shown in Fig. 8.11. The amplitude of the curves at each energy has been arbitrarily adjusted in order to display all curves on one graph. In the graph, $\theta$ has been allowed to go to zero, which implies infinite resolution; however, for exactness, $\theta$ should approach $\theta_{min}$, which corresponds to approximately 0.05°. The peak of the curves occurring at energies greater than $\theta_{min}$ implies that the most probable scattering angle increases with decreasing energies and that the majority of collisions involving inelastic events are scattered at a small angle rather than scattered in the forward direction. The integral of each curve is proportional to the stripping cross section $\sigma_{01}$ as noted in the preceding paragraph. Since the curves are not Gaussian the angle at half maximum intensity has little meaning. We have chosen to characterize these curves by specifying the angle within which either 50% of the scattered particles are contained, $\theta(0.5)$, or 90% are contained, $\theta(0.9)$. A summary of the results for the processes $H + N_2 \rightarrow H^+$, $H + N_2 \rightarrow H^-$, and $D + N_2 \rightarrow D^-$ is presented in Table 8.3. For these processes we expect either $\theta(0.5)$ or $\theta(0.9)$ to show some functional relationship with the energy or velocity. The angle at which $\theta = \theta(0.5)$ and $\theta(0.9)$ is plotted as a function of $E^{-1/2}$ in Fig. 8.12. Both curves are fitted to the data by a least-squares fit and approximate a straight line. For the three-body collision process of forming either $H^-$ or $D^-$ no apparent relationship exists with energy. The data for $H^-$ can be represented with an $E^{-n}$ fit if the 10-keV results are deleted. The value of $\theta(0.9)$ for $H^-$ at 1 keV

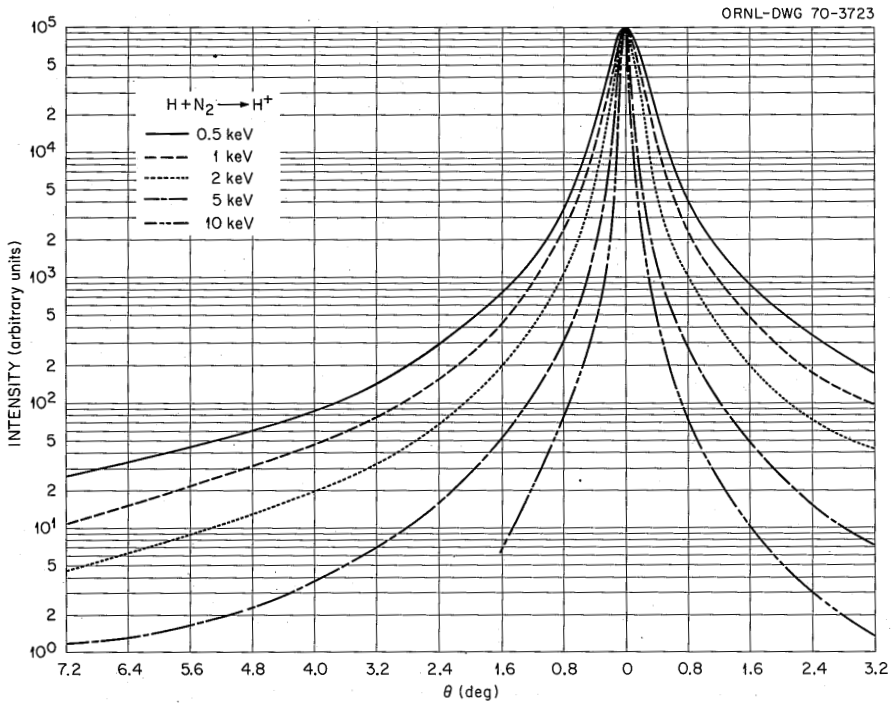


**Fig. 8.10. The Scattering Intensity of $H^+$ Formed by Stripping Collisions of Hydrogen Atoms in Nitrogen.** The intensity is the counting rate of the detector with 1 or 0.5 mm aperture as it is rotated through angle $\theta$ with respect to the beam axis.

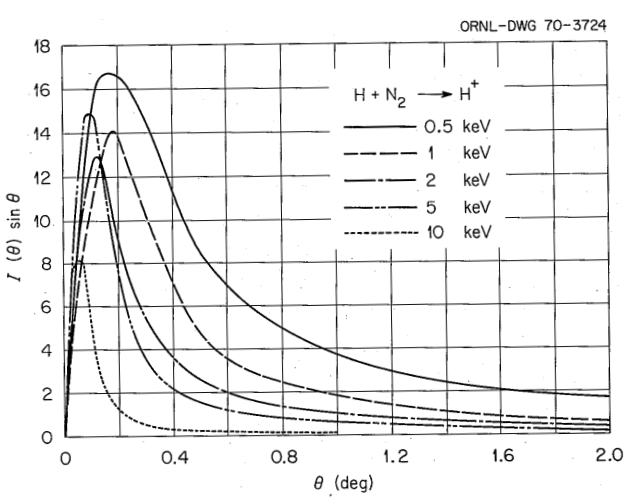


**Fig. 8.11. The Intensity or Relative Differential Scattering Cross Section as a Function of the Scattering Angle $\theta$.**

appears large but was consistent for various sets of data taken months apart. Surprising are the results for $D^-$, which do not appear to correlate with $H^-$ either as a function of energy or velocity.

**Table 8.3. Comparison of the Angles at Which 90% and 50% of the Beam Is Contained for Stripping and Electron Capture of H and D in Nitrogen**

| Energy (keV) | $H + N_2 \rightarrow H^+$ | | $H + N_2 \rightarrow H^-$ | | $D + N_2 \rightarrow D^-$ | |
|---|---|---|---|---|---|---|
| | $\theta(0.9)$ | $\theta(0.5)$ | $\theta(0.9)$ | $\theta(0.5)$ | $\theta(0.9)$ | $\theta(0.5)$ |
| 0.5 | 3.9 | 0.7 | | | 2.6 | 0.6 |
| 1.0 | 3.0 | 0.4 | 3.3 | 0.5 | 2.3 | 0.4 |
| 2.0 | 2.5 | 0.3 | 1.3 | 0.3 | 2.0 | 0.3 |
| 5.0 | 1.4 | 0.2 | 0.4 | 0.1 | | |
| 10.0 | 0.6 | 0.1 | 0.2 | 0.07 | | |

Comparison has been made between the angular scattering of $H^+$ and $D^+$ from $N_2$ gas targets. The results are shown in Fig. 8.13, where again the intensity $I(\theta)$ is plotted as a function of $\theta$ for $H^+$ and $D^+$ energies of 1 keV. The angular distribution is exact except at angles greater than 4.7°, although it was expected that $H^0$ and $D^0$ would scale as the velocity. This energy relationship was observed at 0.5, 1, 2, and 5 keV with a small departure at 10 keV. These results do not imply that the stripping cross sections are equal at the same energy, since the curves were normalized to the same peak intensity.

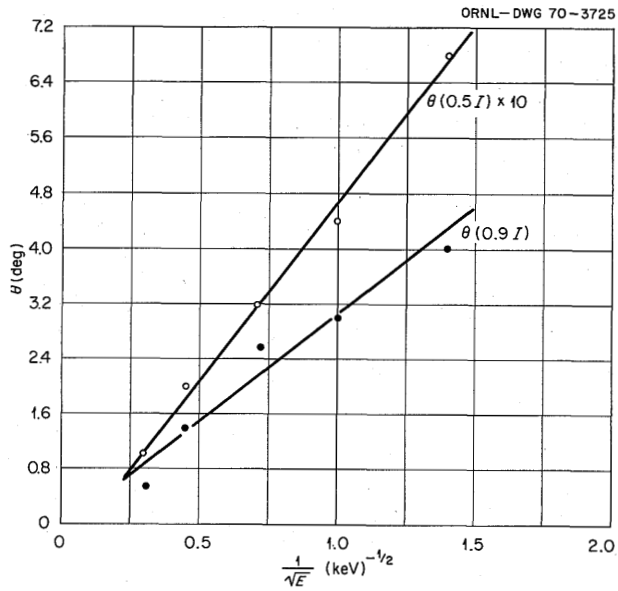


**Fig. 8.12. The Angle at Which 0.9 or 0.5 of the Beam is Contained as a Function of $E^{-1/2}$. $H^+$ formed from H in nitrogen gas.**

To obtain some knowledge of the absolute conversion of H to $H^+$ or $H^-$, experiments were done at 1 keV in which the incident H beam intensity remained constant during the measurements of the angular distribution for both $H^+$ and $H^-$ formed in $H_2$ and $C_6H_6$ gas. The results are shown in Figs. 8.14 and 8.15. The angular distribution is much smaller for $H^-$ production in both gases. The beam intensity at small angles (forward scattering) is a factor of 6 less for $H^-$ than for $H^+$ in $H_2$ gas and a factor of 1.5 more for $H^-$ than for $H^+$ in $C_6H_6$. Of more significance is the integral of these two curves, since

$$\frac{\int_{H^-}}{\int_{H^+}} = \sigma_{0-1}/\sigma_{01} .$$

For $H_2$ gas the ratio is 0.019, and for $C_6H_6$ the ratio is 0.58.

As a final note a remark should be made that all energies refer to accelerating voltage, and to obtain exact energies the energy of the ions emerging from the ion source should be added (~150 eV).

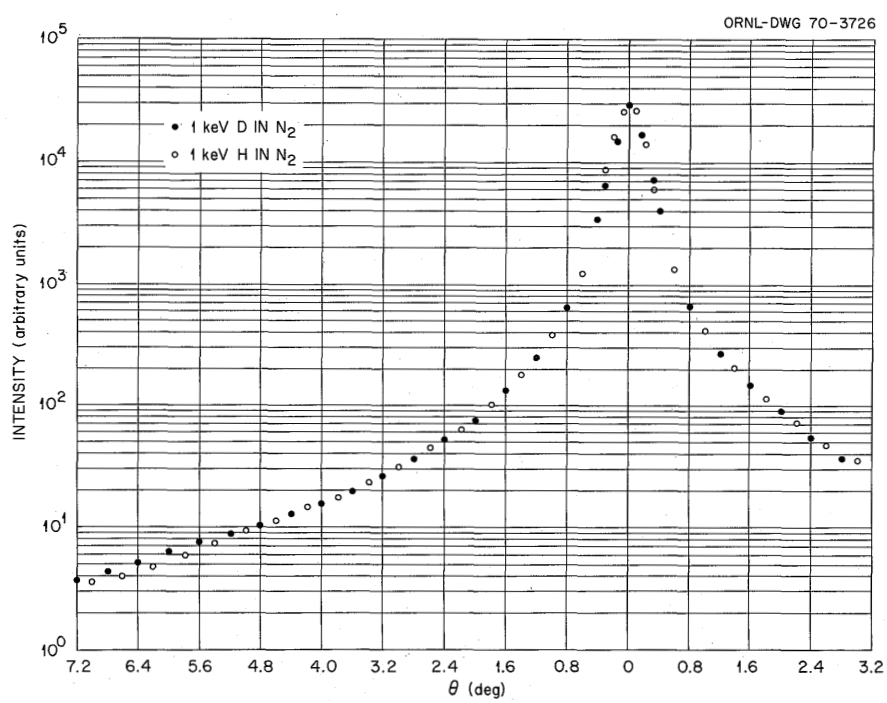


**Fig. 8.13. Comparison of the Scattering Angle for the Processes $H + N_2 \rightarrow H^+$ and $D + N_2 \rightarrow D^+$ at 1 keV.**

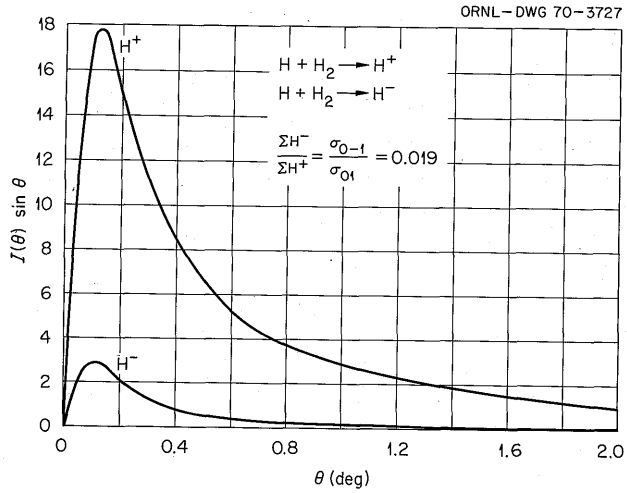


**Fig. 8.14. The Relative Differential Scattering Cross Section for the Processes $H + H_2 \rightarrow H^-$ and $H + H_2 \rightarrow H^+$ at 1 keV.**

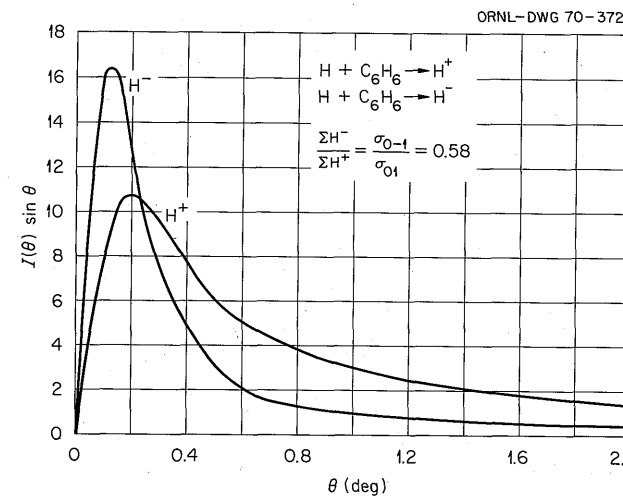


**Fig. 8.15. The Relative Differential Scattering Cross Section for the Processes $H + C_6H_6 \rightarrow H^+$ and $H + C_6H_6 \rightarrow H^-$.**

## 8.6 ENERGY LOSS IN FOILS

J. A. Ray C. F. Barnett

In the last annual report a new and novel technique was described in which the energy loss in thin films was determined with the expectation that one could use foils in measuring the energy spectrum of energetic hydrogen or deuterium atoms escaping plasmas. In this method a carbon foil was mounted at +10 kV potential, and immediately behind the foil a high-resolution solid-state detector was placed. The pulse spectrum obtained from the detector corresponded to $H^+$ particles with energies equivalent to the initial neutral energy ($E_0$) minus the energy loss in the foil ($E_f$) plus the post bias accelerating potential ($E_B$). Thus $E_f$ can be determined by comparing the peak of a spectrum with the foil in place with calibration spectra obtained with the foil removed. During the past year several foils have been tested to determine the reproducibility of foil thickness. Results obtained from two foils are shown in Fig. 8.16. Shown is the energy loss $E_f$ in kilo-electron volts as a function of the H energy. Three disconcerting facts arise from the data: (1) The energy loss for the 100-Å foil is greater than for the 150-Å foil, which indicates that the foil thickness is not known. (2) The energy loss maximizes at approximately 12 keV, which is unexpected and unbelievable. (3) Not shown in the figure are results obtained at 0.5 and 1 keV. The peak pulse spectrum for particles of these incident energies was less than the calibrating energy of 10 keV, which indicates the particle lost more energy than the initial energy. These results are unexplainable at the present time.

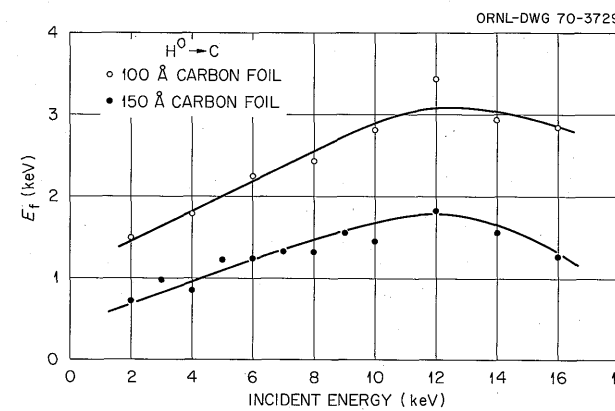


**Fig. 8.16. The Energy Loss of Hydrogen Atoms Traversing a 100- and a 150-Å Carbon Foil in the Energy Range 2 to 16 keV.**

## 8.7 DETECTOR DEVELOPMENT

C. F. Barnett J. A. Ray

The Johnston electron multiplier has many favorable characteristics, such as large entrance (~4 cm in diameter), dynodes relatively insensitive to atmosphere, easily reactivated, high gain, etc. The disadvantage of the multiplier is the low counting efficiency of 30 to 40%. Previously, we had increased the multiplier efficiency by inserting an auxiliary grid in front of the

multiplier such that by placing a negative bias on the grid, electrons escaping the dynode structure would be returned. The multiplier as constructed by the manufacturer consists of a high-transparency grid mounted on the first dynode structure, symbolically shown in the inset of Fig. 8.17. By electrically isolating this grid and varying the potential we have been able to increase the detection efficiency. Plotted in Fig. 8.17 is the counting rate as a function of the negative grid bias for a constant-input 20-keV H beam. Saturation of the efficiency was obtained when the bias was set between 20 and 50 V negative with respect to the first dynode. The pulse spectrum obtained under these conditions is shown in Fig. 8.18. Comparing the counting rate of a silicon barrier detector with the Johnston multiplier indicated a counting efficiency of 97% for 20-keV H.

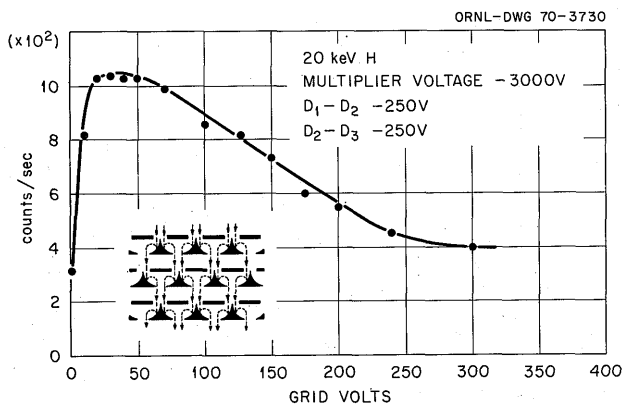


**Fig. 8.17. The Counting Rate for Constant Input Flux of Hydrogen Atoms as a Function of the Bias Applied to the Grid of the Johnston Multiplier.** 20-keV H particles incident. Multiplier voltage −3000 V.

## 8.8 ATOMIC AND MOLECULAR PROCESSES INFORMATION CENTER

C. F. Barnett
D. A. Griffin
Manfred O. Krause
J. Rand McNally, Jr.
J. A. Ray
L. D. Vest

The current atomic and molecular physics literature is being searched and evaluated on a monthly basis. With the increased costs of publication of the bibliographies, the decision has been made to publish them twice a year in the journal *Atomic Data.* A new computer printout format has been devised to condense the printed material and increase the usefulness of the bibliography. At the present time the two bibliographies for the six-month periods of 1969 are ready for publication pending the final debugging of the program. Programming for retrieval of references for specified collision reactants has proceeded to the stage that the reference data base is being increased by adding one past bibliography at a time. Problems have arisen in the transfer of large amounts of data in updating the magnetic tape.

Fourteen months after submitting the monograph *Ion-Molecule Reactions* we are still awaiting publication by John Wiley and Sons. The second monograph to be finished, *Dissociation by Heavy Particles,* has been reviewed and is now being assembled in final form for publication. The third monograph, *Theory of Charge Exchange,* is now being reviewed. *Excitation by Heavy Particles* has been completed, and the final draft of the manuscript is now being prepared for review. The fifth and sixth monographs, *Experimental Data of Charge Exchange* and *Ionization by Heavy Particles,* are in various stages of completion.

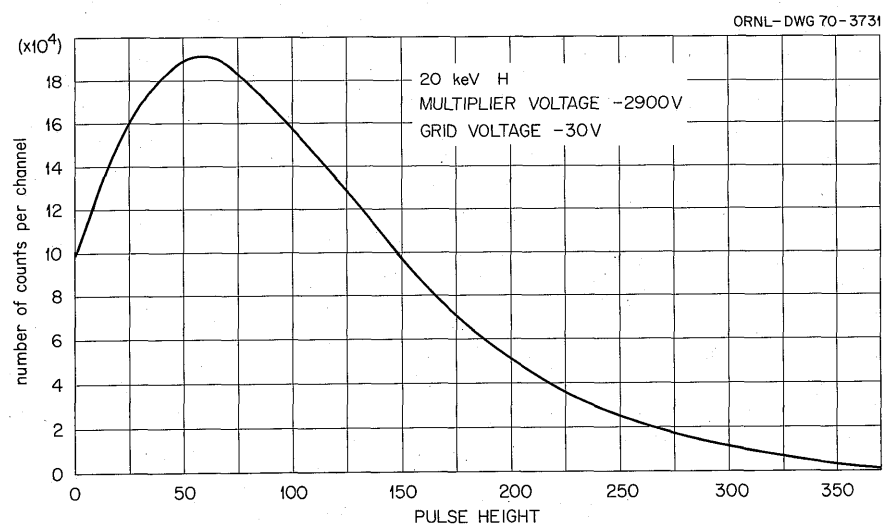


**Fig. 8.18. Pulse-Height Spectrum Obtained from 20-keV Atoms Impinging on the Johnston Multiplier.** Grid at −30 V with respect to the first dynode. Multiplier voltage −2900 V.

# 9. Energetic-Particle Injection

R. C. Davis R. R. Hall
H. K. Forsen[1] G. G. Kelley
O. B. Morgan

## 9.1 INTRODUCTION

Plasma physics experiments with minimum $B$ magnetic mirror geometries are concentrating on high-frequency electrostatic instabilities of the velocity-space type caused by non-Maxwellian velocity distributions.[2] The most pertinent distribution to study is the collisional-dominated loss-cone distribution that will ultimately be necessary in a mirror reactor. Broadening the ion distribution from a 1-keV injector by Coulomb collisions in a target plasma is a technique for achieving these loss-cone distributions. Developing intense low-energy injectors for these experiments has been emphasized during this report period. Using a duoplasmatron ion source with optimized beam-space-charge neutralization has resulted in an injector that should deliver 20 to 50 mA of 1-keV $H^0$ particles into the INTEREM target plasma experiment.

A hydrogen cluster ion source has been developed that delivers milliamperes particle equivalent of useful mass size particles. This project is still in the early stages of development but could provide an intense beam of low-energy ions with a large energy spread. Despite the pertinence of these low-energy injectors for present plasma physics experiments, it remains essential to continue the development of intense, more-energetic injectors for future plasma physics and reactor applications. Therefore, the previous Oak Ridge work,[3] with hundreds of milliamperes of tens to hundreds of kiloelectron-volt particles, remains important and hopefully can receive even more attention for improvement and for evaluation of new ideas and approaches in the future.

## 9.2 INTENSE LOW-ENERGY HYDROGEN ION BEAMS

As emphasized previously,[4] the attainment of space-charge neutralization is very essential for intense low-energy ion beams. With no space-charge neutralization only 5 mA of an initially parallel 2-cm-diam 1-keV $H^+$ ion beam transported through a drift space of 50 cm would increase in diameter to 4 cm from space charge "blowup." Since greater ion current with less beam spread is essential for doing pertinent plasma experiments, the degree of space-charge neutralization must be as great as possible. A decreasing ionization cross section and secondary electron production coefficient for these ions at low energy makes the attainment of space-charge neutralization more difficult. Increasing the neutral-particle density in the beam drift region to compensate for the decreasing ionization cross section makes the differential vacuum requirements more difficult. This space-charge problem has been investigated in detail for hydrogen ion beams in the energy range of 0.1 to 1 keV. Electron addition techniques have been found to be absolutely essential for $H^+$ ion energies of $\approx$0.1 to 0.5 keV and allow bright beams of $\approx$0.5 to 1 keV to be attained independent of the background pressure in the beam drift region.

The system diagram for this work is illustrated in Fig. 9.1. Either a three- or four-electrode duoplasmatron[3,4] ion source is utilized with an anode expansion cup that provides an ion extraction surface ranging from 1 to 2

[1] Consultant, University of Wisconsin.

[2] T. K. Fowler *et al.*, *Report of the Ad Hoc Panel on Fusion Research on Low-Beta Plasmas Confined in Open-Ended Geometries*, TID-24254 (March 1968).

[3] O. B. Morgan, G. G. Kelley, and R. C. Davis, *Rev. Sci. Instr.* **38**, 467 (1967).

[4] G. G. Kelley, N. H. Lazar, and O. B. Morgan, *Nucl. Instr. Methods* **10**, 263 (1961).

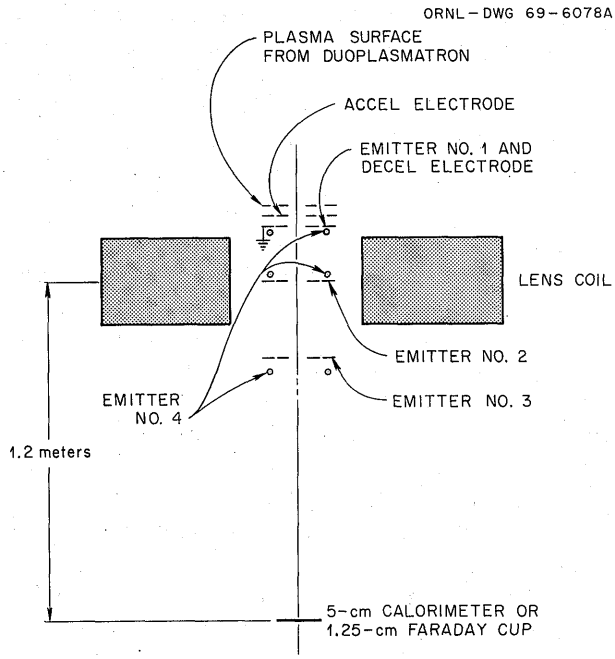


**Fig. 9.1. Low-Energy Hydrogen Ion Beam Space-Charge Neutralization Test Stand Illustrating the Location of Electron Emitters No. 1, 2, and 3 and the Three Alternative Locations of Emitter No. 4.**

cm. Using fine-mesh tungsten gauze or copper sheet with many small apertures allows space-charge-limited currents of hundreds of milliamperes to be extracted from the plasma surface. By keeping the dimensions of the individual plasma surfaces, which are defined by the grid mesh size, equal to or less than the spacing between electrodes, one can extract a large ion current with a small initial divergence. One can crudely define an aspect ratio, $R = 2r/s$, for these individual beams, where $r$ equals the plasma radius and $s$ equals the electrode spacing. One finds that, similar to large single-aperture ion beams, an aspect ratio less than 1 increases the beam divergence. As described previously,[5] the decel electrode shown in Fig. 9.1 is made of 80 to 90% transparent thoriated tungsten gauze which can be heated and used simultaneously as a source of electrons for space-charge neutralization. The No. 2 and No. 3 emitters shown in Fig. 9.1 are also made from transparent thoriated tungsten gauze and are also used to add electrons to the beam. The No. 4 emitter is a thoriated tungsten wire placed around the periphery of the ion beam in one of the locations indicated. The ion beam current density is monitored at distances up to 1.2 m by using either a calorimeter or a 1.25-cm-diam Faraday cup. The Faraday cup (Fig. 9.2) consists of a collector covered with a 1.25-cm-diam 80% transparent grid that is biased negatively to repel secondary electrons, and by a second 80% transparent tungsten grid at ground potential. The cup can be scanned across the ion beam and gives results which agree, within the expected experimental accuracy of 5%, with the ion current measurements made with a 5-cm-diam calorimeter.

The ion beam was first evaluated without the magnetic lens shown in Fig. 9.1, and a typical set of data is shown in Fig. 9.3. This shows the variation in ion beam current obtained on the 5-cm-diam target located at 1.1 m as a function of ion energy. This is done with and without electrons added from emitter No. 1 at various background pressures in the beam drift region. These are uncorrected gage pressure readings in the presence of a hydrogen ion beam. A three-electrode duoplasmatron ion source is used with 15 to 20 A arc current for the results shown in Fig. 9.3. From previous work[3] the beam consists of at least 80% $H^+$. The measurements in Fig. 9.3 are normalized with a constant extracted total hydrogen ion current of 100 mA. From these results it

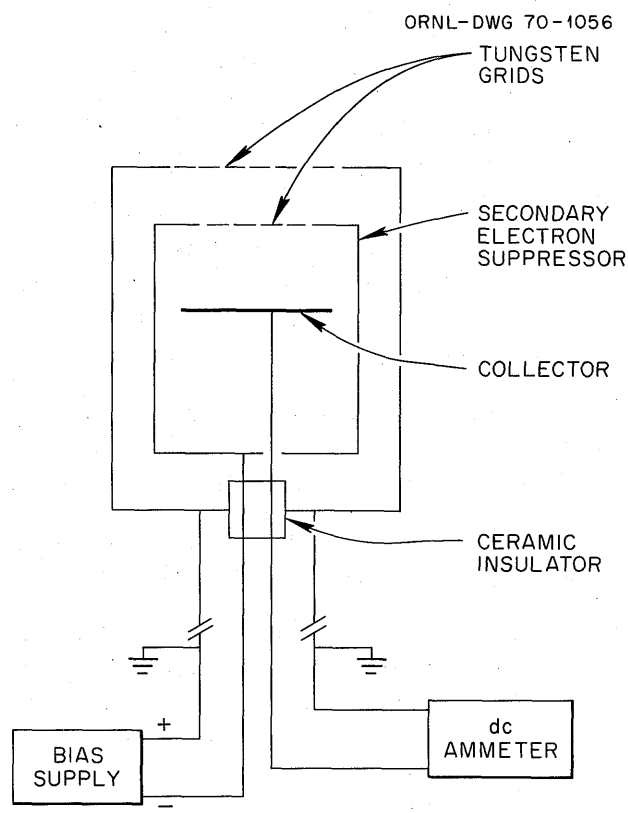


**Fig. 9.2. Faraday Cup for Current Density Measurements with Low-Energy Ion Beams.**

[5] *Thermonuclear Div. Ann. Progr. Rept. Dec. 31, 1968,* ORNL-4401, pp. 176–81.

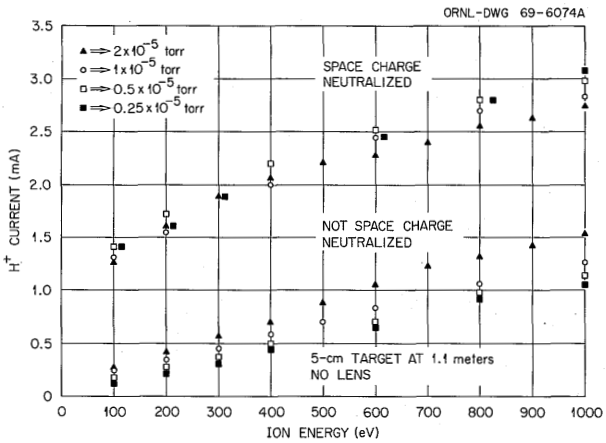


**Fig. 9.3. Hydrogen Ion Current Incident on a 5-cm-diam Target at 1.1 m from the Ion Source as a Function of Energy and Drift Pressure With and Without Electron Addition from Emitter No. 1 (Fig. 9.1).** The magnetic lens is not energized.

is evident that with beam drift pressures up to $2 \times 10^{-5}$ torr, the ion beam is not adequately space-charge neutralized unless electrons are added from emitter No. 1. The space-charge blowup of the beam becomes more severe as the background pressure is reduced if no electrons are added. However, when one properly adds electrons to the ion beam the beam intensity increases as the background pressure is decreased. This can be expected if the ion beam is still adequately space-charged neutralized, since the low-energy scattering on the background neutral particles is decreasing. It should be emphasized that if one increases the extracted ion current at each energy up to the Child-Langmuir space-charge limit, there would be an additional possible increase in the beam that would be expected to be proportional to $V^{3/2}$. However, for the electrode geometries used, the Child-Langmuir space-charge-limited current would be 0.5 to 1.0 A at 1 keV, but this is difficult to achieve because of the required thermal dissipation of the plasma energy from the duoplasmatron by the electrodes. Contrary to the results shown in Fig. 9.3, the addition of electrons from emitters No. 2, 3, or 4 shown in Fig. 9.1 only increased the intensity of 1-keV ion beams by 5 to 20% at pressures of $2 \times 10^{-5}$ torr.

The addition of a magnetic lens to the low-energy $H^+$ ion beam work makes very significant differences. The ion beam intensity increases by using the lens if the object distance is optimum and if the beam is properly space-charge neutralized. For partially space-charge-neutralized beams the beam intensity may actually decrease by using a lens. The addition of electrons to adequately space-charge neutralize the ion beam gives entirely different results when contrasted to the above results without a lens. A typical set of data is shown in Fig. 9.4 for a 100-mA $H^+$ ion beam as a function of energy for three background pressures in the beam drift region. Again, one has a decrease in the beam intensity as the pressure is decreased with no electrons added to the beam. Note that with these inadequately space-charge-neutralized beams the target current at the lower energies is actually less than obtained at a similar pressure without the lens (Fig. 9.3). When electrons are added to the ion beam from emitter No. 1 the results shown in Fig. 9.4 again show a constant or slight increase in beam intensity as the beam drift pressure is reduced. However, as shown in Fig. 9.5, the addition of electrons from emitter No. 2 is now very efficient in attaining optimum space-charge neutralization. This might be expected since electrons from emitter No. 1 have to penetrate the mirror magnetic field of the lens. The combination of the No. 1 and No. 2 emitters further increases the beam intensity. The addition of electrons from emitter No. 3 increases the beam intensity significantly if the No. 1 and No. 2 emitters are not utilized. One can obtain an increase of about 50% in the beam intensity of 1-keV ions at $2 \times 10^{-5}$ torr using emitter No. 4 if neither the No. 1 nor No. 2 emitter is utilized. However, if the No. 2 emitter is utilized, one can see no improvement in the beam intensity by using either the No. 3 or No. 4 emitter.

These results indicate that one is trying to produce an electron distribution from sheet sources to approach the ideal distribution required for complete space-charge neutralization. It has been demonstrated earlier[3]

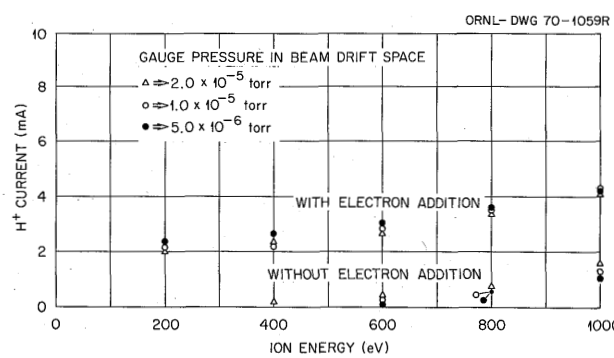


**Fig. 9.4. Hydrogen Ion Current Incident on a 5-cm-diam Target at 1.2 m from the Magnetic Lens as a Function of Energy With and Without Electron Addition from Emitter No. 1 (Fig. 9.1) at Three Different Beam Drift Pressures.**

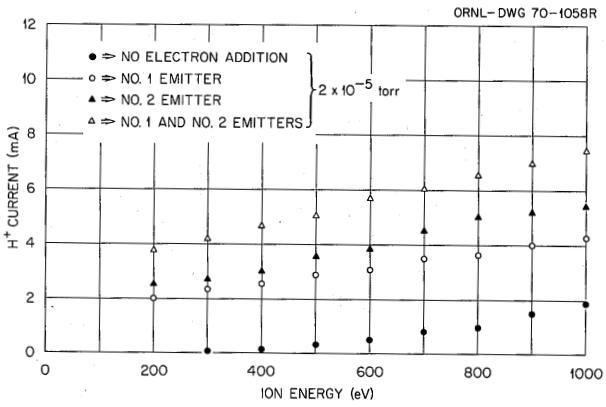


**Fig. 9.5. Hydrogen Ion Current Incident on a 5-cm-diam Target at 1.2 m from the Magnetic Lens as a Function of Energy at a Beam Drift Pressure of $2 \times 10^{-5}$ Torr for Four States of Space-Charge Neutralization.**

that the simplest way to achieve this distribution for higher-energy ion beams is from ionizing collisions of the ions within the beam drift region. However, this becomes more difficult as the ion energy is decreased. One must increase the neutral density to compensate for the decreasing ionization cross section to the point where background gas streaming becomes serious for the plasma physics injector.

With this information as a background, a program has been started to utilize these low-energy ion beams in an injector for target plasmas. Other parametric and technological problems are being evaluated. The ion beam intensity is found to increase up to the space-charge extraction limit, and the attainment of the maximum ion beam near 1 keV is limited by the ability to dissipate the plasma thermal load on the anode grid. It is believed that either tungsten or well-cooled copper is the best prospective material for these electrodes, and they are being evaluated in detail for various geometries without increasing the beam divergence significantly. Detailed ion beam profiles are being determined, and as shown in Fig. 9.6 a useful beam of 30 mA can be obtained through a 5-cm gas cell located 50 cm from the lens from an initial extracted ion beam of only 70 mA. From gas cell streaming measurements it appears that all of this beam can be injected into the INTEREM target plasma. Since 1- to 2-keV $H^+$ ion beams of several hundred milliamperes can be produced, a compromise between ion beam quality and thermal dissipation capacity of the ion beam extraction electrodes should result in even more intense beams. The ion beam profiles shown in Fig. 9.6 include electron addition only from emitter No. 1, and, as is evident from Fig. 9.4, including emitter No. 2 should further increase the beam intensity. This work will continue with both charged- and neutral-particle beams and with further evaluation of the above work using new ideas and techniques.

## 9.3 HYDROGEN CLUSTER ION SOURCE

The low-energy hydrogen ion beam previously discussed is adequate to perform useful target plasma experiments, but the hot ion density attainable in a target plasma is always directly proportional to the injected current.[6] Therefore, investigating other promising sources of energetic particles is felt to be essential. The first new source chosen to study is a hydrogen cluster ion beam injector. This effort is based on the work of Becker and his co-workers at Karlsruhe.[7,8] In their work, hydrogen gas is cooled to near the liquid temperature by using a liquid-hydrogen cryostat before it is expanded through a nozzle into a low-pressure region. Axial skimmer and collimator apertures are then used to limit the core of the resulting jet as it expands into a high vacuum. This expansion results in supersaturation of the gas, and clusters of atoms, in the mass range up to many thousands, are formed and collimated into a beam.

To build an injector for plasma physics it is essential to see if one can produce, ionize, and accelerate an intense beam of these particles within a desirable mass range and therefore a resulting particle energy range of interest. For particles with energies around 1 keV and the need to limit the accelerating potential to 1 MeV, this implies a charge-to-mass ratio of about 1000. Some advantages of this injector are:

1. Space-charge forces are smaller because of small average $e/m$.
2. A distribution in mass implies a distribution in energy.
3. The large Larmor radius implies direct injection into a magnetic trap without neutral-forming gas cells or shielded injected ducts.
4. A large flux of neutral cluster particles should be attainable.

---

[6] *Thermonuclear Div. Semiann. Progr. Rept. Oct. 31, 1967*, ORNL-4238, pp. 61–64.

[7] E. W. Becker, R. Klingelhofer, and P. Lohse, *Z. Naturforsch.* **179**, 432–38 (1962).

[8] E. W. Becker, K. Bier, and W. Henkes, *Z. Physik* **146**, 333–38 (1956).

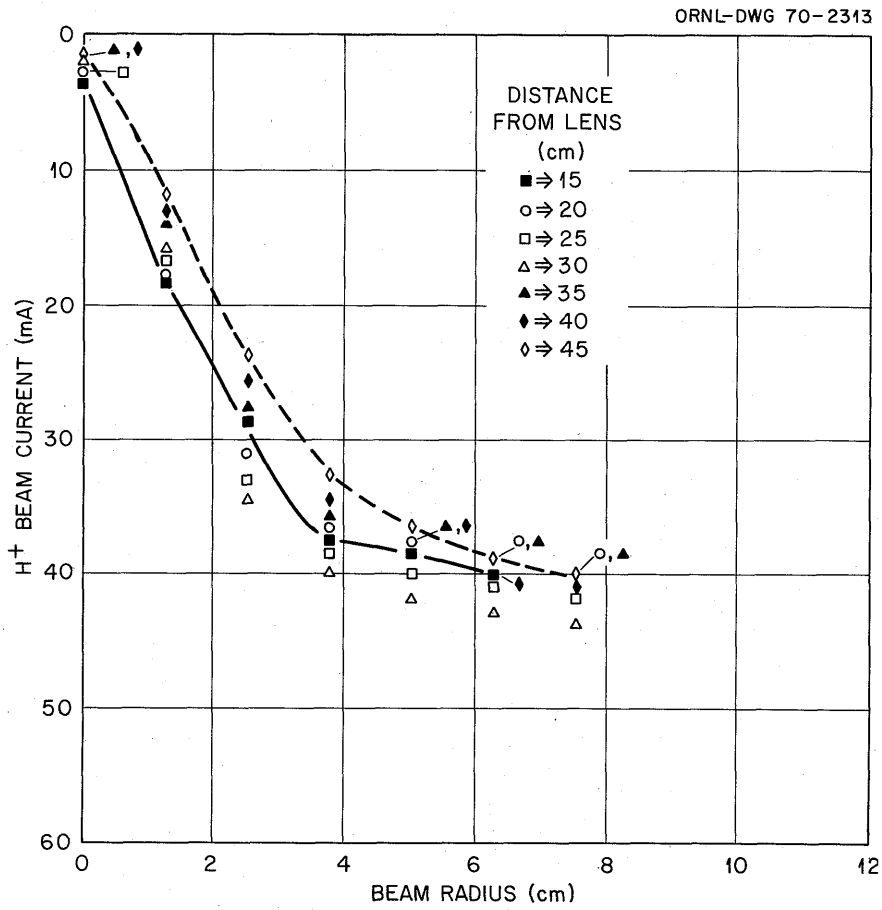


**Fig. 9.6. 1-keV $H^+$ Ion Current as a Function of Beam Radius at Indicated Distances from the Lens.** Emitter No. 1 (Fig. 9.1) is used. Total extracted current is 80 mA, and the drift pressure is $2.3 \times 10^{-5}$ Torr.

The system built to conduct this research is shown in Fig. 9.7. Since the interest is in a system that can easily be used as an injector, one is motivated to avoid the complexity of using the liquid-hydrogen cryostat, used at Karlsruhe, if possible. Therefore, it was decided to use warmed liquid-helium vapors to cool the hydrogen gas and apertures. The helium vapors are obtained directly from a commercial liquid-helium container, and the flow rate of the vapors, and therefore the resulting temperature of the nozzles and hydrogen gas, is controlled by varying the helium evaporation rate with a small constantan wire heater. The heater is placed on the end of a commercial liquid-helium transfer tube and submerged into the liquid-helium container. Using this technique, one is able to accurately control the temperature of the cryostat throughout a temperature range of 15°K to room temperature. As indicated in Fig. 9.7 and labeled "heat exch No. 2," the exhausting helium vapors cool the incoming hydrogen gas by being piped through concentric tubes. The inner 20°K cryostat is surrounded by liquid-nitrogen-cooled surfaces. The first pumping stage of the system consists of a Roots blower–Kinney pump combination with a pumping speed of 550 liters/sec. The second stage consists of two 10-in. diffusion pumps, and the third stage consists of three 10-in. diffusion pumps plus getter pumping.

The neutral cluster jet emerging from the collimator drifts through a 100-kV insulating bushing to the ionizer. The ionizer is a variable energy and density electron source that was built to try to eliminate any low-frequency or direct-current electric fields that would disperse the very low energy cluster ions. The ionization cross section of the hydrogen clusters increases with the mass number,[9] and therefore the electron density can be adjusted to provide a mean free path of 1 for the mass range of interest.

[9]W. Henkes and O. F. Hagena, report KVT/9/19, Karlsruhe Technical University.

ORNL-DWG 69-6082A

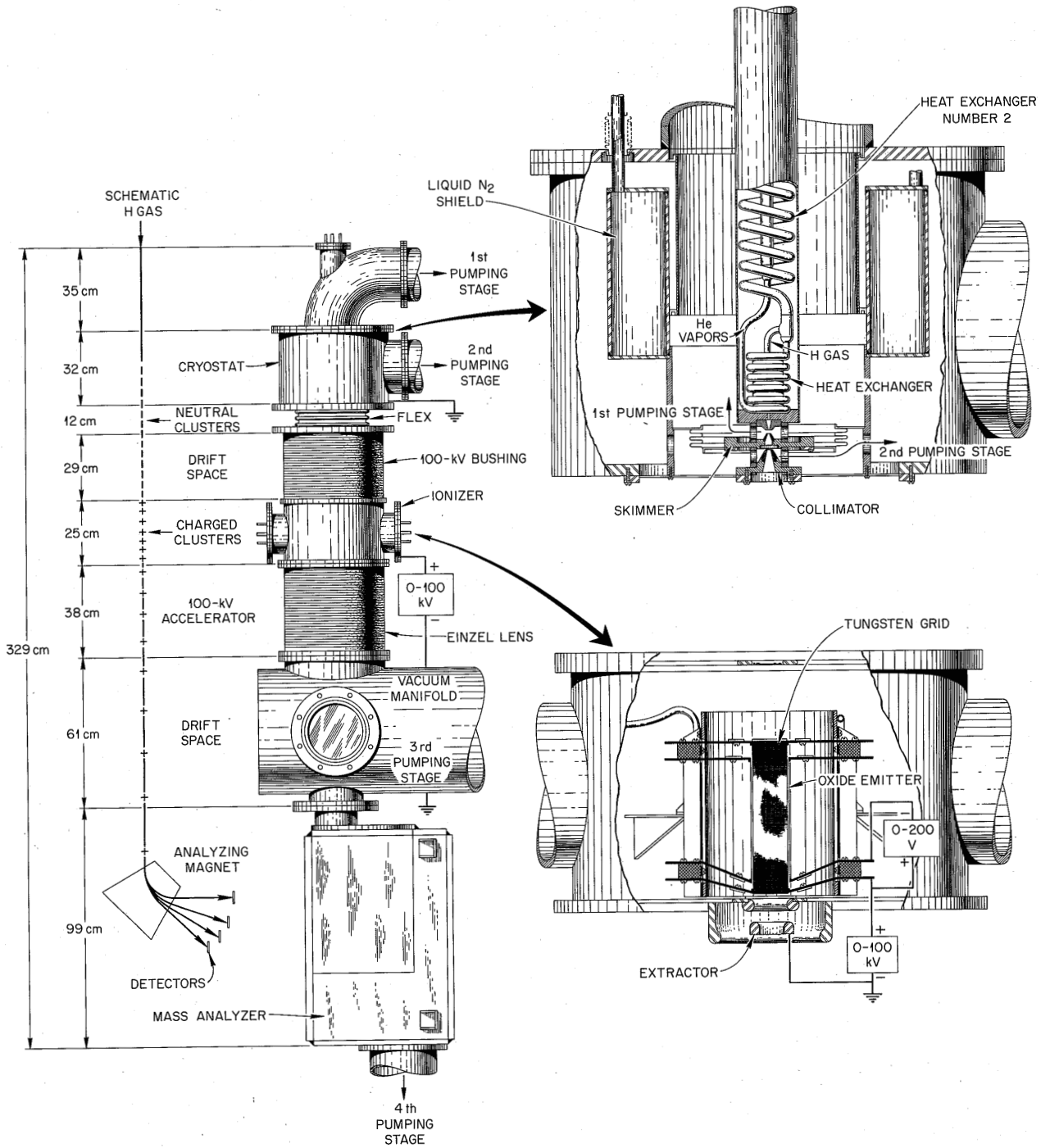


**Fig. 9.7. Hydrogen Cluster Ion Injector Test Stand.**

The ionized hydrogen clusters are accelerated up to 100 keV and focused with an electrostatic lens into a parallel beam that is mass analyzed in a 3-kG transverse magnetic field. The resulting ion currents are detected with a scanning probe within the magnetic field. Large hydrogen clusters with tens of keV total energy are capable of producing large secondary particle currents of both ions and electrons,[10] and consequently an accurate detection of the cluster currents is difficult. By using a sweeping probe within the magnetic field of the mass analyzer one can restrict the ability of the low-energy secondary ions or electrons to "flow" from the probe. Using this technique it is believed that the charged-particle currents are accurate for particles within a mass range up to several hundred. However, for ion currents corresponding to a mass range of thousands and greater, one is not sure of detecting the current accurately. Assuming one can increase the particle current, this difficulty will hopefully eventually be eliminated by using a calorimeter.

Initially the neutral-particle density of the jet was measured as a function of gas throughput and temperature by using an ion gage probe with a small aperture to scan the beam. Particle current densities up to $5 \times 10^{17}$ atoms $cm^{-2}$ $sec^{-1}$ at a distance of 11 cm from the collimator (Fig. 9.7) were found.

In the first attempts to ionize and accelerate cluster ions to 30 keV, the system became very unstable, with periodic electrical discharges between the ionizer and cryostat. The breakdowns were caused by condensable vapors from the vacuum system accumulating on the liquid-nitrogen surface of the cryostat. They were eliminated by shielding this surface from the 30-kV potential with a thin room-temperature copper shield.

The system has been operated for a fairly complete set of parametric variations using the set of expansion and collimation apertures shown in Fig. 9.8. A typical mass-analyzed beam spectrum is shown in Fig. 9.9. The bottom curve shows the mass spectrum recorded on an *x-y* recorder by the scanning probe. The mass numbers are indicated on the abscissa and the charged-particle current in microamperes on the ordinate. Note that in the low mass range one finds odd-numbered mass peaks starting with mass 3, 5, 7, etc. These are typical for hydrogen clusters and are formed because of the exothermic reaction between the molecular ion and the neutral molecule ($H_2^+ + H_2^0 \rightarrow H_3^+ + H^0$) taking place

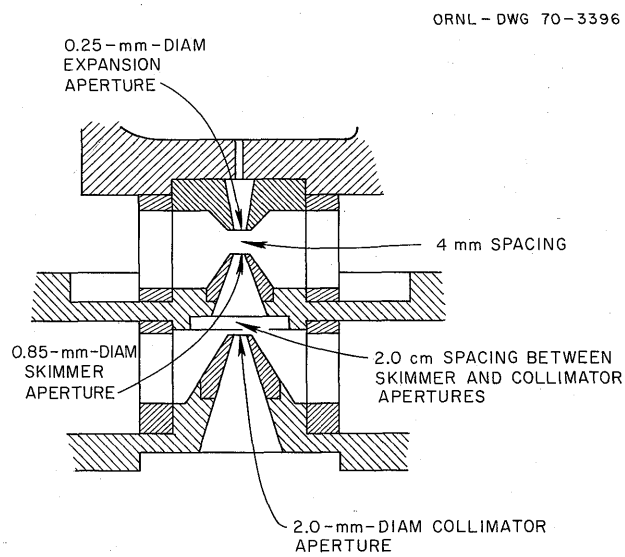


**Fig. 9.8. An Enlarged View of the Expansion and Collimation Section of the Hydrogen Cluster Cryostat Shown in Fig. 9.7.**

in the condensed phase and the resulting kinetic emission of the released atom.[11] Notice that this is not a high-resolution mass spectrometer. The object was to build a spectrometer that would analyze the entire beam and determine the cluster current available within a useful mass range rather than study a small beam sample with a better resolution. The second curve indicated the equivalent particle currents in microamperes. Notice that there is a peak in particle current corresponding to mass 100–400. This mass range would be expected to correspond to approximately one mean free path in the ionizer.

Figures 9.10 and 9.11 show the variation of the low-mass-number peak heights of the spectrometer at three different hydrogen flow rates through the apertures shown in Fig. 9.8. Notice that for each of these flow rates one reaches an instability as the temperature of the aperture and gas is reduced. As the temperature is lowered, the pressure in the three pumping stages begins to fluctuate violently. These oscillations have been observed in other cluster experiments.[7,12,13] Figure 9.12 shows the variation of the temperature at

[10] B. V. Panin, *Soviet Phys. JETP* (English Transl.) **14**, 1 (1962).

[11] K. Buchheit, thesis, Karlsruhe Technical University, pp. 1–22, 1967.

[12] E. S. Tay *et al.*, A.P.&T. Division Memo No. 1, Culham Laboratory (June 24, 1969).

[13] B. J. C. Burrows *et al.*, "Experiments on Hydrogen Clusters," 5th Symposium on Fusion Technology, Oxford, 1968.

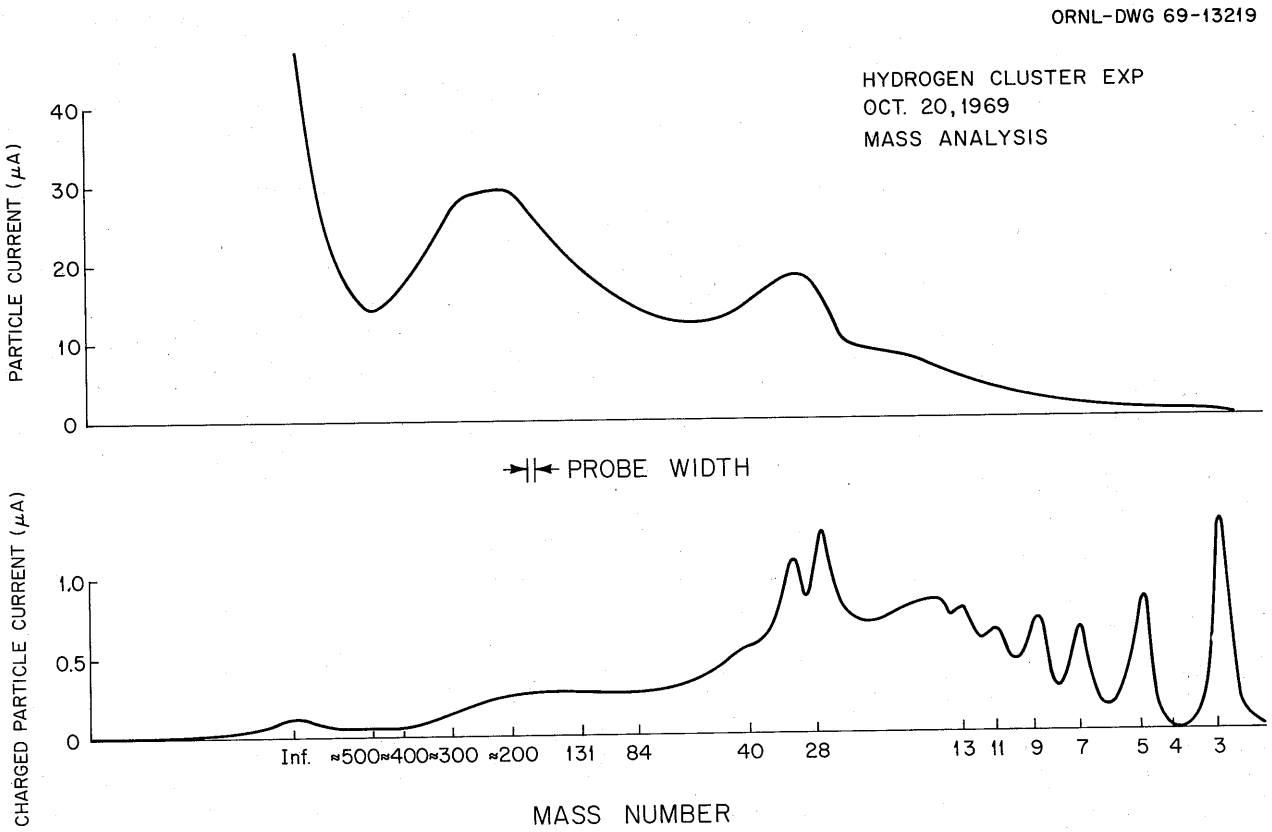


**Fig. 9.9. Typical Hydrogen Cluster Ion and Equivalent Particle Currents with Expansion Geometry Shown in Fig. 9.8.** The $H_2^0$ flow rate is 40 atm-cc/sec at a temperature of 17°K.

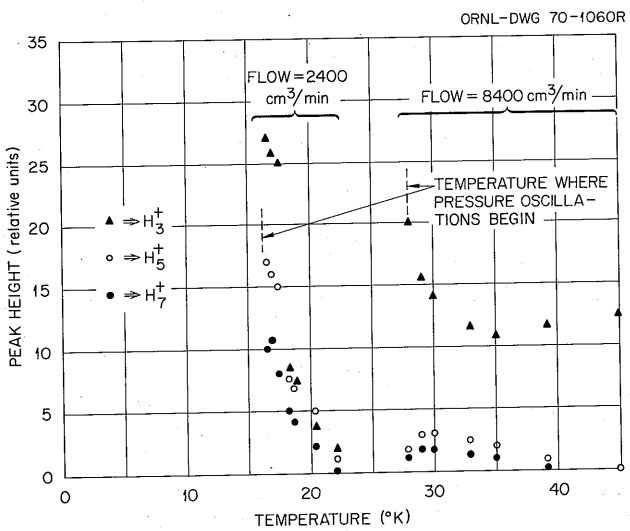


**Fig. 9.10. Hydrogen Spectrometer Peak Height Variations as a Function of Temperature for Two Flow Rates.** Aperture sizes shown in Fig. 9.8.

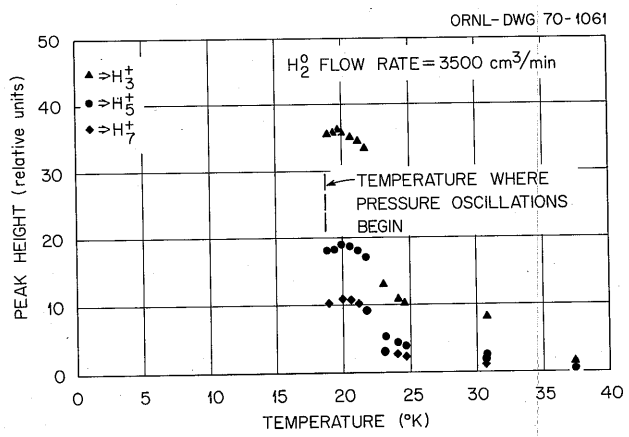


**Fig. 9.11. Hydrogen Spectrometer Peak Height Variations as a Function of Temperature.** Aperture sizes shown in Fig. 9.8.

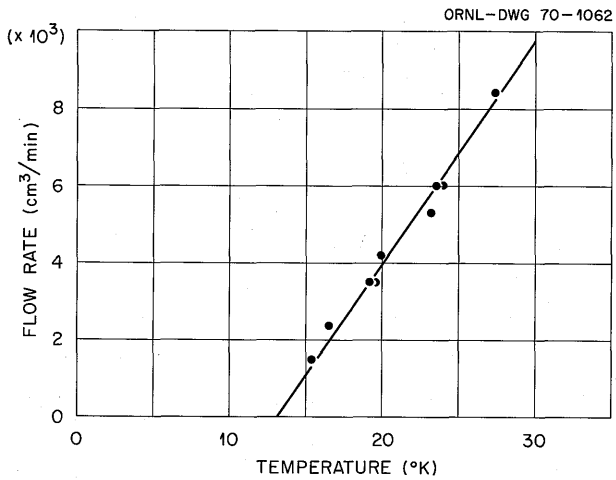


**Fig. 9.12. Hydrogen Pressure Oscillation Temperature as a Function of Hydrogen Gas Flow Rate.**

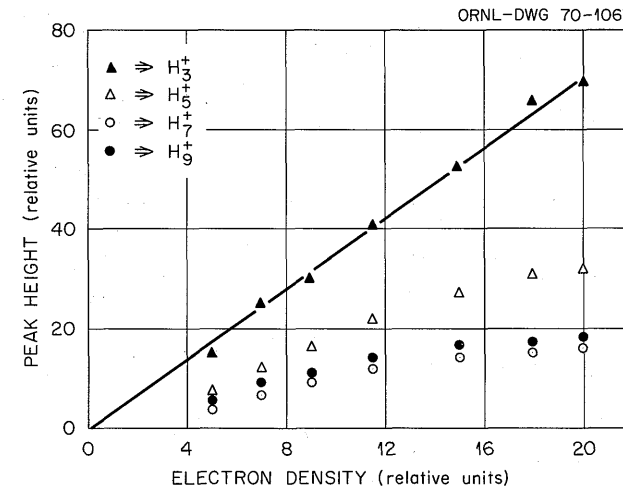


**Fig. 9.13. Hydrogen Spectrometer Peak Heights as a Function of Electron Density in Ionizer.** Electron energy is 160 eV.

which this instability appears as a function of the hydrogen flow rate through the apertures of Fig. 9.8. The 1-cps frequency of these pressure fluctuations indicates that thermal oscillations are a possible cause. The thermal conductivity and heat capacity of the cryostat assembly are being improved to study this possibility.

The amplitude variation of some of the mass peaks as a function of the electron density is shown in Fig. 9.13. The peak height of the mass 3 ions increases linearly with the electron density in the ionizer, but the peak heights of the higher-mass ions saturate. If the higher-mass ions were being disassociated, one should see a substantial increase in the mass 3 component. Another possibility is that as one increases the electron density in the ionizer, low-frequency electric fields disperse the massive low-energy cluster ions and prevent them from reaching the acceleration region. A probe is currently being installed in the system to monitor the cluster jet neutral-particle intensity with and without the ionizer.

An unsuccessful attempt has been made to extract negative hydrogen clusters from the system. No detectable clusters were extracted, although electron currents of several hundred milliamperes were obtained. These cluster beam studies will continue in parallel with the low- and high-energy ion beam work discussed above. The requirements of the Thermonuclear Division for pertinent plasma physics experiments will determine the future distribution between these various projects.

# 10. Magnetics and Superconductivity

## 10.1 REVIEW OF BASIC WORK ON APPLIED SUPERCONDUCTIVITY


K. R. Efferson
W. F. Gauster
J. L. Horton[1]
S. Ihara[2]
D. M. Kroeger[3]
G. F. Leichsenring
M. S. Lubell
J. D. McDowell[4]
J. E. Simpkins
S. L. Wipf[5]


During this report period our basic work on applied superconductivity has again been jointly sponsored by the Controlled Thermonuclear Branch of AEC and by the George C. Marshall Space Flight Center of NASA (NASA Government Order No. H-29278A, "Magnetic Flux Flow and Superconductor Stabilization"). The last three of our NASA progress reports and several of our papers published or to be published in the open literature give a good picture of our basic work on applied superconductivity; therefore it is sufficient to quote the following abstracts:

1. ORNL-TM-2534 (February 1969)

Maxima in curves of critical current versus temperature at fixed fields have been found to be associated with the peak effect in a Nb–5 at. % Ti strip. The data are in qualitative accord with recent suggestions that a superconductor with $\partial J_c/\partial T > 0$ should show unusual stability. The ratio of the field at the peak to the upper critical field was found to be independent of temperature, having a value 0.84. There is an indication that the dependence of thermal conductivity on temperature is anomalous in the region of the maxima. Flux jumping experiments have been performed on cylindrical tubes of Nb-Ti alloys believed to possess $\partial J_c/\partial T > 0$ in a reasonable field range. Due to the low $J_c$ in these materials, there was no flux jumping seen at all even where $\partial J_c/\partial T < 0$ for a wide range of $dH/dt$. Flux jump experiments were made on Nb–25% Zr to see if the onset of "limited instabilities" rather than the flux jump field could be correlated with $H_{fj} = \text{const.}[C(T)f(T)]^{1/2}$, where $C$ is heat capacity. A "limited instability" region was observed well below the first flux jump field. A low frequency (1.2 Hz) oscillatory voltage was observed on the pickup coil starting at about ½ kG before some of the flux jumps. Additional calculations of the thermal equilibrium states of multistrand compound conductors have been made for various copper to superconductor ratios. These calculations consider the actual heat transfer to the liquid helium bath and the dependence of the superconductor current on magnetic field, temperature, and voltage. The current-voltage characteristics obtained in this way (in contrast to those calculated with simpler models) demonstrate the great variety of possible thermal equilibrium states as indicated by experiments.

2. ORNL-TM-2641 (June 1969)

The steady state current-voltage characteristic of a single filament Nb-Ti wire (superconductor diameter 10 mils = 0.0254 cm, total diameter 20 mils = 0.0508 cm) has been calculated. The actual heat transfer between conductor surface and the liquid helium bath and the dependence of the flux flow voltage on the magnetic field strength $H$, the electric field strength $E$, and the temperature $T$ has been considered. The temperature dependence of the heat conductivity inside the superconductor has been taken into account. The resulting $V$-$I$ characteristic is compared with the $V$-$I$ characteristic calculated under the assumption that the superconductor is divided into a great number of fine filaments. The major difference between these two $V$-$I$ characteristics is adequately explained. Wires of Nb with 5, 10, and 25% Ti were investigated at large $dH/dt$ but no evidence of flux jumping was found. Flux jumping experiments were performed on a Nb–56% Ti cylindrical tube to investigate the importance of surface heat transfer. Experiments were made with the sample completely immersed in helium, partially covered with helium, and in vapor. Three surface conditions were investigated – bare, copper coated, and epoxy coated. These experiments indicate that surface heat transfer cannot be neglected in an analysis of flux jumping. Flux flow experiments were performed on a thin copper coated strip of Nb–10% Ti and compared with the bare strip measured at various voltage criteria for $J_c$. The critical current of the copper coated strip was much larger than the bare strip except in the region of the peak. In contrast to recently published data, the peak could not be eliminated by using a more insensitive voltage level for the critical current determination. An apparatus suitable for measuring thermal conductivity and critical temperatures in a magnetic field has been constructed and tested. An appendix covering work on flux jumping in Nb-Ti rings performed at ORNL is enclosed.

---

[1] Instrumentation and Controls Division.

[2] On temporary assignment with ORNL. Permanent address: Electrotechnical Laboratory, Ministry of International Trade and Industry, Tokyo, Japan.

[3] Now with the Metals and Ceramics Division.

[4] Mathematics Division.

[5] On temporary assignment with ORNL. Present address: Atomics International, a Division of North American Rockwell Corp., Canoga Park, Calif.

3. The appendix to the preceding report is "Flux Jumping in Rings of Niobium-Titanium" by S. L. Wipf, with the following abstract:

An experimental study has been made of the limit between stable and unstable critical current flow in rings of Nb-Ti. If a ring is in the creep state (stable critical current) in a decreasing field, this limit is given by the first flux jump (i.e., total breakdown of the critical current). In a plot of electric field along ring versus critical current, the stability limit follows a line of constant power dissipation; this power dissipation per unit surface is of the order of $10^{-5}$ to $10^{-4}$ W/cm$^2$ and, roughly, inversely proportional to the inductance of the rings. At high currents and correspondingly low fields, a cutoff seems to be given by flux annihilation. At low currents (high fields) the flux jumps are not complete. In comparing these experiments with existing theory it is found that the simplest criterion for full stability does not apply. According to this criterion an instability can only occur if for a given temperature change the change in stored magnetic energy is equal or larger than the change in enthalpy – this has hitherto been considered a "necessary" condition for flux jumping. If applied to the present situation, flux jumps should only occur at much higher currents. Arguments are presented suggesting a modification of the criterion to allow for "hot" spots or "non-uniform" flux flow. A set of three equations is given which governs the growth of an instability from an initially non-uniform flux flow state.

4. ORNL-TM-2771 (November 1969)

The stability at the critical current (initial stability) of bare superconducting wires of various diameters is discussed. A "very thin wire" assumes the bath temperature, is initially stable, and displays either an initial flux creep regime or an immediate linear flux flow. A wire of the same material, but with a larger diameter ("thin wire"), assumes almost a uniform temperature which is larger than the bath temperature. With still larger diameter, the temperature distribution will be non-uniform ("thick wire"). If a distinct flux creep regime can be observed with the "very thin wire," then the "thin" and the "thick wire" are both initially stable. For the case of initial linear flux flow displayed by the "very thin wire," criteria for the initial stability of the "thin" and the "thick wire" are derived. A discussion is presented on the relationship between the definition for a pure and dirty superconductor and the Ginzburg-Landau kappa. The result $\xi_0/l = 1.34\ \kappa_l/\kappa_0$ illustrates that the dirty limit $\xi_0/l \gg 1$ implies $\kappa_{GL} \gg \kappa_0$ not $\kappa_{GL} \gg 1$. The thermal conductivity apparatus has been finished and a preliminary measurement of $\lambda$ vs $H$ for a Nb–5% Ti wire (diam. = 0.77 mm) is shown. A compilation covering the upper critical field and the critical temperature for the Nb-Ti alloy system is also included as much of the data has been published only recently and is not available in any of the standard material reviews.

5. The appendix to the preceding report is "Evidence to Support the Rigidly Pinned Vortex Model for the Peak Effect" by M. S. Lubell and D. M. Kroeger. This paper was presented by M. S. Lubell at the Conference on the Science of Superconductivity, Stanford, California (August 26–29, 1969), and has been accepted for publication in *Physica*. The abstract reads:

Data are presented on the peak effect of a Nb-Ti alloy. The temperature dependence of the critical current at a field equal to or higher than the peak field is shown to agree with a model of a rigidly pinned vortex lattice.

## 10.2 THERMAL EQUILIBRIUM OF SUPERCONDUCTING WIRES IN THE FLUX-FLOW STATE

W. F. Gauster M. S. Lubell

In Sect. 10.1 of this report, a short review of our work on basic applied superconductivity is given. We think that one of the main achievements of these efforts is that we reached a decisive phase in the understanding of the thermal equilibrium of bare and of stabilized superconducting wires and ribbons which are in the flux-flow state. In another paper,[6] this approach will be discussed in detail, including the basic equations. Here, we will restrict ourselves to reviewing the physics involved and to pointing out which known basic physical data can be employed and which additional data are still in need of the nonlinear theory in order to achieve a perfect experimental verification. We do not include any literature here but refer in this respect to ref. 6.

The main motivation of all these efforts is to find practically usable stability criteria for superconducting magnet systems. Unfortunately, to date, the engineering experience with large and especially with nonaxisymmetrical superconducting magnet systems is not sufficient to predict the performance of designs which deviate appreciably either in size, shape, or field strength from already-tested prototypes. There is, of course, one way out, namely, to build extremely well-stabilized systems which represent essentially cryogenic coils with additional superconducting current paths, which reduce the helium evaporation during regular operation. This solution is, of course, very expensive, and in many cases it is not applicable for other reasons (space requirement, etc.) also.

Recent research has shown that the following phenomena determine the stability of superconducting magnet systems: the thermal equilibrium of the superconductor in the flux-flow state; the velocity of propagation of the boundaries separating the superconducting, the flux-flow, and the normal state in a superconducting winding; the occurrence of local flux jumps; and the performance of the superconducting and normal parts of the system initiated by such flux jumps.

[6]Final report of NASA Government Order No. H-29278A, "Magnetic Flux Flow and Superconductor Stabilization." (ORNL-TM-2980)

Of special practical importance is the influence of the twisting of the superconducting filaments (see Sect. 10.3).

During the last few years, some simple engineering criteria for the electric stability of superconducting magnet systems have been widely used. These criteria have yielded good practical results when employed conservatively for the design of superconducting magnet systems that were not too different from already well-tested similar designs (since empirical constants could be properly chosen) or when a generous degree of safety could be afforded.

Some of the most important of these engineering criteria are based on a linearized theory of the thermal equilibrium of stabilized superconductors in the flux-flow state. The linearized theory assumes that the heat transfer from the compound conductor surface to the liquid-helium bath can be expressed by one linear relation between the heat flux and the temperature difference. This linear relation is supposed to hold from zero heat transfer up to the beginning of film boiling, that is, over the entire regimes of heat convection and nucleate boiling. This coefficient is in the order of about $\frac{1}{2}$ to 1 W/cm$^2$ and is at least one order of magnitude larger than the coefficient for heat transfer by heat convection, which determines the heat flux for very small temperature differences between conductor surface and liquid helium. Another assumption is that from the very beginning of the flux-flow regime the flux-flow resistance is so much greater than the stabilizer resistance that, immediately after the critical current is exceeded, the superconductor current is a function of the temperature and the magnetic field only, that is, independent of the electric field strength along the conductor. Using these assumptions, the linearized theory shows that if thermal equilibrium is achieved at the beginning of the flux-flow regime (i.e., as soon as the current just exceeds its critical value), then, for the usual type of compound conductors (those with fine filaments which are well bonded with the stabilizer) thermal equilibrium will persist until the maximum nucleate heat flux is reached or until the flux-flow state of the superconductor is terminated by attaining the normal state. Therefore, the "initial stability" is a necessary and sufficient stability criterion of the linearized theory of the thermal equilibrium of compound conductors. In other words, following the linearized theory, a compound conductor with thin superconducting filaments that are well bonded with the stabilizer should display one of the two following types of performance. The first possibility is that the compound conductor is initially stable; that is, after the critical current is exceeded, the compound conductor goes steadily into the current-sharing state. With increasing current, the heat transfer into the liquid helium increases continuously and, when the film boiling regime or the critical temperature is reached, the flux-flow state of the superconductor changes into the normal state. The second possibility predicted by the linearized theory is that the compound conductor is initially unstable and "jumps" into the normal state at the critical current.

Experiments clearly show several other types of performance. For instance, when the current is increased over the critical value, an initial voltage instability may occur; however, after this voltage jump the voltage increases continuously, indicating that a distinct zone of stable current-sharing states has been reached. After a sufficient further increase of the current, a new instability can be observed which finally brings the conductor into the normal state. This and several other types of performance that have been observed cannot be explained by means of the linearized theory of the thermal equilibrium of stabilized compound conductors.

For bare superconductors, it can easily be shown that the assumption, made in the linearized theory, that the superconductor current (or current density) depends on temperature and field only (and not on the voltage across the sample) leads to paradoxical results. Suppose that a bare superconducting sample exposed to a constant external magnetic field reaches thermal equilibrium with a certain current flowing through it and with a certain voltage across it; then the product of current and voltage is equal to the heat transferred to the liquid helium. In general, with increasing temperature the critical current of a superconductor decreases and, therefore, an increase of the superconducting current would call for a decrease of the temperature, a decrease of the electric power, and thus a decrease of the voltage. Such a current-voltage characteristic with negative slope would indicate instability. It would follow that any bare superconducting wire should be intrinsically unstable; this contradicts well-known experimental evidence.

Our new approach to the thermal equilibrium considers nonlinear heat transfer and a nonlinear flux-flow characteristic. This nonlinearized theory takes into account the previously mentioned fact that the initial heat transfer coefficient (i.e., at the beginning of the heat convection regime) is at least one order of magnitude smaller than the constant heat transfer coefficient that is used in the linearized theory. Furthermore, it is considered that the flux-flow resist-

ance of the superconductor can steadily increase from an initial value of zero to its constant value (which is much larger than the stabilizer resistance). This type of flux-flow performance indicates that the flux-flow resistance is not only a function of the temperature and the magnetic field but also of the electric field strength along the superconductor.

It is possible to perform the necessary calculations of the nonlinear theory of the thermal equilibrium in a relatively simple way. We developed a semigraphical method[6] for the case where the superconductor is divided into thin superconducting strands that are well bonded with the common stabilizer matrix. The method can also be applied to thick superconducting filaments if we assume an average value for the coefficient of the heat conductivity of the superconducting material. In order to take care of a variable heat conductivity, an appropriate computer code has been developed.

This relatively simple mathematical treatment is only possible if the assumption is made that the superconductor current density, which depends on three variables, namely, the temperature and the electric and magnetic field strengths, can be expressed in the form of a product of two functions, each of them being a function of two variables only. The first is a function of temperature and magnetic field strength, the second a function of the electric and magnetic field strengths.

Experimental checks made up to now have clearly shown that the nonlinearized theory, in contrast to the linearized theory, is able to explain in a semiquantitative way the sometimes very intricate pattern of the thermal equilibrium of compound and bare superconductors in the flux-flow state. For a further refinement of the experimental checks of the nonlinearized theory in its present form, it will be necessary to determine several basic physical relations in more detail. For instance, additional data on the heat transfer from the conductor surface to the liquid helium, on the heat conductivity, and on the flux-flow performance of superconducting materials are needed. Finally, it should be mentioned that the nonlinearized theory of the thermal equilibrium of superconductors in the flux-flow state could, and should, be relatively easily extended to nonlinearized theories of dynamic phenomena. An important first step would be a nonlinear theory of the minimum propagating current. To continue this research program would greatly contribute toward the final goal of establishing reliable stability criteria for new, pioneer-type superconducting magnet systems.

## 10.3 NIOBIUM-TITANIUM COMPOUND CONDUCTORS WITH TWISTED FILAMENTS

D. L. Coffey W. F. Gauster M. S. Lubell

### 10.3.1 Short-Sample Tests

We have tested some of the newest forms of niobium-titanium compound conductors with twisted filaments, and our results on short samples, cusp coils, and magnets will be presented here.

Table 10.1 is a compilation of the characteristics of the niobium-titanium material tested. Figure 10.1 summarizes the short-sample current density over the entire cross-sectional area taken with unrestricted helium flow,[7] in transverse magnetic fields, for niobium-titanium compound conductors with and without twisted filaments. For the rectangular-shaped conductors (samples 1, 2, 6, and 7), the magnetic field was perpendicular to the larger face. From the shape of the curves at high fields, it seems likely that the niobium-

[7]W. F. Gauster and J. B. Hendricks, *J. Appl. Phys.* **39**, 2572 (1968).

**Table 10.1. Characteristics of the Multifilament Niobium-Titanium Wire**

| Sample No. | Manufacturer's Designation | Size (mils) | No. of Filaments | Diameter of Filament (mils) | Ratio of Copper to Superconductor | $\frac{R_{300°K}}{R_{4.2°K}}$ | No. of Twists per Foot |
|---|---|---|---|---|---|---|---|
| 1 | Supercon 24T | 51 X 123 | 24 | 10 | 2.3 | 173 | 4 |
| 2 | Supercon 15 | 57 X 114 | 15 | 11 | 3.5 | 154 | None |
| 3 | Airco 187T | 30 diam | 187 | 1.4 | 1.6 | *a* | 36 |
| 4 | Airco 68T | 30.7 diam | 68 | 1.9 | 3 | *a* | 24 |
| 5 | Cryomag 51 | 20 diam | 51 | 1.6 | 2.0 | *a* | None |
| 6 | Cryomag 62T | 50 X 125 | 62 | 5.5 | 3.2 | 198 | 12 |
| 7 | Cryomag 62 | 50 X 125 | 62 | 5.5 | 3.2 | 198 | None |

[a]Not measured.

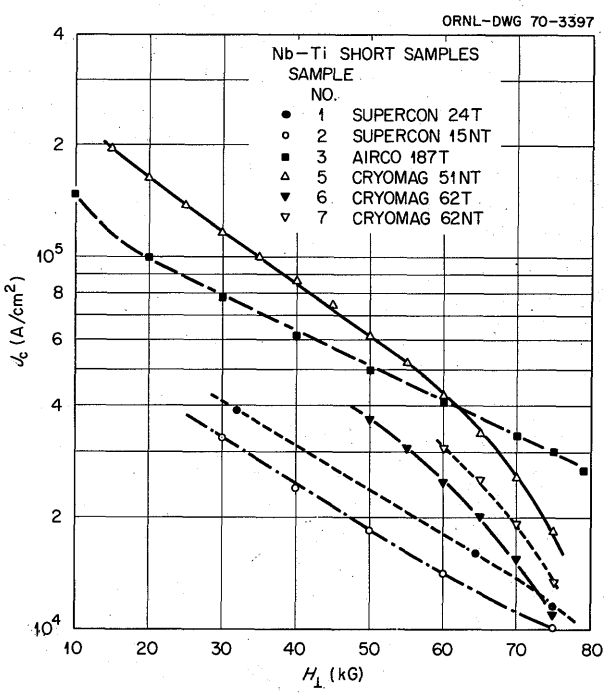


**Fig. 10.1. Natural Logarithm of Overall Current Density $J_c$ vs Preset Transverse Magnetic Field in Unrestricted Helium Flow for a Variety of Niobium-Titanium Short Samples.** The first number after the manufacturer's name gives the number of filaments, and the T or NT designates whether or not the filaments were twisted. See Table 10.1 for other details.

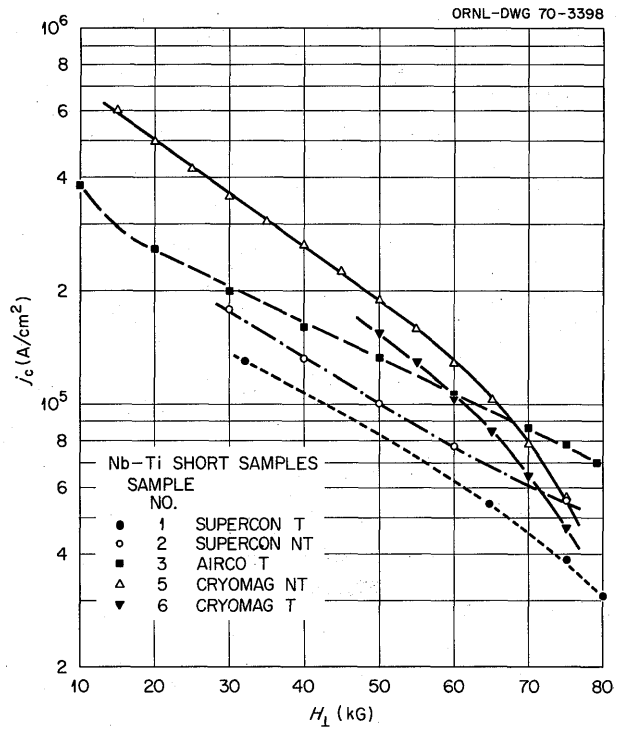


**Fig. 10.2. Natural Logarithm of Superconducting Critical Current Density $j_c$ vs Preset Transverse Magnetic Field for the Specimens of Fig. 10.1.** The two untwisted Cryomag conductors have the same critical current density, and hence only five curves are shown.

titanium alloy composition employed in samples 5, 6, and 7 is not the same as that used in samples 1, 2, and 3. The data shown in Fig. 10.2 (derived from the measurements of Fig. 10.1) are displayed as a graph of the critical current density (in the superconductor only) vs applied field. The interesting feature here is the fact that in all cases of similar-size filaments and the same manufacturer, the superconducting critical current density is lower for the twisted wires than for the straight-filament conductors. While from a practical point of view, the 20% decrease in intrinsic current density does not preclude the utilization of this material, it is possible that once the problem is realized by the manufacturers, other drawing processes could be devised to prevent this deterioration.

The major advantage of the twisted material is the elimination of most of the parasitic current loops[8] and the subsequent losses and degradation that accompany them. The greater stability with twisted filaments over the straight ones is demonstrated in Fig. 10.3. Samples with identical dimensions and number and diameter of filaments were prepared, but in one sample the filaments were twisted with a pitch of one turn per inch. For the sample with twisted filaments, the short-sample critical current is seen to be independent of the mode of excitation; for the sample with straight filaments, a significant difference is observed depending on whether the current or field is fixed first, with the other varied. In the twisted-filament sample, critical currents obtained by presetting the current and sweeping the field are almost the same as those achieved when current and field are simultaneously programmed (coil simulation test). It is clear that the degradation due to the quenching of induced currents caused by the changing magnetic field is eliminated in the twisted wire.

Of the niobium-titanium wires with twisted filaments, the one that was most extensively investigated was the Supercon 24T, which in overall size and filament diameter was similar to the straight-filament material

[8] D. L. Coffey and W. F. Gauster, to be published in *Proceedings of Symposium on Engineering Problems of Fusion Research,* Los Alamos Scientific Laboratory, Los Alamos, N.M., Apr. 8–11, 1969, LASL-4250.

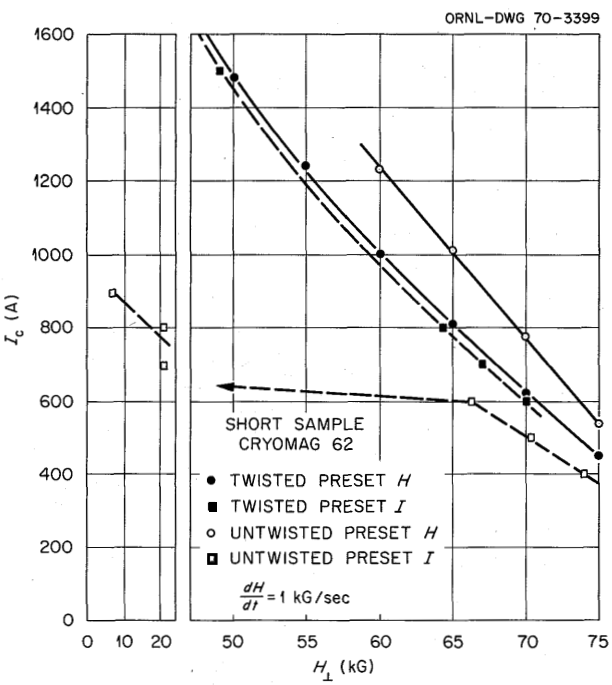


**Fig. 10.3. A Comparison of the Short-Sample Critical Current $I_c$ vs Transverse Field for Identical Niobium-Titanium Wires With and Without Twisted Filaments in Unrestricted Helium Flow.** Measurements were made with field preset and current varied and vice versa.

used in the IMP mirror coils (Supercon 15). Figure 10.4 is a graph of the short-sample, cusp-coil, and magnet performance of this wire, which is insulated with a thin oxide coating. The short-sample data presented here were obtained with the field preset and the current varied until a quench occurred. For each field value, two critical currents were obtained depending on the direction of the field relative to the surfaces of the strip. In all cases the field was transverse to the current (see inset of Fig. 10.4).

### 10.3.2 Cusp-Coil Tests

A cusp-coil test[9] was made with Supercon 24T. The cusp coil has an inside diameter of 3.5 in. and an outside diameter of 5.25 in. Each coil section has an axial length of 3 in. The cusp coil has a $^3/_8$-in. gap and was wound with 1000 ft of wire (approx 21 lb). When energized in an applied uniform transverse field, the cusp coil gave essentially short-sample performance for the self-field maximum value at the winding. Fast rates of increase of current or self-field also cause premature quench, and for this material, with only four twists per foot for the filaments, the maximum safe rate of energizing in the cusp-coil mode was about $dI/dt = 5$ A/sec, corresponding approximately to $dH/dt = 134$ G/sec. The maximum $J_c$ achieved in these tests was 28,600 A/cm$^2$. In addition to these tests a few cusp-coil measurements were made with the current preset and the external field varied at various rates from 0 to 60 kG or to the quench point. On the basis of these limited tests, sensitivity to rate of change of field was again verified, and it was concluded that the cusp coil was stable against a slowly changing magnetic field.

### 10.3.3 Magnets

Since the twisted-filament material appeared satisfactory in the cusp-coil mode, a relatively large 4-in.-bore magnet was constructed of sample 1, and preliminary test results are in quantitative agreement with design criteria. In Fig. 10.4 the maximum total field at the winding is indicated for the maximum attainable quench current. It is seen to agree with the short-sample data for the field parallel to the broad face of the strip. Further pertinent data on this magnet are given in Table 10.2. The mechanical details are shown in Fig. 10.5. Starting at the left and moving clockwise, we see one of the three support holders and vertical height adjusters for the magnet (*a*). Owing to the long length of the magnet support system, these height adjusters were necessary to keep the magnet properly centered in the Dewar. The support holders attach to hollow stainless steel tubes, and the first one attached to the coil form (*b*) allows fast cooldown by first precooling with nitrogen gas and then admitting helium gas, which passes through a gap in the windings and finally exits at the bottom of the coil form. The second tube (*d*) is used for rapidly collecting liquid helium once the system is cooled down to 4.2°K. A level detector (*c*) is attached to the second tube, and thus the height of the liquid helium above the magnet contacts (*e*) can be continuously monitored. A copper rod with an $Nb_3Sn$ ribbon (*f*) soldered to one side conducts current from a vapor-cooled lead optimized for 500 A to a copper contact on the coil form. The bottom ends of the vapor-cooled leads are high enough for 2 ft of helium

[9] *Thermonuclear Div. Semiann. Progr. Rept. Oct. 31, 1967,* ORNL-4238, p. 134.

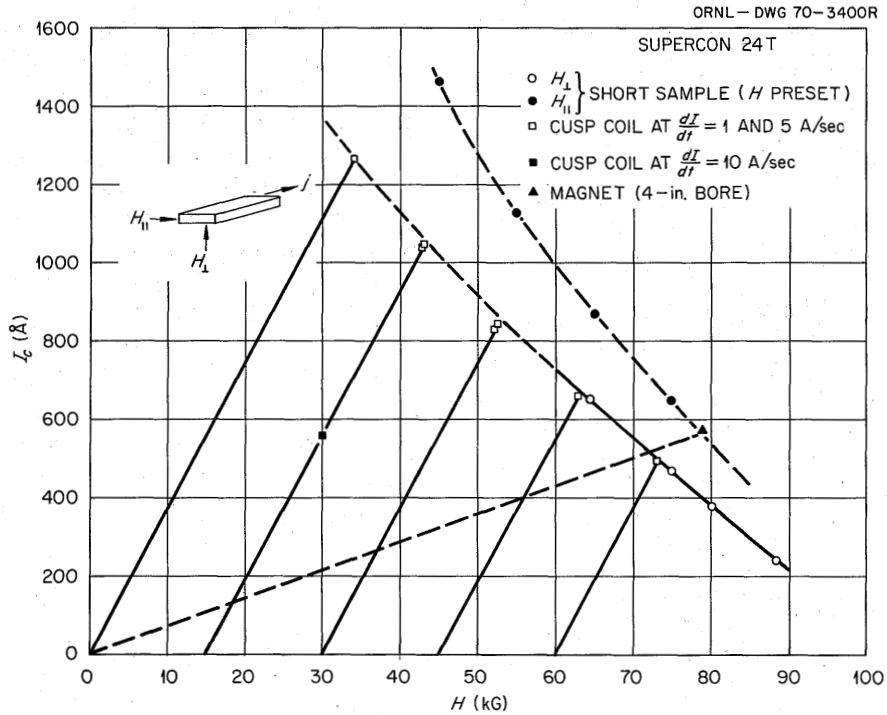


**Fig. 10.4. Critical Current vs Total Magnetic Field for a Short Sample in Two Different Orientations, for a Cusp Coil, and for a Magnet.** The load lines for the cusp-coil data start from the initial applied field. The external field is perpendicular to the axis of the cusp coil. The field for the magnet is the maximum value at the material.

(25 liters) above the magnet, which is enough for one day's operation on one transfer of helium. Between the two current contact blocks, a platinum resistance thermometer (*g*) is attached to the coil form. This is extremely useful during the cooldown procedure and will probably be a standard fixture on all our future large magnet installations. Cooldown starting from room temperature takes about 2.5 h and requires about 30 liters of helium. The mass of the magnet is about 115 lb. If the Dewar is kept filled with liquid nitrogen, the magnet does not even warm up to 77°K overnight, and subsequent cooldowns and collection of helium are much quicker.

**Table 10.2. Design Characteristics and Performance Data on Magnets Wound with Twisted Multifilament Niobium-Titanium Wire**

| Magnet size | 4-in. bore | 3-in. bore[a] | 2-in. bore |
|---|---|---|---|
| Wire type | Supercon 24T | Airco 68T | Airco 187T |
| $a_1$, cm | 5.105 | 3.937 | 2.54 |
| $a_2$, cm | 10.775 | 7.564 | 3.778 |
| $b$, cm | 12.15 | 7.874 | 5.2197 |
| $N$, turns | 30.95 | 6229 | ~2080[b] |
| $L$, mH | 579 | ~1700 | ~89 |
| $H/I$, G/A | 133.9 | 352 | ~214 |
| $I_c$, A | 578 | 144 | 189 |
| $H_{max}$, kG | 77.4 | 50.7 | ~40.5 |
| $J_c$, A/cm$^2$ | $1.3 \times 10^4$ | $1.96 \times 10^4$ | $\sim 3.0 \times 10^4$ |
| $\lambda$ | 0.91 | 0.62 | ~0.74 |
| $E_{stored}$, kJ | 96.8 | ~17.6 | ~1.6 |

[a]High-homogeneity design with a gap characterized by $a_1$ = 3.937 cm, $a_2$ = 5.1816 cm, and $b$ = 4.572 cm.
[b]The exact number of turns is not known.

Because the magnet is wound with twisted-filament material with a copper-to-superconductor ratio of 2.3 to 1 and because the conductor is insulated with an oxide coating, no cooling channels (other than that mentioned above, which is used for cooldown) are provided between layers or turns. The relatively close winding resulted in a high packing factor, $\lambda = 0.91$, and a reasonable overall current density at the maximum critical current attained, $J_c = 1.3 \times 10^4$ A/cm$^2$ at 79 kG. As is seen in Fig. 10.4, this magnet performs up to, and is limited by, the short-sample critical current. It is, however, very rate sensitive, and high values of field (over 50 kG) can be obtained only by keeping the rate of increase of field below about 75 G/sec. Presumably this sensitivity to $dH/dt$ is caused by the relatively slight filament twist ($^1/_3$ turn/in.). Many field plots have been

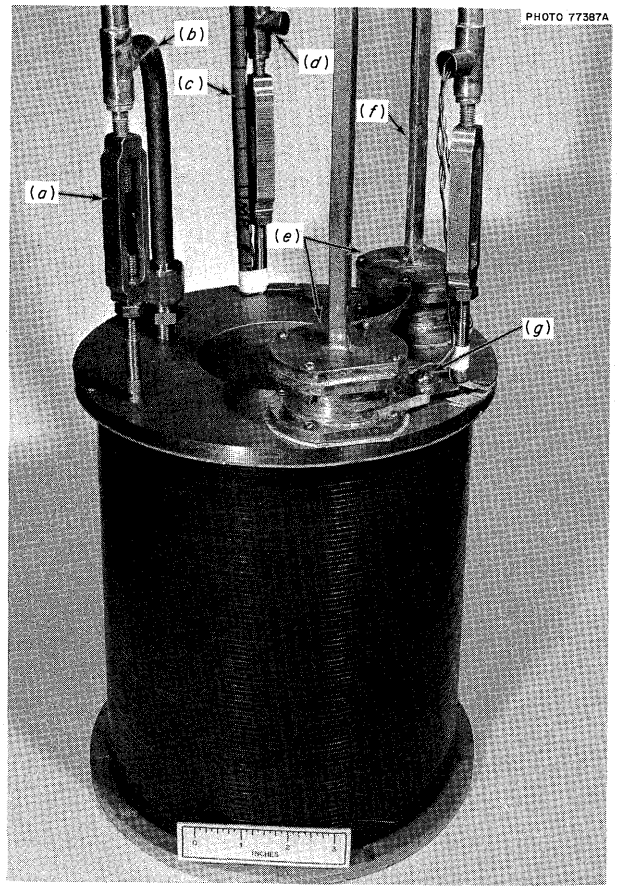


**Fig. 10.5. Picture of 4-in.-bore Superconducting Magnet Wound with Supercon 24T.** (*a*) Support holder and vertical height adjuster, (*b*) precooling tube for channel in magnet windings, (*c*) helium level detector, (*d*) transfer tube outlet, (*e*) magnet current contacts, (*f*) $Nb_3Sn$ ribbon soldered to side of copper rods connected between the magnet contacts and vapor cooled leads, (*g*) platinum resistance thermometer soldered to top of form.

made of this magnet with a calibrated Hall probe. The field variation along the axial direction has been measured for the total half length of the magnet, both in the center of the bore and in two radial positions out from the axis. In addition, the remanent field has been measured after successively energizing the magnet to higher fields. It was anticipated that the twisted-filament material would trap less flux and hence have a smaller remanent field than would be expected with straight-filament magnets of similar size and field strength. Preliminary analysis of the data bears out this contention and also yields reasonable agreement between the measured field profile along the coil axis and the calculated values.

In addition to this large magnet (stored energy of 97 kJ), we have also built a 3-in.-bore 50-kG magnet with an inserted 2-in.-bore 37-kG magnet (total stored energy of 15 kJ). Although the combination has not been tested as yet, each magnet has been separately tested once. The 3-in.-bore magnet was close to, but did not attain, the short-sample performance. Considering the stored energy at the maximum field, 17.6 kJ, the overall critical current density of $1.96 \times 10^4$ A/cm$^2$ is adequate. The wire used in the 3-in.-bore magnet has a fairly large copper-to-superconductor ratio and a low packing factor; on the other hand, the 2-in.-bore insert magnet, with a relatively small copper-to-superconductor ratio, was appreciably below (~20%) short-sample performance, and furthermore this magnet showed "training," with successive quenches of 177, 190, and 200 A. The quench current of 189 A used in Table 10.2 was the mean value of these data. Attempts will be made to vacuum impregnate this magnet both to see if the "training" can be removed and to see if higher critical currents can be attained.

The technique of impregnating magnets with paraffin or epoxy has been found to be necessary and effective by the magnet group at Rutherford,[10] particularly for the new generation of twisted niobium-titanium wires, where the copper-to-superconductor ratio has been lowered. Since the twisted wire with thin filaments is more stable to changing magnetic fields (maybe even intrinsically stable against flux jumping), it was found that less copper was needed to stabilize the material. This, however, made the wire more susceptible to small motion (due to the decreased enthalpy). Hence the Rutherford group employed the technique of potting the coils and achieved excellent results (3 to $6 \times 10^4$ A/cm$^2$) for magnets with stored energies below 20 kJ.

### 10.3.4 Conclusion

There is no doubt that the use of twisted superconducting filaments in compound conductors is a major breakthrough.[10] Nevertheless, there are some points which should be discussed here. First, the superconducting current density for a particular size filament proved to be less than for its straight counterpart. This might have purely technological causes, and future improvements might be possible. Since the twisted conductor can be made stable with less copper, the overall current density for the compound conductor with twisted material is appreciably larger than the

[10] Rutherford High Energy Laboratory report RPP/A73 (November 1969).

overall current density of the straight-filament conductor.

A new inconvenience is that, because of the reduced copper ratio, the magnets may have to be potted to ensure complete mechanical and electrical stability. In this connection it should be mentioned that at the present state of technology, the wires with twisted filaments are often slightly deformed, and therefore tight winding is more difficult, which makes potting even more desirable.

Since the twisted-filament conductors generally have less copper, it becomes increasingly important to consider thermal protection of the magnet for larger systems. Finally, the hoop strength of compound conductors with twisted filaments might be less than that of straight-filament conductors, and additional reinforcement against electromagnetic volume forces might be necessary.

## 10.4 A NEW DESIGN PRINCIPLE FOR THREE-DIMENSIONAL MAGNET WINDINGS

R. L. Brown

Plasma physics experiments continue to require very sophisticated magnet field configurations. Sometimes odd-shaped magnet coils are necessary to generate these fields.

Winding problems are often encountered with coils when it is required to bend conductors about axes that are not parallel. Some of the coils that exhibit this property are Saddle, Baseball, and Yin Yang.[11] One way to solve this problem is to curve the surface on which the coil is to be wound in such a way that the conductors are always pulled in normal to the surface. This prevents the conductors from sliding sideways on their winding surfaces. If this condition is met, then layers or pancakes can be wound so that the tendency of the conductors to slip out of position or to bundle is avoided. Figure 10.6 shows winding surfaces that can be used in a Yin Yang coil system. Two O-rings stretched around the surfaces demonstrate that there is no force exerted sideways. A gimbals-type winding machine model is shown in Fig. 10.7. With this type of winding machine, the instantaneous position of the coil allows the feed-in point to remain near the top of the coil.

A Yin Yang-type magnet coil case is shown in Fig. 10.8. The cross section of a coil wound in this case is designed to afford greater accessibility while winding.

[11] R. W. Moir and R. F. Post, "Yin-Yang Minimum-|B| Magnetic Field Coils," *Nucl. Fusion* 9, 253–58 (1969).

Sheet metal or shaped plates may be used for some small coil cases. However, larger coil cases that are subjected to high magnetic forces would probably be more practical if machined from solid pieces of metal. Automatic milling machines having several axes of movement may be necessary for this.

The Saddle coil winding is shown in Fig. 10.9, which also depicts the shape of the coil ends. The formulas for tracing a filament around the coil are as follows (the symbols are defined in the figure):

$$x = \pm[(r_0 - \Delta w)\sin\beta - \Delta d\cos\beta]\left[1 - \left(\frac{\theta}{\theta_0}\right)^2\right]^{1/2} ,$$

$$y = \left[\frac{(r_0 - \Delta w)(\cos\theta_0 - \cos\beta)}{1 - \cos\theta_0} - \Delta d\left(\frac{1}{\sin\theta_0} + \sin\beta\right)\right](1 - \cos\theta) + (r_0 - \Delta w)\cos\beta + \Delta d\sin\beta ,$$

$$z = \Delta w\left(\frac{1 - \cos\beta}{1 - \cos\theta_0}\right)\sin\theta_0 + \left[\frac{(r_0 - \Delta w)(\cos\theta_0 - \cos\beta)}{1 - \cos\theta_0} - \Delta d\left(\frac{1}{\sin\theta_0} + \sin\beta\right)\right]\sin\theta .$$

## 10.5 TEMPERATURE-COMPENSATED TRIMMING WINDINGS FOR WATER-COOLED MAGNET COILS

J. N. Luton, Jr.

It is sometimes necessary, as in the cases of DCX-2[12] and the C coil,[13] to provide means for accurately adjusting the field shape of an existing magnet system. An ideal trimming device must produce a field which exactly follows the main field over the whole range of the coil current and which drifts with the main field as external conditions vary.

Common methods are to use separate compensation windings and to change the current distribution in the coil by means of auxiliary power supplies or external shunts. Both methods have significant disadvantages when used with coils producing high magnetic fields. If

[12] *Thermonuclear Div. Semiann. Progr. Rept. Jan. 31, 1961*, ORNL-3104, p. 19.

[13] *Thermonuclear Div. Semiann. Progr. Rept. Oct. 31, 1965*, ORNL-3908, pp. 116–18.

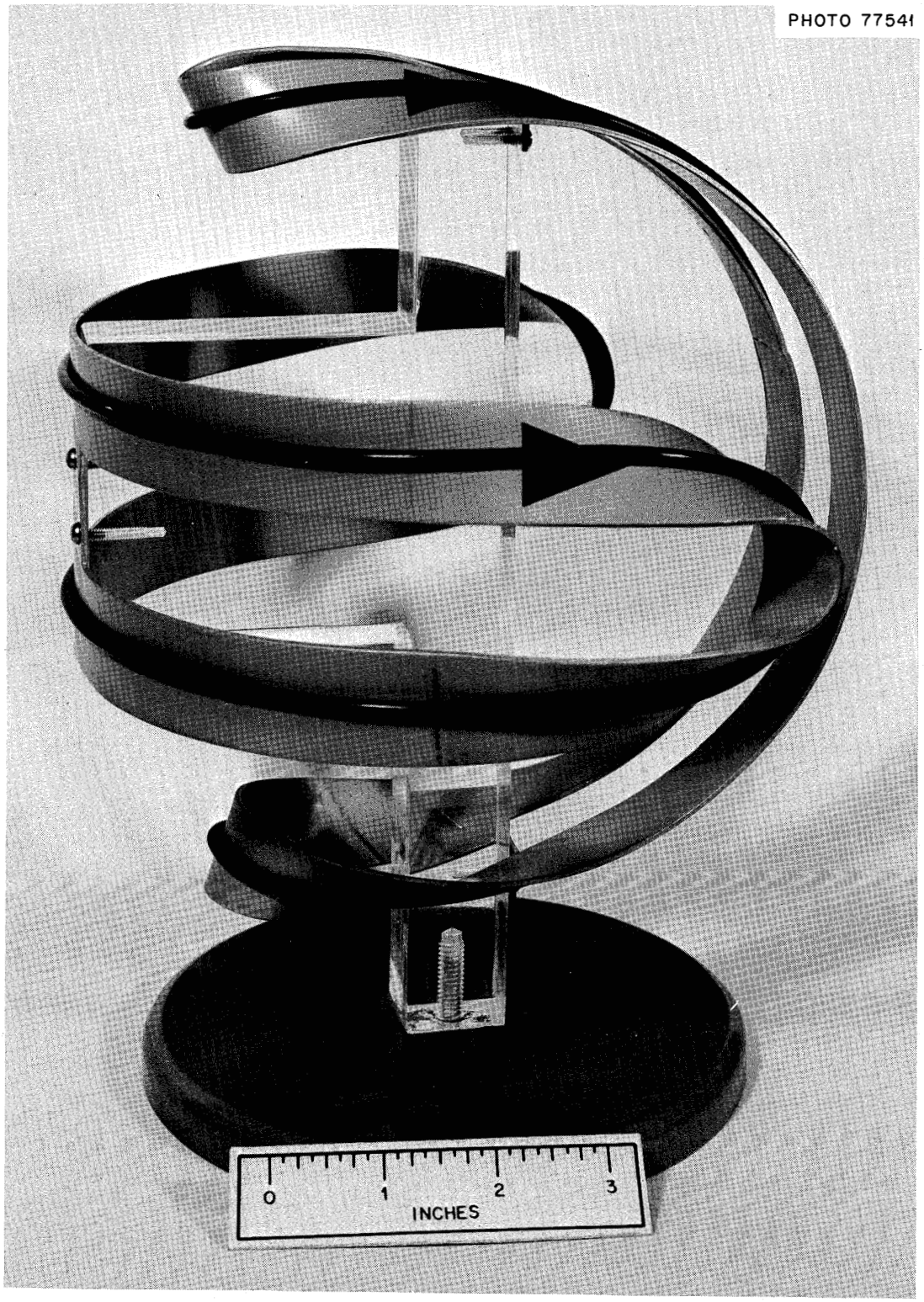


**Fig. 10.6. Winding Surfaces for a Yin Yang Coil.** The stretched O-ring demonstrates that the hoop stresses keep the filament stationary.

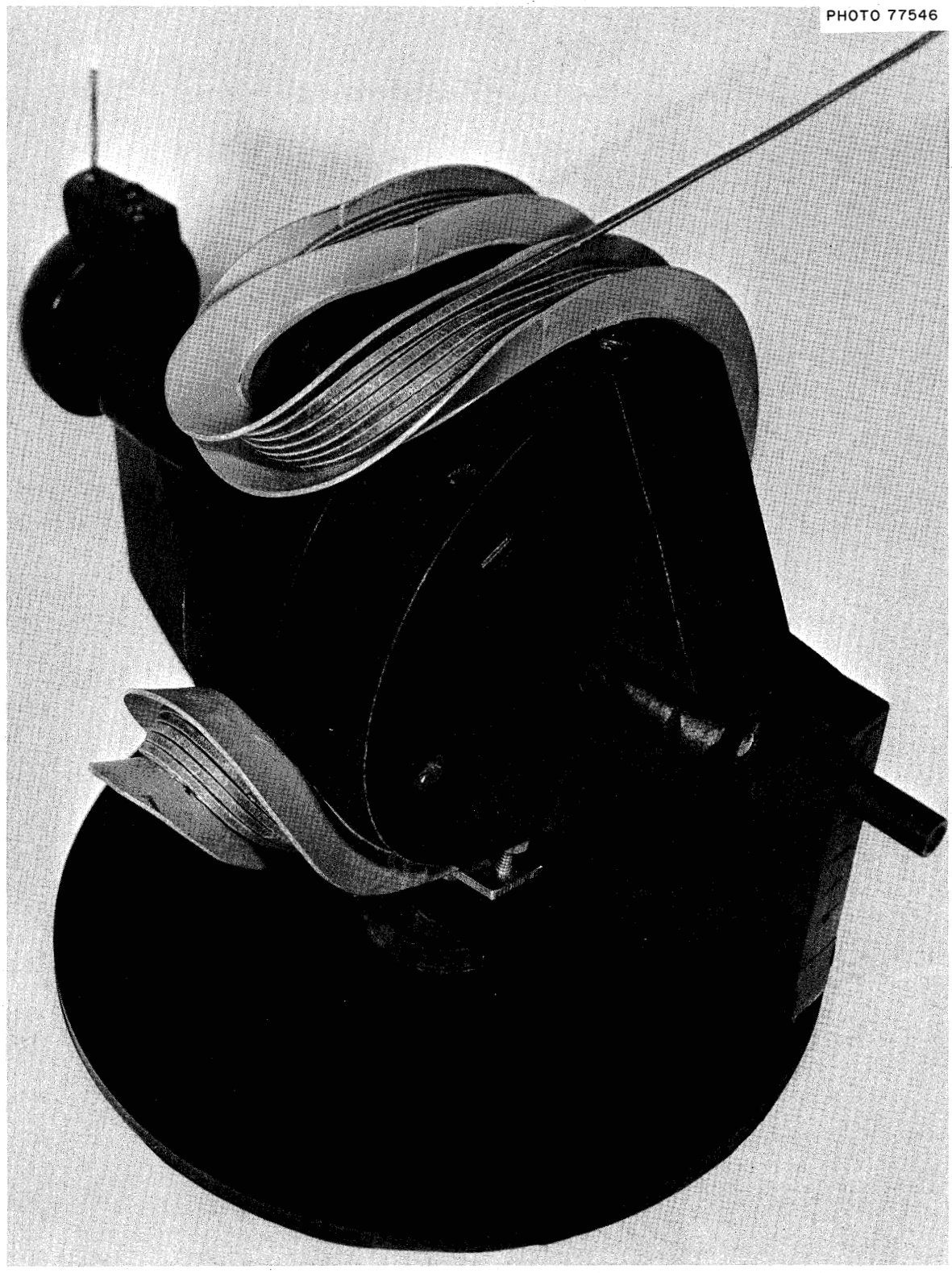


**Fig. 10.7. Model of a Gimbals-Type Machine for Winding Odd-Shaped Magnet Coils.** A single Yin Yang coil is shown partially wound.

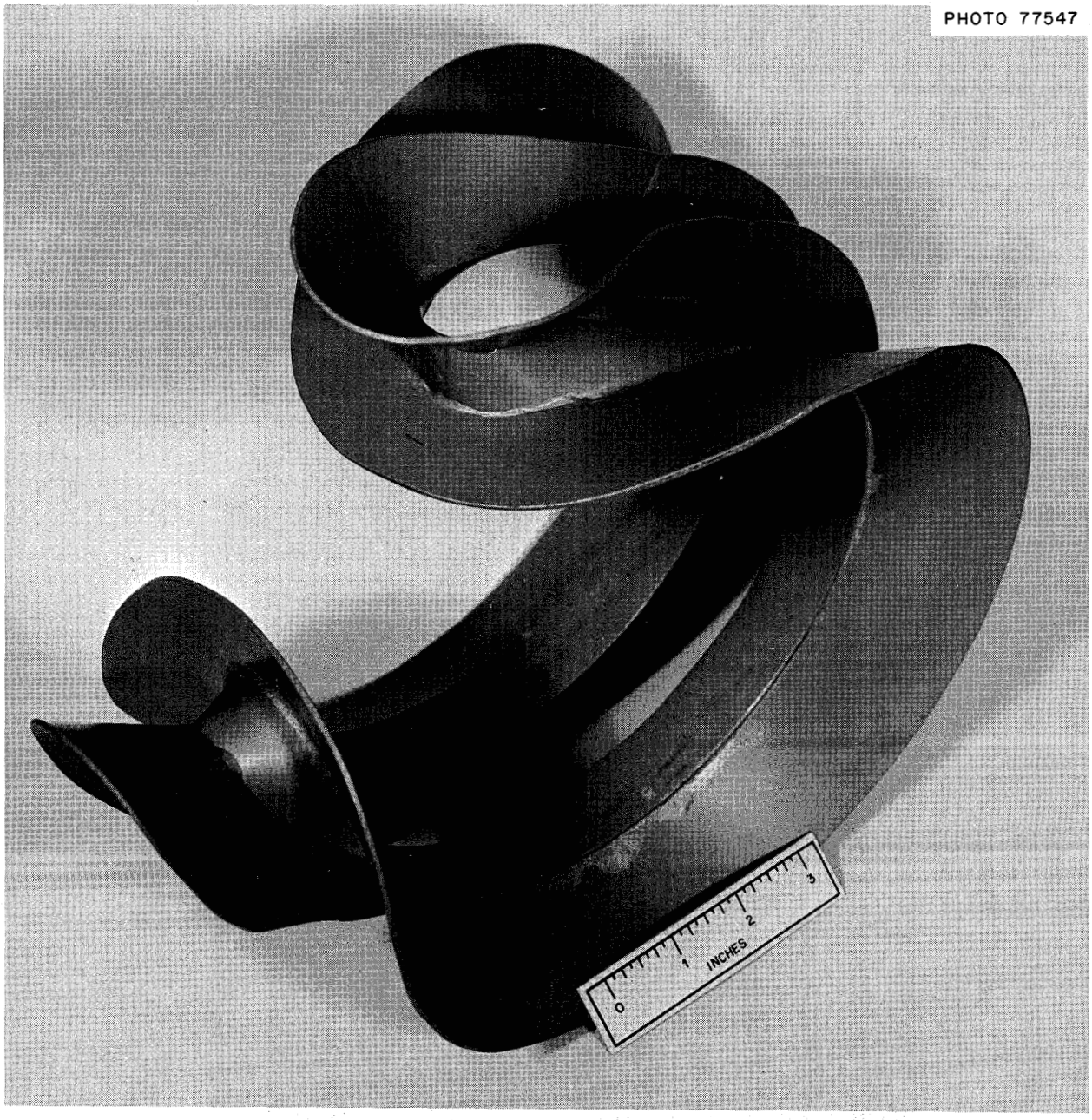


**Fig. 10.8. Coil Case for a Yin Yang-Type Magnet Winding.** The obtuse side wall angles are for the purpose of alleviating difficulties associated with the winding operation.

ORNL-DWG 70-2114A

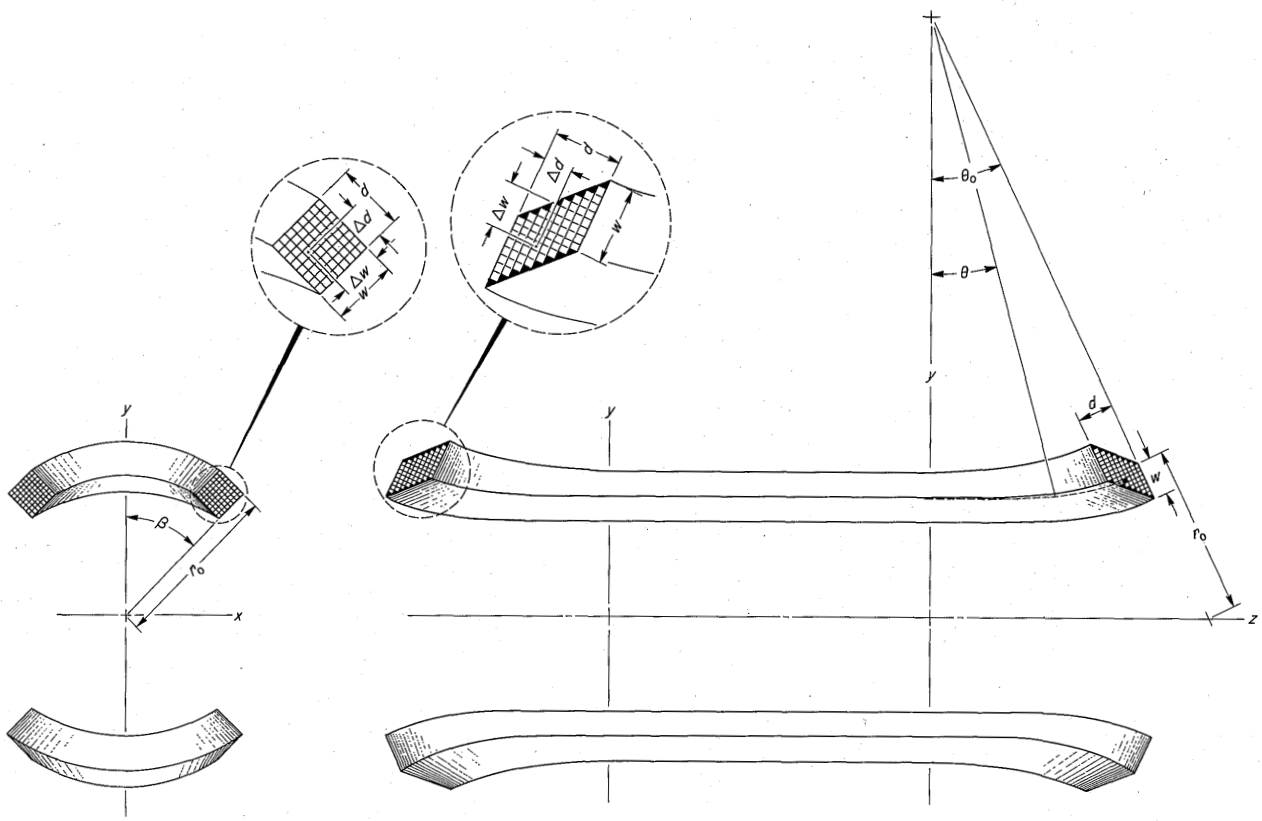


**Fig. 10.9. Schematic of a Saddle Coil Winding.** The quantities $r_0$, $w$, $d$, $\beta$, and $\theta_0$ determine the shape of the winding. The parameters $\Delta w$ and $\Delta d$ characterize one filament of the winding. A point located on this filament is determined by a specified value of the variable $\theta$. The Cartesian coordinates of this point are given in the text.

separate trimming windings are employed, then either they must be placed inside the bore, where they encroach on the useful field volume, or else the bulk of the main coil windings and their terminations forces the location of the compensation windings to be far from the coil center. This reduces their effectiveness for producing local changes in the field shape. When employing the method of changing the current distribution in the coil with power supplies, a separate supply is required for each section whose current is to be altered. Each of these regulated power supplies must provide considerable power and must track and drift with the main generator. If external shunts are used instead of power supplies, then at any setting of the adjustable resistors the ratio of their resistance to that of the coil must remain constant as the coil current is varied. Furthermore, the shunt resistance must vary with time in the same way that the coil resistance does, both over short and long terms. Finally, an external shunt can only decrease the current in the affected turns, not increase it.

We have devised a new system of trimming windings which avoids the above-mentioned difficulties. They are to be placed inside the windings of the main coil in such a way that they assume the winding temperature. For example, if the coil is composed of pancakes[14] wound from hollow tubular conductors, then the trimming winding can be an insulated wire pulled through the hollow conductor whose relative field strength is to be altered. Assume that the wire is connected electrically in parallel with the hollow conductor in which it resides. Then if the polarities are such that the field of the wire aids that of the tube, the total field is unchanged, since the axes of the tube and the wire are

[14] *Thermonuclear Div. Semiann. Progr. Rept. Oct. 31, 1963,* ORNL-3564, pp. 121–25.

(ideally) coincident everywhere. However, if the polarities are reversed, the field at all points in space is reduced exactly as if a current equal to twice the wire current were subtracted from the original tube current. Thus the current and power capacities required of the internal trimming winding are only half those necessary for either an external shunt or an auxiliary power supply which produces the same field change. If it is desired to reduce the current density in some sections of the coil and increase it in others, internal windings fed from the former sections may be inserted with aiding polarity in the latter sections.

As an example, Fig. 10.10 shows this kind of trimming arrangement applied to the C coil[13] of our Magnet Laboratory. The trimming voltage is picked up across three of the eight water paths of pancake No. 4. There are internal trimming wires inside all seven water paths of pancake No. 1 and inside half of the six water paths of pancake No. 3′. The trimming wire is composed of 12- and 14-gage wires in series. By changing the ratio of the lengths of the 12- and 14-gage parts of the wire, the shunt resistance and consequently the values of the trimming current can be smoothly adjusted.

A tube and its trimming wire are both cooled by the water flowing inside the tube. Therefore at any cross section the temperature of the wire and tube tend to remain equal, especially if the wire insulation is thin, even though these temperatures may change as a result of fluctuations in water inlet temperature or flow. In this case, the ratio of the current in the coil to that in the trimming turns and, therefore, the resulting field shape are inherently immune to external changes.

Without going into detail, it can be reported that a testing program was carried out which led to the practical application of this trimming system to the field improvement of the C coil. Figure 10.11 is a photograph of the arrangement. The 15-A, 600-V fuse links were inserted to provide overcurrent protection while joining the wires. Figure 10.12 shows the results of axial field measurements in the C coil before and after the trimming of portions of three pancakes (wiring diagram shown in Fig. 10.10). Further improvement using the same method would still be possible.

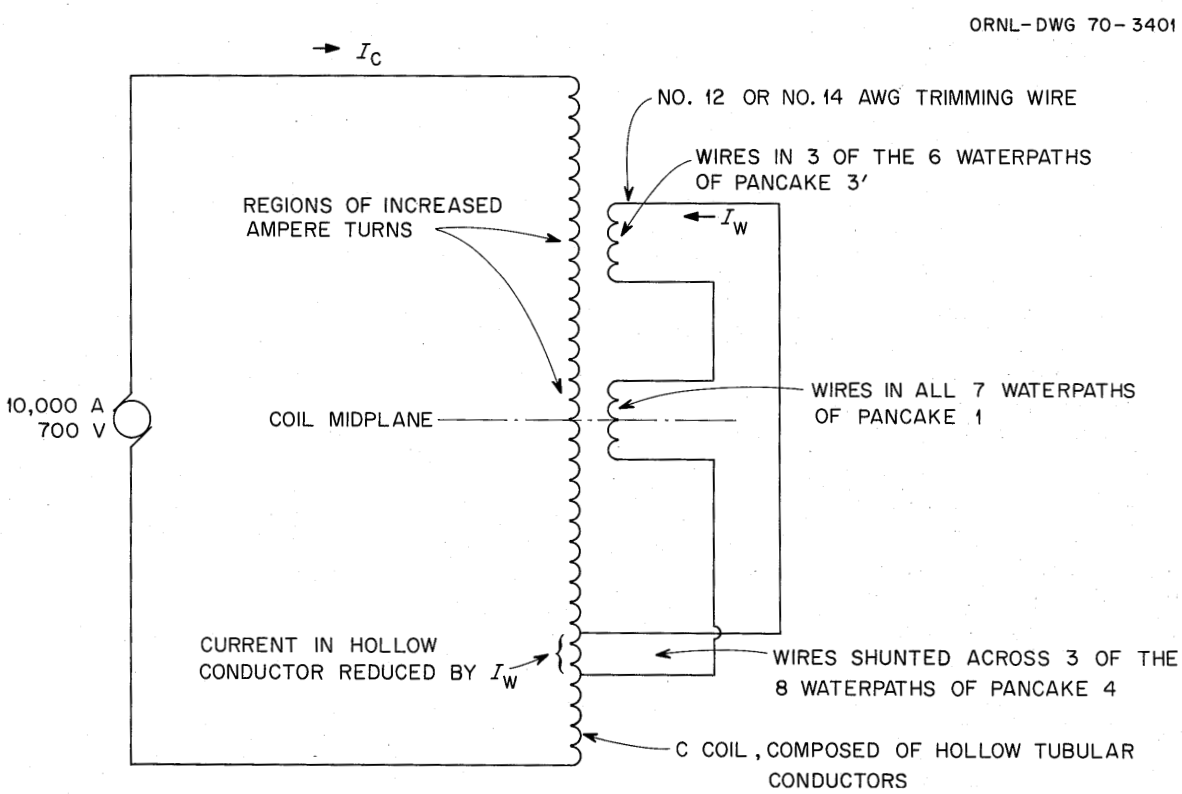


**Fig. 10.10. Electrical Schematic of C Coil Internal Trimming Windings.**

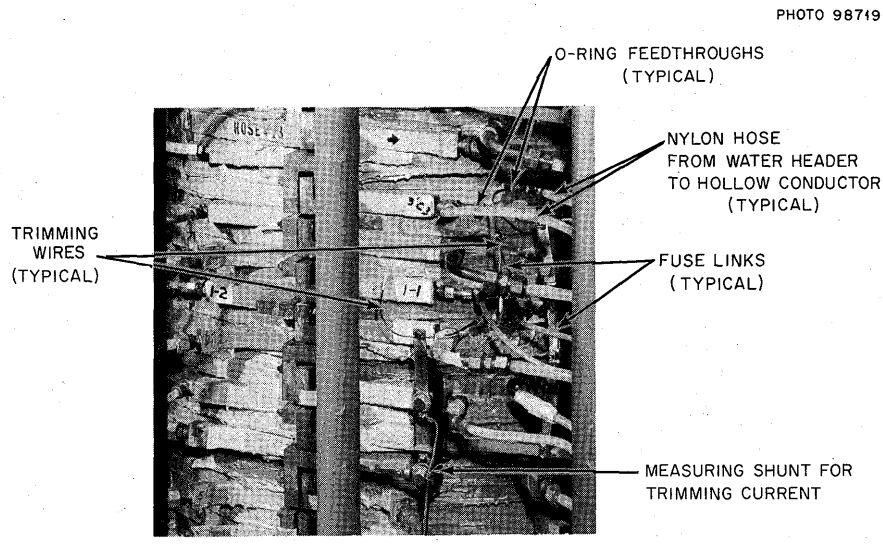


**Fig 10.11. Side View of C Coil After Installation of Internal Trimming Windings.**

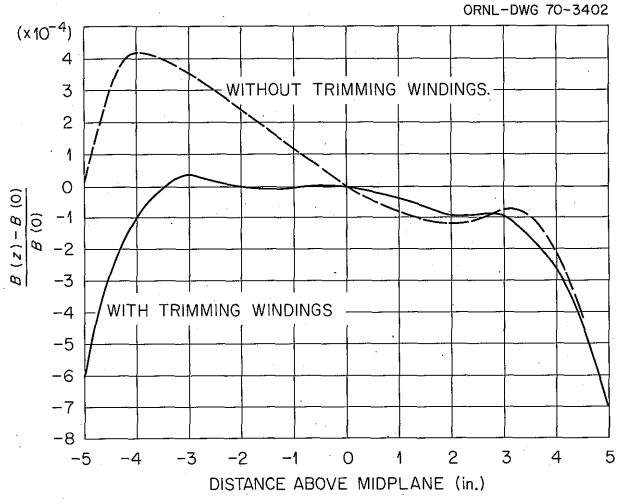


**Fig. 10.12. Measured Axial Field of C Coil With and Without the Use of Internal Trimming Windings (First Trimming Results).**

## 10.6 PROGRESS ON ENGINEERING OF THE IMP FACILITY (PHASE II)

R. L. Brown, D. L. Coffey, J. S. Culver, J. L. Dunlap, K. R. Efferson, W. F. Gauster, J. L. Horton, J. N. Luton, C. E. Parker, E. R. Wells, W. W. Wright

### 10.6.1 Introduction

We describe here work toward the superconducting mirror-quadrupole trap for IMP. The mirror coils are now operational (Sect. 2.3), so effort is presently concentrated on the quadrupole coils. The next section details work on the $Nb_3Sn$ superconductor. After that we summarize the stress analysis of the coil cans and review the status of the principal mechanical components.

### 10.6.2 $Nb_3Sn$ Conductors for the Quadrupoles

As mentioned in our previous report,[15] a diffusion-formed $Nb_3Sn$ conductor was purchased for winding the quadrupole coils of IMP. The conductor is a laminated ½-in.-wide ribbon consisting of 0.002 in. of superconductor (with substrate) with 0.002 in. of OFHC copper and 0.001 in. of stainless steel on each side. Short-sample critical currents of 600 A +15% −10% at the rated transverse field of 80 kG were specified, because samples with excessively high critical currents showed instabilities. Furthermore, for acceptance the conductor had to operate with at least 700 A in a double-pancake coil test. Since cusp-coil tests[16] require cutting of the conductor, these tests were not specified for acceptance.

Before the $Nb_3Sn$ conductor was ordered, the supplier provided a similar sample which remained stable in a cusp-coil test at an external (applied) field of 60 kG, that is, to 97 kG total field. The results of such a cusp-coil test are shown in Fig. 10.13. These preliminary tests were made before our coil-winding tech-

[15] *Thermonuclear Div. Ann. Progr. Rept. Dec. 31, 1968,* ORNL-4401, Sect. 11.5.3.

[16] *Thermonuclear Div. Semiann. Progr. Rept. Oct. 31, 1967,* ORNL-4238, Sect. 8.5.

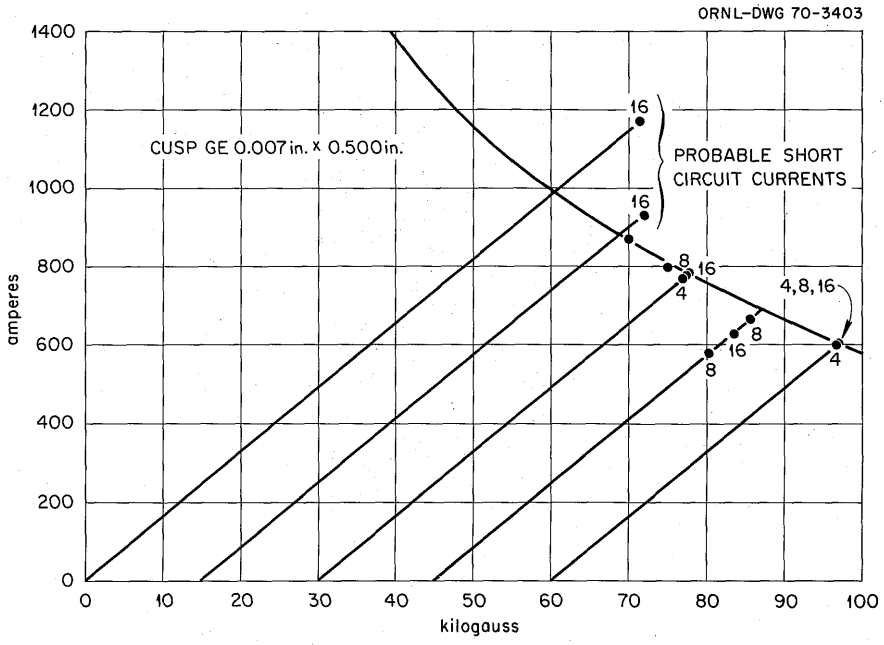


**Fig. 10.13. Results of Cusp-Coil Tests with a Preproduction $Nb_3Sn$ Sample.** $H$ - $\Delta I$ mode. The numbers indicate the rates of current rise in amperes per second. Since no special turn-to-turn insulation was provided, the total current values shown include short-circuit currents shunting the transport current.

nique[17] was developed, and excessive heating was caused by the pancake-to-pancake connections. Though the heating did not seem to affect the coil performance, the helium vaporization was so fast that high sweep rates in energizing the cusp coil were required. With these rapid sweep rates, the measured maximum current values were in excess of the actual critical currents. No special turn-to-turn insulation was provided (relying only on the relatively high resistance of the stainless steel layer of the conductor), and, obviously, radial current components shunted the circulating currents. Despite the experimental problems encountered during these preliminary cusp-coil tests, the conductor seemed to be stable over a wide range of fields and currents.

The difficulty with radial shunting currents due to insufficient turn-to-turn insulation also occurred during the acceptance tests with simple double pancakes. In this geometrical form the material cannot be subjected to any external magnetic field, in contrast to the cusp-coil tests. Early pancake coil tests showed marginally acceptable critical currents of 600 to 800 A. However, the helium losses in charging and discharging the coils indicated a severe problem for the full IMP coils, namely, that charging to the rated current in 1½ h would vaporize more than 1000 liters of liquid helium. Pancake tests with semi-insulated coils (colloidal graphite between turns) showed no measurable reduction of the critical current but more than an order of magnitude less liquid-helium loss in charging or discharging.

These acceptance tests were performed with simple double pancakes using approximately 1000 ft of the conductor. Since scaling laws for superconducting coil systems are not known yet, it seemed to be advisable to make additional tests with larger conductor lengths. A test arrangement was built (see Fig. 10.14) consisting of four double pancakes with an inside diameter of 3¼ in. and conductor length of 8000 ft. In tests with various energizing modes of the four coils, the critical current did not correlate with short-sample test data. However, these tests revealed that transitions occurred whenever the maximum field perpendicular to the ribbon face ($B_\perp$) was 25 to 30 kG. This limitation is not tolerable in IMP, where $B_\perp$ values up to 60 kG will be experienced (Fig. 10.15).

To better understand the influence of $B_\perp$, 1000 ft of conductor was wound into a cusp coil, using an improved winding technique to avoid internal splicing[17] and employing the colloidal graphite insulation

[17] *Thermonuclear Div. Ann. Progr. Rept. Dec. 31, 1968,* ORNL-4401, Sect. 11.3.

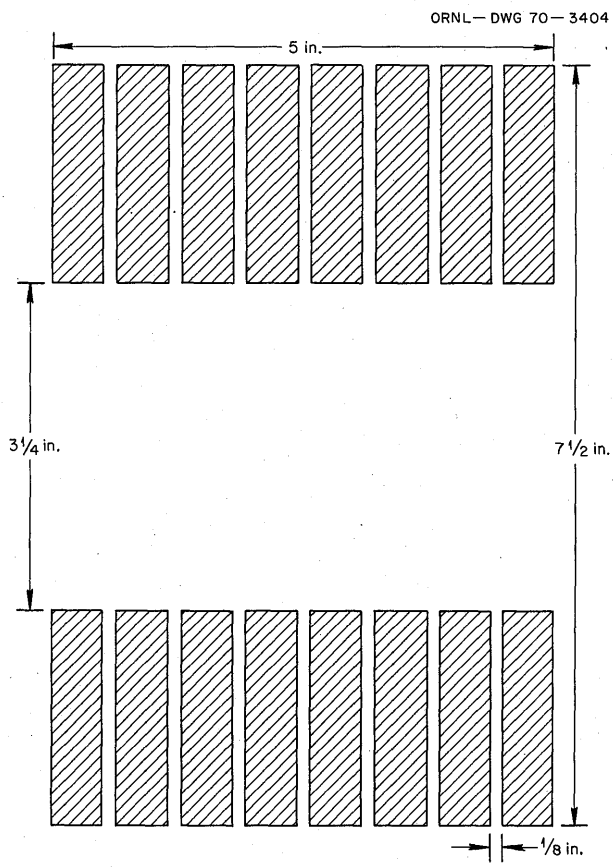


**Fig. 10.14. Winding Dimensions of the Test Arrangement with Four $Nb_3Sn$ Double Pancakes.**

technique. Energizing in the $H$-$\Delta I$ sequence (preset field, programmed current), as was done in the first cusp-coil test, revealed that the new material was in fact not as stable as the preproduction sample (compare Fig. 10.16 with Fig. 10.13). Additionally, it was found that when energizing the coil in the $I$-$\Delta H$ sequence an instability at $B_\perp = 25 \pm 10$ kG was clearly observable, almost independent of the transport current (Fig. 10.17). Other measurements (not shown) indicated that erratic and unpredictable critical currents occurred when a background field of maximum 30 kG was first established, then the cusp-coil current was established, and finally the background field was swept ($H$-$I$-$\Delta H$ sequence). This suggests that a background field such as could be obtained by first energizing the mirror coils probably would not eliminate the instability in the IMP quadrupoles.

At 450 A the cusp coil generates self-fields of 20 kG, which add to or subtract from the background field, depending on location in the coil. Therefore it is possible to select two simultaneous energizing sequences ($\Delta H$-$\Delta I$) which reproduce the load lines of all volume elements in IMP from 0 to 80 kG: one sequence with up to 20 kG external (40 kG total) field (at 450 A) produces in the winding volume all fields in the range 20 ± 20 kG; another with up to 60 kG external (80 kG total) field (at 450 A) generates all fields in the range 60 ± 20 kG. These two sequences and the critical currents achieved are also shown in Fig. 10.17. Again, the evidence points to a $B_\perp$ limit of 25 ± 10 kG.

Figures 10.16 and 10.17 show the great difference in the performance of $Nb_3Sn$ ribbon in cusp coils (due to flux jumps) as compared with the short-sample performance. In some cases such flux jumps can be made harmless by winding high-purity nonsuperconducting metal strips between the superconducting turns. The action of this normal material is very complex; the physics involves eddy current damping, heat conductivity, enthalpy increase, etc., and their mutual interactions are not fully understood. In pursuing this approach we first wound a 0.001-in. OFHC copper ribbon between the superconductor turns of the cusp coil. The resulting reduction of the space factor would be acceptable if it eliminated the instability. However, the influence of the additional ribbon was almost insignificant, in that it raised the critical $B_\perp$ by only 15% at most.

We then tried a technique used by Smulkowski,[18] in which copper shunts were wound into the magnet, each shunt bridging 10 to 20 turns of conductor. The object is to allow the instability and the resulting flux penetration to occur locally without propagating throughout the coil. This is effected if the shunt carries the transport current during the recovery time of the section. The technique limits the magnet charge rate and causes additional liquid-helium loss in charging, but it works (compare Fig. 10.18 with Fig. 10.16). A shortcoming of this method is that considerable difficulty was experienced in maintaining the internal shunts in good mechanical condition inside the magnet.

Finally, following a suggestion by General Electric, the cusp coils were wound with 0.0035-in.-thick high-purity (99.999%) aluminum foil between turns. The substantial thickness of the aluminum alters the space factor significantly, and full field operation could be closely approached only with careful selection of superconductor sections of highest short-sample performance for placement in the critical locations. Figure

[18] O. Smulkowski, pp. 519–23 in *Proceedings International Conference on Magnet Technology*, Oxford, England, December 1967.

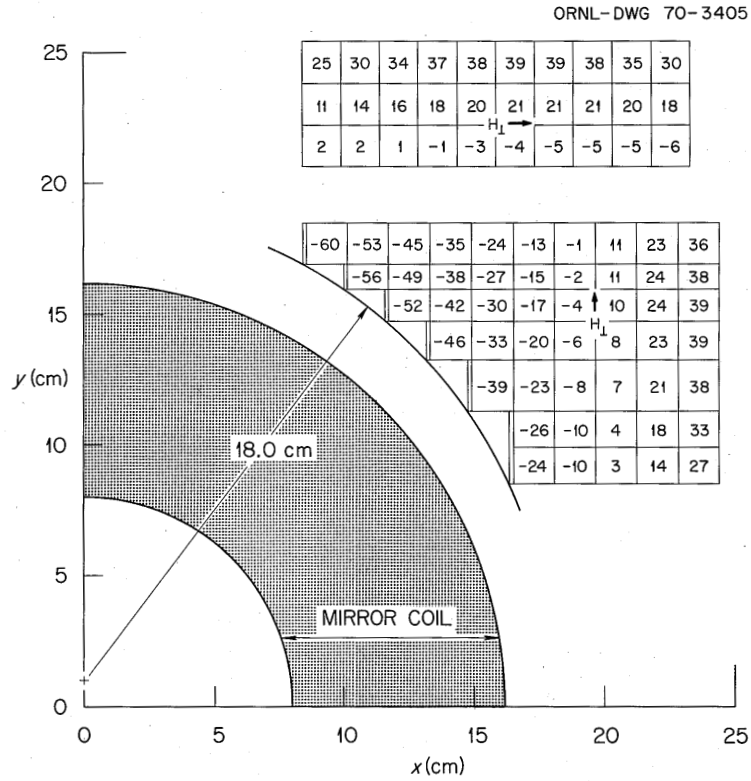


**Fig. 10.15. $B_{\perp}$ Components of IMP in Kilogauss.** Calculated for the midplane cross section of IMP.

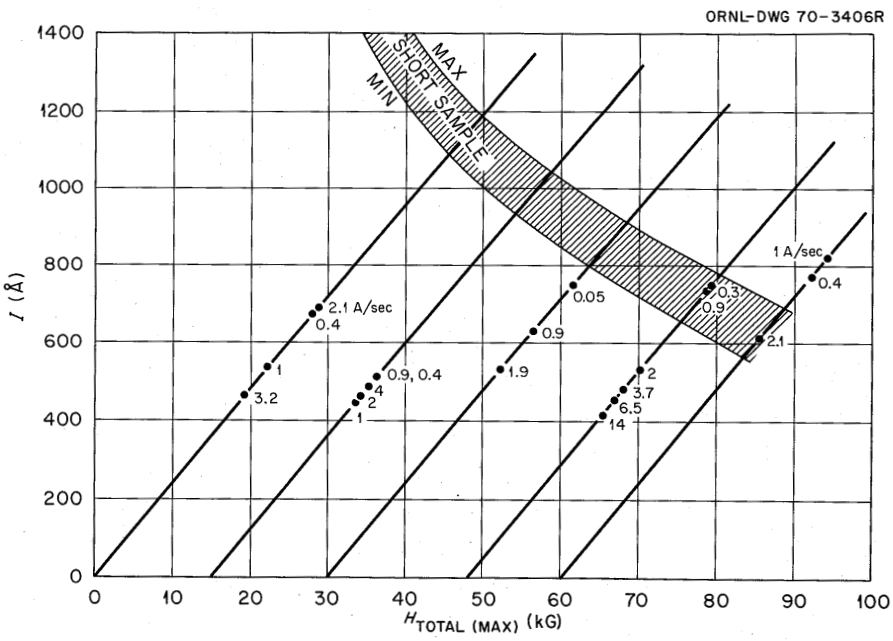


**Fig. 10.16. Results of Cusp-Coil Tests with $Nb_3Sn$ Production Samples.** $H - \Delta I$ sequence. The numbers indicate the rates of current rise in amperes per second.

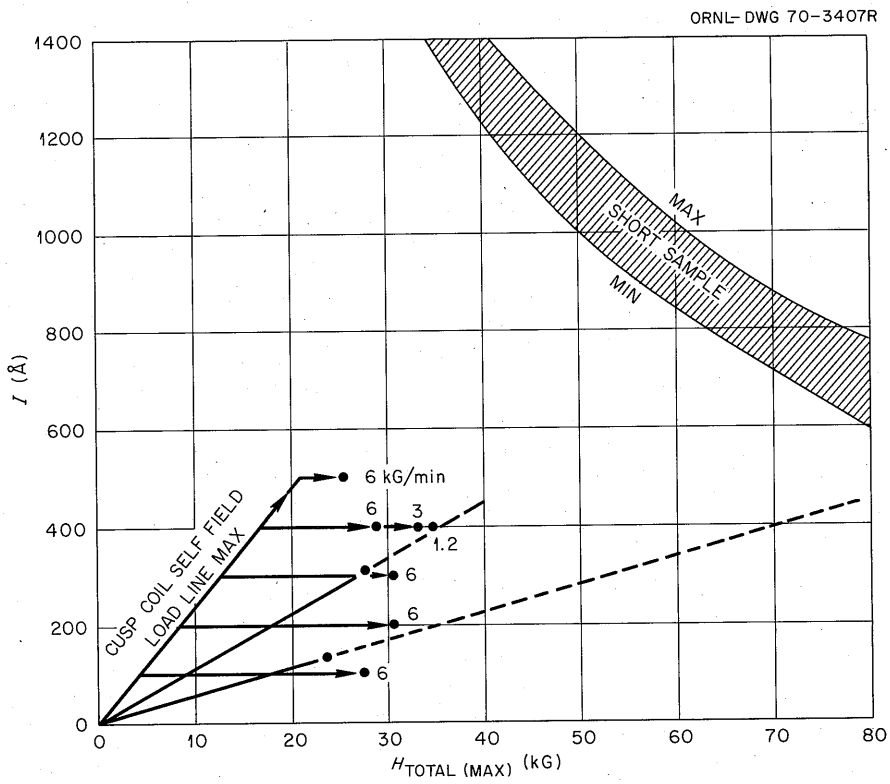


**Fig. 10.17. Results of Cusp-Coil Tests with $Nb_3Sn$ Production Samples.** Solid lines represent $I - \Delta H$ sequences; dashed lines represent $\Delta I - \Delta H$ sequences.

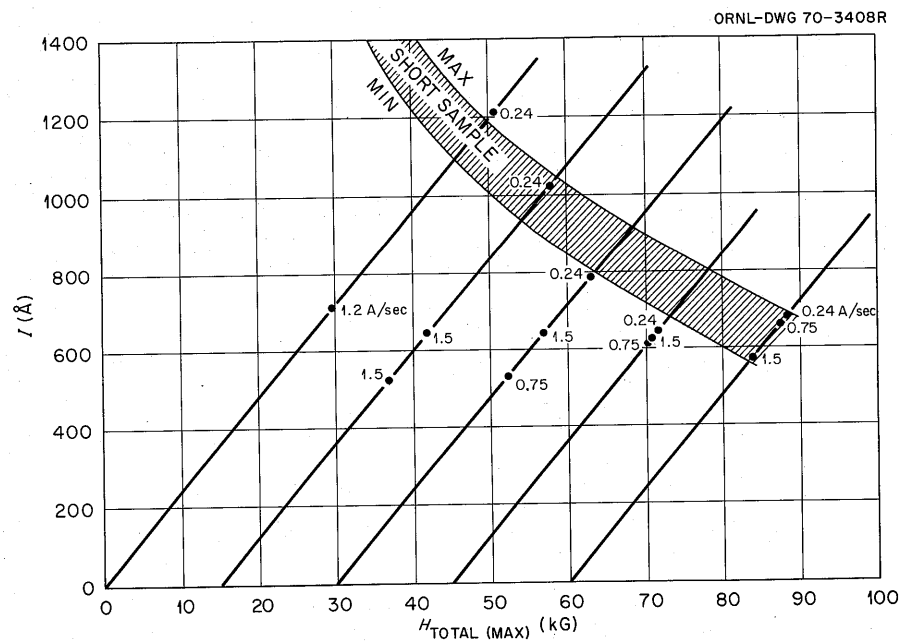


**Fig. 10.18. Results of Cusp-Coil Tests with $Nb_3Sn$ Production Samples Using Stabilization by Shunting Technique.** $H - \Delta I$ sequence.

10.19 shows that the technique is successful. If thinner ribbons (e.g., 0.002 in.) of even higher-purity aluminum are found to be equally effective and if plastic flow of the ribbon is adequately restrained by frictional forces, this will be the preferred method of winding the IMP quadrupole coils.

### 10.6.3 Stress Analysis of the Coil Cans

The mechanical configuration of the IMP mirror-quadrupole system is complex, and the magnetic forces at design central field ($B_0$ = 20 kG, with 1.3:1 radial well depth) are large; as a consequence, stress analysis of the system has been both difficult and protracted. The bulk of the work has been done by an outside contractor,[19] in close coordination with members of our own staff, and using, for the most part, the computing facilities of ORNL.

The approach has been that of finite-element analysis of the six basic portions of the complete coil system: one mirror coil can, one "regular" can and one "irregular" can of the four-coil quadrupole, and their covers. Each of these items appears in duplicate in the full system, but the force loadings are symmetric. The symmetry further made it sufficient to analyze only one-quarter of each basic portion. In developing the forces acting on the mechanical structure, it was not possible to take into account modification of the $\mathbf{j} \times \mathbf{B}$ forces by the coil windings themselves; the $\mathbf{j} \times \mathbf{B}$ forces were simply summed vectorially. Analyses were performed for standard operating conditions (all coils energized at rated currents) and for worst fault conditions (zero currents in certain coils). Most of the calculations assumed rigid bolted connections; the bolt stresses required by this boundary condition were computed from solutions for the body of the coil.

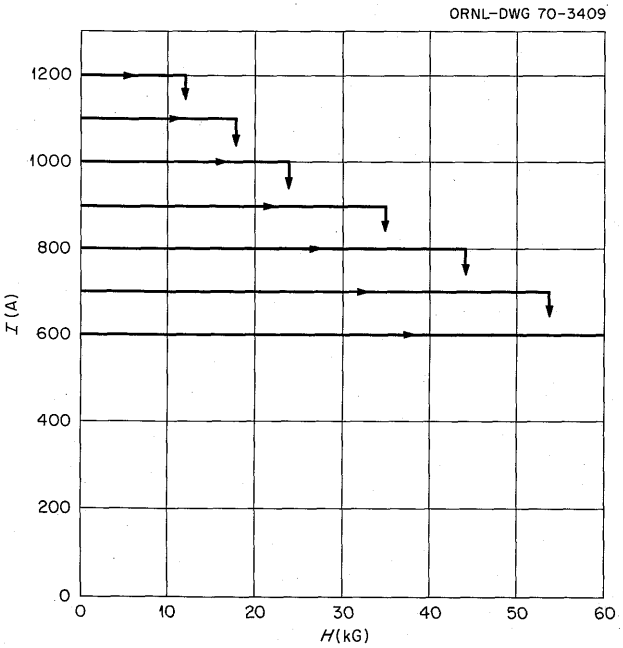


**Fig. 10.19. Results of Cusp-Coil Tests with $Nb_3Sn$ Production Samples Using Interwound 0.0035-in. High-Purity Aluminum Ribbons for Stabilization.** $I$ - $\Delta H$ sequence. At 600 A there was no transition at any applied field up to the maximum available.

For the quadrupole coils, the highest computed stress level was about 105,000 psi in the body of the coils, and the highest bolting stresses were about 125,000 psi. These figures seem quite acceptable, for the coil cans are of 21-6-9 alloy, which has a 0.2% tensile yield strength of about 195,000 psi at 4.2°K, and adequate bolting material seems available.[20]

For the mirror coils, the maximum stresses in the body of the material are about 75,000 psi on the basis of a model for which the rigid bolted connections were assumed. However, the bolt stresses that were computed to satisfy this condition exceed 300,000 psi. Additional computations in which the rigidity constraint was relaxed and the bolts were assumed to remain elastic regardless of stress level yielded similar maximum body stresses but even higher bolt stresses. These coil cans and covers are of annealed 310 stainless steel, for which the 0.2% yield strength is about 105,000 psi at 4.2°K. The material should be adequate at the computed stress levels, but there remains the problem of bolts, since there is no material available that can satisfy the calculated requirements. The highly stressed bolts are the ones that fasten the cylindrical outer covers onto the coils, and the very high stress levels arise here because of the thinness of the members to which these covers bolt. At certain locations there is a considerable bending moment acting to separate the covers from the coil cans, and there is insufficient moment arm with which to counteract this moment.

The experiments for which the completed coil system are intended will utilize considerably reduced fields ($B_{0\,max}$ = 12.5 kG) for an initial period. With a 1.3:1 well depth, the stress levels will therefore be reduced to

[19] The Franklin Institute Research Laboratories, Philadelphia, Pa.

[20] For the bolts, we will use Multiphase (MP35N) material. Test data (at 4.2°K from Lawrence Radiation Laboratory) are:

| | |
|---|---|
| 0.2% yield, 300°K | 260,000 psi |
| 0.2% yield, 4.2°K | 332,000 psi |
| Ultimate tensile, 4.2°K | 349,000 psi |

$(12.5/20)^2$ = 40% of those calculated in the analyses. The present mirror coils are adequate for this level. Studies of the bolting problem at full design level are continuing; it would be a relatively minor task to rebuild these mirror coils and avoid the problem should this prove necessary.

### 10.6.4 Status of Principal Mechanical Components

One pair of coil forms with covers has been completely machined and is on hand. The rest should be completed early in March 1970. The shop hours used on these now total 6664; the balance to completion of machining is estimated at 2213 h.

It is proposed to test the first pair of completed quadrupole coils in closely spaced mirror and cusp configurations. For this purpose, a 5-ft-diam test tank with a nitrogen-cooled radiation shield has been completed and vacuum checked. The helium Dewar for this test is now in the shop; reinforcing members to restrain the coils have been designed, and other items required for the test rig are in a final design state.

The microwave cavity, helium cans, suspension system, and other elements of the complete phase II assembly are in a conceptual design stage, which will soon advance to detailed drawings.

# 11. Fusion Feasibility

## 11.1 INTRODUCTION

H. Postma

The studies of the feasibility of engineering a fusion reactor based on our present concept of relevant plasma physics have continued this year, but at a slightly slower pace than last year. This was mainly a result of the selection of more difficult tasks for which answers were needed, and it is these tasks that are presented in the body of this chapter.

The many studies of feasibility conducted throughout the world for the past year and a half were presented at the International Conference on Nuclear Fusion Reactors, Culham Laboratory, England, September 17–19, 1969. While the object of the conference was to present in a systematic fashion the problems and solutions relating to engineering aspects of fusion reactors, some have interpreted that meeting as indicating that fusion reactors were practically a reality. That, unfortunately, is not true. But, in fact, the working sessions of the conference pointed out very clearly those problem areas needing much more work, and, as a result, many of the questions now being pursued at ORNL reflect these concerns.

The groups at the various laboratories communicate through technical memoranda, and since these are paper studies and are reporting on specific problems, they generally appear rapidly. Therefore, as in last year's annual report, the work of the past year is mainly presented in abstract form; ongoing work is described briefly in the last section.

## 11.2 FUSION REACTOR MATERIALS

The main material problems in a conceptual fusion reactor pertain to the container vacuum wall. There, sputtering by energetic particles, neutron damage by 14-MeV neutrons, and corrosion by 1000°C lithium cooling exact their toll. We have examined some of these difficulties and in this section consider the consequences.

### 11.2.1 Sputtering

O. C. Yonts

During the past year, the sputtering of niobium by 20-keV ions has continued. This work was reported in ORNL-TM-2602[1] and will be published in the proceedings of the Culham conference.

Some additional information on the absorption of gases by Nb-Zr targets has been obtained. In ORNL-TM-2692 it was assumed that the increase in weight of Nb-Zr targets was due to absorbed $D^+$ ions. Chemical analysis of one of the first targets used has shown this to be in error. The primary absorbed gas was oxygen. Normal oxygen content of Nb-Zr is 200 ppm by weight. Samples from various parts of the target ranged from 500 to 1700 ppm. This increase in oxygen content can account for the weight gain of the target. How the oxygen is held or even how it got into the target is not known.

Two recent experiments done with a small target (the size target used to get the niobium data for ORNL-TM-2692) show that with a rapid cool-down in a helium atmosphere Nb-Zr targets lose weight and show a sputtering ratio of 0.009. This compares with a value of 0.0013 for Nb-Zr by indirect methods. Nothing further has been done in this matter.

The results reported in the last annual report were corroborated at the Culham conference by the results of G. M. McCracken.[2]

We repeat here the abstract of ORNL-TM-2692 for completeness.

The sputtering of niobium by $D^+$ and $He^+$ ions has been measured at a temperature of 1100°C. The sputtering ratios of

[1] O. C. Yonts, *Sputtering of Niobium by $D^+$ and $He^+$ Ions*, ORNL-TM-2692 (September 1969).

[2] G. M. McCracken, paper to be published in the proceedings of the International Conference on Nuclear Fusion Reactors held at the Culham Laboratory (UKAEA), England, Sept. 17–19, 1969.

0.0042 and 0.051, respectively, are very low. Some comparative data are given in an estimate made of the lifetime of a niobium wall in a thermonuclear reactor.

### 11.2.2 Radiation Damage

A feature common to all first-generation (D-T) fusion reactors is that the walls of the primary containment vessel will be subjected to a very high flux ($10^{15}$ neutrons $sec^{-1}$ $cm^{-2}$) of 14-MeV neutrons. In the schemes now envisioned the wall will most likely be fabricated from a niobium- or molybdenum-base alloy. The effects of the irradiation-produced atom displacements and transmutations on the properties of these materials cannot now be adequately predicted from presently available data.

A simple theory of radiation damage in solids asserts that the essential variable is the rate at which atoms are displaced from their lattice sites by interactions with incident radiation. If this view is correct, fusion reactor radiation damage can be modeled by fission reactor experiments with due allowances made for the increased neutron energies in the fusion processes. For middle-mass elements such as niobium, the fission reactor dose rate and doses (flux densities and fluences) must be about four times the fusion dose rates and losses being simulated. In order to determine whether the assumptions underlying the modeling are sound or whether significant qualitative changes occur in the 14-MeV neutron irradiation, the Solid State Division is prepared (when adequate financing appears) to investigate this through damage introduced into thin niobium targets by heavy-ion bombardment. By varying the mass and energy of the bombarding ions, the energy spectrum of the niobium recoils could be altered. The damage appears as dislocation loops and small black spots in the electron microscope and thus could be compared with the body of information already available on fission-neutron damage in niobium.

Because of radiation damage the greatest potential problems are the volume increases and ductility decreases that may result from the operating conditions at the wall. The temperatures at which the reactor may operate (1000°C) are nearly identical to the temperature range in which void formation (and swelling) is predicted to occur, based on experience with several other metals. A further complication is the presence of large amounts of transmuted hydrogen and helium and of diffusing tritium, which may enhance the volume change problem. The ductility will also be affected by the reactor conditions. At the upper end of the possible temperature range, helium might affect the fracture mode and lead to a greatly reduced ductility. There are at present no data to suggest how important this effect could be. If the operating temperature of the reactor is lowered, the combination of irradiation and hydrogen-tritium concentration may raise the ductile-to-brittle transition temperature (DBTT) into the temperature range of interest.

Since niobium and Nb–1% Zr are the leading candidate materials, radiation damage studies should be concentrated on these. Experiments should attempt to define the temperature limits of void formation (and hence of swelling) to define the effect of transmutation-produced helium on the swelling behavior during irradiation, and to obtain preliminary results on the ductility following irradiations within the temperature range 500 to 1000°C. The effect of helium produced by fast-neutron transmutation reaction in the reactor can be simulated by using boron-doped niobium alloys to yield helium via the thermal-neutron $^{10}B(n,\alpha)^{7}Li$ reaction. Extensive examination by transmission electron microscopy can be correlated with immersion density measurements and mechanical properties tests. The helium production rate in the fusion reactor is 100 times as great as that resulting from the same flux in a fission reactor. Thus under the combination of high helium production and a factor of 4 due to energy difference, the fusion reactor seemingly faces a more severe radiation damage problem than the LMFBR does. This may drastically limit the useful lifetime of the vacuum wall.

The rationale behind the energy dependence of neutron damage was given at the Culham conference by Mark T. Robinson,[3] and the abstract is presented here:

A displacement cascade may be characterized by the *damage energy,* that is, by the kinetic energy of the primary recoil atom, corrected for the energy lost to electron excitation by all the particles comprising the cascade. The damage energy, suitably averaged over the primary recoil spectrum, is an appropriate measure of the dependence of radiation damage on the incident neutron energy. Mean damage energies have been calculated for 0.1- to 15-MeV neutron irradiation of C, Al, Cu, Nb, and Au, including anisotropic elastic scattering, inelastic scattering, and $(n,2n)$ reactions as the sources of primary recoils. Corrections for losses to electron excitation were based on theoretical calculations by Lindhard. In C, the damage energy reaches a maximum near a neutron energy of 1 MeV and falls slowly to about half this value at 15 MeV. In the other elements, the damage rises from 1 to 15 MeV, but by much

[3] M. T. Robinson, "The Energy Dependence of Neutron Radiation Damage in Solids," to be published in the proceedings of the International Conference on Nuclear Fusion Reactors held at the Culham Laboratory (UKAEA), England, Sept. 17–19, 1969.

smaller factors than the energy increase. In Cu, Nb, and Au, correctly accounting for the nuclear reactions is more important than a highly accurate description of electronic losses, but in C and Al, where the primary recoil energies are much higher, electronic energy losses play a more important role.

## 11.3 NEUTRONICS

The generation of tritium fuel through breeding is essential to the D-T fusion reactor. The work of last year was extended to include neutron spectra and power deposition. The results were presented at the Culham conference and are available in ORNL-TM-2648, the abstract of which is now reproduced.[4]

Two fusion reactor blanket designs have been compared on the basis of their neutronic behavior. The comparison included the areas of (1) tritium breeding, (2) nuclear heating, and (3) neutron irradiation effects within the vacuum wall, i.e., neutron-induced (*a*) atom displacements and (*b*) helium and hydrogen production. The two designs investigated differed only in their assumed vacuum wall coolants; design 1 employs lithium as the vacuum wall coolant, design 2 employs lithium-beryllium fluoride (flibe) as the vacuum wall coolant.

It is concluded that the neutronic behavior of a fusion reactor blanket employing lithium as the vacuum wall coolant is superior to that of one employing flibe. This superiority derives from the following factors: (1) The tritium breeding ratio of design 1 is ~10% higher than that of design 2. (2) The heat load in the niobium walls and the vacuum wall coolant is ~50% lower for design 1 than for design 2. (3) The neutron irradiation effects within the vacuum wall are essentially the same for both designs.

These results have subsequently been corroborated by other investigators using other methods. It now seems that further detailed work in neutronics at this stage is not vital. As cases of interest arise the programs are available, but general development now seems to be complete.

## 11.4 MIRROR FEASIBILITY

One paper dealing with finer details of mirror feasibility was presented at the Culham conference by D. J. Rose,[5] G. L. Flint, Jr.,[6] and F. B. Marcus[7] and was based on much work done at MIT.

An analysis of pulsed fusion systems indicates that operation for about 0.1 second at 10 teslas, in a device approaching 1 meter diameter may be most feasible. Such parameters are not far from those of proposed steady-state devices and are arrived at from studying properties of materials. A titanium-zirconium-molybdenum (TZM) coil appears most nearly satisfactory, taking into account tritium breeding, simple hoop stress, vacuum wall heating, and thermal stress. Energy balance in a steady-state mirror is affected by details of alpha particle slowing down, and by loss of synchrotron radiation. It appears that if the mean alpha slowing down time and lifetime are estimated correctly, the alpha heating will be approximately correctly estimated. Seriousness of synchrotron radiation loss and limitation of electron temperature to about 40 keV are confirmed by calculations made more consistently than hitherto. From these facts and others we conclude that obtaining favorable energy balance in mirrors is becoming even more difficult.

## 11.5 GENERAL CONSIDERATIONS

There were several papers[8,9] that considered the general impact of fusion reactors – hazards, safety, total use of energy, siting, steam cycles, costs, etc. The abstract of the Culham conference paper[8] gives the general appraisal of these considerations:

For study purposes a conceptual design for a thermonuclear power plant has been evolved to meet the total energy requirements of urban complexes in the year 2000. A layout for the plant including the principal auxiliaries is presented and some of the more important plant integration problems are discussed.

The rapid growth of urbanization and the consequent problems of environmental pollution are outlined together with the projected total energy requirements of the U.S. for the year 2000. Means for providing both electric power and heat for buildings and industrial processes with an economically attractive system are outlined together with a preliminary investigation of provisions for distillation of all the sewage from urban complexes. The results of the study show strong incentives to develop high temperature (~1000°C) rather than low temperature (~300°F) reactors, fusion rather than fission reactors, and basic designs suitable for economical plants in capacities down to and including 300 Mw(e), rather than very large plants.

## 11.6 WORK IN PROGRESS

Many crucial items are under study; we mention them only very briefly here, because they appear as mem-

[4] Don Steiner, *Neutronic Behavior of Two Fusion Reactor Blanket Designs,* ORNL-TM-2648 (July 1969); to be published in the proceedings of the International Conference on Nuclear Fusion Reactors held at the Culham Laboratory (UKAEA), England, Sept. 17–19, 1969.

[5] Director's Division.

[6] Nuclear Engineering Department, Massachusetts Institute of Technology, Cambridge, Mass.

[7] 1969 summer student from Massachusetts Institute of Technology.

[8] A. P. Fraas, "Conceptual Design of a Fusion Power Plant to Meet the Total Energy Requirements of an Urban Complex," to be published in the proceedings of the International Conference on Nuclear Fusion Reactors held at the Culham Laboratory (UKAEA), England, Sept. 17–19, 1969.

[9] A. P. Fraas, "Fusion Reactors as a Means of Meeting Our Total Energy Requirements," presented at the 1969 Winter Annual Meeting of the American Society of Mechanical Engineers, Los Angeles, Calif., Nov. 16–19, 1969.

oranda rather quickly. Diffusion of tritium in and its recovery from Nb, Nb-Zr, and Mo are being evaluated. We are investigating the D-D reaction rates and plasma balance much along the lines done by Rose[10] for D-T. Plasma synchrontron radiation is being evaluated. The $Q$ of mirror machines when electron temperatures are augmented is being calculated. The practical problems associated with plasma pumping, fuel feed, injection, and startup are being assessed. The hazards of fusion, particularly tritium, are being calculated and compared with the hazards of alternative energy sources. Altogether, many questions are now being attacked, and the next year is likely to see a much broader approach to fusion feasibility.

[10] D. J. Rose, *Nucl. Fusion* 9, 183–203 (1969).

# Publications, ORNL Reports, and Papers

## OPEN LITERATURE

| Author(s) | Title of Article | Journal (or Book) |
|---|---|---|
| I. Alexeff, G. E. Guest, W. D. Jones, J. R. McNally, Jr., R. V. Neidigh, and F. R. Scott[1] | Wave Correlation and Spectroscopic Studies of Beam Plasma Heating at Oak Ridge National Laboratory | P. 575 in *Proc. Ninth International Conf. Phenomena in Ionized Gases, 1969, Bucharest, Romania, Sept. 1–6, 1969* (ed. by Geavit Musa, Ion Ghica, Alexandrina Popescu, and Ligia Nastase, Inst. of Physics, Acad. of Socialist Republic of Romania) |
| I. Alexeff, G. E. Guest, J. R. McNally, Jr., R. V. Neidigh, and F. R. Scott[1] | Doppler Broadened Spectral Emission from the Turbulently Heated Plasma of Burnout V | *Phys. Rev. Letters* **23**, 281 (1969) |
| I. Alexeff, W. D. Jones, Karl Lonngren,[2] and D. Montgomery[3] | Transient Plasma Sheath – Discovered by Ion-Acoustic Waves | *Phys. Fluids* **12**, 345 (1969) |
| Philip B. Burt[4] | Dispersion in Inhomogeneous Plasma Streams | *J. Plasma Phys.* **3**, 417 (1969) |
| R. A. Dory, W. M. Farr,[5] G. E. Guest, and J. D. Callen[6] | Warm-Plasma Stabilization of Resonant Loss-Cone Instabilities | *Phys. Fluids* **12**, 2117 (1969) |
| H. Odell Eason, Jr. | Microwave Formation and Heating of Plasmas for Controlled Fusion Research | *J. Microwave Power* **4**(2), 88–99 (1969) |
| K. R. Efferson | Heat Transfer from Cylindrical Surfaces to Liquid Helium I | *J. Appl. Phys.* **40**, 1995 (1969) |
| J. Fukai,[7] S. Krishan,[7] and E. G. Harris[1] | Explosive Plasma Instabilities | *Phys. Rev. Letters* **23**, 910 (1969) |
| I. Alexeff, R. V. Neidigh, and W. R. Wing[8] | A Simple Gigacycle Correlator | *Intern. J. Eng. Sci.* **7**, 531–38 (1969) |
| Glenn Joyce,[2] Karl Lonngren,[2] I. Alexeff, and W. D. Jones | Dispersion of Ion-Acoustic Waves | *Phys. Fluids* **12**, 2592 (1969) |
| W. F. Gauster | Steady-State Performance of Multistrand Superconducting Compound Conductors | *J. Appl. Phys.* **40**, 2060–65 (1969) |
| W. F. Gauster | Steady State Stability of Composite Superconductors | *Cryogenics* **9**, 136 (1969) |

[1] Consultant, University of Tennessee.
[2] University of Iowa.
[3] Consultant, University of Iowa.
[4] Consultant, Clemson University.
[5] Present address, University of Arizona.
[6] Consultant, Massachusetts Institute of Technology.
[7] University of Tennessee.
[8] Student guest, University of Iowa.

| Author(s) | Title of Article | Journal (or Book) |
|---|---|---|
| A. Hirose, I. Alexeff, W. D. Jones, N. A. Krall,[9] and D. Montgomery[3] | Landau Damping of Electrostatic Ion Waves in a Uniform Magnetic Field | *Phys. Letters* **29A**, 31 (1969) |
| Wm. Denver Jones | Onde Sonore Nei Plasma [Sound waves in plasmas] | *Scuola Azione,* estratto dal n. 8, pp. 5–34, Metanopoli, San Donato Milanese (Agosto 1969) |
| M. O. Krause | Photo-Ionization of Krypton Between 300 and 1500 eV. Relative Subshell Cross Sections and Angular Distributions of Photoelectrons | *Phys. Rev.* **177**, 151 (1969) |
| D. M. Kroeger | A Peak Effect in Critical Current with Respect to Temperature and Field in a Type-II Superconductor | *Solid State Commun.* **7**(11), 843–47 (1969) |
| K. L. Vander Sluis[10] and J. R. McNally, Jr. | Recent Zeeman Results in Erbium I | *J. Opt. Soc. Am.* **59**, 1202–6 (1969) |
| D. J. Rose[11] | Engineering Feasibility of Controlled Fusion – a Review | *Nucl. Fusion* **9**(3), 183–203 (1969) |
| Ryo Sugihara[12] | Interaction Between an Electromagnetic Wave, Plasma Waves, and an Ion Acoustic Wave | *Phys. Fluids* **11**, 178 (1968) |
| H. Tanaca[12] | Parameter Resonance of an Ion Acoustic Wave in a Plasma | *J. Phys. Soc. Japan* **24**, 969 (1968) |
| R. V. Neidigh, I. Alexeff, G. E. Guest, W. D. Jones, D. C. Montgomery,[3] D. J. Rose,[11] and W. L. Stirling | Experimental Strong Turbulent Heating | *Plasma Physics and Controlled Nuclear Fusion Research,* vol. II, pp. 693–708, IAEA, Vienna, 1969 |
| I. Alexeff, A. Hirose, W. D. Jones, K. E. Lonngren,[2] and M. Widner | Pseudowaves – Multiple and Dispersive; Ion Waves in a Magnetic Field, and Non-Linear Phenomena | Pp. 85–92 in *Proc. International Conference on Physics of Quiescent Plasmas, Paris, France, Sept. 8–13, 1969,* part I, Laboratoire de Physique des Milieux Ionises, Ecole Polytechnique, Paris, 1969 |
| M. Roberts, I. Alexeff, R. A. Dory, W. Halchin, and W. L. Stirling | ORNL Levitated Toroidal Multipole Program | *Plasma Physics and Controlled Nuclear Fusion Research,* vol. I, pp. 351–65, IAEA, Vienna, 1969 |
| M. Widner, I. Alexeff, W. D. Jones, and K. E. Lonngren[2] | Computer Simulation of Ion Burst Excitation in a Plasma by Nonlinear Grid Effects | *Phys. Letters* **30A**, 119 (1969) |
| I. Alexeff and D. F. Howell[13] | Simple Circuit for Obtaining the Electron Energy Distribution in a Plasma | *J. Appl. Phys.* **40**, 4877 (1969) |
| J. F. Clarke | Feedback Destabilization of Mirror Machines by Microinstabilities | *Phys. Rev. Letters* **23**, 1215 (1969) |
| D. L. Coffey and W. F. Gauster | Progress on the IMP Facility | Pp. 929–43 in *Proc. 1968 Summer Study on Superconducting Devices and Accelerators, Brookhaven National Laboratory, Upton, New York, June 10–July 19, 1968,* BNL-50155, vol. III |
| W. F. Gauster | Standardized Tests for Superconducting Materials | Pp. 944–45 in *Proc. 1968 Summer Study on Superconducting Devices and Accelerators, Brookhaven National Laboratory, Upton, New York, June 10–July 15, 1968,* BNL-50155, vol. III |

[9] University of Maryland.
[10] Physics Division.
[11] Director's Division.
[12] Institute for Plasma Physics, Nagoya University, Nagoya, Japan.
[13] Department of Electrical Engineering, University of Tennessee.

| Author(s) | Title of Article | Journal (or Book) |
|---|---|---|
| M. S. Lubell and K. R. Efferson | Flux Pumps as Power Supplies in Comparison with Alternatives | Pp. 667–72 in *Proc. 1968 Summer Study on Superconducting Devices and Accelerators, Brookhaven National Laboratory, Upton, New York, June 10–July 15, 1968,* BNL-50155, vol. III |
| M. S. Lubell and D. M. Kroeger | Flux Flow Studies and Stability Criteria of NbTi Strips | *Advan. Cryogenic Eng.* **14**, 123–32 (1969) |

## ORNL REPORTS

| Author(s) | Title | Number |
|---|---|---|
| G. R. Dyer, W. J. McClain, and M. M. Satterfield | A System for Recording and Displaying Radioisotope Scan Data | ORNL-TM-2396 |
| M. M. Satterfield, G. R. Dyer, D. A. Ross, and W. J. McClain[1] | A New Medical Spectrometer | ORNL-TM-2419 |
| E. G. Harris[2] | Velocity-Anisotropy Instabilities | ORNL-TM-2470 |
| E. G. Harris[2] | Classical Plasma Phenomena from a Quantum Mechanical Viewpoint | ORNL-TM-2519 |
| R. A. Dandl, H. O. Eason, P. H. Edmonds, A. C. England, and A. H. Snell | Radioactivity Induced by Particle Acceleration in an Unstable Laboratory Plasma | ORNL-TM-2540 |
| J. Rand McNally, Jr. | The Coulomb Logarithm for Heavy Test Ions in Plasmas | ORNL-TM-2607 |
| W. L. Stirling and I. Alexeff | A Turbulently Heated Electron Plasma | ORNL-TM-2631 |
| I. Alexeff, W. D. Jones, and M. Widner | Multiple Pseudowaves Produced by a Single Voltage Pulse | ORNL-TM-2634 |
| R. J. Colchin, J. L. Dunlap, and H. Postma | Evolution and Stabilization of Flutes in a Magnetic Mirror | ORNL-TM-2639 |
| W. F. Gauster, K. R. Efferson, M. S. Lubell, J. D. McDowell, and S. L. Wipf | Magnetic Flux Flow and Superconductor Stabilization | ORNL-TM-2641 |
| Don Steiner[3] | Neutronic Behavior of Two Fusion Reactor Blanket Designs | ORNL-TM-2648 |
| J. Fukai,[4] S. Krishan,[5] and E. G. Harris[2] | Explosive Plasma Instabilities | ORNL-TM-2652 |
| M. M. Satterfield, G. R. Dyer, and W. J. McClain[1] | An Overload Cancellation Circuit for a Charge-Sensitive Preamplifier | ORNL-TM-2654 |
| I. Alexeff, W. D. Jones, and M. Widner | Multiple Pseudowaves Produced by a Single Voltage Pulse (expanded version of ORNL-TM-2634) | ORNL-TM-2656 |
| Philip B. Burt[6] | Integral Solutions to the Generalized Helmholtz Equation | ORNL-TM-2658 |
| Igor Alexeff and Wm. Denver Jones | Basic Interaction Producing Plasma Heating in the Oak Ridge National Laboratory Mode II Pressure Gradient Arc | ORNL-TM-2661 |
| K. R. Efferson | A Superconducting (Nb-Ti) Liquid Helium Level Detector | ORNL-TM-2665 |

[1] ORGDP.
[2] Consultant, University of Tennessee.
[3] Reactor Division.
[4] University of Tennessee summer guest, 1969.
[5] Summer Faculty, University of Tennessee, 1969.
[6] Consultant, Clemson University.

| Author(s) | Title | Number |
|---|---|---|
| A. Hirose, I. Alexeff, and W. D. Jones | Landau Damping of Ion Acoustic Waves in a Uniform Magnetic Field | ORNL-TM-2678 |
| O. C. Yonts | Sputtering of Niobium By $D^+$ and $He^+$ Ions | ORNL-TM-2692 |
| W. L. Stirling, M. Roberts, and I. Alexeff | Effects of Introducing Supports in a Levitated Toroidal Quadrupole | ORNL-TM-2701 |
| M. Widner, I. Alexeff, and W. D. Jones | Ion Acoustic Wave Excitation and Ion Sheath Evolution | ORNL-TM-2754 |
| A. Hirose, I. Alexeff, and W. D. Jones | Dispersion Measurements of Electrostatic Ion Waves in a Uniform Magnetic Field | ORNL-TM-2761 |
| Edward G. Harris[2] | Stability of Tokamaks | ORNL-TM-2766 |
| R. J. Colchin and J. L. Dunlap | Harris Instabilities in a Plasma of Finite Length | ORNL-TM-2767 |
| W. F. Gauster, K. R. Efferson, D. M. Kroeger, and M. S. Lubell | Magnetic Flux Flow and Superconductor Stabilization | ORNL-TM-2771 |
| J. E. Robinson[7] and J. F. Clarke | Time Resolution of Plasma Potential Using Gridded Electrostatic Analyzers | ORNL-TM-2789 |
| G. E. Guest, R. A. Dory, and W. M. Farr[8] | High Frequency Flute-Like Instabilities in Multi-Component Plasmas | ORNL-TM-2798 |
| C. F. Barnett, D. A. Griffin, M. O. Krause, J. R. McNally, Jr., J. A. Ray, and I. A. Sellin | Bibliography of Atomic and Molecular Processes for July–December 1968 | ORNL-AMPIC-12 |
| Milan Wayne Garrett[9] | Tables of the Fabry Factors *G* and *V*, and of Magnetic Field Homogeneity for Thick Cylindrical Coils | ORNL-4281 |
| Thermonuclear Division Staff | Thermonuclear Division Annual Progress Report for Period Ending December 31, 1968 | ORNL-4401 |
| J. A. Ray and C. F. Barnett | Characteristics of a Funnel Type Electron Channel Multiplier with a Grid Entrance Window | ORNL-TM-2818 |
| G. G. Kelley, M. Roberts, and J. F. Clarke | Conceptual Design of ORMAK Facility | ORNL-TM-2821 |
| W. F. Gauster, J. L. Horton,[10] D. M. Kroeger, G. F. Leichsenring, M. S. Lubell, and J. D. McDowell[11] | Magnetic Flux Flow and Superconductor Stabilization | ORNL-TM-2534 |

[7] Massachusetts Institute of Technology.
[8] University of Arizona.
[9] Consultant, Swarthmore College.
[10] Instrumentation and Controls Division.
[11] Mathematics Division.

## PAPERS PRESENTED AT SCIENTIFIC AND TECHNICAL MEETINGS

*American Physical Society, New York, N.Y., February 3–6, 1969* [*Bull. Am. Phys. Soc.* **14** (January 1969)]

I. Alexeff, "Ionic Sound Waves in Plasmas – Problems Past and Future Plans" (invited paper).

*Physics Symposium of Berea Physics Department, Berea College, Kentucky, March 28–29, 1969* [Proc. Waldemar Noll Physics Symposium, *The Berea Alumnus*, Mar. 28–29, 1969]

Wm. Denver Jones, "Ion Acoustic Waves."

*Annual Sherwood Theory Meeting, Gatlinburg, Tennessee, April 24–25, 1969* (will not be published)

E. G. Harris,[1] J. Fukai,[2] and S. Krishan,[2] "Wave-Wave Interactions, Wave Particle Scattering, and Explosive Instabilities."

*American Physical Society Spring Meeting, Washington, D.C., April 28–May 1, 1969* [*Bull. Am. Phys. Soc.* **14** (April 1969)]

Melvin Widner, Igor Alexeff, and Wm. Denver Jones, "Computer Simulation of Ion Sheath Evolution and Ion Acoustic Wave Excitation."

Michael Roberts and Igor Alexeff, "A Quasi-Superconducting Mode for the Levitated Toroidal (Copper) Quadrupole Magnetic Field."

A. Hirose, I. Alexeff, and W. D. Jones, "Electrostatic Ion Waves in a Uniform Magnetic Field."

*Symposium on Engineering Problems of Fusion Research, Los Alamos Scientific Laboratory, Los Alamos, New Mexico, April 8–11, 1969* (*Proc. Symp. on Engineering Problems of Fusion Research,* Los Alamos report LA-4250)

E. A. Ferguson, J. L. Horton,[3] C. E. Parker, E. R. Wells, W. L. Wright, Z. Zudans,[4] and A. G. Hopper,[4] "Coil Forces and Coil Case Stresses in the ORNL IMP Machine."

R. C. Davis, J. N. Luton, Jr., O. D. Matlock, and W. L. Wright, "Minimum-*B* Configuration in the INTEREM Facility."

J. S. Culver, "A Simple Inexpensive Titanium Sublimator."

D. L. Coffey and W. F. Gauster, "Superconductor Evaluation Tests for IMP."

R. J. Colchin, J. L. Dunlap, R. S. Edwards, D. P. Hammond,[5] L. A. Massengill, T. F. Rayburn, R. G. Reinhardt, and E. R. Wells, "The IMP Facility at Oak Ridge National Laboratory."

R. L. Brown, "Winding Techniques for Superconducting Magnets."

M. Roberts, I. Alexeff, W. L. Stirling, and W. Halchin, "Magnetic Properties of the ORNL Levitated Toroidal Quadrupole."

*1969 Symposium on Microwave Power (4th Technical Conference and Meeting of the International Microwave Power Institute), Edmonton, Alberta, Canada, May 21–23, 1969* [*J. Microwave Power* **4**(2) (1969)]

H. Odell Eason, Jr., "Microwave Formation and Heating of Plasmas for Controlled Fusion Research."

*1969 Cryogenic Engineering Conference, University of California, Los Angeles, California, June 16–18, 1969* (to be published in *Advances in Cryogenic Engineering,* vol. 15, K. D. Timmerhaus, ed.; 1969)

K. R. Efferson, "A Superconducting (Nb-Ti) Liquid Helium Level Detector."

---

[1] Consultant, University of Tennessee.
[2] Department of Physics, University of Tennessee.
[3] Instrumentation and Controls Division.
[4] The Franklin Institute Research Laboratories, Philadelphia, Pa.
[5] On leave from Culham Laboratory, England.

*American Physical Society, Rochester, New York, June 18–20, 1969* [*Bull. Am. Phys. Soc.* **14** (June 1969)]

M. Widner, I. Alexeff, and W. D. Jones, "Further Investigation of Ion Sheath Evolution and Ion Acoustic Wave Excitation."

J. Rand McNally, Jr., "A Novel Concept for Startup of Controlled Fusion Reactions."

W. D. Jones and I. Alexeff, "Multiple Pseudowaves Produced by a Single Voltage Pulse."

I. Alexeff, W. D. Jones, and A. Hirose, "Electron Landau Damping of Ion Acoustic Waves in a Uniform Magnetic Field."

Richard J. Colchin, "Plasma Model Including Finite Length Effects."

I. Alexeff and R. V. Neidigh, "Correlation Studies of Turbulent Heating of Ions in Burnout V."

*International Conference on Ion Sources, CEN, Saclay, France, June 18–20, 1969* (proceedings to be published)

George G. Kelley, O. B. Morgan, and R. C. Davis, "Ion Source Development for Thermonuclear Research."

*International Symposium on Closed Confinement Systems, Dubna, U.S.S.R., September 29–October 3, 1969* (proceedings to be published)

G. G. Kelley, M. Roberts, and J. F. Clarke, "Conceptual Design of ORMAK Facility."

M. J. Lubin,[6] M. Roberts, W. Friedman,[7] and I. Alexeff, "Plasma Confinement in the University of Rochester–ORNL Toroidal Quadrupole."

*Third European Conference on Controlled Fusion and Plasma Physics, Utrecht, Netherlands, June 23–27, 1969*

J. L. Dunlap, G. R. Haste, W. J. Herrmann,[8] and N. H. Lazar, "Electron-Cyclotron Heated Plasmas in a Minimum-*B* Configuration."

C. O. Beasley, Jr., W. M. Farr, and Hubert Grawe,[8] "Microinstabilities in Finite Mirror Plasmas."

*Eighth Annual Argonne Universities Association–Argonne National Laboratory Student-Faculty Conference, August 18–22, 1969, Argonne, Illinois*

Gareth E. Guest, "Theory of High-Frequency Instabilities in Mirror-Confined Plasmas."

*Conference on Science of Superconductivity, Stanford University, Stanford, California, August 26–29, 1969* (to be published in *Physica*)

M. S. Lubell and D. M. Kroeger, "Evidence to Support the Rigidly Pinned Vortex Model for the Peak Effect."

*Ninth International Conference on Phenomena in Ionized Gases, Bucharest, Romania, September 1–6, 1969 (Proc. Ninth International Conf. on Phenomena in Ionized Gases, Bucharest, 1969)*

I. Alexeff, G. E. Guest, W. D. Jones, J. R. McNally, Jr., R. V. Neidigh, and F. R. Scott,[1] "Wave Correlation and Spectroscopic Studies of Beam Plasma Heating at Oak Ridge National Laboratory."

*International Conference on Physics of Quiescent Plasmas, Ecole Polytechnique, Paris, France, September 8–13, 1969 (Proc. Intern. Conf. on Physics of Quiescent Plasmas, Paris, France, Sept. 8–13;* publ. Laboratoire de Physique des Milieux Ionises, Ecole Polytechnique, Paris, France, 1969, part 1)

I. Alexeff, A. Hirose, W. D. Jones, K. E. Lonngren,[9] and M. Widner, "Pseudowaves – Multiple and Dispersive; Ion Waves in a Magnetic Field; and, Non-Linear Phenomena."

---

[6]Consultant, University of Rochester.
[7]University of Rochester.
[8]Institut für Plasmaphysik, West Germany.
[9]University of Iowa.

*International Conference on Nuclear Fusion Reactors, Culham Laboratory, Abingdon, Berks., England, September 17–19, 1969* (proceedings to be published)

Don Steiner,[10] "Neutronic Behavior of Two Fusion Reactor Blanket Designs."

A. P. Fraas,[10] "Conceptual Design of a Fusion Power Plant to Meet the Total Energy Requirements of an Urban Complex."

O. C. Yonts, "Sputtering Measurements on Vacuum Walls by Energetic Deuterons and Protons."

*Mid-Southeastern Chapter, Association for Computing Machinery, Atlanta, Georgia, October 10, 1969* (proceedings will not be published)

W. J. McClain,[11] G. R. Dyer, and D. A. Ross, "The Use of the Digital Computer for Processing Radioisotope Scan Data."

*American Physical Society, 22nd Annual Gaseous Electronics Conference and High Pressure Arc Symposium, Gatlinburg, Tennessee, October 29–31, 1969* (to be published in *Bull. Am. Phys. Soc.*)

J. Rand McNally, Jr., "The Coulomb Logarithm for Ions Slowing Down on Electrons in a Plasma."

M. O. Krause, F. A. Stevie,[12] L. J. Lewis,[13] T. A. Carlson,[14] and W. E. Moddeman,[12] "Multiple Electron Ionization of Neon by Electron and Photon Impact."

Hans Fleischmann,[15] C. F. Barnett, and J. A. Ray, "Small-Angle Scattering of Stripping Collisions of Hydrogen Atoms on Various Gases."

*IEEE Nuclear Science Symposium, San Francisco, California, October 29–31, 1969* [to be published in *IEEE Trans. Nucl. Sci.* **NS-17** (February 1970)]

J. A. Ray and C. F. Barnett, "Characteristics of a Funnel Type Electron Channel Multiplier with a Grid Entrance Window."

*American Society of Mechanical Engineers, Los Angeles, California, November 16–19, 1969*

A. P. Fraas[10] and D. J. Rose,[16] "Fusion Reactors as a Means of Meeting Our Total Energy Requirements."

*American Physical Society, Division of Plasma Physics, Los Angeles, California, November 12–15, 1969* [*Bull. Am. Phys. Soc.* **14** (November 1969)]

I. Alexeff, W. D. Jones, and K. Lonngren,[9] "Violent Turbulence in a Simple Discharge-Tube Plasma."

I. Alexeff, W. D. Jones, K. Lonngren,[9] F. R. Scott,[1] and K. G. Estabrook,[17] "Reflection of Ion Bursts (Pseudowaves)."

C. O. Beasley, W. M. Farr,[18] and H. Grawe,[8] "Effects of Plasma Inhomogeneities on Microinstabilities in Mirror Confined Plasmas: Theory."

R. A. Blanken,[19] N. H. Lazar, and W. J. Herrmann, "Low Density Cyclotron Instability in a Hot Electron Plasma."

P. B. Burt,[20] "Dispersion in Inhomogeneous Plasma Streams."

---

[10] Reactor Division.
[11] ORGDP.
[12] Vanderbilt University.
[13] 1969 summer student, Morehouse College.
[14] Physics Division.
[15] Consultant, Cornell University.
[16] Director's Division.
[17] Student guest, University of Tennessee.
[18] University of Arizona.
[19] Consultant, Massachusetts Institute of Technology.
[20] Consultant, Clemson University.

J. D. Callen[19] and G. E. Guest, "Ion-Ion and Ion-Electron Electrostatic Cyclotron Instabilities: When Do Electromagnetic Corrections Become Important?"

R. J. Colchin and J. L. Dunlap, "Harris Modes of Finite Length."

R. A. Dandl, W. B. Ard, H. O. Eason, P. H. Edmonds, A. C. England, and S. T. Nolan,[21] "Stochastic and Resonant Heating of Plasma Electrons."

R. A. Dory, "High Beta Equilibria in Tokamaks with Large Toroidal Curvature."

Owen Eldridge,[1] "Non-Linear Landau Damping Boundaries."

A. C. England, R. A. Dandl,[3] H. O. Eason, P. H. Edmonds, and A. H. Snell,[16] "Radioactivity Induced by Particle Acceleration in an Unstable Laboratory Plasma."

W. M. Farr,[18] C. O. Beasley, and H. Grawe,[8] "Effects of Plasma Inhomogeneities on Microinstabilities in Mirror Confined Plasmas: Results."

H. K. Forsen[22] and O. B. Morgan, "Space Charge Neutralization of Ion Beams for Intense Low Energy Plasma Physics Injectors."

G. E. Guest and L. S. Hall,[23] "The Beam-Plasma Interaction with a Plasma Density Gradient."

E. G. Harris,[1] "Stability of the Bennett Pinch."

A. Hirose and Karl Lonngren,[9] "Dispersion of Drift Waves."

W. D. Jones, I. Alexeff, and W. L. Stirling, "Mechanism of the First Oak Ridge Beam-Plasma-Interaction Device – Mode II."

S. Krishan[2] and A. A. Selim,[24] "Linear and Non-Linear Collisional Interaction of Waves."

N. H. Lazar, "Electron Cyclotron Heated Plasma in a Magnetic Well Geometry" (invited paper).

K. E. Lonngren,[9] I. Alexeff, O. Eldridge,[1] and W. D. Jones, "Ion Bursts and the Ballistic Term in Landau's Paper."

O. B. Morgan, R. C. Davis, and G. G. Kelley, "A Hydrogen Cluster Ion Source for Thermonuclear Research."

J. Rand McNally, Jr., R. V. Neidigh, and F. R. Scott,[1] "Doppler Studies in the Burnout V Device."

R. V. Neidigh, I. Alexeff, G. E. Guest, F. R. Scott,[1] and J. R. McNally, Jr., "Doppler Broadened Spectra and Transient Electric Fields in Burnout V."

J. N. Olsen,[25] C. E. Nielsen,[26] and R. V. Neidigh, "Far Infrared Laser Interferometer Measurement of Plasma Density."

M. Roberts, J. F. Clarke, and G. G. Kelley, "Design of ORMAK."

F. R. Scott,[1] J. R. McNally, Jr., and R. V. Neidigh, "Electric Field Measurements in Burnout V Using the Satellite Lines of Helium."

D. J. Sigmar and J. D. Callen,[19] "Wave-Particle Energy Transfer and Wave Amplitude Limiting Effects."

D. J. Sigmar, "Effect of Cold Electrons on Target Plasma Instabilities."

W. L. Stirling, I. Alexeff, R. V. Neidigh, and K. G. Estabrook,[17] "Soft X-Ray Spectrum Emitted from the Electron Beam of Burnout V."

M. Widner, I. Alexeff, and W. D. Jones, "Interaction of an Ion Acoustic Wave with a Steady-State Sheath."

---

[21] Research Participant, 1969, from University of South Alabama.
[22] Consultant, University of Wisconsin.
[23] Lawrence Radiation Laboratory.
[24] University of Alberta, Canada.
[25] ORAU Graduate Fellow, Ohio State University.
[26] Consultant, Ohio State University.